Structure and mobility of solvents and solutes at solid-liquid interfaces in mesopore models with different pore geometries obtained from molecular dynamics simulations

Kumulative Dissertation

zur Erlangung des Grades eines

Doktor der Naturwissenschaften

(Dr. rer. nat.)

des Fachbereichs Chemie der Philipps-Universität Marburg

vorgelegt von

Nicole Trebel

geboren in Fulda

Marburg an der Lahn, 2023

Abgabedatum: 18.08.2023.

Vom Fachbereich Chemie der Philipps-Universität Marburg (Hochschulkennziffer 1180) als Dissertation angenommen am: 18.08.2023.

Erstgutachter: Prof. Dr. Ulrich Tallarek

Zweitgutachter: apl. Prof. Dr.-Ing. Niels Hansen

Tag der mündlichen Prüfung: 23.10.2023.

Die vorliegende Arbeit wurde in der Zeit von August 2019 bis August 2023 am Fachbereich Chemie der Philipps-Universität Marburg unter Leitung von Herrn Prof. Dr. Ulrich Tallarek angefertigt.

Teile der Dissertation wurden bereits in den folgenden Artikeln veröffentlicht:

1 N. Trebel, A. Höltzel, A. Steinhoff, U. Tallarek
„Insights from molecular simulations about dead time markers in reversed-phase liquid chromatography"
J. Chromatogr. A **2021**, *1640*, 461958. DOI: 10.1016/j.chroma.2021.461958.

2 N. Trebel, A. Höltzel, J. K. Lutz, U. Tallarek
„Consequences of Cylindrical Pore Geometry for Interfacial Phenomena in Reversed-Phase Liquid Chromatography"
J. Phys. Chem. B **2021**, *125*, 11320−11336. DOI: 10.1021/acs.jpcb.1c06732.

3 N. Trebel, A. Höltzel, U. Tallarek
„Confinement Effects on Distribution and Transport of Neutral Solutes in a Small Hydrophobic Nanopore"
J. Phys. Chem. B **2022**, *126*, 7781–7795. DOI: 10.1021/acs.jpcb.2c04924.

4 F. Gritti, N. Trebel, A. Höltzel, U. Tallarek
„Prediction of surface excess adsorption and retention factors in reversed-phase liquid chromatography from molecular dynamics simulations"
J. Chromatogr. A **2022**, *1685*, 463627. DOI: 10.1016/j.chroma.2022.463627.

5 U. Tallarek, D. Hlushkou, N. Trebel, A. Höltzel
„Probing Surface Chemistry Effects on Effective Diffusion Coefficients in Hierarchically Porous Media Through Multiscale Simulations"
Chem. Ing. Tech. **2023**, *95*, in press. DOI: 10.1002/cite.202300027.

Danksagung

An dieser Stelle möchte ich gerne den Menschen danken, die in den letzten vier Jahren mit mir zusammengearbeitet und mich im Rahmen meiner Promotion und darüber hinaus unterstützt haben.

Mein besonderer Dank gilt meinem Doktorvater Herrn Prof. Dr. Ulrich Tallarek, der es mir ermöglichte, an dieser sehr interessanten und anspruchsvollen Thematik zu arbeiten. Ich möchte mich für unsere zahlreichen Diskussionen und die Förderung meiner wissenschaftlichen Arbeit bedanken, nicht zuletzt aufgrund der Möglichkeit, meine Forschung auf verschiedenen internationalen Konferenzen präsentieren zu können.

Herrn apl. Prof. Dr.-Ing. Niels Hansen danke ich herzlich für die Übernahme des Zweitgutachtens. Außerdem bedanke ich mich bei Herrn Prof. Dr. Lars-Oliver Essen dafür, als drittes Mitglied die Prüfungskommission zu vervollständigen.

Des Weiteren möchte ich mich bei den Mitgliedern der Arbeitsgruppe Tallarek für die gemeinsam verbrachte Zeit bedanken. Frau Dr. Alexandra Höltzel danke ich für die zahlreichen fruchtbaren Diskussionen und die Unterstützung bei meinen wissenschaftlichen Fragenstellungen. Bei Frau Dr. Julia Rybka möchte ich mich für die Einarbeitung in meine Thematik sowie die hilfreichen fachlichen Gespräche bedanken. Herrn Dr.-Ing. Dzmitry Hlushkou danke ich für die technischen Ratschläge und die Zusammenarbeit im Rahmen unseres gemeinsamen Projektes. Für die engagierte Zusammenarbeit im Rahmen von Forschungspraktika und Masterarbeiten möchte ich mich bei Daniel Frerichs, Julia Lutz, Andreas Steinhoff und Konstantin Stumpf bedanken.

Meiner Familie und meinem Freund danke ich von ganzem Herzen für die fortwährende Unterstützung, ohne die mein Studium und diese Arbeit nicht möglich gewesen wären.

Contents

I. Zusammenfassung

Mithilfe von Computersimulationen können chemische Prozesse auf molekularer Ebene untersucht werden und finden daher in vielen Teilbereichen der Chemie und für zahlreiche chemische (Mess)methoden Anwendung. In der Hochleistungsflüssigkeitschromatographie (HPLC, high performance liquid chromatography) werden theoretische Modelle und Berechnungen herangezogen, um vorherrschende Wechselwirkungen an fest-flüssig Grenzflächen der verwendeten porösen Materialien zu charakterisieren, was einen entscheidenden Beitrag zum grundlegenden Verständnis, aber auch zur Optimierung dieser Trenntechnik liefert. Die vorliegende Arbeit befasst sich mit dem molekularen Bild einzelner Mesoporen aus der stationären Phase in der Umkehrphasenchromatographie (RPLC, *reversed-phase liquid chromatography*). Die RPLC ist die am häufigsten eingesetzte HPLC-Methode, die sich für die Trennung von unpolaren bis mäßig polaren Analyten eignet. Als stationäre Phasen werden hydrophob modifizierte Silica-Partikel oder Silica-Monolithen und als mobile Phasen wässrig-polare binäre Lösungsmittelgemische verwendet. Zur Bestimmung von Retentionsfaktoren wird die Totzeit der chromatographischen Säule benötigt. Hierfür werden Totzeitmarker eingesetzt; kleine, inerte Moleküle, die idealerweise keine Wechselwirkungen mit der stationären Phase eingehen. Ein Teil dieser Arbeit beschäftigt sich mit der Untersuchung von zwei gängigen Totzeitmarker-Molekülen hinsichtlich ihrer Eigenschaften an sowie in der chromatographischen Grenzfläche mittels Molekulardynamik-(MD) Simulationen in Schlitzporensystemen. Aus den erhaltenen Daten wird ein theoretisches Modell zur Vorhersage von Retentionsfaktoren entwickelt und mit experimentellen Daten verglichen. Vorausgehende MD Simulationen konnten bereits die Funktionsweise und Eigenschaften der Oberflächendiffusion charakterisieren, welche eine entscheidende Rolle für den Transport durch das chromatographische Festbett spielt, da sie für relativ hohe Diffusionskoeffizienten der Analyten in der RPLC verantwortlich ist. Mittels eines Multiskalensimulationsansatzes wird der effektive makroskopische Diffusionskoeffizient von Analytmolekülen im makro-mesoporösen Raum des chromatographischen Festbettes berechnet. In einem weiteren Teil dieser Arbeit werden Modellmesoporen unterschiedlicher Zylindergeometrie mittels MD Simulationen untersucht, um den Einfluss der Krümmung auf die Struktur der chromatographische Grenzfläche zu untersuchen, sowie die Verteilung und Mobilität der verschiedenen Spezies in den Simulationssystemen zu charakterisieren.

Kapitel 1 umfasst das molekulare Bild der in der RPLC-Praxis gängigen Totzeitmarker Aceton und Uracil in einer RPLC-Modellmesopore mit planarer Oberflächengeometrie. Als Lösungsmittel werden Wasser (W) und Acetonitril (ACN) in einem Bereich von 80/20 bis 10/90 (v/v) W/ACN verwendet. Bei dem Porenmodell handelt es sich um eine 10-nm Kieselgel-Schlitzpore mit einer Oberflächenmodifizierung von 3.11 µmol m^{-2} Dimethyloctadecylsilyl (C_{18})- und 0.93 µmol m^{-2} Trimethylsilyl (C_1)-Gruppen. In dieser Studie werden die Dichteverteilung, die Orientierung, Wasserstoffbrückenbindungen sowie die Diffusivität der zwei Totzeitmarker untersucht, um zu beleuchten, wie sie mit der chromatographischen Grenzfläche wechselwirken. Die Dichteprofile

beider Soluten zeigt eine eindeutige Anreicherung in der Grenzfläche bei niedrigem ACN-Gehalt der mobilen Phase (bis zu 70-80 vol % ACN), was darauf hindeutet, dass beide Soluten in geringem Maße mit der gebundenen Phase wechselwirken und nicht vollständig inert sind. Für Aceton zeigt sich des Weiteren eine Ähnlichkeit zu ACN aufgrund seiner Lösungsmitteleigenschaften sowie Ähnlichkeiten zum Analytmolekül Acetophenon, was auf die ähnliche Molekülstruktur zurückzuführen ist. Die Oberflächenanreicherung und die Orientierung in den entsprechenden Oberflächenpeaks ist hierbei vergleichbar mit ACN. In der Grenzflächenregion ist die Orientierung sowie der Mobilitätsgewinn zur Bulkdiffusion vergleichbar mit Acetophenon, was mit der Wasserstoffbrückenbindungsfähigkeit erklärt wird. Uracil hingegen wird hauptsächlich mit Aceton verglichen, da es keine RPLC-analyttypische Molekülstruktur aufweist. Dieser Vergleich zeigt eine geringere Wechselwirkung von Uracil mit der stationären Phase, was in der Praxis durch eine geringere Totzeit als Aceton bestätigt wird. Die Orientierungs- und Wasserstoffbrückenbindungsanalyse zeigt, dass Uracil keine eindeutige Orientierung in der Grenzflächenregion bevorzugt, um seine Wasserstoffbrückenbindungen zu maximieren, was wiederum das Fehlen eines Mobilitätsmaximums erklärt. Im Gegensatz zu Analytmolekülen bevorzugen beide Totzeitmarker die Ausbildung von Wasserstoffbrücken statt Kontakte zur gebundenen Phase. Mithilfe dieser Studie werden die Vor- und Nachteile beider Totzeitmarkermoleküle aufgezeigt und damit die Wahl des Totzeitmarkers von der Art des Trennmechanismus abhängig gemacht.

In Kapitel 2 wird der Einfluss von Krümmung auf die chromatographische Grenzfläche in einer RPLC-Mesopore untersucht. Hierfür wird ein zylindrisches Porenmodell verwendet, welches aus einer Zylinderpore in einer Schlitzpore besteht. Die Zylinderpore hat eine Länge von 9.61 nm mit einem Durchmesser von 9.0 nm und stellt somit eine durchschnittliche Mesoporengröße in einer RPLC-Säule dar. Angrenzend an beiden Enden der Zylinderpore befinden sich zwei Lösungsmittelreservoirs mit einer Länge von 5.53 nm. Um die Unterschiede zwischen der planaren Schlitzporen- und der gekrümmten Zylinderporenfläche hinsichtlich Verteilung und Mobilität des Lösungsmittels sowie ausgewählter Analytmoleküle zu untersuchen, sind beide Oberflächentypen mit C_{18}-Gruppen ähnlichen Belegungsgrades (2.89 µmol m^{-2} innen und 2.96 µmol m^{-2} außen) modifiziert, was einen direkten Vergleich der Grenzflächen erlaubt. Des Weiteren ist eine hydrophob modifizierte Außenfläche notwendig, um *hydrohpilic interaction liquid chromatography* (HILIC)-Retention an den Poreneingängen zu verhindern. Um eine Gesamtbelegung von etwa 54%, wie sie in der RPLC-Praxis häufig vorzufinden ist, zu erreichen, sind beide Oberflächentypen nach der C_{18}-Modifizierung mit C_1-Gruppen (1.71 µmol m^{-2} innen und 1.32 µmol m^{-2} außen) versehen Das unpolare Ethylbenzol sowie das moderat polare Acetohpenon werden in der mobilen Phase der Zusammensetzung 70/30 (v/v) W/ACN simuliert. Eine wasserreiche Phase wurde aufgrund des erwarteten hohen ACN Exzesses sowie erhöhter Oberflächendiffusion gewählt, was bereits in vorangegangenen Schlitzporensimulationen gezeigt werden konnte. Die Auswertung der durchgeführten MD Simulationen der beschriebenen Systeme zeigt, dass die Zylinderporengeometrie die Grenzflächenregion aufgrund der durch die Krümmung

gestreckter vorliegenden C_{18}-Ketten weiter Richtung Bulk verschiebt. Durch die höhere lokale Dichte der gebundenen Phase im Inneren der Pore ist die ACN-Anreicherung (als ACN-Ditch bezeichnet) höher als an der planaren Oberfläche, wodurch der lokale ACN-Exzess im ACN-Dichtemaximum von 32 vol % (außen) auf 39 vol % (innen) ansteigt. Der erhöhte ACN-Excess bedingt außerdem auch eine erhöhte ACN-Mobilität in der Zylinderpore: $2.46 \pm 0.10\ 10^{-9}\ m^2\ s^{-1}$ vs $2.16 \pm 0.08\ 10^{-9}\ m^2\ s^{-1}$. Für die Analyten Ethylbenzol und Acetophenon wird ebenfalls ein Anstieg der Mobilität innerhalb der Zylinderpore beobachtet. In Hinblick auf die Analytverteilung zeigt sich für Ethylbenzol eine erhöhte Präferenz für die Zylinderpore, während sich Acetophenon gleichmäßig zwischen dem planaren Außen- und Innenbereich verteilt, da sich der Anstieg Kontakten mit der gebundenen Phase und die Abnahme an W-Kontakten für Acetophenon ausgleicht.

Kapitel 3 beschäftigt sich mit dem Vergleich von einer simulierten Zylinderpore mit 6 nm Durchmesser und der 10-nm Schlitzpore aus Kapitel 1. Die Zylinderpore hat eine Oberflächenbelegung von 2.87 µmol m^{-2} C_{18} Ketten und 1.77 µmol m^{-2} C_1 Gruppen. Für die MD Simulationen von Ethylbenzol und Acetophenon werden Lösungsmittelzusammensetzungen zwischen 70/30 (v/v) und 10/90 (v/v) W/ACN gewählt. Die ausgewerteten Dichteprofile des Solvents zeigen, dass sich, bedingt durch den kleinen Porendurchmesser, im Poreninneren keine Bulkregion ausbildet, sondern der ACN-Ditch-Bereich überlappt. Durch die starke Krümmung liegen die C_{18}-Ketten gestreckter vor als an der planaren Oberfläche und durch die hohe lokale Dichte der gebundenen Phase können die Kettenenden nicht mehr von ACN Molekülen solvatisiert werden, sodass sich die Grenzflächenregion weiter ins Poreninnere verschiebt. Durch das Phänomen der ACN-Ditch-Überlappung ist die gemittelte Lösungsmittelzusammensetzung des gesamten Zylinderporenbereiches für die wasserreichen Phasen deutlich ACN reicher als für die gesamte Schlitzpore und gleicht sich erst bei 90 vol % ACN an, was die ACN-Mobilität beeinflusst. Das Mobilitätsmaximum des ACN-Diffusionskoeffizienten $D_{\parallel,ACN,max}$ in der Zylinderpore übersteigt den Wert der Schlitzpore in allen Lösungmittelzusammensetzungen (12% Erhöhung bei 90 vol % ACN bis hin zu 38% bei 50 vol % ACN). Die beobachtete ACN-Überlappung und die damit verbundene erhöhte Hydrophobizität der Zylinderpore beeinflusst und verstärkt polaritätsabhängige Unterschiede zwischen Ethylbenzol und Acetophenon. Im Fall der Schlitzpore sind beide Analyten abhängig von der Lösungsmittelzusammensetzung zwischen der chromatographischen Grenzfläche und der Bulkregion verteilt: je wasserreicher das Lösungsmittelgemisch (starke Retention), desto mehr Analyt befindet sich in der Region der gebundenen Phase und in der Grenzfläche, was für apolare Analyten stärker ausgeprägt ist. Innerhalb der Zylinderpore sind die Intensitätsunterschiede der Analytdichten zwischen den einzelnen Lösungsmittelzusammensetzungen geringer, was auf den sogenannten *confinement effect* des kleinen Zylindervolumens zurückzuführen ist. Das unpolare Ethylbenzol ist vermehrt zwischen den C_{18} Ketten verteilt und Acetophenon weist einen asymmetrischen Adsorptionspeak auf, welcher stärker Richtung Grenzflächenregion gewichtet ist. Dies beeinflusst unmittelbar die porengemittelte Analytmobilität: $\langle D_{\parallel,Analyt} \rangle$: obwohl für beide Analyten eine erhöhte

Oberflächendiffusion $D_{\|,\text{Analyt}}$ in der Zylinderpore beobachtet wird, ist nur $<D_{\|,\text{Acetophenon}}>$ im Vergleich zur Schlitzpore erhöht (außer für 10/90 (v/v) W/ACN, da es sich angleicht), da Ethylbenzol durch den niedrigen Mobilitätsbereich der gebundenen Phase verlangsamt wird.

Im vierten Kapitel wird mithilfe von bereits simulierten Schlitzporensystemen ein theoretischer Ansatz entwickelt, um Retentionsfaktoren *a priori* vorhersagen zu können. Allgemein setzt sich der Retentionsfaktor aus dem Verhältnis der Differenz von retardiertem Analyten und Totzeitmarker zu der Gesamtmenge an Totzeitmarker in der Säule zusammen. Um diesen aus den MD-Simulationen zu berechnen, werden Dichteprofile der Analyten Ethylbenzol, Benzol, Acetophenon und Benzylalkohol, sowie vom Totzeitmarker Uracil im Bereich von 80/20 bis 10/90 (v/v) W/ACN in der 10-nm Schlitzpore aus Kapitel 1 verwendet. Die Differenz der auf den jeweiligen Bulkwert normierten Dichteprofile von Analyt und Uracil beschreibt hierbei den Oberflächenexzess des entsprechenden Analyten; die Anzahl an Totzeitmarker im interpartikulärem Raum kann aus der Schlitzpore nicht erhalten werden, wodurch eine direkte Berechnung des Retentionsfaktors nicht möglich ist. Mithilfe experimenteller Messungen der Analyten auf einer 5 µm C_{18} High Strength Silica (HSS) Säule wird daher überprüft, ob ein linearer Zusammenhang zwischen den gemessenen Retentionsfaktoren und dem Oberflächenexcess vorliegt. Des Weiteren sollte die daraus erhaltene Proportionalitätskonstante mit der Retentionszeit von Uracil skalieren. Die Ergebnisse zeigen, dass für alle gemessenen Zusammensetzungen ein linearer Zusammenhang zwischen berechnetem Oberflächenexcess und entsprechendem Retentionsfaktor mit einer Güte von $R^2 > 0.985$ erhalten wird und damit die erste Hypothese bestätigt werden kann. Die erhaltene Steigung dieser linearen Fitfunktionen aufgetragen gegen die gemessene Retentionszeit von Uracil zeigt zwar keinen eindeutig linearen Zusammenhang ($R^2 = 0.29$), allerdings findet sich die experimentell beobachtete U-förmige Elutionskurve von Uracil auch in der entsprechenden Auftragung wieder. Der in diesem Kapitel etablierte Ansatz zur Vorhersage von Retentionsfaktoren aus vorhandenen MD Simulationen eignet sich daher für kleine, neutrale Analyten in der RPLC. Die Genauigkeit beschränkt sich hierbei auf ein Limit von < 1 % als relativen Fehler, was hauptsächlich auf die folgenden Annahmen in dieser Studie zurückzuführen ist: i) die gesamte Morphologie des Mesoporennetzwerkes eines Partikels wird vereinfacht mit einer Schlitzporengeometrie dargestellt, ii) die tatsächliche Porengrößenverteilung innerhalb eines mesoporösen Partikels wird auf eine konstante Größe von 10 nm reduziert und iii) die Oberflächenmodifzierung der verwendeten HSS-C_{18} Säule weicht um 13% von der der Schlitzpore ab.

Im fünften Kapitel wird der Einfluss von Länge und Belegungsgrad der Oberflächenmodifizierung in RPLC Porenräumen auf effektive Mesoporen- und Festbett-Diffusionskoeffizienten mithilfe eines hierarchischen Simulationsansatzes untersucht. Hierfür werden zunächst die aus den MD Simulationen erhaltenen Dichte- und Diffusionsprofile der Analytmoleküle in der RPLC Schlitzpore aus Kapitel 1 für Brownsche Dynamiksimulationen in einem mittels

Rastertransmissionselektronenmikroskopie physikalisch rekonstruierten Mesoporenraum implementiert, um detaillierte, räumlich-abhängige Informationen in der Grenzflächenregion auf molekularer Ebene abbilden zu können. Für den Vergleich zwischen verschiedenen Oberflächen werden MD Simulationen von C_{18}, C_8, sowie *high density* (hd)-C_8 modifizierten Schlitzporen verwendet. Durch einen modifzierten RWPT (*random walk particle tracking*)-Ansatz können dann die effektiven Diffusionskoeffizienten D_{meso} der Analyten berechnet werden. Auf der höchsten Porenraumebene wird der Massentransfer von Analytmolekülen zwischen Mesoporen- und Makroporenraum simuliert. Hierzu wird in der mittels Focused-Ion-Beam Rasterelektronen-mikroskopie rekonstruierten Makroporendomäne der effektive Diffusionskoeffizient im gesamten chromatographischen Festbett (D_{bed}) ermittelt. In der Schlitzpore, und damit auf der Ebene einer einzelnen Mesopore, dominieren die Eigenschaften der Analytretention sowie der Oberflächenmodifizierung (längere Ketten bzw. höhere Kettendichte erhöht Oberflächendiffusion). Im Mesoporenraum wird die Analytmobilität durch die Oberflächentortuosität verringert; die Diffusionskoeffizienten der Analyten in der C_{18} Phase sind außerdem niedriger verglichen mit den C_8-Phasen. Mithilfe einer 2D-*distance map* der Mesoporenraumkonstruktion kann gezeigt werden, dass sich der Abstand zwischen gegenüberliegenden Porenwänden so verringern kann, dass die Grenzflächenregionen überlappen. Dadurch kann sich der Bereich der erhöhten Mobilität teilweise nicht mehr ausbilden, was für die C_{18}-Phase aufgrund der Kettenlänge schneller erreicht wird und mit einem größeren Shift der Grenzflächenregion zur Bulkregion verbunden ist (verglichen mit den C_8-Phasen). Im Makroporenraum zeigen die berechneten Festbettdiffusionskoeffizienten der Analyten, dass D_{bed} stärker von der analytspezifischen Retention abhängt als von den Oberflächeneigenschaften (Kettenlänge und Belegungsgrad der Alkylketten).

II. Abstract

Computer simulations contribute significantly to the understanding of chemical processes at the molecular level and are used in many areas of chemistry. In high performance liquid chromatography (HPLC), theoretical models and calculations are essential to characterize occurring interactions at the solid-liquid interface of porous materials and develop improvements for this separation technique. This work deals with the molecular-level picture of single mesopores present in stationary phases for reversed phase liquid chromatography (RPLC). RPLC is the most commonly used HPLC method for the separation of nonpolar to moderately polar analytes using a hydrophobically modified stationary phase and an aqueous-organic mobile phase. Retention factors of analytes are calculated from their retention time relative to the retention of dead time markers; small, inert molecules that ideally do not interact with the stationary phase. In the first part of this work, two common dead-time marker molecules are investigated regarding their interactions with the chromatographic interface using molecular dynamics (MD) simulations of slit pore models. From the obtained data, a theoretical model for the prediction of retention factors is developed and compared with experimental measurements. Preliminary MD simulations of analyte molecules in single mespores were already able to characterize the origin and properties of surface diffusion, which plays a crucial role for transport through the chromatographic fixed bed, as it is responsible for relatively high diffusion coefficients of analytes in RPLC. With a multiscale simulation approach, the effective macroscopic diffusion coefficient of analyte molecules are calculated in the macro-mesoporous space of the chromatographic bed. The second part of this work deals with MD simulations of model mesopores with different pore geometry to investigate the influence of curvature on the structure of the chromatographic interface and characterize the distribution and mobility of different species in the simulation systems.

In Chapter 1, MD simulations of the dead time markers acetone and uracil in an RPLC slit pore model are used to elucidate their interactions with the chromatographic interface. Water (W) and acetonitrile (ACN) are used as mobile phase in the range of 80/20 to 10/90 (v/v) W/ACN. The pore model is a 10-nm silica slit pore modified with 3.11 µmol m^{-2} dimethyl octadecylsilyl (C_{18}) and 0.93 µmol m^{-2} trimethyl silyl (C_1) groups on the surface, representing an RPLC pore with column-averaged surface geometry. In this study, the density distribution, orientation, hydrogen bonding, and diffusivity of acetone and uracil are investigated to compare their behavior to solvent molecules and true analyte molecules. The density profiles of both solutes show a clear enrichment in the interface at low ACN content of the mobile phase (up to 70-80 vol %-ACN), indicating that they are not completely inert molecules. The calculated data of acetone are compared with ACN and acetophenone based on similarities in solvent properties and molecular structure, respectively. Regarding surface attachment and orientation in the corresponding surface peaks, acetone resembles ACN. In the interfacial region, orientation as well as the mobility gain relative to the bulk liquid region of acetone resembles acetophenone due to the similarity in their hydrogen bonding (HB) pattern. The simulated data of uracil are mostly compared to acetone because it

differs from typical RPLC solutes regarding its hydrophilic molecular structure. In general, the interaction of uracil with the bonded phase is weaker than that of acetone, reflecting a shorter dead time than acetone. Orientation and HB analysis show that uracil does not require a particular orientation to maximize its HB coordination in the interfacial region, which prevents uracil from exhibiting a higher diffusive mobility there. In contrast to analyte molecules in the chromatographic interface, the dead time markers prefer HB to solvent molecules over bonded-phase contacts. Overall, this study provides insights into the advantages and disadvantages of the two dead time markers and shows that their suitability depends on the retention type.

In Chapter 2, the influence of surface curvature on the chromatographic interface is investigated with MD simulations of a cylindrical mesopore model. The simulation box contains a silica block with a carved out cylinder of 9 nm in length, representing a mesopore in an RPLC column of average pore size. Adjacent to both sides of the cylinder pore are two solvent reservoirs with a length of 5.53 nm, resulting in a cylindrical-inside-a-slitpore model and allowing a direct comparison of the competition between planar and curved surface regarding distribution and mobility of solvent and analyte molecules. The inner cylindrical and outer planar surface are modified with C_{18} groups of similar occupancy (2.89 µmol m^{-2} inside and 2.96 µmol m^{-2} outside), preventing hydrophilic interaction liquid chromatography (HILIC) retention at the pore entrances. A bonded-phase coverage of 54% in total was achieved by endcapping with C_1 groups (1.71 µmol m^{-2} inside and 1.32 µmol m^{-2} outside). The apolar ethylbenzene and moderately polar acetophenone are simulated in a 70/30 (v/v) W/ACN mobile phase. A W-rich mobile phase was chosen because of the expected high local ACN excess and surface diffusion effects observed in previous simulated slit pore systems. The results show that the cylinder pore geometry leads to more stretched C_{18} chains which shift the interfacial region further towards the bulk region. Due to the higher local density of the bonded phase inside the pore, ACN enrichment in the so-called ACN ditch is higher than at the planar surface, increasing the local ACN excess in the ACN density maximum from 32 vol% (outside) to 39 vol% (inside). The increased ACN excess is accompanied by an increase in ACN mobility: $2.46 \pm 0.10\ 10^{-9}$ m^2 s^{-1} (inside) vs $2.16 \pm 0.08\ 10^{-9}$ m^2 s^{-1} (outside). This affects the analyte molecules in the same way, since a mobility increase for both molecules is observed in the interfacial region of the cylindrical pore. Regarding analyte distribution, the data show a strong preference of ethylbenzene for the inner curved surface (because of the higher hydrophobcitiy) whereas acetophenone distributes equally between inner curved and outer planar surface, because the increased bonded-phase contacts at the curved surface do not compensate for a loss of W contacts. The cylindrical pore geometry therefore enhances the local pore-scale selectivity of the stationary phase for apolar analytes.

In Chapter 3, the confinement effect of a small 6-nm RPLC cylindrical pore on solvent and analyte behavior is compared to MD simulations of the 10-nm slit pore from Chapter 1. The pore surface bears 2.87 µmol m^{-2} C_{18} and 1.77 µmol m^{-2} C_1 groups and MD simulations for ethylbenzene and acetophenone were carried out for four mobile phases in the range between 70/30 and 10/90 (v/v)

W/ACN. The data show that, due to the small pore diameter, no bulk liquid region is formed inside the cylindrical pore and as a consequence, the ACN-ditch region forms an overlap in the pore lumen. The strong surface curvature leads to a greater extension of the C_{18} chains compared to the planar surface (and also more than in the 9-nm cylindrical pore) and, consequently, to a higher local bonded-phase density at the chain ends, preventing the solvation by ACN molecules. Therefore, the interface region shifts further into the pore interior. Due to the ACN ditch overlap phenomenon, the local averaged solvent composition of the entire cylindrical pore region is much richer in ACN compared to the slit pore and only matches at 90 vol % ACN. This affects surface diffusion in a positive way: The mobility maximum of the ACN diffusion coefficient $D_{\parallel,ACN,max}$ in the cylindrical pore is higher than in the slit pore for all solvent compositions (from 12% increase at 90 vol % ACN to 38% increase at 50 vol % ACN). The data show further, that the increased hydrophobicity inside the cylindrical pore enhances polarity-dependent differences between analyte molecules. In the slit pore, analyte distribution between the chromatographic interface and the bulk liquid region strongly varies with the solvent composition: the more W the mobile phase contains (strong retention), the more analyte is found inside the bonded phase and interface region, which is more pronounced for apolar molecules. In the cylindrical pore, differences of analyte density intensities are smaller, which is explained with the confinement effect of the small cylindrical pore volume. The apolar ethylbenzene is more distributed into the C_{18} chains than acetophenone, the latter one showing a broader, asymmetric adsorption peak weighted toward the interfacial region. This directly influences the pore-averaged analyte mobility $<D_{\parallel,analyte}>$: although surface diffusion $D_{\parallel,analyte}$ inside the cylindrical pore is increased for both analytes, only $<D_{\parallel,acetophenone}>$ is higher than in the slit pore (except for 10/90 (v/v) W/ACN, where the difference becomes insignificant); ethylbenzene is slowed down because of the lower mobility inside the bonded-phase region.

In Chapter 4, a theoretical approach is developed using previously simulated slit pore data to predict retention factors *a priori*. In general, the retention factor k is the ratio of the difference between the retained analyte and a non-retained molecule (dead time marker) to the total amount of dead time marker in the column (assuming an equal concentration of both compounds in the bulk volume). Direct calculation of retention factors based on the slit pore simulation is not possible because of the unknown number of dead time marker molecules in the interparticle space. Therefore, normalized density profiles of the analytes ethylbenzene, benzene, acetophenone, and benzyl alcohol, as well as the dead time marker uracil simulated from 80/20 to 10/90 (v/v) W/ACN in the 10-nm slit pore are used to calculate the respective analyte surface excess by subtracting uracil from the analyte density values. In addition, the same solute set is measured on a 5 µm C_{18} High Strength Silica (HSS) column to investigate if the measured retention factors are in a linear relationship to the calculated surface excesses. This proportionality constant should further scale with the retention time of uracil. The data show that, for all measured compositions a linear relationship between calculated surface excess and corresponding retention factor is obtained ($R^2 > 0.98$), confirming the first assumption. The slope obtained from the linear fit functions does

not show a visible linear relationship ($R^2 = 0.29$), so that the second assumption cannot be verified with the results. The obtained plot, however, resembles the experimentally observed U-shaped elution curve of uracil. The approach established in this chapter is well suited for predicting retention factors from existing MD simulations for small, neutral analytes in RPLC. The accuracy, however, is limited to < 1% as a relative error, which is mainly due to the following assumptions made in this study: i) the entire mesopore network morphology of a particle is neglected by using the averaged slit pore geometry, ii) the actual pore size distribution within a mesoporous particle is reduced to a constant size of 10 nm, and iii) the surface modification on the used HSS-C_{18} column differs by 13% from the slit pore (2.70 µmol m^{-2} vs 3.11 µmol m^{-2}).

In Chapter 5, the influence of length and ligand density of surface-attached alkyl groups in RPLC pore spaces on effective mesopore and fixed-bed diffusion coefficients is investigated using a hierarchical simulation approach. For this purpose, the density and diffusion profiles of analyte molecules in the RPLC slit pore obtained from MD simulations discussed in Chapter 1 are first implemented for Brownian dynamics simulations in a mesopore space physically reconstructed using scanning transmission electron microscopy to ensure detailed, spatially-dependent information in the interfacial region at the molecular level. For the comparison of chain length and ligand densities, MD simulations of C_{18}, C_8, as well as high density (hd)-C_8 modified slit pores are chosen. A modified random walk particle tracking (RWPT) approach is then carried out to calculate the effective diffusion coefficients D_{meso} of the analytes. At the largest of length scale, the mass transfer of analyte molecules between mesopore and macropore space is simulated. This is achieved by determining the effective diffusion coefficient in the chromatographic bed (D_{bed}) for which a macropore space reconstructed by focused ion-beam scanning electron microscopy is used. The data show that in the slit pore, and thus at the level of a single mesopore, analyte retention properties and surface modification dominate: the longer and higher the density of the alkyl chains, the higher are surface diffusion coefficients of the analyte molcules. In the mesopore space, analyte mobility is reduced by surface tortuosity; analyte diffusion coefficients in the C_{18} phase are also lower compared to the C_8 phases. Using a 2D distance map of the mesopore space reconstruction shows that opposite pore walls can approach each other closely, resulting in an overlap of the interfacial regions. Consequently, high mobility regions cannot fully develop, disfavoring the C_{18} phase due to its chain length and the associated shift of the interface region towards the bulk liquid (compared to shorter chain lengths). In the macropore space, the calculated bed diffusion coefficients of the analytes show that D_{bed} depend strongly on the analyte-specific retention but rather little on surface properties (chain length and ligand density).

III. Introduction

Development and optimization of chromatographic techniques profit significantly from the understanding of the underlying molecular processes. Over the last decades, the molecular-level picture of the chromatographic interface in high performance liquid chromatography (HPLC), which represents the most important separation and purification technique, has been established by molecular simulations and is still expanding. Many characteristics are not accessible by experimental data, which is why theoretical models and simulations become the methods of choice. Regarding retention mechanisms in particular, molecular simulations offer insights into separation selectivity, mass transfer and structural properties of the chromatographic interface and its interacting species.

The most common HPLC mode, reversed-phase liquid chromatography (RPLC), is widely applied in academic and industrial settings, since it is suitable for the separation of apolar to moderately polar analytes. Stationary phases of RPLC columns consist of hydrophobically modified silica, which can be particle based or monolithic. Typical surface ligands are dimethyl octadecylsilyl (C_{18}) or dimethyl octyl (C_8) chains, with which a coverage of about 50% can be achieved.[1] Lowering the amount of free surface silanols further can be achieved by grafting endcapping groups, such as trimethylsilyl (C_1) onto the surface. Mobile phases are mixtures of water (W) and an organic solvent, usually methanol (MeOH) or acetonitrile (ACN). Analyte molecules are retained on the surface of the stationary phase based on the interactions with the solvent and bonded phase of the chromatographic interface. Understanding the underlying retention mechanisms is essential for improving the performance of existing chromatographic systems as well as the development of new stationary phases in RPLC practice. This work provides simulation studies of RPLC pore models, which mimic the conditions in a single mesopore found in a chromatographic RPLC column. The obtained data do not only contribute to the understanding of the underlying retention mechanisms, but are also used for establishing an approach to predict measured retention factors and for implementation in multiscale diffusion simulations to calculate transport properties on larger time and length scales.

III.1 The chromatographic interface at the molecular level

Molecular simulations of RPLC systems should ideally give insights about the complex interplay between solid silica surface with its surface-tethered bonded-phase groups, the mobile-phase and analyte molecules to allow the characterization of retention processes. The most established methods so far are Monte Carlo (MC) and molecular dynamics (MD) simulations.[2] Both MC and MD simulations generate phase-space trajectories of individual molecules in a simulation system. MC simulations compute trial configurations by the use of random sampling and different methods of statistical analysis,[3] whereas MD simulations are based on solving the classical equations of motions numerically.[4]

The first simulations of RPLC systems were conducted without the presence of solvent molecules to study the conformation and mobility of the alkylic surface modification by varying chain length and surface density.[5,6] A large contribution to the understanding of the chromatographic interface including the structure and distribution of bonded-phase chains and solvent molecules was achieved by the group of Siepmann.[7-15] By the use of MC simulations, they established the presence of three different regions in a slit pore modified with C_{18} groups that is equilibrated with W–MeOH and W–ACN mixtures: i) the bonded-phase region which starts from the silica surface and ends at the location where the total solvent density reaches 10 % of its bulk value, ii) the interfacial region, where the total solvent density increases from 10 to 90 % of its bulk value, and iii) the bulk region, where the properties of the liquid mixture are attained.[7,14] Calculated density profiles of the bonded phase exhibit distinct peaks at the surface (reflecting their rigid anchoring) and more diffuse peaks towards the chain ends, where the segment densities approach a value close to that for bulk liquid *n*-hexadecane.[14] The density profiles of the solvent molecules show an enrichment of the organic modifier at the chain ends in the interfacial region, before reaching their bulk value. This enrichment is more pronounced at low concentrations of the organic modifier[7] and an orientational preference is given for MeOH molecules (so it can maximize its hydrogen bonds (HBs) with the mobile phase solvent), whereas ACN is rather randomly distributed in the interfacial region.[14] Further MC studies of Siepmann and coworkers included the investigation of bonded-phase density,[9,10] bonded-phase chain length,[12] polar embedded groups,[11,12] pressure[12] and pore shape[12] on the solvent and bonded-phase structure in RPLC systems. Simulations of small solute molecules elucidated the retention mechanisms of polar and apolar molecule types,[10,15] which was complemented by very detailed MD simulation studies of Rybka et al. For their investigations of solvent, bonded phase, and analyte distribution and mobility in RPLC systems, they used C_{18} and C_8 modified silica slit pores of 10 nm width. MD simulations of the mobile phase range between 80/20 (v/v) W/ACN and 10/90 (v/v) W/ACN confirmed the ACN enrichment in the interfacial region which was termed as the "ACN ditch".[16,17,19] Figure III.1 shows a snapshot of the simulated C_{18}-modified silica slit pore with a mobile phase of 70/30 (v/v) W/ACN and aligned atom density profiles of bonded phase, W and ACN molecules, visualizing solvent and bonded-phase distribution inside the 10-nm pore. The last layer of silica-surface atoms is defined as $d = 0$ nm (distance from the silica surface). The density profiles clearly show the sharp bonded-phase peaks close to the surface and a more diffuse distribution towards the chain ends at $d \sim 2$ nm. Both ACN and W exhibit surface peaks, which result from hydrogen bonding to residual surface silanol groups (and ACN molecules forming hydrogen bonds to surface adsorbed W).[17] The W density profile increases afterwards until bulk value is reached and the ACN density shows the previously described ditch formation around $d \sim 1.75$ nm before reaching its bulk value. The segregation of the liquid mixture around the chain ends is caused by the hydrophobic effect, which is driven by the preference of W molecules to establish hydrogen bonds between other W molecules instead of forming W–ACN HBs.[20]

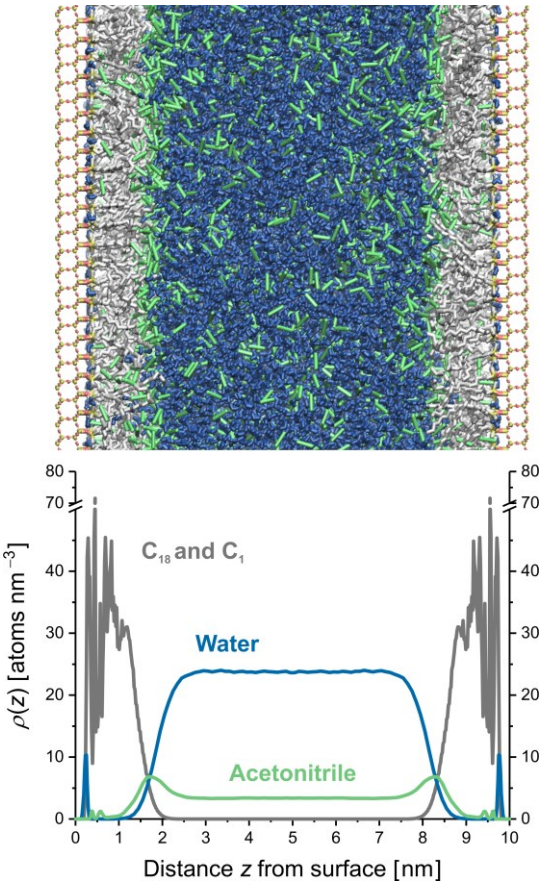

Figure III.1.1. Snapshot of the RPLC mesopore model equilibrated with a 70/30 (v/v) W/ACN mobile phase (top) and calculated density profiles from bonded-phase groups, W, and ACN molecules with matching color code (bottom). Si, O, and H atoms are colored red, yellow, and white, respectively.

Calculation of diffusion coefficient profiles showed that the lateral mobility of ACN molecules in the interface region is increased which directly affects retained analyte molecules.[16,17,19] This was shown by MD simulations of the four aromatic hydrocarbons ethylbenzene, benzene, acetophenone, and benzyl alcohol, which were chosen as representative RPLC analytes varying in size and polarity.[17,19] All four analyte molecules exhibit a lateral mobility increase up to 80 vol % ACN, which is explained by the higher mobility region in the ACN ditch due to its lower viscosity (compared to the bulk liquid mixture) and the lubrication effect of the bonded phase groups.[19] In general, analyte molecules move through the mesoporous space by a combination of pore diffusion (in the pore liquid) and surface diffusion (along the surface of the stationary phase).[21] Surface diffusion, which is much discussed in literature,[22–27] is an important contribution to the mass transfer in porous adsorbent systems and is thought to be the reason of higher intraparticle diffusivities compared to the observed diffusion coefficient in the bulk mobile phase.[28–31] Furthermore, Gritti et al. [25] showed that the stronger the interaction between the stationary phase, and, thus, the higher the retention, the faster is surface diffusion of the analyte. This was also observed for the simulated analyte molecules by Rybka et al.[17] and expanded by the observation

that at comparable polarity, the lateral mobility increases with decreasing molecule size. A following MD study with the same analyte molecule set comprised the investigation of the influence of bonded-phase chain length and grafting density on surface diffusion. Rybka et al.[32] simulated two W/ACN mobile phases for a C_{18} phase, a complementary C_8 phase and a C_8 phase with a higher grafting density. Shortening the chain length leads to a more focused distribution of chain ends which results in a higher ACN excess compared to the C_{18} phase, but also to a decrease in bonded-phase mobility which also decreases analyte mobility. Increased ligand density, however, shifts the ditch region closer towards the bulk liquid, increasing the lateral mobility gain from surface diffusion at low ACN content of the mobile phase.[32] Apart from different surface modifications, the study of different pore geometries also gives important insights into the formation of the chromatographic interface. Columns in RPLC practice contain positive and negative surface curvature of different degrees, which is why the RPLC slit pore model is assumed to represent column-averaged data.[2,19] However, only few simulation studies of chromatographic processes were conducted in cylindrical pore models,[33–37] because of the vast increase in system complexity, which is accompanied by a more complicated pore generation procedure as well as higher simulation times. Rafferty et al.[33] investigated a C_{18}-modified silica cylindrical pore with 6 nm in diameter and equilibrated with a W/MeOH mobile phase by MC simulations. Calculated density profiles showed that the bonded-phase region width has increased by about 30% compared to the slit pore with a comparable C_{18} grafting density. Consequently, the solvent-depleted area in the bonded-phase region inside the cylindrical pore is larger and the enrichment of the organic modifier is shifted closer towards the pore center. Furthermore, they showed that partitioning of apolar analyte molecules is more favorable in the inner chain region of the cylindrical pore and that in case of polar analyte molecules, adsorption is enhanced compared to the slit pore.

III.2 Molecular dynamics simulations with GROMACS

The GROMACS (GROningen Machine for Chemical Simulation) software is a free open source program for high-performance MD simulations and output analysis. GROMACS' source code is primarily written in C, which resulted originally from the idea of a portable scientific code for efficient parallel molecular dynamics implementation.[38] Thus, GROMACS can be used for parallelization of processor clusters,[39] but also on single processors and on GPUs.[40] It was developed to simulate biological (macro)molecules in aqueous and membrane environments, but has gained many more fields of application, e.g., material science,[41,42] electrochemisty and energy storage,[43,44] or, as covered by this thesis, the study of solid-liquid interfaces relevant in chromatography.[16–19,32,35]

In general, a pre-run simulation system used for MD calculations is defined by its size and shape, the containing number and types of molecules, and the coordinates of all atoms. Velocities are either generated from a Maxwellian distribution or already given as input values.[39] The usual box geometry, which was also chosen for all pore models of this work, is a rectangular box with periodic boundary conditions (PBC). When PBCs are applied, the simulation box is surrounded by

translated copies of itself to minimize edge effects and allow constant atom numbers in an equilibrated system. Figure III.2 shows the PBC-translation of the simulation box with the centered, modified silica slab into the 10-nm slit pore, which was simulated for Chapter 1 of this work.

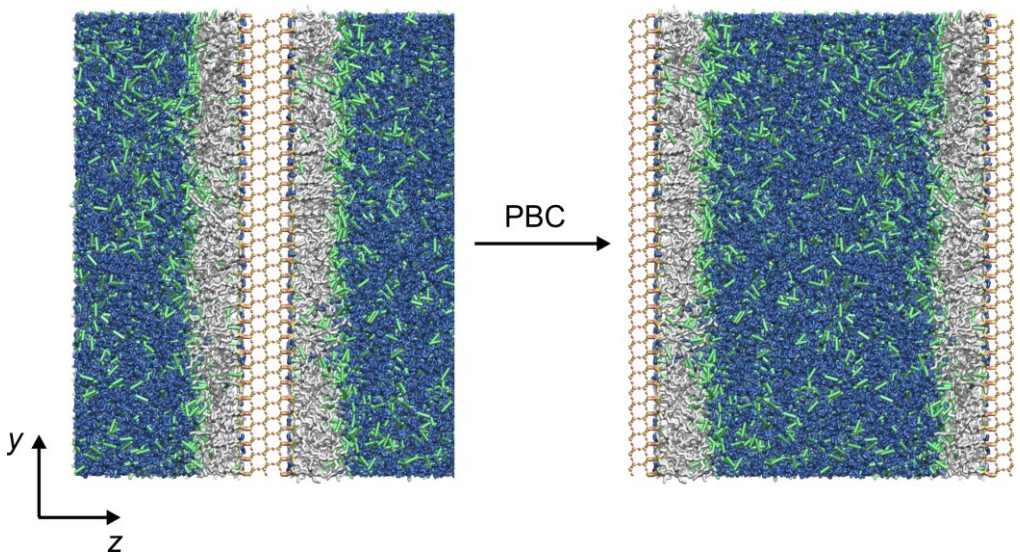

Figure III.2.1. Visualizing PBCs with the RPLC slit pore model. Bonded-phase groups, W, and ACN molecules are shown as gray, dark blue, and green sticks, respectively. Si, O, and H atoms are colored red, yellow, and white, respectively.

The simulation of thermodynamic properties in a chemical system requires suitable force fields (or a validated force field combination). GROMACS is compatible with a wide range of force fields, including GROMOS-96,[45] Encad[46], OPLS,[47,48] AMBER,[49] and CHARMM.[50] In general, there are three different types of force fields: the all-atom force fields, the united-atom force fields and the coarse-grained force fields. All-atom force fields provide parameters of each atom type of a molecule/particle and require the most computational effort. United-atom force fields describe atom groups such as CH-segments of alkyl chains as a single unit, and with coarse grained force fields, larger entities such as proteins can be computed with viable resources. Calculating the energies and forces of particles in a simulation system is based on bonded and nonbonded interactions.[39] Bonded interactions cover the functions and potentials of chemical bonds (bond stretching) between two atoms, bond angles between three atoms and bond dihedrals between four atoms. Nonbonded interactions between pairs of atoms or particles are described by a Lennard-Jones or Buckingham potential, and by Coulomb interaction.[39] Force field validation of this work was focused on the correct representation of the important interactions in the chromatographic system, which includes solvent-solvent, solvent-silica surface, solvent-bonded phase, solvent-solute, solute-silica surface, and solute-bonded phase interactions. In particular, the force field selection of this work reproduces retention data (calculated from density profiles) and approximates solvent diffusivity, which is essential for describing transport effects in the RPLC pore models. After setting up a simulation system, energy minimization is recommended to prevent system

crashes. Insertion of molecules or atoms into a simulation box is usually a randomized process and if neighbored atoms are placed too close to each other, their potential energy increases greatly, which leads to an abrupt stop of a simulation run. GROMACS provides multiple methods for energy minimization, from which steepest descent is the default setting. With this method, atom coordinates with a high potential energy are shifted until the maximum of the absolute values of the force gradient components is smaller than a user-specified value.

MD simulations in general compute phase-space trajectories of particles by integrating Newton's equations of motion. The time step of integration should be set between 1-2 fs and is limited by the highest frequency of bond vibration (but can be increased by applying bond constraints).[51] The default MD integrator in GROMACS is the leap-frog algorithm, which calculates positions and velocities of atoms or particles at different interleaved time points.[52] Another integrator implemented in GROMACS is the velocity Verlet method, which differs from the leap-frog algorithm only by calculating velocities not at the same time as positions.[53]
Depending on the thermodynamic properties of the simulation system, different statistical ensembles are required. The most common ensembles used in MD simulations are i) the isothermal-isobaric ensemble (*NPT*) with a constant number of atoms *N*, pressure *P*, and temperature *T* and ii) the canonical ensemble (*NVT*) with constant *N*, volume *V*, and *T*. *NPT* simulations are useful for equilibrating liquids, especially for determining and validating their bulk liquid density. In this work, box simulations with W and ACN or MeOH molecules were necessary to calculate bulk number densities, which were then used for solvent equilibration and productive *NVT* simulation runs in the RPLC pore models.

III.3 RPLC pore models and high-performance computing

Apart from choosing a suitable and validated force field combination, representation of a single mesopore inside a chromatographic RPLC column requires a detailed atomistic structure of the solid stationary phase. The cylindrical mesopores studied in this work were specifically designed and built with the object-oriented program PoreMS. The PoreMS software generates user-specified silica pores with different pore geometry, chemical structure and ligand density of surface groups, and hydroxylation of the silica surface can be generated and its algorithm is briefly explained.[54] In the first step, a rectangular silica crystal lattice with the structure of β-cristobalite is built from the smallest possible grid unit of Si and O atoms, from which a cylindrical shape along a given drill axis is then carved out. Full hydroxylation of the silica surface is followed by the rules of Coasne et al.[55] Chemical ligands such as C_{18} chains and C_1 groups are randomly grafted onto the surface with a user-specified ligand exclusion radius to prevent ligand overlap. With the option of adding solvent reservoirs to each side of the pore entrance, an exchange between inner curved and outer planar pore space is possible, which is studied in detail in Chapter 2.
Simulating a realistic cylindrical RPLC pore equilibrated with solvent molecules requires a large

amount of computing resources. Efficiently generating phase-space trajectories of individual atoms over simulated time spans up to 500–1000 ns makes the use of high-performance computing (HPC) inevitable. HPC (synonymous with supercomputing) in general is accomplished by parallelism, fast-dense circuitry, and packaging technology[56] and is associated with the achievement of the greatest computing capability with the possible technology at any time.[57] HPC has a variety of applications, reaching from the classical fields of science and engineering to socioeconomics, big data (management and learning), or national security (e.g., including modelling climate or the spread of diseases).[57] Architecture of HPC clusters depends on the field of application and new technological developments. The HoreKa (Hochleistungsrechner Karlsruhe) computer cluster, successor of the ForHLR II (Forschungshochleistungsrechner II) used for the major part of simulations in this work, for example, is specifically designed for scientific research projects with a high amount of data generation. With nearly 800 compute nodes each consisting of 76 central processing units (CPUs), single job runs of multiple hundred nodes and multiple thousand CPUs are possible.[58] For the best computing efficiency, performance tests and scaling of the simulation systems of interest are obligatory. To provide insight into this process and demonstrate the computational demands of the cylindrical pore models, performance and scaling are shown for three different pore sizes, all equilibrated with a 70/30 (v/v) W/ACN mobile phase: the 6 nm and 9 nm pore size from Chapter 3 and Chapter 2, respectively, as well as a pore with 12 nm in pore diameter, simulated for a current MD study[59] (see Chapter IV). Multiples of 72 cores per node were used for a single simulation run, because the domain decomposition algorithm of GROMACS (which divides the system into smaller domains for the integration of the equations of motion) works best with small prime factors in the number of tasks. As shown in Figure III.3.1, the larger the system, the lower its performance due to the higher amount of particles (6 nm pore: ~287400 atoms vs. 12 nm pore: 606600 atoms), but the better is its scaling with a larger number of cores. Efficiency should not be much lower than 80 % (upon the advice of technical support), which is why the minimum for the cylindrical pore models were simulations with 288 cores. The slit pore, equilibrated with the same mobile phase, by comparison, contains ~115000 atoms and requires 144 cores for optimal efficiency.

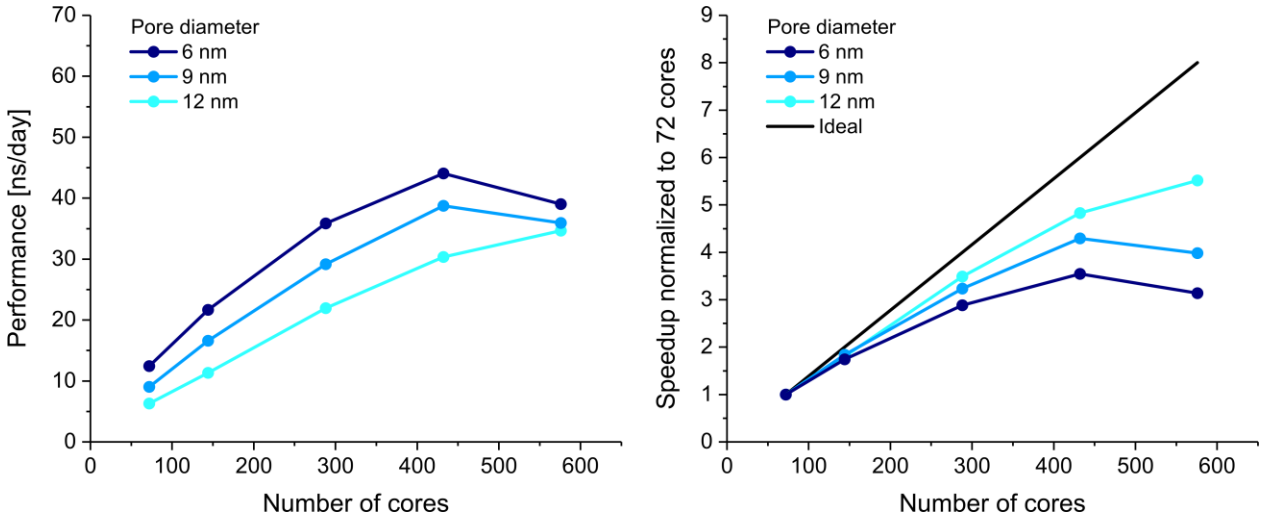

Figure III.3.1. Performance (left) and speedup (right) of cylindrical pore models with different pore diameter equilibrated with a 70/30 (v/v) W/ACN mobile phase simulated for 500,000 steps. Performance is measured by the length of the output trajectory extrapolated to 24h. Speedup shows the scaling of each system compared to the ideal efficiency of 100 %.

References

1 U. D. Neue, *HPLC Columns: Theory, Technology, and Practice*; Wiley–VCH: New York **1997**.

2 R. K. Lindsey, J. L. Rafferty, B. L. Eggimann, J. I. Siepmann, M. R. Schure, *J. Chromatogr. A* **2013**, *1287*, 60–82.

3 R. L. Harrison, *AIP Conf. Proc.* **2010**, *1204*, 17–21.

4 K. Binder, J. Horbach, W. Kob, W. Paul, F. Varnik, *J. Phys.: Condens Matter* **2004**, *16(5)*, S429.

5 S. J. Klatte, T. L. Beck, *J. Phys. Chem.* **1995**, *99*, 16024–16032.

6 I. Yarovsky, M.-I. Aguilar, M. T. W. Hearn, *J. Chromatogr. A* **1994**, *660*, 75–84.

7 L. Zhang, J. L. Rafferty, J. I. Siepmann, B. Chen, M. R. Schure, *J. Chromatogr. A* **2006**, *1126*, 219–231.

8 J. L. Rafferty, L. Zhang, J. I. Siepmann, M. R. Schure, *Anal. Chem.* **2007**, *79*, 6551–6558.

9 J. L. Rafferty, J. I. Siepmann, M. R. Schure, *J. Chromatogr. A* **2008**, *1204*, 11–19.

10 J. L. Rafferty, J. I. Siepmann, M. R. Schure, *J. Chromatogr. A* **2008**, *1204*, 20–27.

11 J. L. Rafferty, J. I. Siepmann, M. R. Schure, *Anal. Chem.* **2008**, *80*, 6214–6221.

12 J. L. Rafferty, J. I. Siepmann, M. R. Schure, *J. Chromatogr. A* **2009**, *1216*, 2320–2331.

13 J. L. Rafferty, L. Sun, J. I. Siepmann, M. R. Schure, *Fluid Phase Equilib.* **2010**, *290*, 25–35.

14 J. L. Rafferty, J. I. Siepmann, M. R. Schure, *J. Chromatogr. A* **2011**, *1218*, 2203–2213.

15 J. L. Rafferty, J. I. Siepmann, M. R. Schure, *J. Chromatogr. A* **2011**, *1218*, 9183–9193.

16 J. Rybka, A. Höltzel, S. M. Melnikov, A. Seidel-Morgenstern, U. Tallarek, *Fluid Phase Equilib.* **2016**, *407*, 177–187.

17 J. Rybka, A. Höltzel, U. Tallarek, *J. Phys. Chem. C* **2017**, *121*, 17907–17920.

18 J. Rybka, J. Kärger, U. Tallarek, *ChemPhysChem* **2017**, *18*, 2094–2102.

19 J. Rybka, A. Höltzel, A. Steinhoff, U. Tallarek, *J. Phys. Chem. C* **2019**, *123*, 3672–3681.

20 D. Chandler, *Nature* **2005**, *437*, 640–647.

21 F. Gritti, G. Guiochon, *Anal. Chem.* **2006**, *78*, 5329–5347.

22 J.-G. Choi, D. D. Do, H. D. Do, *Ind. Eng. Chem. Res.* **2001**, *40*, 4005–4031.

23 J. A. Wessenlingh, J. C. Bosma, *AIChE J.* **2001**, *47*, 1571–1580.
24 K. Miyabe, G. Guiochon, *J. Sep. Sci.* **2003**, *26*, 155–173.
25 K. Miyabe, G. Guiochon, *J. Chromatogr. A* **2010**, *1217*, 1713–1734.
26 K. Yang, Y. Sun, *Biochem. Eng. J.* **2007**, *37*, 2983–310.
27 I. Medved, R. Cerný, *Microporous Mesoporous Mater.* **2011**, *142*, 405–442.
28 F. Gritti, G. Guiochon, *Anal. Chem*. **2013**, *85*, 3017–3035.
29 F. Gritti, G. Guiochon, *Anal. Chem.* **2006**, *78*, 5329–5347.
30 K. Miyabe, G. Guiochon, *J. Chromatogr. A* **2010**, *1217*, 1713–1734.
31 F. Gritti, G. Guiochon, *AIChE J.* **2011**, *57*, 333–345.
32 F. Gritti, G. Guiochon, *AIChE J.* **2011**, *57*, 346–358.
33 J. Rybka, A. Höltzel, N. Trebel, U. Tallarek, *J. Phys. Chem. C* **2019**, *123*, 21617–21628.
34 J. L. Rafferty, J. I. Siepmann, M. R. Schure, *J. Chromatogr. A* **2009**, *1216*, 2320–2331.
35 S. M. Melnikov, A. Höltzel, A. Seidel-Morgenstern, U. Tallarek, *Angew. Chem. Int. Ed.* **2012**, *51*, 6251–6254.
36 S. M. Melnikov, A. Höltzel, A. Seidel-Morgenstern, U. Tallarek, *Anal. Chem.* **2013**, *85*, 8850–8856.
37 Q. P. Chen, M. R. Schure, J. I. Siepmann, *J. Chromatogr. A* **2018**, *1573*, 78–86.
38 R. S. Maier, M. R. Schure, *Chem. Eng. Sci.* **2018**, *185*, 243–255.
39 D. van der Spoel, H. J. C. Berendsen, In Aspects of Computational Science; A. J. van der Steen, Ed.; *National Computing Facilities Foundation (NDF): Den Haag, The Netherlands* **1995**.
40 D. van der Spoel, E. Lindahl, B. Hess. G. Groenhof, A. E. Mark, H. J. C. Berendsen, *J. Comput. Chem.* **2005**, *26*, 1701–1718.
41 M. J. Abraham, T. Murtola, R. Schulz, S. Páll, J. C. Smith, B. Hess, E. Lindahl, *SoftwareX* **2015**, *1–2*, 19–25.
42 S. Engelmann, J. Meyer, R. Hentschke, *Phys. Rev. B* **2017**, *96*, 054110.
43 Y. Zhang, Y. Y. Chen, L. Lin, P. B. Ma, *Therm. Sci.* **2015**, *18*, 1459–1461.
44 N. von Aspern, M. Leissing, C. Wölke, D. Diddens, T. Kobayashi, M. Börner, O. Stubbmann-Kazakova, V. Kozel, G.-V. Röschenthaler, J. Smiatek, S. Nowak, M. Winter, I. Cekic-Laskovic, *ChemElectroChem* **2020**, *7*, 1499–1508.
45 C. Chen, F. Pei, S. Feng, M. Xia, F. Wang, Q. Hao, W. Lei, *Nano* **2021**, 2150092.
46 W. F. van Gunsteren, S. R. Billeter, A. A. Eising, P. A. Hünenberger, P. Krüger, A. E. Mark, W. R. P. Scott, I. G. Tironi, *Biomolecular Simulation: The GROMOS96 Manual and User Guide*; Hochschulverlag AG der ETH: Zürich, **1996**.
47 M. Levitt, M. Hirshberg, R. Sharon, V. Dagett, *Comput. Phys. Commun.* **1995**, *91*, 215–231.
48 W. L. Jorgensen, S. Maxwell, J. J. Tirado-Rives, *J. Am. Chem. Soc.* **1996**, *118*, 11225–11236.

49 G. A. Kaminski, R. A. Friesner, T. Tirado–Rives, W. L. Jorgensen, *J. Phys. Chem. B* **2001**, *105*, 6474–6487.

50 A. D. Case, T. E. III. Cheatman, T. Darden, H. Gohlke, R. Luo, K. M. Jr. Merz, A. Onufriev, C. Simmerling, B. Wang, R. J. Woods, *J. Comput. Chem.* **2005**, *26*, 1668–1688.

51 B. R. Brooks, R. E. Bruccoler, B. D. Olafson, D. J. States, S. Swaminathan, M. Karplus, *J. Comput. Chem.* **1983**, *4*, 187–217.

52 B. Hess, C. Kutzner, D. van der Spoel, E. Lindahl, *J. Chem. Theory Comput.* **2008**, *4*, 435–447.

53 R. W. Hockney, S. P. Goel, J. Eastwood, *J. Comp. Phys.***1974**, *14*, 148–158.

54 W. C. Swope, H. C. Andersen, P. H. Berens, K. R. Wilson, *J. Chem. Phys.* **1982**, *76*, 637–649.

55 H. Kraus, J. Rybka, N. Trebel, A. Höltzel, U. Tallarek, *Mol. Simul.* **2021**, *47*, 306–316.

56 B. Coasne, F. Di Renzo, A. Galarneau, R. J. M. Pellenq, *Langmuir* **2008**, *24*, 7285–7293.

57 G. Bell, J. Gray, *Commun. ACM* **2002**, *45*, 91–95.

58 https://www.nhr.kit.edu/userdocs/horeka/hardware/, accessed August 2023.

59 N. Trebel, A. Höltzel, D. Frerichs, U. Tallarek, *J. Chromatogr. A* **2023**, in preparation.

Chapter 1

Insights from molecular simulations about dead time markers in reversed-phase liquid chromatography

Authors

Nicole Trebel, Alexandra Höltzel, Andreas Steinhoff, Ulrich Tallarek

State of publication

Published 15 March 2021 in *Journal of Chromatography A*, Vol. 1640, 461958.
DOI: 10.1016/j.chroma.2021.461958

Abstract

Among the most popular compounds to estimate the hold-up time in reversed-phase liquid chromatography (RPLC) are acetone and uracil, which are considered as too small and too polar, respectively, for retention by the hydrophobic stationary phase, although their observed elution behavior does not fully support this assumption. We investigate how acetone and uracil as solutes interact with the chromatographic interface through molecular dynamics simulations in an RPLC mesopore model of a silica-supported, endcapped, C_{18} phase equilibrated with a water (W)–acetonitrile (ACN) mobile phase. The simulation results provide a molecular-level explanation for the observed elution behavior of acetone and uracil, but also question whether true dead time markers for RPLC exist. Both solutes have a density maximum in the interfacial region in addition to a low presence in the bonded-phase region, but these density peaks clearly differ from the adsorption and partitioning peaks of true analytes. Acetone partially behaves like a co-solvent of ACN and partially like the analyte acetophenone. Like ACN, acetone can be found in the first and second layer of solvent molecules at the silica surface; like acetophenone, acetone adsorbs to the bonded-phase chains by orienting its polar group to the bulk region to sustain hydrogen bonds with W molecules. Uracil behavior is governed by a need for extensive hydrogen-bond coordination by W molecules. Uracil adsorbs to the very edge of the bonded-phase chains, on the bulk-region side of the ACN density maximum in the interfacial region. Further penetration into the chains is prevented by the absence of W molecules, which are not found deeper in the bonded phase, except at the silica surface. Contrary to true analytes, accumulation of uracil and acetone in the interfacial region ceases at an equimolar presence of W and ACN in the mobile phase (at 70–80% ACN volume fraction). Uracil achieves a closer approximation of the stationary-phase limit than acetone, but carries the risk of HILIC retention at high ACN fraction in the mobile phase.

1.1 Introduction

Calculation of analyte retention factors k from the analyte retention time t_r in HPLC requires knowledge of the column's hold-up time t_m:

$$k = (t_r - t_m)/t_m \quad (1.1)$$

Through multiplication with the flow rate, the hold-up time t_m is equivalent to the column's hold-up volume V_m. In chromatographic jargon, the hold-up time used to be known and is still often referred to as the dead time and the hold-up volume as dead volume or void volume.[1] Several definitions of what exactly constitutes the void volume exist in the literature, along with a variety of methods to determine or rather estimate the void volume.[2,3] These include extrapolation of the retention time data of a homologous compounds series, injection of a deuterated mobile-phase solvent, inverse size-exclusion chromatography, pycnometry, and an alternating iterative regression method that uses the retention data of the target analytes.[4–8] In practice, the most convenient way is to equate t_m with the elution time of a presumably unretained compound, referred to as a dead time or void volume marker.

The rationale behind the unretained solute approach is to approximate the time required for travel through the column without retention by the stationary phase through the elution time of a compound that, based on its molecular properties, can be expected to be barely retained by the stationary phase. Dead time markers for reversed-phase liquid chromatography (RPLC) must be small and uncharged to avoid size exclusion and Donnan exclusion,[9] respectively, from smaller mesopores, but polar enough to experience as little retention as possible by the hydrophobic stationary phase. These requirements are fulfilled by the most popular dead time markers uracil, (thio)urea, and acetone, the latter of which is also used as a cheaper and greener substitute for acetonitrile (ACN) as mobile-phase solvent in RPLC[10,11] as well as hydrophilic interaction liquid chromatography (HILIC).[12–14]

The elution time behavior for the said dead time markers exhibits two patterns: either a decline of the elution time with increasing organic solvent fraction in the mobile phase, usually shown by acetone, or a U-shaped elution time curve, as has been observed for uracil with water (W)–ACN mobile phases.[8,15–17] The former pattern could be interpreted as weak RPLC retention, whereas the U-shaped pattern could be interpreted as RPLC-type retention at low ACN volume fraction and HILIC-type retention at high ACN volume fraction.[18,19] If this is true, the question arises why and how the dead time markers acetone and uracil, which were selected for their supposed inertia towards the hydrophobic stationary phase, are retained in the first place.

Answering this question requires a molecular-level picture of the chromatographic interface, as available from molecular simulations.[20] What we know about the chromatographic interface in RPLC today was essentially established through Monte Carlo simulations by Siepmann and co-workers[20–26], with important contributions from molecular dynamics (MD) simulations, particularly regarding W–ACN mobile phases and solute, solvent, and bonded-phase diffusivities, by other groups.[20,27–35] The chromatographic interface results from equilibration of the stationary

phase with the mobile phase (during column equilibration) and spans the region between the surface of the solid support structure, typically silica, and the bulk liquid phase. On the basis of the total solvent density, Siepmann and co-workers distinguished between the bonded-phase region (I) containing the silica surface and most of the bonded-phase chains, the interfacial region (II) containing the terminal part of the bonded-phase chains and the adsorbed solvent layer, and the bulk liquid region of the pore (III). The borders between the regions are located where the total solvent density is 10% and 90% of the total solvent density in the bulk liquid.[20] The regions and their distinctive properties are visualized in Figure 1.1, which shows a simulation snapshot of our established RPLC mesopore model along with the respective solvent and bonded- phase density profiles.[34]

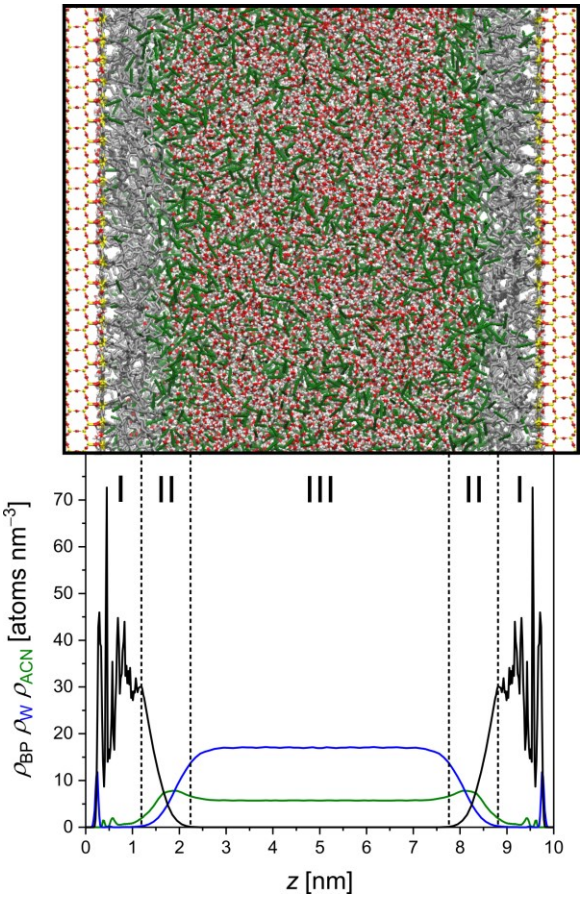

Figure 1.1. Properties of the chromatographic interface formed by a silica-supported, endcapped, C_{18} stationary phase and a W–ACN mobile phase. Top: Snapshot of the RPLC mesopore model equilibrated with 50/50 (v/v) W/ACN. The ACN ditch is visible as an ACN-rich solvent layer adjacent to the C_{18} chains. Color-code: Si, yellow; O, red; H, white; bonded phase (C_{18} chains and TMS endcapping groups), grey; ACN molecules, green. Bottom: Associated bonded-phase and solvent density profiles. Distances *z* are measured from the location of the Si surface atoms. Color-code: W, blue; ACN, green; bonded phase, black. Dashed lines separate bonded-phase region (I), interfacial region (II), and bulk liquid region (III) of the pore. The borders between the regions (z

I/II and z II/III, respectively) are located at 10% and 90% of the total solvent density in the bulk liquid.

The slit-pore model is based on two identical silica planes of 10 nm distance; the silica surface bears randomly distributed dimethyloctadecylsilane (C_{18}) chains, trimethylsilane (TMS) endcapping groups, and residual OH groups at densities representative of commercial C_{18} columns. The snapshot shows the stationary phase equilibrated with a mobile phase of 50/50 (v/v) W/ACN. The bonded-phase region comprises the residual surface OH groups, the TMS endcapping groups, all hydrocarbon groups of backfolded C_{18} chains, and most hydrocarbon groups of extended C_{18} chains.[35] Solvent presence in the bonded-phase region is predominantly related to silica surface co-ordination through hydrogen bonds (HBs). Residual surface OH groups form HBs with solvent molecules, preferably W molecules (~2 HBs per W molecule), which are in turn coordinated by the second layer of ACN molecules (~1 HB per ACN molecule). The most interesting feature of the chromatographic interface from a physicochemical as well as a chromatographic perspective is the interfacial region, where the flexible ends of the extended C_{18} chains meet the bulk liquid phase. The W density decreases sharply over the interfacial region, whereas the ACN density has a maximum there, referred to as the ACN ditch,[30] which is experimentally reflected in the excess amount of organic solvent adsorbed on an RPLC phase.[36] The interfacial region constitutes the transition between stationary phase and mobile phase, which is relevant to the measurement of analyte retention[20,34], and accommodates the ACN ditch, which enables fast surface diffusion of analytes, a unique property of RPLC.[30,31,37]

The chromatographic interface as displayed in Figure 1.1 is the stage on which analyte retention takes place. The retention factor k is defined as the ratio of the amount n of analyte in the stationary phase to the amount of analyte in the mobile phase and via concentration c of analyte in the stationary and mobile phase and the volume V of stationary and mobile phase as the product of the partition or distribution coefficient K and the phase ratio β:

$$k = n_{\mathrm{SP}}/n_{\mathrm{MP}} = (c_{\mathrm{SP}}V_{\mathrm{SP}})/(c_{\mathrm{MP}}V_{\mathrm{MP}}) = (c_{\mathrm{SP}}/c_{\mathrm{MP}}) \cdot (V_{\mathrm{SP}}/V_{\mathrm{MP}}) = K\beta \qquad (1.2)$$

According to expression (1.2), determination of k requires knowledge of the border between stationary phase and mobile phase for the determination of K as well as of β. Molecular-level knowledge of the chromatographic interface, however, does not suggest a definitive and obvious location for this border. Possibilities are, for example, the average location of the terminal methyl group of the extended C_{18} chains (z_{CH3}), the location where the bonded-phase density has relaxed to nearly zero, or the border between interfacial and bulk liquid region ($z_{\mathrm{II/III}}$). Each of these locations is sensitive to the organic solvent fraction in the mobile phase: whereas z_{CH3} and the extension of the bonded phase increase with the ACN volume fraction as the chains elongate, $z_{\mathrm{II/III}}$ goes through a minimum at an ACN volume fraction of 60%.[34]

How the three possibilities relate to actual analyte density profiles is shown in Figure 1.2 for ethylbenzene and acetophenone.[34]

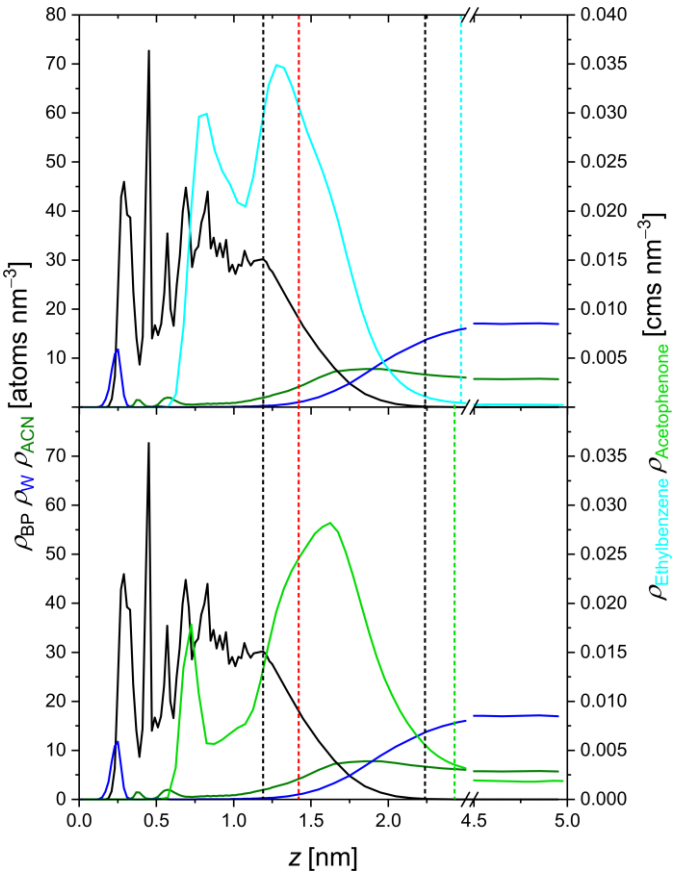

Figure 1.2. Defining the stationary-phase limit in RPLC. Density distribution of the analytes ethylbenzene (aqua) and acetophenone (light green) in the chromatographic interface shown in Figure 1.1. Bonded-phase, W, and ACN density profiles (averaged from both halves of the 10 nm pore) are shown in black, blue, and green, respectively. Dashed lines indicate the borders of bonded-phase and interfacial region (black), the average location of the terminal methyl groups of extended C_{18} chains (red), and the analyte-specific stationary-phase limits (aqua and light green). Analyte profiles have a density peak in the bonded-phase region (partitioning peak) and their density maximum in the interfacial region (adsorption peak).

The density profiles of both compounds (as indeed of any small molecule on a C_{18} phase studied so far by molecular simulations) contain two maxima: a partitioning peak in the bonded-phase region and an adsorption peak in the interfacial region. z_{CH3}, which is located closer to the limit of the bonded-phase region $z_{I/II}$ than to $z_{II/III}$, cuts off most of the adsorption peak and is thus an obviously unsuitable stationary-phase limit. The average location of the chain ends, z_{CH3}, and the location where the bonded-phase density approaches zero are ~0.8 nm apart, which reflects the frayed character of the bonded phase in the interfacial region. $z_{II/III}$ covers most, but not all of the adsorption peaks of the analytes. As analyte density profiles were calculated from the molecules' center-of-mass (cms) and do not reflect the molecules' extension, the cutoff by $z_{II/III}$ is more serious than is apparent from Figure 1.2. (This also means that analyte molecules in the ACN ditch are in contact with bonded-phase groups, contradicting the notion that analyte molecules are dissolved in

the "adsorbed" ACN-rich solvent layer) Moreover, more density is cut off from the acetophenone profile than from that of ethylbenzene. The latter observation ties in with the idea that the stationary-phase limit is not solely defined by the chromatographic interface, but is also sensitive to analyte properties.

The possibility of an analyte-sensitive stationary-phase limit (and thus an analyte-sensitive void volume) was insightfully suggested long before molecular-level details of the chromatographic interface became known.[38] Faced with the problem of how to define the stationary-phase limit to determine distribution coefficients from simulated analyte density profiles in a previous study,[34] we took up this idea and calculated analyte-specific stationary-phase limits (z_{SP}) based on the number of contacts between analyte molecules and the bonded phase. For each analyte species and W/ACN ratio of the mobile phase, we determined z_{SP} as the location where analyte molecules had on average less than one contact with the bonded-phase chains. Our definition of the stationary-phase limit is admittedly arbitrary considering that the question of how many bonded-phase contacts are required for retention is debatable, but has the merit of being unequivocal as well as sensitive to analyte properties and the W/ACN ratio of the mobile phase. The analyte distribution coefficients K calculated from simulated analyte density profiles using this definition of the stationary-phase limit compared very well to experimental retention factors k determined on an endcapped C_{18} column over a range from 80/20 to 10/90 (v/v) W/ACN.[34]

Figure 1.1 visualizes that even with molecular-detail knowledge of the chromatographic interface, the location of the stationary-phase limit and thus the definition of the dead volume in RPLC remain arbitrary. This leads to the question of what the elution time of dead time markers such as acetone and uracil actually reflects. It is conceivable that the elution time curve of a dead time marker (its elution time as a function of the organic-solvent fraction in the mobile phase) reflects the location of a specific property of the chromatographic interface. A decrease of the elution time with increasing organic-solvent fraction in the mobile phase, such as shown by acetone,[39] could thus possibly reflect a decrease in void volume caused by the elongating C_{18} chains. And the location of the border between interfacial and bulk liquid region, $z_{II/III}$, goes through a minimum at 60% ACN volume fraction, as does the elution time curve of uracil.[8,15–17] If this is true, acetone and uracil must possess molecular properties that enable the sensing of a particular location in the chromatographic interface. Alternatively, the elution time curves of the dead time markers might reflect their retention behavior. In that case, the dead time markers are not as inert towards the hydrophobic stationary phase as their chemical structures and negative log$P$ (logarithm of the octanol–water partition coefficient) values[40] suggest.

To find out how the dead time markers interact with the chromatographic interface in RPLC, we perform MD simulations of acetone and uracil as solutes in our established RPLC mesopore model of a silica-supported, endcapped, C_{18} phase with mobile phases between 80/20 and 10/90 (v/v) W/ACN. The density distribution, orientation, hydrogen bonding, and diffusive mobility of acetone and uracil will be analyzed and compared with the respective data for RPLC analytes, available from previous simulations in our RPLC mesopore model,[31,34] to pinpoint where dead time markers differ from true analytes.

1.2 Methods

1.2.1 Simulation box and force-field parameters

The RPLC mesopore model used for all simulations consists of a three-layer silica slab of 0.93 nm width (z-direction) placed between 5 nm wide solvent reservoirs in a ($x \times y \times z$) = 12.14 × 13.2 × 10.93 nm^3 simulation box. With the applied periodic boundary conditions, the system equals a 10 nm wide slit pore. The silica slab was cut from β-cristobalite SiO_2 parallel to the (111) face, resulting in a surface bearing 4.5 single silanol groups nm^{-2} (7.5 μmol m^{-2}). The surface was then randomly grafted with C_{18} chains and TMS groups at densities of 1.87 chains nm^{-2} (3.11 μmol m^{-2}) and 0.56 groups nm^{-2} (0.93 μmol m^{-2}), respectively, which left 2.06 residual OH groups nm^{-2} (3.42 μmol m^{-2}) on the surface. For the silica surface atoms (Si, O, and H) force-field parameters from Gulmen and Thompson were taken.[41] C_{18} chains, TMS groups, and ACN molecules were described by the transferable potentials for phase equilibria united-atom (TraPPE-UA) force field.[42,43] The simple point charge/extended (SPC/E) force field was used for W molecules.[44] All solute molecules (acetone and uracil as well as analyte compounds in previous simulations[30,31,34,35] were treated with the explicit CHARMM general force field (CGenFF).[45,46]

The force fields used for simulations of RPLC systems have to appropriately account for the following interactions: solvent–solvent, solvent–silica surface, solvent–bonded phase, solvent–solute, solute–silica surface, and solute–bonded phase. Thus, the force field chosen for a specific component may differ from the appropriate force-field choice for the same component in a different system, for example, for the simulation of the liquid–liquid equilibria of water–alkane mixtures.[47] Our force-field selection focused on finding the right combination to closely approximate experimental conditions in RPLC. We arrived at the described combination in several stages. First, the force fields for the W and ACN molecules of the mobile phase were chosen following a recommendation of Mountain,[48] who showed that the combination of SPC/E and TraPPE-UA reproduces the hydrogen bonding in and liquid density of W–ACN mixtures well. This is a major requisite for recovering the experimental diffusion coefficients of solvent and solute molecules in bulk liquid. It was next established that the chosen force fields for the mobile-phase solvents and the silica surface account for the interaction of W–ACN mixtures with bare-silica surfaces and reproduce the experimentally observed dependence of the retention factor from the ACN fraction in the mobile phase in HILIC.[49,50] The introduction of the force field for the bonded phase yielded solvent and solute density profiles[30,31] that were consistent with those simulated earlier for RPLC systems by the Siepmann group[24,25] and the Meuwly group[27,28] who had used different force fields for the mobile-phase solvents. The CHARMM force field for the solutes was chosen because it provided parameters for every solute species we intended to study. Comparison of distribution coefficients calculated from the simulated density profiles of RPLC analytes with their experimental retention factors proved that our mesopore model and particular force-field combination are able to reproduce the retentive properties of an RPLC column.[34] Molecular dynamics simulations using the described force-field combination[30,31,50,51] have successfully explained and predicted the experimentally observed retention and surface diffusion behavior of analytes in RPLC and HILIC systems.[36,37,52]

1.2.2 Molecular dynamics simulations

MD simulations were carried out with GROMACS 2018.5[53,54] at 300 K for a canonical *NVT* ensemble (constant number of molecules *N*, simulation box volume *V*, and temperature *T*). Acetone and uracil were each simulated (N_{solute} = 10 corresponding to c_{solute} = 10 mmol L^{-1}) for eight W/ACN ratios between 80/20 and 10/90 (v/v), yielding a total of 2 × 8 = 16 simulation systems. New data for analyte compounds were calculated from previously simulated trajectories.[34] The required number of solvent molecules in the simulation box for each W/ACN ratio (Table 1.S1) was determined in preliminary simulations.[34] At the low solute concentration in the simulation box, the different partial molar volumes of acetone and uracil did not lead to detectable changes in the properties of the chromatographic interface, as monitored through bonded-phase and solvent densities as well as solvent diffusion coefficients. The equilibrated simulation systems reproduce the result of column equilibration in chromatographic practice, that is, the W and ACN number densities in the bulk region of the pore recover the targeted W/ACN ratio of the mobile phase (with an accuracy ±1%) after ACN ditch formation is complete. After an equilibration period of 50–70 ns, productive simulations were run for 500 ns with a time step of 1 fs for the integration of the equations of motions. The output frequency was set to 0.5 ps. Energy minimization was conducted with the steepest descent method. Initial velocities were randomly assigned according to a Maxwell–Boltzmann distribution. Long-range electrostatic interactions were provided by the particle-mesh Ewald algorithm,[55] and nonbonded interactions were modeled with a 12–6 Lennard-Jones potential. Lennard-Jones parameters for unlike interactions were treated with the Lorentz–Berthelot combination rules. A cutoff radius of 1.4 nm, validated earlier,[30] was used for all interactions.

1.2.3 Calculation of density profiles

Solvent, bonded-phase, and solute density profiles were calculated from the atom number densities of the O atom of W, the central C atom of ACN, the CH_2 and CH_3 united-atom groups of the bonded phase, and the cms of solute molecules. The distance was measured relative to the location of the Si surface atoms (z = 0). Density profiles for bonded-phase groups and solvent molecules were calculated from 20 ns trajectories, using bin sizes of 0.02 nm and 0.1 nm at $z < 1$ nm and $z > 1$ nm, respectively. Density profiles for solute molecules were calculated from the complete trajectories using a bin size of 0.05 nm.

1.2.4 Analysis of solute orientation

For the analysis of solute orientation, molecular vectors were defined as shown in Figure 1.3.

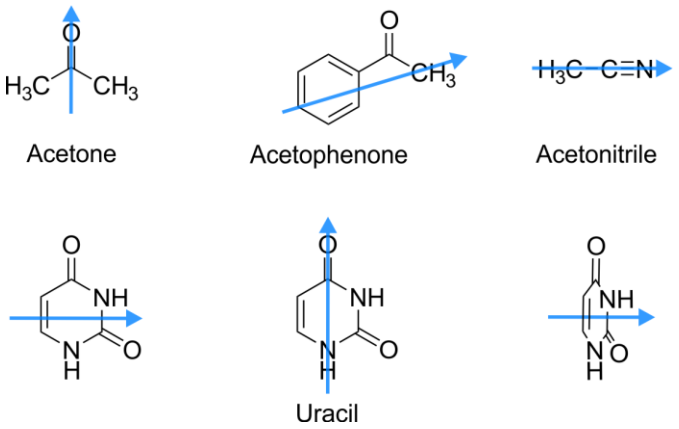

Figure 1.3. Definition of molecular vectors used to calculate the orientation of solute molecules with respect to the surface normal at different locations in the chromatographic interface.

The unambiguous description of the uracil orientation required three orthogonal molecular vectors. The solute orientation, described by the cosine of the angle α between the molecular vector and the surface normal (Figure 1.4), was determined from the complete trajectory for z-intervals of ±0.025 nm around the respective solute density maxima.

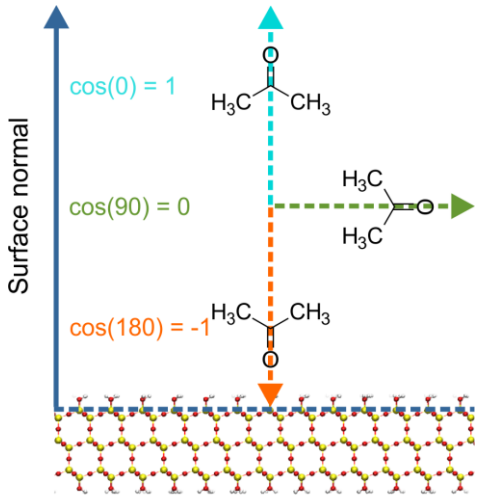

Figure 1.4. Schematic representation of the relation between the molecular vector of acetone and the surface normal. For simplicity, the silica surface is shown without the bonded phase. Color code: Si, yellow; O, red; H, white.

1.2.5 Determination of solute hydrogen bonds

For hydrogen-bond analysis, radial distribution functions (RDFs) were first calculated for all potential donor–acceptor pairs X-H–X (X = N, O) between solute and solvent molecules as well as between solute molecules and residual surface OH groups. The minimum following the first maximum in an RDF was taken as the cutoff radius r_{HB} (Table 1.S2). A HB was counted when the distance criterion ($r \leq r_{HB}$) for the respective donor–acceptor pair was fulfilled. HBs were determined from 10 ns trajectories for z-intervals of ±0.025 nm around the respective solute density

maxima and for z = 3.025–4.025 nm in the bulk liquid region of the pore. Uncertainty estimates for the calculated solute–solvent HBs were in the range of ±0.01–0.04 (acetone–W), ±0.02–0.07 (acetophenone–W), ±0.04–0.10 (uracil–W), and ±0.02–0.04 (uracil–ACN).

1.2.6 Calculation of parallel diffusion coefficients

The distance-dependent diffusion coefficient of solvent and solute molecules parallel to the silica surface, $D_{||}(z)$, was calculated following an approach by Liu et al.,[56] as established in our previous MD studies of liquid chromatography systems.[14,30,31,34,35,50,51,57] To obtain spatial resolution, each solvent or solute molecule was indexed according to its initial z-position and allowed a maximum shift of ±0.3 nm around this z-position during the observation interval. (If the shift exceeded the allowed tolerance, the displacement was discarded from the data.) The mean squared displacement $\langle r^2(t)\rangle = \langle x^2(t) + y^2(t)\rangle$ of the observed species along the x- and y-axes was repeatedly recorded during 20 ps time intervals shifted consecutively in 0.5 ps time steps throughout the whole trajectory. $D_{||}$ was calculated using a bin size of 0.2 nm from the linear slope of the observation curve (t = 4–16 ps) according to the Einstein equation:

$$D_{||}(z) = \frac{1}{4}\frac{d\langle r^2(t)\rangle}{dt} \tag{1.3}$$

Additionally, two $D_{||}(z)$ values were calculated in the same way from the linear slope of the observation curve between t = 4–10 and 10–16 ps, and the difference between these values was used to give an error estimate. Uncertainty estimates for the calculated $D_{||,bulk}$ values were in the range of ±0.02–0.06 for ACN and analytes (ethylbenzene, benzene, acetophenone, and benzyl alcohol) and ±0.04–0.09 for dead time markers (acetone, uracil). Uncertainty estimates for the calculated $D_{||,max}$ values were in the range of ±0.02–0.12 for analytes and ±0.02–0.16 for dead time markers. $D_{||,max}$ and $D_{||,bulk}$ values with their error estimates are listed in Table 1.S3 for the dead time markers. Corresponding data for the analytes can be found in a previous publication (cf. Tables S10–S13[34]).

1.2.7 Calculation of the stationary-phase limit and of distribution coefficients

The stationary-phase limit z_{SP} was determined for each solute and W/ACN ratio of the mobile phase as the distance from the silica surface where – averaged over a 20 ns trajectory – a solute molecule had less than one contact with bonded-phase groups (Table 1.S4). Distribution coefficients $K = c_{SP}/c_{MP}$ (Table 1.S5) were then determined for each solute and W/ACN ratio of the mobile phase from the respective solute density profiles as the ratio between the average solute concentration from $z = 0$ nm to z_{SP} (c_{SP}) and the average solute concentration from z_{SP} to $z = 5$ nm (c_{MP}).

1.2.8 Contact analysis

To determine the number of solute–solvent and solute–bonded phase contacts, RDFs were first calculated between the cms of a solute and the O atom of W, the central C atom of ACN, or the united-atom groups of the bonded phase. The minimum following the first maximum in an RDF was taken as the cutoff radius r_C (Table 1.S6) that indicates the first coordination shell for a particular solute–solvent and solute–bonded phase pair. A contact was counted when the distance criterion ($r \leq r_C$) was fulfilled. The number of counted contacts for a particular solute–solvent or solute–bonded phase pair was normalized by the volume of a sphere with radius r_C (i.e., by the volume of the first coordination shell) to enable the quantitative comparison between solutes of different chemical structure and molecular size and thus differently sized coordination shells. Contacts were determined from 20 ns trajectories for z-intervals of ±0.025 nm around the respective solute density maxima.

1.3 Results and discussion

1.3.1 Interaction of acetone with the chromatographic interface

How acetone as a dead time marker interacts with the chromatographic interface formed by an endcapped C_{18} stationary phase and W–ACN mobile phase is described through an analysis of the interrelated density distribution, orientation, hydrogen bonding, and lateral mobility of acetone. Throughout the analysis, acetone is compared with ACN and acetophenone based on similarities in solvent properties and molecular structure, respectively. We begin with the density distribution: Figure 1.5 shows the acetone, acetophenone, bonded-phase, and solvent density profiles at a selected solvent ratio of 80/20 (v/v) W/ACN, as well as the acetone and ACN density profiles for the whole simulated W/ACN range.

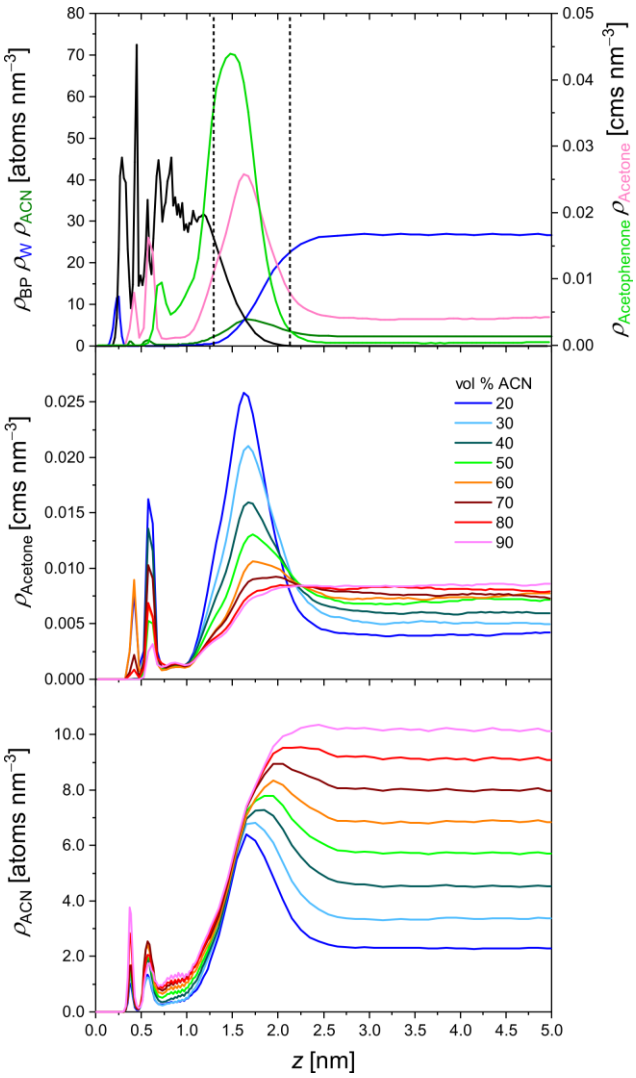

Figure 1.5. Density distribution of the dead time marker acetone in the chromatographic interface. Top: Comparison of the density profiles of acetone (pink) and acetophenone (light green) at 80/20 (v/v) W/ACN. Bonded-phase, W, and ACN density profiles are colored black, blue, and green, respectively. Dashed black lines indicate the borders of bonded-phase and interfacial region. Middle: Evolution of the acetone density profiles at increasing ACN volume fraction in the mobile phase. Bottom: Evolution of the ACN density profiles at increasing ACN volume fraction in the mobile phase.

The similarity between the acetone and ACN density distributions is striking. Like ACN, acetone has two small density peaks in the bonded-phase region (at z = 0.425 and 0.575 nm) and a broad density maximum in the interfacial region. With increasing ACN volume fraction, the acetone density maximum broadens and shifts towards the mobile phase (from z = 1.575 to 1.975 nm between 20% and 70% ACN). At 80% ACN, the acetone density maximum has flattened out into the level of the bulk liquid region, whereas the two surface peaks remain detectable. Essentially the same applies to the density profile of ACN, whereby the ACN density maximum is located a

bit closer to the bulk liquid region than the acetone density maximum and has not flattened out completely at 80% ACN volume fraction in the mobile phase.
Figure 1.6 shows the orientation of acetone molecules in the density peaks, Figure 1.7 the respective data for ACN and acetophenone.

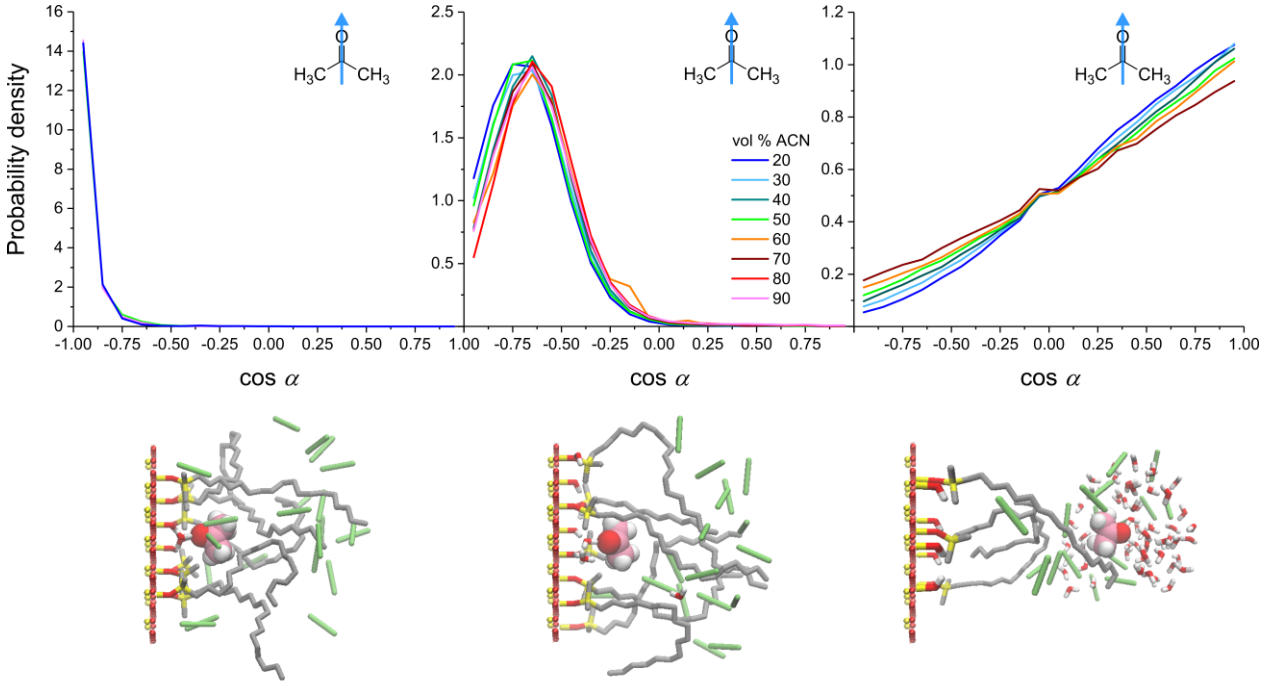

Figure 1.6. Acetone orientation at characteristic locations in the chromatographic interface. Shown are the probability distributions for the angle α between the surface normal and the molecular vector of acetone for density peaks in the bonded-phase region (first and second surface peak; left and middle panel, respectively) and the interfacial region (right panel). Acetone orientation in the first surface peak is shown only for low, medium, and high ACN volume fraction in the mobile phase as the respective probability distributions all fall onto each other. Snapshots illustrate the typical acetone orientation for each density peak. The snapshots show only selected solvent molecules within reasonable distance (less than ~1 nm) to the respective acetone molecules.

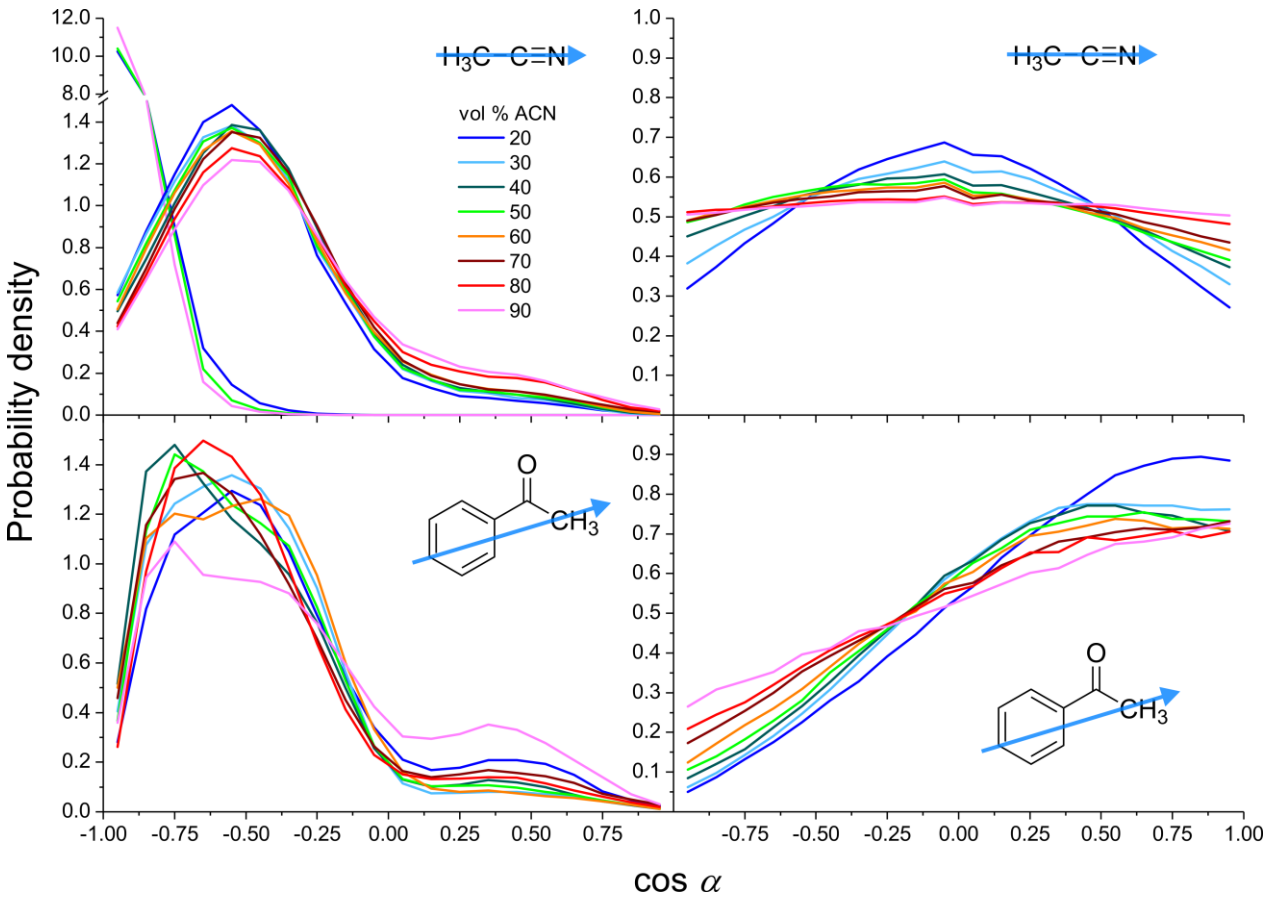

Figure 1.7. Orientation of ACN (top) and acetophenone (bottom) at characteristic locations in the chromatographic interface. Shown are the probability distributions for the angle α between the surface normal and the molecular vector of ACN or acetophenone, respectively, for density peaks in the bonded-phase region (first and second surface peak of ACN, respectively, partitioning peak of acetophenone; left panels) and the interfacial region (ACN ditch and adsorption peak of acetophenone; right panels). ACN orientation in the first surface peak is shown only for low, medium, and high ACN volume fraction in the mobile phase as the respective probability distributions all fall onto each other.

The density peaks of acetone in the bonded-phase region are associated with the silica surface, where solute orientation is determined by hydrogen-bonding opportunities. The first surface peak consists of acetone molecules strictly turning the O atom to the surface. Direct HB contact between acetone molecules and residual OH groups is occasionally observed during simulations, but these events are rare. An acetone molecule of the first surface peak forms on average 0.67 HBs with W molecules at the surface. Occupation of the first surface layer by acetone molecules is very low (0.5% of acetone molecules in the simulation box), but the population probability increases for the second surface peak (4% of acetone molecules in the simulation box). Here, acetone molecules still point the O atom towards the silica surface, but with less rigidity of the angle between the surface normal and the molecular vector of acetone. Acetone molecules of the second surface peak also act as HB acceptors to surface-attached W molecules (1.02 HBs per acetone molecule).

Comparison of Figures 1.6 and 1.7 shows that acetone and ACN orientation are practically identical in the first surface peak, similar in the second surface peak, but different in the interfacial region. Whereas all acetone molecules of the second surface peak turn their heteroatom to the surface, a small percentage of ACN molecules of the second surface peak show the opposite orientation. These ACN molecules coordinate the first layer of surface-adsorbed ACN molecules as well as the endcapping groups. In the interfacial region, ACN molecules are nearly randomly oriented, with a slight preference for a surface-parallel orientation at W-rich mobile phases, whereas acetone molecules prefer to turn the O atom towards the bulk region to accept HBs from W molecules.
Further, comparison of Figures 1.6 and 1.7 shows that acetone orientation resembles acetophenone orientation in the interfacial region, but not in the bonded-phase region. Acetophenone molecules in the bonded-phase region (partitioning peak) form ~1 HB per molecule with surface-attached W molecules, like acetone molecules of the second surface peak, but the acetophenone partitioning peak also contains a sizable portion (~10%) of oppositely oriented molecules, like ACN molecules of the second surface peak. The population probability for the partitioning peak of acetophenone is also higher than for the second surface peak of acetone (7% vs 4% of solute molecules in the simulation box).
The similarity between acetophenone and acetone orientation in the interfacial region is related to the HB patterns of the two solutes (Figure 1.8).

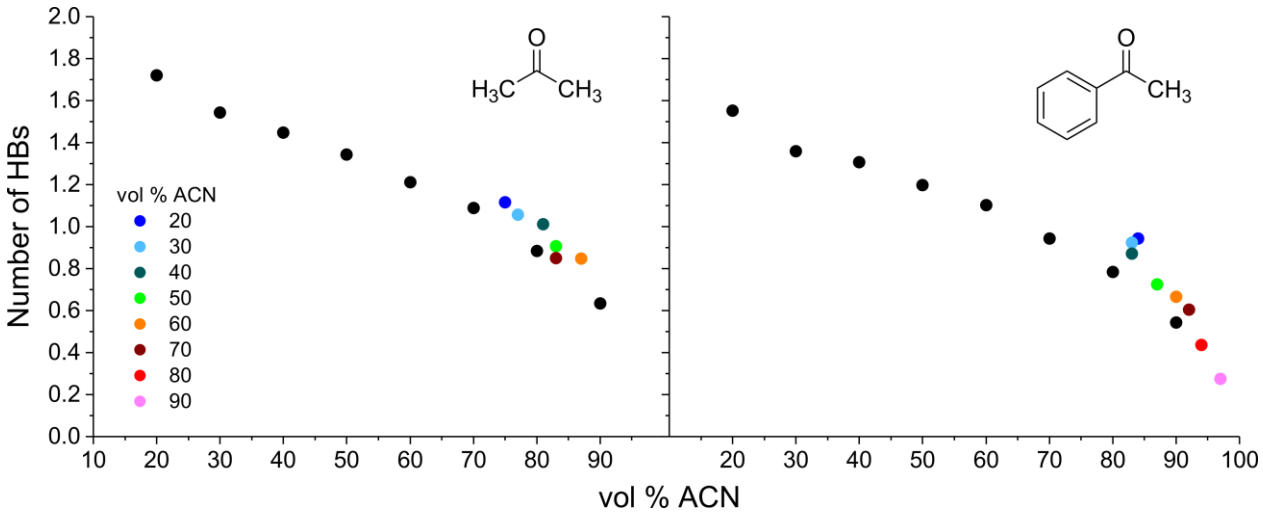

Figure 1.8. Comparison of solute–solvent hydrogen bonding in the interfacial region and the bulk liquid region of the pore for acetone (left) and acetophenone (right). Shown are the average number of hydrogen bonds (HBs) per solute molecule with W at the solute density maximum (colored) and in the bulk region (black). Data for the inter- facial region consider the local solvent environment of the solute molecules and are color-coded to indicate the respective ACN volume fraction in the mobile phase.

Because compounds are either limited to or prefer W molecules as HB partner, the number of solute–solvent HBs is generally sensitive to the local solvent composition, which in turn depends

on the W/ACN ratio of the mobile phase. (Except at the silica surface, where the local solvent composition is largely insensitive to the W/ACN ratio of the mobile phase.) At 80/20 (v/v) W/ACN, acetone and acetophenone molecules in the bulk liquid region form on average 1.72 and 1.55 HBs, respectively, with W molecules. The number of HBs decreases with the ACN volume fraction in the mobile phase to 0.63 and 0.54 HBs per molecule at 10/90 (v/v) W/ACN. Because of the ACN ditch, solute molecules in the interfacial region experience a solvent environment that is richer in ACN than the bulk liquid region. At 80/20 (v/v) W/ACN, the local solvent ratio for acetone and acetophenone molecules in the interfacial region is 25/75 and 16/84 (v/v) W/ACN, respectively. Acetone and acetophenone molecules in the interfacial region form 1.12 and 0.94 HBs with W molecules, which is slightly above the values expected for the solutes in the bulk liquid region at the respective W/ACN ratios. For both solutes the number of HBs per molecule in the interfacial region tends to be higher than expected from the local solvent composition, because alignment of the molecular vector with the surface normal by acetone and acetophenone molecules in the interfacial region favors the formation of solute–W HBs.

Figure 1.9 compares the parallel diffusion coefficient profiles of acetone, ACN, and acetophenone. From earlier MD simulation studies conducted in RPLC mesopores[30,31,34,35] a pattern has emerged for the lateral mobility of solutes over the pore diameter: solutes go through a lateral mobility maximum in the interfacial region before their mobility predictably decreases with increasing penetration into the bonded phase.

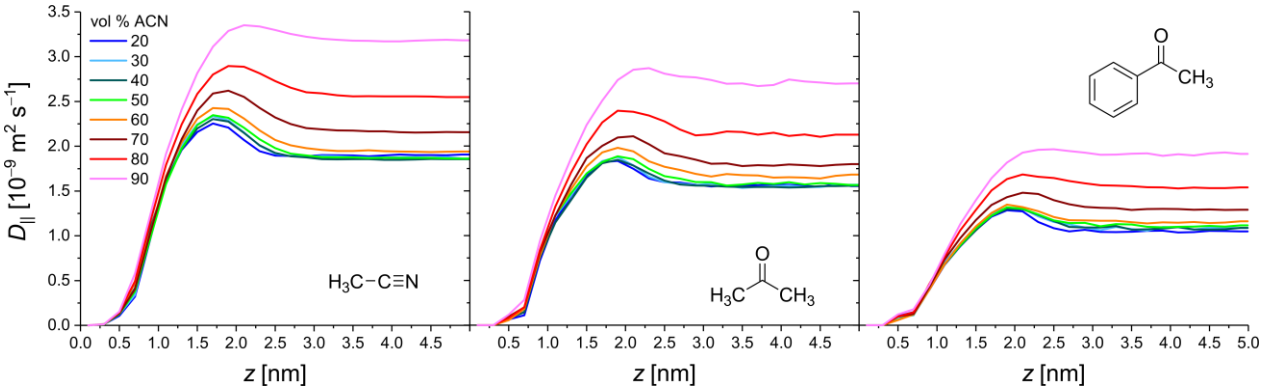

Figure 1.9. Comparison of the lateral diffusive mobility of ACN (left), acetone (middle), and acetophenone (right) in the pore. Shown is the evolution of the parallel diffusion coefficient profiles at increasing ACN volume fraction in the mobile phase.

As proved then,[30,31] fast surface diffusion in the interfacial region results from the ACN-rich local solvent composition that favors the diffusive mobility of organic compounds (including ACN) and chain ends alike. In the ACN ditch, the lateral mobility of the terminal methyl and next-to-terminal methylene groups of the C_{18} chains (i.e., $CH_3(18)$ and $CH_2(17)$) is comparable to that of ethylbenzene and acetophenone, respectively.[31,34] For a given stationary phase, the extent of the mobility gain from surface diffusion depends on the ACN excess in the interfacial region (which decreases with increasing ACN volume fraction in the mobile phase), but also on solute properties.[30,31,34,35]

The parallel diffusion coefficient profiles of acetone share similarities with those of ACN and acetophenone. Regarding diffusivity in the bulk liquid region, acetone is much closer to ACN than to acetophenone, which is expected given that molecular size plays a major role for the diffusivity. Like ACN, acetone also still retains a pronounced lateral mobility maximum at 80% ACN and a discernible maximum at 90% ACN, whereas this is not the case for acetophenone. This indicates a similar dependence of the lateral mobility gain from the W/ACN ratio of the mobile phase for acetone and ACN. When it comes to the actual extent of the lateral mobility gain, however, acetone is closer to acetophenone than to ACN. Instead of mimicking the largely random orientation of ACN in the interfacial region, acetone shares the directed orientation and HB pattern of acetophenone. A directed molecular orientation that supports solute–W HBs has already been shown to be responsible for the lower mobility gain of acetophenone (and benzyl alcohol) compared with an apolar analyte of similar molecular size, such as ethylbenzene.[34]

1.3.2 Interaction of uracil with the chromatographic interface

Its heteroatom-heavy molecular structure differentiates uracil clearly from all other solutes whose RPLC behavior has been studied so far.[20,30–33] Uracil behavior will therefore be primarily referenced to acetone behavior to directly compare the two dead time markers. Figure 1.10 shows the uracil, acetone, bonded-phase, and solvent density profiles at 80/20 (v/v) W/ACN as well as the evolution of the uracil density profiles with increasing ACN volume fraction in the mobile phase.

Uracil has a density maximum in the interfacial region and a tiny density peak in the bonded-phase phase region (at z = 0.675–0.725 nm). As observed for acetone and acetophenone, the uracil density maximum in the interfacial region broadens and shifts to the bulk liquid region with increasing ACN volume fraction (from z = 1.675 to 2.175 nm between 20% and 60% ACN). The density maximum has flattened out at 70% ACN, that is, uracil accumulation at the bonded-phase chain ends stops at lower ACN volume fraction than observed for acetone (whose density maximum has vanished at 80% ACN, cf. Figure 1.5). This is not the only indication that uracil interaction with the bonded phase is weaker than observed for acetone: 1) the uracil density maximum is located on the bulk liquid side of the ACN density maximum (as opposed to the acetone density maximum, which is located on the silica surface side of the ACN maximum), 2) the uracil density peaks are consistently lower than the acetone density peaks at equal W/ACN ratio of the mobile phase, and 3) the uracil density in the bulk liquid region of the pore is higher than the acetone density there.

The simulated density profiles for the dead time markers reflect that uracil yields a shorter dead time than acetone for the same C_{18} column, as typically observed in chromatographic practice.[2] Another important concurrence with chromatographic practice is the vanishing of the uracil density maximum in the interfacial region at high ACN volume fraction in the mobile phase. The density maximum is last observed at 60% ACN, where the elution time curve of uracil displays a minimum.[8,15–17] The evolution of the uracil density maximum in the interfacial region strongly suggests that the descending branch of the elution time curve indicates decreasing interaction of

uracil with the chain ends of the bonded phase and the loss of RPLC-type retention at >60% ACN volume fraction in the mobile phase.

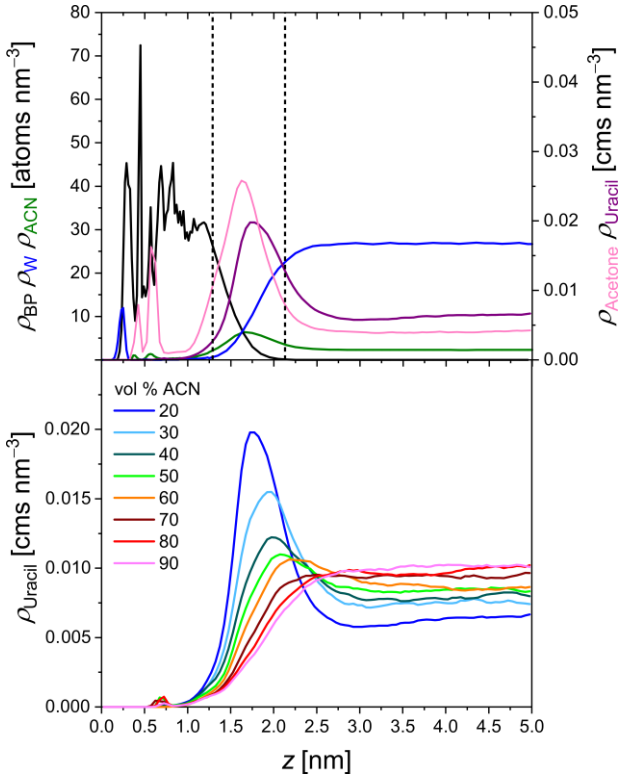

Figure 1.10. Density distribution of the dead time marker uracil in the chromatographic interface. Top: Comparison of the density profiles of uracil (purple) and acetone (pink) at 80/20 (v/v) W/ACN. Bonded-phase, W, and ACN density profiles are colored black, blue, and green, respectively. Dashed black lines indicate the borders of bonded-phase and interfacial region. Bottom: Evolution of the uracil density profiles at increasing ACN volume fraction in the mobile phase.

The tiny surface peak of uracil in the bonded-phase region represents (averaged over all W/ACN ratios) only 0.17% of uracil molecules in the simulation box. Molecules in this peak preferentially orient the NO vector towards the silica surface (Figure 1.11).

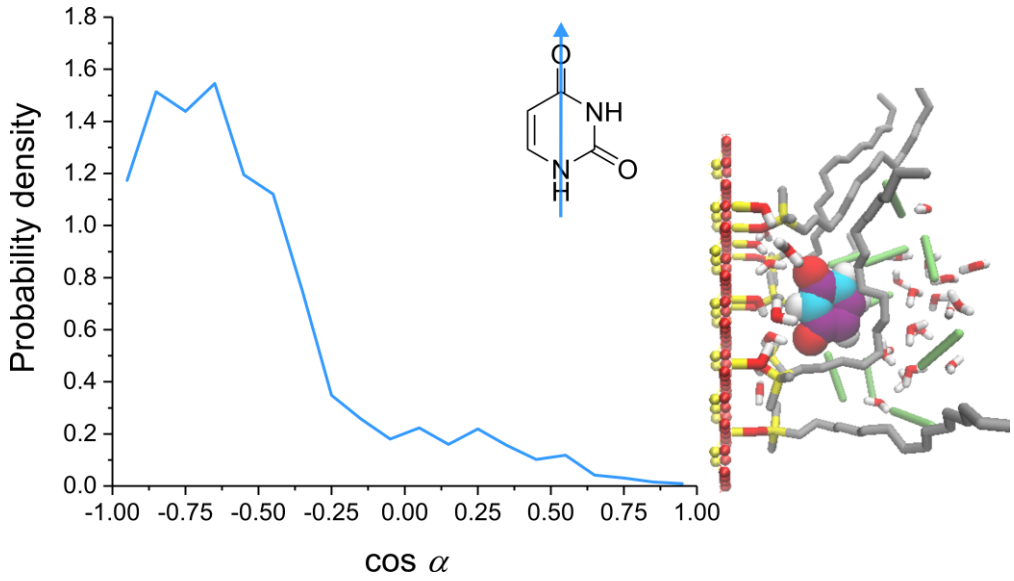

Figure 1.11. Uracil orientation at the silica surface. Shown is the probability distribution for the angle α between the surface normal and the NO vector of uracil. As observed for acetone and ACN, uracil orientation at the silica surface is insensitive to the W/ACN ratio of the mobile phase. The probability distribution was thus averaged over several W/ACN ratios to improve statistics for the very small density peak. The snapshot illustrates the typical uracil orientation at the silica surface.

A small fraction of uracil molecules (~10%) has the opposite orientation, a feature shared by acetophenone molecules of the partitioning peak and ACN molecules of the second surface peak (cf. Figure 1.7). In the latter cases, the opposite orientation involves loss of hydrogen bonding with the surface-attached W layer. ACN and acetophenone molecules then turn their hydrophobic side to the surface to make contact with surface-adsorbed ACN molecules and endcapping groups. Uracil presence at the silica surface is, however, always driven by hydrogen-bonding opportunities. Pointing the NO vector away from the silica surface still enables uracil molecules to make HB contact with the surface-attached solvent layer. An uracil molecule in the surface peak (regardless of orientation) forms on average 1.64 HBs with W and 0.88 HBs with ACN molecules; direct HBs with residual surface OH groups are extremely rare. As Figure 1.13 will show, the HB coordination of uracil molecules at the silica surface is far from ideal. The restricted space and mobility of solvent molecules and bonded-phase groups at the silica surface prevents an optimal HB coordination of uracil molecules there.

Although the surface peak density is very low, uracil behavior at the silica surface hints at HILIC retention. In our pore model the bonded phase is rather homogeneously distributed on an idealized, planar silica surface. This arrangement captures analyte retention on an RPLC column well, as proved earlier through comparing simulated distribution coefficients with experimental retention factors.[34] But the bonded-phase distribution on the silica support in real-life columns is hardly as homogeneous as depicted in our pore model. When a column contains bare-silica patches that enable the formation of multiple uracil–surface HBs (mediated via the surface-attached W layer)

and/or bears residual surface charges, surface adsorption of uracil molecules and thus local HILIC retention of uracil is the probable outcome.

Contrary to expectation, uracil orientation in the interfacial region is neither the mirror image of uracil orientation at the silica surface (i.e., uracil does not point the NO vector away from the bulk liquid region) nor follows the easy logic of aligning the hydrophobic and hydrophilic sides of the molecule with the bonded-phase and bulk liquid region, respectively. Figure 1.12 shows broad distributions for the angle between surface normal and the NO vector, between surface normal and the CC vector, and between surface normal and the vector perpendicular to the molecular plane of uracil. The CC vector orientation is random, except for a slight preference for angles of 84°±37° at 20% ACN. The NO vector orientation shows a mild preference for angles of 100°±32°, which is more pronounced at 20% ACN. The orientation for the vector perpendicular to the molecular plane shows a mild to moderate preference for angles close to 0° and 180°, that is, for a surface-parallel arrangement of the molecular plane. Together, CC and NO vector orientations negate any alignment of the hydrophilic side of uracil with the bulk liquid side of the pore. In this respect as well as in the tendency to lie flat over the bonded-phase chains at low ACN volume fraction in the mobile phase, uracil resembles ACN (cf. Figure 1.7).

Uracil is characterized by extensive HB coordination (primarily by W molecules) in the bulk liquid phase. At 80/20 (v/v) W/ACN, an uracil molecule in the bulk liquid region forms on average 4.95 HBs, 4.63 HBs with W and 0.32 HBs with ACN. At 20/80 (v/v) W/ACN, the number of uracil–solvent HBs has decreased to 3.13, 2.02 with W and 1.1 with ACN. Only at 10/90 (v/v) W/ACN, that is, at a molar ratio of approximately 1/3 (*n*/*n*) W/ACN, W and ACN approach equal HB partner status for uracil (1.28 and 1.24 HBs, respectively), but at this point the overall number of uracil–solvent HBs is also down to 2.52, ~50% of the value at 80/20 (v/v) W/ACN. These numbers reflect that uracil molecules strongly prefer W molecules for HB coordination and are slow to accept ACN molecules as HB partner at increasing ACN volume fraction in the mobile phase.

Uracil molecules do not require a particular orientation to achieve sufficient HB coordination in the interfacial region, as Figure 1.13 shows. The number of uracil–solvent HBs in the interfacial region is overall only slightly lower than expected from the local solvent environment and still dominated by uracil–W HBs. Between 20% and 60% ACN in the mobile phase, the number of uracil–W HBs in the interfacial region decreases by only 16% from 2.88 to 2.42 HBs while the number of uracil–ACN HBs increases by 31% from 0.71 to 0.93 HBs. At 20% ACN, where uracil molecules have a more pronounced preference for a surface-parallel arrangement of the molecular plane (cf. Figure 1.12), uracil–W hydrogen bonding in the interfacial region exceeds the value expected from the local solvent composition (while uracil–ACN hydrogen bonding remains below) so that uracil–solvent HBs are actually slightly above the expected value. The need for extensive HB coordination by solvent molecules explains why the uracil density maximum remains on the very fringe of the bonded-phase chains: further penetration into the bonded phase would mean a loss of suitable HB partners.

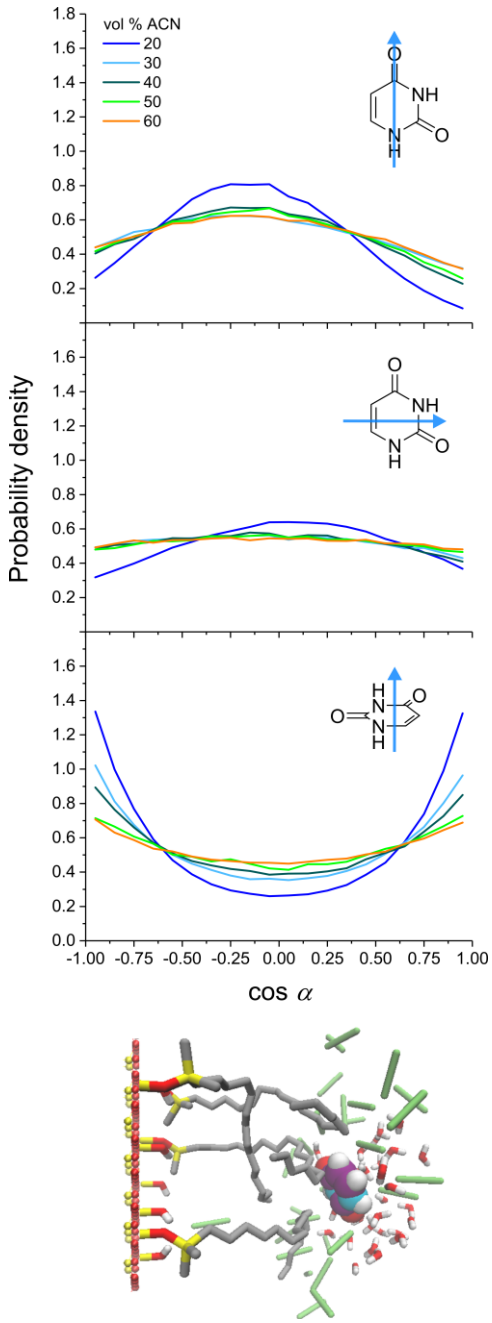

Figure 1.12. Uracil orientation in the interfacial region of the pore. Shown are probability distributions for the angle α between the surface normal and the NO vector (top), between the surface normal and the CC vector (middle), and between the surface normal and the vector perpendicular to the molecular plane of uracil (bottom). The snapshot illustrates the typical uracil orientation at the uracil density maximum in the interfacial region. The snapshot shows only selected solvent molecules within reasonable distance (less than ~1 nm) to the uracil molecule.

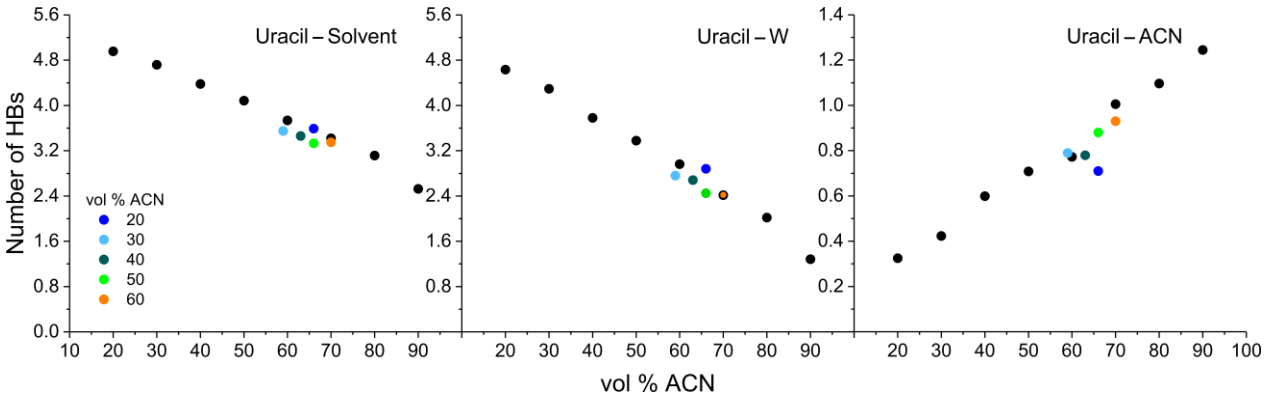

Figure 1.13. Comparison of uracil–solvent hydrogen bonding in the interfacial region and the bulk liquid region of the pore. Shown are the average number of hydrogen bonds (HBs) per uracil molecule with W and/or ACN at the uracil density maximum (colored) and in the bulk region (black). Data for the interfacial region consider the local solvent environment of the uracil molecules and are color-coded to indicate the respective ACN volume fraction in the bulk mobile phase.

Considering the lateral mobility of uracil molecules over the pore diameter, Figure 1.14 shows that the parallel diffusion coefficient profiles of uracil do not exhibit an easily discernible maximum.

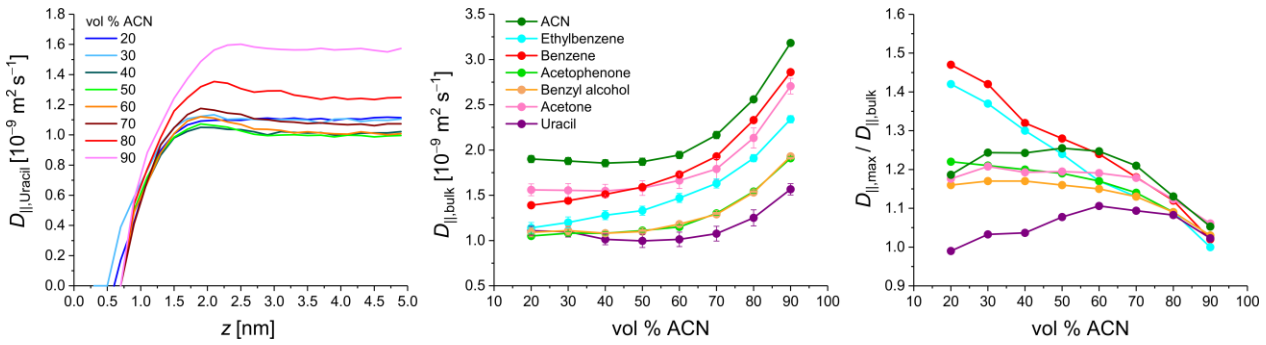

Figure 1.14. Diffusive mobility of analytes, ACN, and dead time markers in the pore. Left: Evolution of the parallel diffusion coefficient profiles of uracil at increasing ACN volume fraction in the mobile phase. Middle: Sensitivity of the diffusivity of analytes, ACN, and dead time markers in the bulk liquid region to the ACN volume fraction in the mobile phase. Right: Maximum lateral mobility gain from surface diffusion in the interfacial region for analytes, ACN, and dead time markers. Shown is the ratio of the maximum parallel diffusion coefficient to the diffusivity in the bulk liquid region of the pore at increasing ACN volume fraction in the mobile phase.

This implies that the uracil mobility is hardly susceptible to the ACN-rich solvent composition in the ditch, although position and orientation of uracil molecules in the interfacial region, namely largely random or surface-parallel with their molecular plane over the flexible chain ends, suggest otherwise. The extent of uracil–solvent hydrogen bonding in the interfacial region, however, makes fast surface diffusion almost impossible.

As mentioned before, the ACN-rich solvent composition in the interfacial region is the main reason why solute molecules experience higher diffusive mobility there.[30] The maximum lateral mobility gain from surface diffusion in the interfacial region compared with the diffusive mobility in the bulk liquid region can be expressed as $D_{\parallel,max}/D_{\parallel,bulk}$, that is, the ratio between the maximum value in the parallel diffusion coefficient profile and the constant value observed in the bulk liquid region of the profile. Generally, $D_{\parallel,max}/D_{\parallel,bulk}$ depends on the W/ACN ratio of the mobile phase, which determines the ACN excess in the interfacial region, and on the sensitivity of the diffusive mobility of a compound to its solvent environment.[34] The latter is quantified in the $D_{\parallel,bulk}$ curve (Figure 1.14), which shows diffusive mobility values taken from the bulk liquid region of the pore and thus equivalent to the bulk molecular diffusivity D_m. The $D_{\parallel,bulk}$ curves of acetone and ACN are nearly invariant up to 50% ACN, whereas the $D_{\parallel,bulk}$ curve of acetophenone increases steadily over the ACN range and the $D_{\parallel,bulk}$ curve of uracil goes through a shallow minimum at 50–60% ACN. All $D_{\parallel,bulk}$ curves in Figure 1.14 show the steepest increase at ≥70% ACN, but the increase is steeper for ACN and acetone than for acetophenone and uracil.

The $D_{\parallel,bulk}$ curves provide a good idea of the degree to which a compound is likely to undergo fast surface diffusion in the ACN ditch, but the actual $D_{\parallel,max}/D_{\parallel,bulk}$ value of a compound depends not only on its local solvent environment, but also on its local orientation and HB pattern, as already explained in the context of the parallel diffusion coefficient profiles of acetone. The $D_{\parallel,max}/D_{\parallel,bulk}$ curves shown in Figure 1.14 for analytes, ACN, and dead time markers can be grouped into four different categories: 1) the apolar analytes benzene and ethylbenzene, which exhibit the largest lateral mobility gain of the compounds at low ACN volume fraction; 2) the solvents ACN and acetone; 3) the moderately polar compounds acetophenone and benzyl alcohol; and 4) uracil. The right panel of Figure 1.14 visualizes the similarity of acetone with ACN (in curve shape) and acetophenone (in values), also that the solvents are in a similar value range as the moderately polar analytes, with whom they share molecular structures that contain one heteroatom. Benzyl alcohol is below acetophenone, because the hydroxyl group forms more HBs with W than the carbonyl oxygen.[34] Unsurprisingly given its heteroatom-heavy structure, uracil is in a category all of its own: as opposed to what is observed for the other compounds, the $D_{\parallel,max}/D_{\parallel,bulk}$ curve of uracil increases towards larger ACN volume fractions only to meet the low end of the other $D_{\parallel,max}/D_{\parallel,bulk}$ curves.

1.3.3 Dead time markers versus analytes

We now turn to the question of how acetone and uracil differ from RPLC analytes and what their interaction with the chromatographic interface signifies for their use as dead time markers. First, we compare distribution coefficients calculated for acetone and uracil from the simulated density profiles using solute-specific stationary-phase limits with previously calculated distribution coefficients for analytes.[34] (For the sake of comparison, K values were calculated over the complete W/ACN range, regardless of whether dead time markers exhibited a density maximum in the interfacial region or not.) Figure 1.15 shows that the dead time markers have negligibly small K values compared with apolar analytes, but not necessarily compared with moderately polar analytes. Between 20% and 90% ACN volume fraction in the mobile phase, acetone and uracil

have *K* values of 2.11–0.48 and 0.95–0.25, respectively, whereas acetophenone and benzyl alcohol have *K* values of 33.36–0.90 and 22.18–0.59.

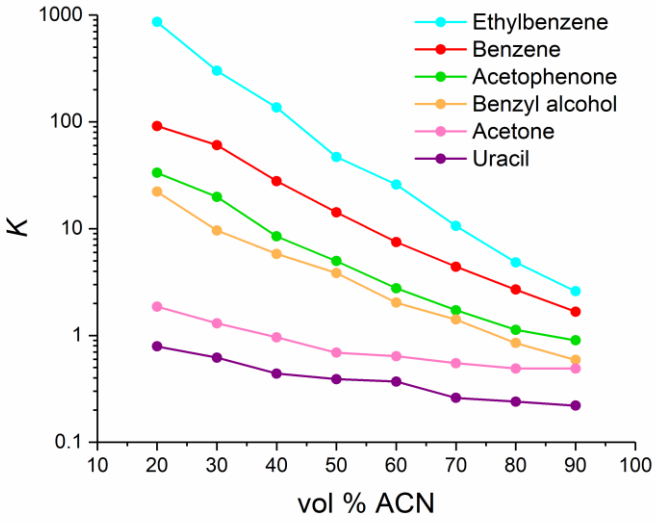

Figure 1.15. RPLC retention of analytes and dead time markers. Shown is the evolution of the distribution coefficients *K* at increasing ACN volume fraction in the mobile phase. *K* values were calculated from the respective density profiles using solute-specific stationary-phase limits.

This comparison shows that 1) uracil has consistently lower *K* values than acetone, which, as already discussed in the context of the density profiles, agrees with a lower elution time of uracil in practice,[2] and 2) the drop in *K* between 20% and 90% ACN is more shallow for dead time markers than for analytes (by 74–77% vs 97%, respectively). At 20% ACN, the *K* values of the dead time markers amount to 6–10% (acetone) and 3–4% (uracil) of the *K* values of benzyl alcohol and acetophenone. At 50% ACN, which is the highest ACN volume fraction at which benzyl alcohol and acetophenone could be separated given that the least retained compound should have $k \approx 1$ and assuming a reasonable phase ratio of $\beta = 0.3$ for the column,[58] the *K* values of the dead time markers already make up 15–20% (acetone) and 9–11% (uracil) of the *K* values of benzyl alcohol and acetophenone. These numbers illustrate how the error introduced into the calculated retention factors *k* through dead time marker interaction with the stationary phase depends on the relative retention of the analytes.

From the comparison of *K* values in Figure 1.15 it is tempting to classify acetone and uracil as barely to weakly retained compounds on a C_{18} phase, that is, to deduce that the dead time markers differ from true analytes only in their degree of retention by the stationary phase. The molecular simulation data, however, paint a more detailed picture. Although acetone and uracil have density peaks in the bonded-phase and interfacial region (cf. Figures 1.5 and 1.10), these cannot be equated with the partitioning and adsorption peaks of true analytes. Analyte partitioning is driven by maximizing contact with bonded-phase groups and requires a sufficient number of hydrophobic structural elements in a molecule. In contrast, the density peaks of acetone and uracil in the bonded-

phase region reflect their interaction with the silica surface and its associated solvent layer. Likewise, the location of the density maximum of acetone and uracil in the interfacial region (and the HB pattern observed there) indicates an unwillingness of the dead time markers to lose contact with the bulk liquid region.

This is analyzed in depth by comparing the average number of bonded-phase contacts with the average number of solvent contacts for a solute molecule at its density maximum in the interfacial region. To enable the quantitative comparison between solutes of different molecular size and chemical structure, the contact determination relied on RDFs to determine for each type of solute–solvent and solute–bonded phase pair a cutoff radius representing the first coordination shell within which contacts were counted. The count for each type of contact was normalized by the respective coordination shell volume. The data in Figure 1.16 show that uracil molecules have (averaged over all available W/ACN ratios) about four times more solvent than bonded-phase contacts, acetone molecules have equal solvent and bonded-phase contacts, which confirms the suitability of acetone as a mobile-phase solvent for RPLC, and analytes have more bonded-phase than solvent contacts (analytes with polar groups ≤2 times, apolar analytes ≥4 times). Overall, the interaction of the dead time markers with the chromatographic interface is characterized by an affinity for solute–solvent hydrogen bonding that is not offset by a greater affinity for bonded-phase contact, and this differentiates dead time markers from true analytes.

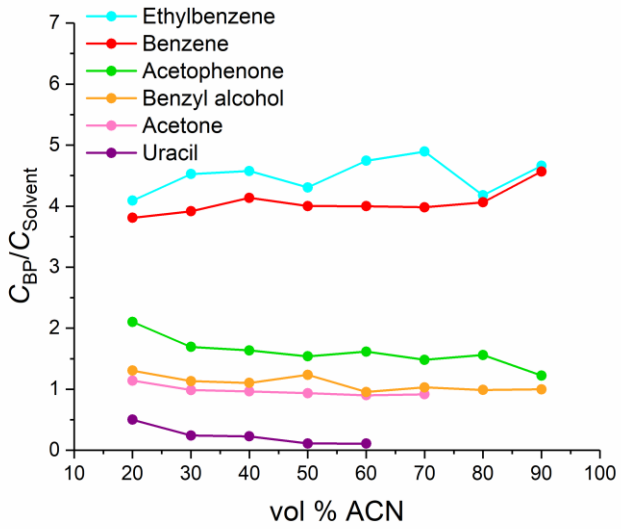

Figure 1.16. Bonded-phase contacts versus solvent contacts for analytes and dead time markers at their density maximum in the interfacial region. Shown is the ratio between the number of contacts with bonded-phase groups C_{BP} and with solvent molecules $C_{Solvent}$ per solute molecule. Contacts were counted within a cutoff radius determined for each type of solute–solvent and solute–bonded phase pair from radial distribution functions. Counts were normalized by the volume of a sphere with the respective cutoff radius to enable the quantitative comparison between solutes of different molecular size and chemical structure.

1.4 Conclusions

In this MD simulations study we generated a molecular-level picture of dead time marker interaction with the chromatographic interface in RPLC as exemplified by an endcapped C_{18} column equilibrated with a W–ACN mobile phase. The studied dead time markers, acetone and uracil, are not confined to the bulk liquid region of the pore, but accumulate in the interfacial region and even penetrate the bonded-phase region. Nevertheless, the interaction of dead time markers with the chromatographic interface differs from that of true analytes in several critical aspects: 1) As opposed to the partitioning peaks of analytes, the (low-level) presence of dead time markers in the bonded-phase region is confined to the immediate neighborhood of the supporting silica surface and characterized by HBs with the surface-attached solvent layer. 2) The density maximum of dead time markers in the interfacial region is located closer to the bulk liquid region than the adsorption peaks of analytes and reflects an ongoing attachment of the dead time markers to the bulk liquid phase, characterized by a low (≤1) ratio of bonded-phase to solvent contacts. 3) The density peaks of dead time markers in the interfacial region, which are approximately co-localized with the ACN ditch, have vanished at a volume fraction of 70–80% ACN, whereas the adsorption peaks of analytes remain detectable at 90% ACN volume fraction. This means that RPLC-type retention of dead time markers (but not of analytes) ceases when the mobile phase ceases to contain more W than ACN molecules.

At a closer look, acetone and uracil show differences in their behavior that are related to their respective molecular structures and bear implications for their use as dead time markers. Acetone acts mostly like a co-solvent of ACN, exhibiting the same density profile, a similar interaction with the silica surface and its attached solvent layer, and some aspects of surface diffusion. The similarity between acetone and ACN is expected given that both belong to the same solvent category (polar aprotic) and have been employed as mobile-phase solvent for RPLC and HILIC separations. Regarding orientation, HB pattern, and the mobility gain from surface diffusion in the interfacial region, acetone mimics acetophenone rather than ACN. Uracil acts as a truly hydrophilic molecule, that is, it finds locations in the pore that support a minimum of solute–solvent HBs. Thus, uracil is present at the silica surface (tolerating a less than satisfactory HB coordination) and at the fringe of the bonded-phase chains. Compared with acetone, whose interaction with the chromatographic interface can be considered as neutral based on its equal preference for bonded-phase and solvent contacts, uracil needs more solvent contacts than bonded-phase contacts. That said, the uracil density maximum in the interfacial region indicates that the preferred environment of uracil molecules still includes some contact with the bonded-phase chains, unless the bulk liquid region of the pore contains nearly equal amounts of W and ACN molecules.

The presented molecular simulation data cannot decide whether uracil or acetone is the better dead time marker in practice, but they provide valuable information on the advantages and disadvantages of the two compounds. Regarding RPLC retention, the better dead time marker is uracil, because its bonded-phase interaction is very weak and clearly differs from that of analytes, whereas acetone retains aspects of analyte behavior. Consequently, the uracil density maximum is located a bit closer to the bulk liquid region and the analyte-specific stationary-phase limits than the acetone

density maximum. On the other hand, the solvent behavior of acetone at the silica surface avoids the risk of HILIC retention that is possible with uracil as dead time marker.

1.5 Supplementary data

Table 1.S1. Number of W and ACN molecules in the simulation box during productive simulations.

W/ACN (v/v)	N_W	N_{ACN}
80/20	27482	3689
70/30	23671	5014
60/40	20433	6227
50/50	16979	7440
40/60	13604	8565
30/70	10169	9740
20/80	6647	10842
10/90	3368	11833

Table 1.S2. Maximum distance between donor X-H and acceptor X atoms for solute–solvent (W, ACN) and solute–silica surface (sl) hydrogen bonds.

	r_{HB} [nm]				
	H (W)	O (W)	N (ACN)	H (sl)	O (sl)
O (Acetone)	0.25	0.33	--	0.26	0.34
O (Acetophenone)	0.25	0.33	--	0.25	0.34
O (Uracil)	0.26	0.34	--	0.26	0.34
N (Uracil)	--	0.34	0.34	--	--
H (Uracil)	--	0.26	0.26	--	0.26

Table 1.S3. Diffusive mobile data calculated for the dead time markers acetone and uracil.

W/ACN (v/v)	Acetone		Uracil	
	$D_{\|\|,\mathrm{bulk}}$	$D_{\|\|,\mathrm{max}}$	$D_{\|\|,bulk}$	$D_{\|\|,max}$
	[10^{-9} m^2 s^{-1}]		[10^{-9} m^2 s^{-1}]	
80/20	1.56 ± 0.06	1.83 ± 0.15	1.11 ± 0.05	1.10 ± 0.16
70/30	1.55 ± 0.07	1.88 ± 0.07	1.10 ± 0.04	1.13 ± 0.11
60/40	1.55 ± 0.07	1.86 ± 0.05	1.01 ± 0.06	1.05 ± 0.15
50/50	1.58 ± 0.07	1.89 ± 0.07	1.00 ± 0.06	1.07 ± 0.09
40/60	1.66 ± 0.08	1.98 ± 0.13	1.01 ± 0.07	1.12 ± 0.06
30/70	1.79 ± 0.08	2.11 ± 0.11	1.08 ± 0.08	1.12 ± 0.08
20/80	2.13 ± 0.09	2.39 ± 0.02	1.25 ± 0.09	1.35 ± 0.12
10/90	2.71 ± 0.09	2.87 ± 0.07	1.57 ± 0.06	1.60 ± 0.07

Table 1.S4. Solute-specific stationary-phase limits for calculation of acetone and uracil distribution coefficients.

W/ACN (v/v)	z_{SP} [nm]	
	Acetone	Uracil
80/20	2.325	2.275
70/30	2.375	2.375
60/40	2.375	2.325
50/50	2.375	2.375
40/60	2.425	2.425
30/70	2.425	2.375
20/80	2.425	2.425
10/90	2.525	2.425

Table 1.S5. Distribution coefficients calculated for the dead time markers acetone and uracil.

W/ACN	*K*	
(v/v)	Acetone	Uracil
80/20	2.11 ± 0.00	0.95 ± 0.05
70/30	1.41 ± 0.01	0.68 ± 0.02
60/40	1.05 ± 0.01	0.53 ± 0.04
50/50	0.76 ± 0.01	0.44 ± 0.02
40/60	0.68 ± 0.01	0.39 ± 0.02
30/70	0.62 ± 0.01	0.31 ± 0.03
20/80	0.52 ± 0.01	0.26 ± 0.02
10/90	0.48 ± 0.01	0.25 ± 0.03

Table 1.S6. Maximum distance between the center-of-mass of solutes and the O atom of W, the central C atom of ACN, and the united-atoms groups of the bonded phase (BP) for contact analysis.

	r_C [nm]		
	W	ACN	BP
Acetone	0.41	0.67	0.74
Acetophenone	0.55	0.76	0.81
Benzene	0.63	0.71	0.80
Benzyl alcohol	0.64	0.77	0.81
Ethylbenzene	0.64	0.77	0.84
Uracil	0.59	0.68	0.70

Acknowledgments

This work was supported by the Deutsche Forschungsgemeinschaft DFG (Bonn, Germany) under grant TA 268/11-1. Simulations were performed on the supercomputer ForHLR II funded by the Ministry of Science, Research and the Arts Baden-Württemberg and by the Federal Ministry of Education and Research under the project acronym RPLCMD.

References

1 J. V. Hinshaw, *LC–GC North Am* **2015**, *33*, 850–855.
2 C. A. Rimmer, C. R. Simmons, J. G. Dorsey, *J. Chromatogr. A* **2002**, *965*, 219–232.
3 M. Wang, J. Mallette, J. F. Parcher, *J. Chromatogr. A* **2008**, *1190*, 1–7.
4 B. A. Bidlingmeyer, F. V. Warren, A. Weston, C. Nugent, P. M. Froehlich, *J. Chromatogr. Sci.* **1991**, *29*, 275–279.
5 F. Gritti, Y. Kazakevich, G. Guiochon, *J. Chromatogr. A* **2007**, *1161*, 157–169.
6 F. Tsopelas, M. Ochsenkühn-Petropoulou, A. Tsantili-Kakoulidou, *J. Chromatogr. A* **2010**, *1217*, 2847–2854.
7 M. Wang, J. Mallette, J. F. Parcher, *J. Chromatogr. A* **2011**, *1218*, 2995–3001.
8 S. Pous-Torres, J.R. Torres-Lapasió, J.J. Baeza-Baeza, M.C. Garciá-Álvarez-Coque, *Anal. Bioanal. Chem.* **2009**, *394*, 625–636.
9 S. Jung, S. Ehlert, M. Pattky, U. Tallarek, *J. Chromatogr. A* **2010**, *1217*, 696–704.
10 C. S. Funari, R. L. Carneiro, M. M. Khandagale, A. J. Cavalheiro, E. F. Hilder, *J. Sep. Sci.* **2015**, *38*, 1458–1465.
11 N. Maljurić, B. Otašević, J. Golubović, J. Krmar, M. Zečević, A. Protić, *Microchem. J.* **2020**, *153*, 104394.
12 E. M. Hetrick, T. T. Kramer, D. S. Risley, *J. Chromatogr. A* **2017**, *1489*, 65–74.
13 C.-E. Roy, T. Kauss, S. Prevot, P. Barthelemy, K. Gaudin, *J. Chromatogr. A* **2015**, *1383*, 121–126.
14 S. M. Melnikov, A. Höltzel, A. Seidel-Morgenstern, U. Tallarek, *J. Phys. Chem. C* **2015**, *119*, 512–523.
15 P. L. Zhu, *Chromatographia* **1985**, *20*, 425–433.
16 P. R. Perry, J. W. Coym, *J. Sep. Sci.* **2010**, *33*, 2310–2315.
17 S. Pous-Torres, J.R. Torres-Lapasió, M.C. García-Álvarez-Coque, *J. Liq. Chromatogr. Relat. Technol.* **2009**, *32*, 1065–1083.
18 K.E. Bij, Cs. Horvath, W.R. Melander, A. Nahum, *J. Chromatogr. A* **1981**, *203*, 65–84.
19 M. Sarker, K.J. Duff, "U-shaped" retention profile as an indicator of the level of silanol activity of HPLC silica phases. https://www.sigmaaldrich.com/Graphics/Supelco/objects/12000/11910.pdf **2021**, accessed 26th January 2021.
20 R. K. Lindsey, J. L. Rafferty, B. L. Eggiman, J. I. Siepmann, M. R. Schure, *J. Chromatogr. A* **2013**, *1287*, 60–82.
21 J. L. Rafferty, L. Zhang, J. I. Siepmann, M. R. Schure, *Anal. Chem.* **2007**, *79*, 6551–6558.
22 J. L. Rafferty, J. I. Siepmann, M. R. Schure, *J. Chromatogr. A* **2008**, *1204*, 11–19.
23 J. L. Rafferty, J. I. Siepmann, M. R. Schure, *J. Chromatogr. A* **2008**, *1204*, 20–27.
24 J. L. Rafferty, J. I. Siepmann, M. R. Schure, *J. Chromatogr. A* **2011**, *1218*, 2203–2213.
25 J. L. Rafferty, J.I. Siepmann, M.R. Schure, *J. Chromatogr. A* **2011**, *1223*, 9183–9193.
26 J. L. Rafferty, J. I. Siepmann, M. R. Schure, *J. Chromatogr. A* **2012**, *1223*, 24–34.

27 J. Braun, A. Fouqueau, R. J. Bemish, M. Meuwly, *Phys. Chem. Chem. Phys.* **2008**, *10*, 4765–4777.
28 A. Fouqueau, M. Meuwly, R. J. Bemish, *J. Phys. Chem. B* **2007**, *111*, 10208–10216.
29 P. K. Gupta, M. Meuwly, *J. Phys. Chem. B* **2012**, *116*, 10951–10959.
30 J. Rybka, A. Höltzel, S. M. Melnikov, *Fluid Phase Equilib.* **2016**, *407*, 177–187.
31 J. Rybka, A. Höltzel, U. Tallarek, *J. Phys. Chem. C* **2017**, *121*, 17907–17920.
32 K. El Hage, P.K. Gupta, R.J. Bemish, M. Meuwly, *J. Phys. Chem. Lett.* **2017**, *8*, 4600–4607.
33 K. El Hage, R.J. Bemish, M. Meuwly, *Phys. Chem. Chem. Phys.* **2018**, *20*, 18610–18622.
34 J. Rybka, A. Höltzel, A. Steinhoff, U. Tallarek, *J. Phys. Chem. C* **2019**, *123*, 3672–3681.
35 J. Rybka, A. Höltzel, N. Trebel, U. Tallarek, *J. Phys. Chem. C* **2019**, *123*, 21617–21628.
36 F. Gritti, *J. Chromatogr. A* **2015**, *1410*, 90–98.
37 F. Gritti, G. Guiochon, *J. Chromatogr. A* **2013**, *1297*, 85–95.
38 A. Aldehai, D.E. Martire, R.P.W. Scott, *Analyst* **1989**, *114*, 869–875.
39 F. Gritti, W. Piatkowsi, G. Guiochon, *J. Chromatogr. A* **2002**, *978*, 81–107.
40 A. Leo, C. Hansch, D. Elkins, *Chem. Rev.* **1971**, *71*, 525–616.
41 T. S. Gulmen, W. H. Thompson, *Langmuir* **2006**, *22*, 10919–10923.
42 M. G. Martin, J. I. Siepmann, *J. Phys. Chem. B* **1998**, *102*, 2569–2577.
43 C. D. Wick, J. M. Stubbs, N. Rai, J. I. Siepmann, *J. Phys. Chem. B* **2005**, *109*, 18974–18982.
44 H. J. C. Berendsen, J. R. Grigera, T. P. Straatsma, *J. Phys. Chem.* **1987**, *91*, 6269–6271.
45 K. Vanommeslaeghe, E. Hatcher, C. Acharya, S. Kundu, S. Zhong, J. Shim, E. Darian, O. Guvench, P. Lopes, I. Vorobyov, A.D. Mackerell Jr., *J. Comput. Chem.* **2010**, *31*, 671–690.
46 N. M. Fischer, P. J. van Maaren, J. C. Ditz, A. Yildirim, D. van der Spoel, *J. Chem. Theory Comput.* **2015**, *11*, 2938–2944.
47 B. Xue, D. B. Harwood, J. L. Chen, J. I. Siepmann, *J. Chem. Eng. Data* **2018**, *63*, 4256–4268.
48 R. D. Mountain, *J. Phys. Chem. B* **2010**, *114*, 16460–16464.
49 R. D. Mountain, *J. Phys. Chem. C* **2013**, *117*, 3923–3929.
50 S. M. Melnikov, A. Höltzel, A. Seidel-Morgenstern, U. Tallarek, *Angew. Chem. Int. Ed.* **2012**, *51*, 6251–6254.
51 S.M. Melnikov, A. Höltzel, A. Seidel-Morgenstern, U. Tallarek, *Anal. Chem.* **2013**, *85*, 8850–8856.
52 F. Gritti, A. Höltzel, U. Tallarek, G. Guiochon, *J. Chromatogr. A* **2015**, *1376*, 112–125.

53 B. Hess, C. Kutzner, D. van der Spoel, E. Lindahl, *J. Chem. Theory Comput.* **2008**, *4*, 435–447.
54 M. J. Abraham, T. Murtola, R. Schulz, S. Páll, J. C. Smith, B. Hess, E. Lindahl, *SoftwareX* **2015**, *1–2*, 19–25.
55 U. Essmann, L. Perera, M.L. Berkowitz, T. Darden, H. Lee, L.G. Pedersen, *J. Chem. Phys.* **1995**, *103*, 8577–8593.
56 P. Liu, E. Harder, B.J. Berne, *J. Phys. Chem. B* **2004**, *108*, 6595–6602.
57 S.M. Melnikov, A. Höltzel, A. Seidel-Morgenstern, U. Tallarek, *J. Phys. Chem. C* **2016**, *120*, 13126–13138.
58 S. Moldoveanu, V. David, *J. Chromatogr. A* **2015**, *1381*, 194–201.

Chapter 2

Consequences of Cylindrical Pore Geometry for Interfacial Phenomena in Reversed-Phase Liquid Chromatography

Authors

Nicole Trebel, Alexandra Höltzel, Julia K. Lutz, and Ulrich Tallarek

State of publication

Published 5 October 2021 in *Journal of Physical Chemistry B*, Vol. 125, pp. 11320–11336.
DOI: 10.1021/acs.jpcb.1c06732

Table of content

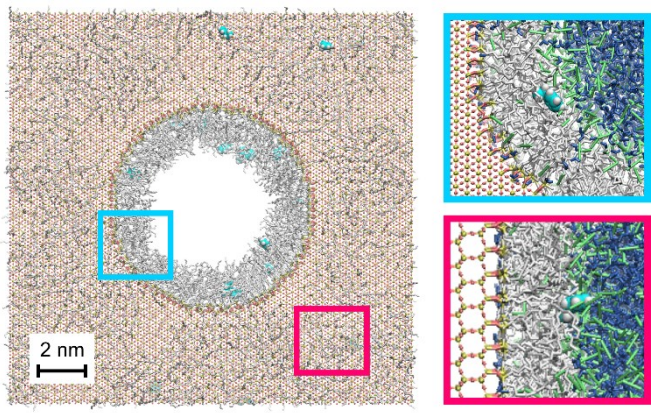

Abstract

The interfacial phenomena behind analyte separation in a reversed-phase liquid chromatography column take place nearly exclusively inside the silica mesopores. Their cylindrical geometry can be expected to shape the properties of the chromatographic interface with consequences for the analyte density distribution and diffusivity. To investigate this topic through molecular dynamics simulations we introduce a cylindrical pore inside a slit pore configuration, where inner curved and outer planar silica surface bear the same bonded phase. The present model replicates an average-sized (9 nm) mesopore in an endcapped C_{18} column equilibrated with a mobile phase of 70/30 (v/v) water/acetonitrile. Simulations performed for ethylbenzene and acetophenone show that the surface curvature shifts bonded-phase and analyte density towards the pore center, decreases the solvent density in the bonded-phase region, increases the acetonitrile excess in the interfacial region, and considerably enhances the surface diffusivity of both analytes. Overall, the cylindrical pore

provides a more hydrophobic environment than the slit pore. Ethylbenzene density is decidedly increased in the cylindrical pore, whereas acetophenone density is nearly equally distributed between cylindrical and slit pore. The cylindrical pore geometry thus sharpens the discrimination between apolar and moderately polar analytes, while enhancing the mass transport of both.

2.1 Introduction

Most analyses and purifications of (bio)chemical, pharmaceutical, and food products today rely on high-performance liquid chromatography (HPLC) separations. A typical HPLC column is a stainless-steel conduit containing a silica-based, fixed bed, either a tight packing of µm-sized particles with nm-sized pores (mesopores) or, less frequently, a monolith with a hierarchical, bimodal pore structure.[1] The macro–mesoporous architecture of the chromatographic bed intentionally combines quick transport of analytes in the mobile phase (through the macropores) with a large surface area (inside the mesopores) for analyte retention and separation. The silica structure can be the stationary phase (in normal-phase liquid chromatography, NPLC, and in hydrophilic interaction liquid chromatography, HILIC),[2] but more often serves as the solid support for a chemically bonded phase, whose properties largely determine the range of compounds that can be separated on the column as well as the composition of the mobile phase. The mobile phase in reversed-phase liquid chromatography (RPLC), HILIC, and NPLC is a binary (eventually ternary or quaternary) solvent mixture. In RPLC, the bonded phase is hydrophobic and the mobile phase is a mixture of water (W) with methanol, acetonitrile (ACN), or, more rarely, tetrahydrofuran. Of the available bonded-phase options for RPLC, octadecylsilane (C_{18}) columns are the most successful by far. Having been on the market for approximately 45 years, their popularity endures, not only because C_{18} columns separate a wide range of compounds with high reproducibility, but also due to the vast empirical knowledge that has been amassed with these columns.[3]

Progress in RPLC has always been driven by technical innovation, culminating in a plethora of columns with subtle differences and increasingly sophisticated (and expensive) instrumentation. Success of innovation is measured through practical applications, with explanations based on physicochemical evidence lagging years or decades behind. The discrepancy between practical success and theoretical knowledge was mainly caused by the lack of a molecular-level picture for the processes behind analyte separation inside an RPLC column. In the last 20 years, however, dedicated molecular simulations studies have brought essential details of the chromatographic process in RPLC to light.[4–8] Probably the most important contribution of molecular simulations studies to the understanding of chromatography was to reveal the complex and highly dynamic nature of the chromatographic interface. Textbooks describe the chromatographic principle as the physical separation of compounds according to their relative distribution between the stationary phase (in RPLC, this is the silica support with the bonded phase) and the mobile phase. This description conveys the notion that stationary and mobile phase remain permanently separate entities, but in reality, the equilibration of the stationary phase with the mobile phase (prior to

sample injection onto the column) results in the formation of the chromatographic interface. During column equilibration, solvent molecules penetrate the bonded-phase chains, adsorb to the silica surface, and accumulate around and on top of the chain ends, whereby the two components of the mobile phase, W and the organic solvent, have different roles in this process.[9,10] The properties of the chromatographic interface are sensitive to type and ligand density of the bonded phase as well as to composition and solvent ratio of the mobile phase.[9–17]

Molecular simulation studies have further provided new knowledge about the main interfacial phenomena behind analyte separation in RPLC, namely retention and mass transport via surface diffusion. It was shown that differential retention on the column is related to the way in which compounds of different chemical structure explore the chromatographic interface,[5,18–20] how the diffusivity of solute molecules varies depending on their position within the chromatographic interface and their chemical structure,[5,8,17,21] and that fast surface diffusion, unique to RPLC among the liquid-chromatography modes and critical to the column efficiency, originates from the properties of the chromatographic interface.[22–25]

As opposed to the closely related topic of organic liquids confined in cylindrical pores,[26–36] simulation studies of chromatographic processes have – with few exceptions[37–41] – so far been conducted in slit pore models. Changing from planar to cylindrical pore geometry introduces considerable complexity to the system, which has consequences for the pore model generation and the simulation times. Slit pores are usually derived from crystalline surfaces and thus possess a simplified surface chemistry compared with amorphous silica. The most popular surface for molecular simulation studies of chromatographic systems,[42] the (111) face of β-cristobalite silica, for example, bears only equidistant, single, and isolated silanol groups. A cylindrical pore, whether generated through pore drilling or cylindrical resist algorithms, possesses a certain degree of surface roughness as well as amorphous surface chemistry.[43] These differences in the underlying surface chemistry of cylindrical and slit pores have to be considered (and partially adjusted) during functionalization with the bonded phase to obtain comparable chromatographic surfaces.[44] A cylindrical pore model also entails a larger system size (simulation box dimensions and number of solvent molecules) than a slit pore model. Apart from requiring more time and effort to replicate the results of column equilibration with the binary mobile phase, the increased system size raises the computational expense for data generation and analysis considerably. On the other hand, the experimental adsorption isotherms of analytes on RPLC columns strongly suggest a heterogeneous chromatographic surface, which originates from the curvature, surface roughness, and surface chemistry of the silica support and shapes the interfacial processes behind analyte separation.[45,46]

To study the cylindrical pore geometry and associated heterogeneity of the chromatographic surface, we use a cylindrical pore within a slit pore configuration (Figure 2.1).

The cylindrical pore runs along the long axis of a rectangular silica block that is placed between two solvent reservoirs; the silica block's planar surfaces towards the solvent reservoirs form a slit pore when periodic boundary conditions are applied. The configuration shown in Figure 2.1 can be conceived as a tiny piece from an HPLC column, namely a cylindrical mesopore inside a µm-sized silica particle. The planar surface represents the outside surface of the silica particle (which, given

the particle's µm-size, is approximately planar compared with the inner pore surface) and the solvent reservoirs mimic the interstitial pore space in the column.

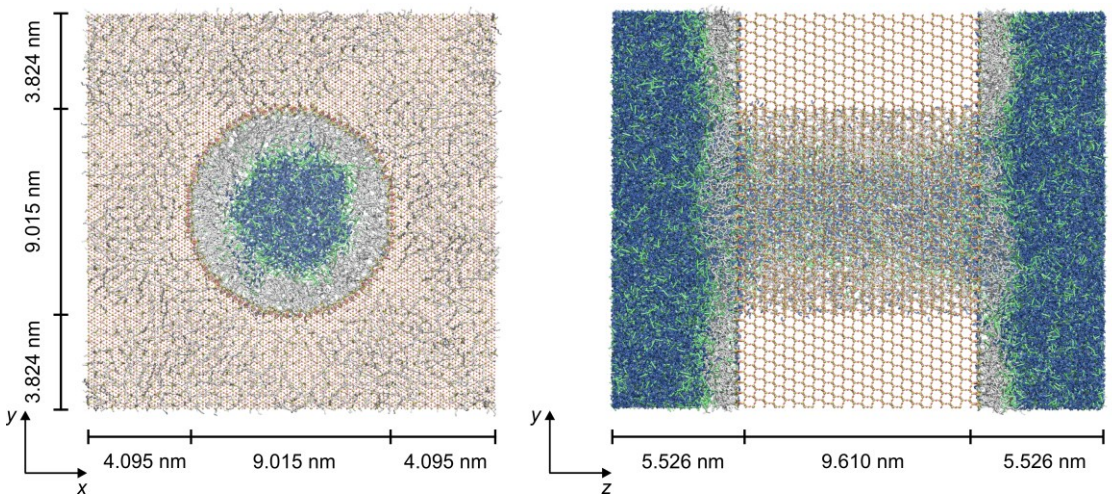

Figure 2.1. Front (left) and side views (right) of the simulation box. Dimensions of the silica block and the cylindrical pore in the *xy*-direction (front view, pore diameter) and in *yz*-direction (side view, pore length) are indicated. In the front view, only solvent molecules inside the cylindrical pore are shown to visualize the modification of the inner curved and outer planar silica surface with the bonded phase. The ACN excess (ACN ditch) at the inner curved and outer planar surface is clearly visible in the front and side view, respectively. Si and O atoms of the silica block are represented by yellow and red balls, respectively, and Si, O, and H atoms of the silica surface as yellow, red, and white sticks, respectively; united-atom groups of the bonded phase are shown as gray sticks; W and ACN molecules are shown as dark blue and green sticks, respectively.

In an RPLC column, the bonded phase is present inside the mesopores as well as on the outer surface of the particles or the monolithic skeleton. Although constituting <5% of the available surface area, modification of the outer surface with the bonded phase is essential. Otherwise, the W-rich layer that forms at an unmodified, hydroxylated silica surface in contact with a W–ACN mobile phase[47,48] controls the entrance of analyte molecules into the pore by an orthogonal (HILIC) retention mechanism.[2,38]

Ligand type (monomeric C_{18}), ligand density (2.9 µmol m^{-2}), and bonded-phase coverage (~50%) of our pore model are representative of mainstream RPLC columns for small-molecule separations.[3,45] We opted for a closely similar ligand density and overall bonded-phase coverage at the inner curved and outer planar surface. There is no proof for identical bonded-phase coverage on the inside and outside of mesoporous silica particles, as methods to probe the local ligand density do not exist yet. But assuming a highly similar bonded-phase coverage for the particle inside and outside allows the comparison of the interfacial phenomena at a curved and planar surface within the same pore model, which gives a more accurate assessment of the influence of pore geometry than the comparison with data obtained from slit pores with different bonded-phase coverage and

simpler surface chemistry. Moreover, the particular configuration mimics the competition between curved and planar surface for retention of analyte molecules inside an RPLC column.
We probe the interfacial phenomena at a mobile phase of 70/30 (v/v) W/ACN, because slit pore simulations have shown high local ACN excess in the interfacial region and distinct surface diffusion effects for this solvent ratio.[5,8,17] Ethylbenzene and acetophenone, as low-molecular-weight compounds of similar size and structure but different polarity, serve as the model analytes. The properties of the analyte compounds are important to the study. Both compounds need to be small and stiff enough to access and distinguish between the different parts of the chromatographic interface. The polarity of a compound (at conserved molecular size) determines its distribution between the stationary and mobile phase as well as its surface diffusivity.[5,8] In the following, we investigate through molecular dynamics (MD) simulations how the pore geometry shapes the properties of the chromatographic interface in RPLC and explore the consequences for the distribution, orientation, and diffusivity of typical analytes.

2.2 Computational details

2.2.1 Pore model generation

For pore carving, we used a preliminary version of the object-oriented program PoreMS.[44] The general outline of pore carving with PoreMS is briefly outlined here. First, the program built a rectangular silica grid by multiplicating the smallest possible grid unit of Si and O atoms of the β-cristobalite SiO_2 structure to user-specified *xyz*-dimensions. The grid was rotated so that the user-specified drill axis for the pore became the *z*-axis of the coordinate system. Solvent reservoirs of user-specified extension were added in *z*-direction at each side of the silica block. Next, all Si and O atoms within a given distance from the *z*-axis were removed to carve a cylindrical pore of user-defined diameter out of the silica block. The carved-out, curved surface as well as the planar surfaces facing the solvent reservoirs were then reconstructed towards the chemistry of a fully hydroxylated silica surface following the rules of Coasne et al.[49] From this stage on, pore model generation progressed manually. Please note that the current version of PoreMS supports the generation of cylindrical silica pore models with user-defined surface functionalization.
Figure 2.1 shows a front and side view of the simulation box. The whole model can be considered as a cylindrical pore inserted into a slit pore. The slit pore is the inbuilt standard configuration against which the influence of cylindrical pore geometry on interfacial phenomena is measured. The silica block is based on β-cristobalite silica with the (111) face normal to the *z*-axis, that is, the outer planar surface bears mostly single silanol groups, but pore carving leaves geminal silanol groups at the rim. The target dimension of the pore were a diameter of 9 nm, length of 10 nm, and an outer surface area of 16×16 nm^2, sufficient to yield representative analyte and solvent density profiles when subtracting the pore entrance zone. For each solvent reservoir we planned a length of ~5 nm, sufficient to observe bulk liquid behavior of the mobile phase.[5,8,17]
Due to the bond lengths between the involved atoms, the actual dimensions vary slightly from the target dimensions. The dimensions of the simulation box are $xyz = 17.204 \times 16.663 \times 20.662$ nm^3.

Each solvent reservoir is 5.526 nm long, which translates to a slit pore "diameter" (distance between the planes) of 11.05 nm. The cylindrical pore has a length of 9.610 nm and an average radius of 4.50 nm. The latter was derived from the distances of the Si atoms at the inner curved surface to the inner pore center, which fall within 4.50±0.26 nm (with 78% of the Si atoms located within 4.50±0.1 nm), reflecting the silica-surface roughness of the cylindrical pore.

For functionalization (Table 2.1), 77 siloxane bridges were introduced to the inner surface to decrease its hydroxylation from 9.69 to 8.75 μmol m^{-2} and thus bring it closer to the outside surface hydroxylation of 7.78 μmol m^{-2}.

Table 2.1. Details of the silica surface modification.

Process stage	Inner curved surface[a]		Outer planar surface[a]	
	Number and type of groups	Density (μmol m^{-2})	Number and type of groups	Density (μmol m^{-2})
After pore carving	1588 OH	9.69	2088 OH	7.78
After siloxane bridge formation	1434 OH	8.75	2088 OH	7.78
After main functionalization	473 C_{18}	2.89	794 C_{18}	2.96
After endcapping	281 C_1	1.71	354 C_1	1.32
Residual hydroxylation	680 OH	4.15	940 OH	3.50

[a] Surface area: A_{inside} = 272 nm^2 and $A_{outside}$ = 2×223 nm^2.

Siloxane bridges were formed between randomly chosen surface OH groups if the distance between the two O atoms was <0.3 nm. Inner curved and outer planar silica surface were then modified with 2.89 and 2.96 μmol m^{-2} dimethyloctadecyl silane (C_{18}) chains and endcapped with 1.71 and 1.32 μmol m^{-2} trimethyl silane (C_1) groups, respectively, leaving residual OH groups at 4.15 and 3.50 μmol m^{-2} and corresponding to a bonded-phase coverage (with C_{18} ligands and C_1 groups) of 53% inside and 55% outside. Ligand density and bonded-phase coverage are informed by RPLC columns on the market.[45]

The bonded-phase placement on the surfaces proceeded in three consecutive steps: 1) spatially random distribution of C_{18} chains over the available binding sites up to the targeted ligand density, 2) spatially random distribution of C_1 groups over the remaining available binding sites up to the targeted overall bonded-phase coverage, and 3) placement of additional C_{18} chains and C_1 groups on binding sites at the rim, where pore carving had left geminal silanols and thus a higher number of surface OH groups.

1.2.2 Force field parameters

Force field parameters for the silica-surface atoms (Si, O, and H) were taken from Gulmen and Thompson.[50] The transferable potentials for phase equilibria united-atom (TraPPE-UA) force field

was used for C_1 groups, C_{18} chains, and ACN molecules.[51,52] W molecules were described by the extended simple point charge (SPC/E) force field.[53] Analyte molecules were treated with the explicit CHARMM general force field (CGenFF).[54] A detailed description of our force field choices and their stepwise validation was given previously.[21] Comparison with chromatographic experiments has shown that analyte retention data simulated with this force field combination recover the cornerstones of RPLC separations in practice, namely i) the relation between analyte retention and molecular properties, and ii) the dependence of analyte retention on the ACN volume fraction in the mobile phase.[8] The analyte mobility data simulated with this force field combination[5,8,17,21] reflect the available experimental evidence about surface diffusion in RPLC.[22,55]

1.2.3 Simulation details

MD simulations were carried out in GROMACS (Groningen Machine for Chemical Simulation) version 2018.8-impi[56,57] for a canonical *NVT* ensemble (constant number of molecules *N*, simulation box volume *V*, and temperature *T*) at a temperature of 300 K. The temperature was controlled by a Nosé–Hoover thermostat with a 0.25 ps coupling constant. The correct number of W and ACN molecules in the simulation box necessary to obtain the solvent composition of the targeted mobile phase of 70/30 (v/v) W/ACN in the bulk region of the slit pore (i.e., equivalent to the interstitial pore space in a column) was determined through preliminary simulation runs with intermittent manual correction of the solvent density. This process took six runs of 72 h and 2 runs of 24 h to yield N_w = 59902 and N_{ACN} = 11679 for productive simulation runs. The number of analyte molecules in the box was set to $N_{analyte}$ = 20, which corresponds to an analyte concentration of 10^{-2} mol L^{-1} in the solvent reservoirs.

Analyte molecules were placed in the solvent reservoirs prior to system equilibration, while solvent molecules were randomly distributed over the whole non-solid box volume. Energy minimization was conducted with the steepest descent method and initial velocities were randomly assigned according to a Maxwell–Boltzmann distribution. Long-range electrostatic interactions were provided by the particle-mesh Ewald algorithm.[58] Nonbonded interactions were modeled with a 12–6 Lennard-Jones potential. Lennard-Jones parameters for unlike interactions were treated with the Lorentz–Berthelot combination rules. A cutoff radius of 1.4 nm, validated earlier,[24] was used for all interactions. Equations of motion were integrated with a 1 fs time step with an output frequency of 0.5 ps. Each simulation system was equilibrated for 100 ns before productive simulations were run, which lasted until the spatially-resolved density and parallel diffusion coefficient profiles showed no further changes with increasing simulation time.

Simulations were performed on the high performance computer ForHLR II of the Steinbuch Centre for Computing at the Karlsruhe Institute of Technology (Karlsruhe, Germany). Simulation of the ethylbenzene system (100 ns equilibration and 950 ns production) took 379680 hours on 320 cores, simulation of the acetophenone system (100 ns equilibration and 710 ns production) took 292896 hours on 320 cores. For comparison, simulation of an analyte system (60 ns equilibration and 750 ns production) in a 10 nm slit pore model bearing the same bonded phase as the present

pore model would require 65837 hours on 160 cores, as we know from performance tests on the ForHLR II.

1.2.4 Data analysis

1.2.4.1 Discrimination between inner curved and outer planar surface

Bonded-phase chains whose grafting point is located at the rim can protrude from the cylindrical pore into the slit pore and vice versa. These chains as well as the solvent and analyte molecules in their vicinity cannot be unequivocally assigned to a particular surface. For a clear distinction between the two pore geometries, we excluded the region around the pore entrance from the data analysis (Figure 2.S1). For the inner surface, this meant that a cylindrical volume of 4.50 nm radius and 0.5 nm height was cut off at each end of the inner pore (i.e., the cylindrical pore length was reduced by 0.5 nm at each end). For the outer surface, this meant that a cylindrical volume of 5.0 nm radius and 5.526 nm height was excluded from each solvent reservoir.
Stretching the pore entrance zone over the slit pore diameter effectively reduced the calculation time for the solvent density and diffusion coefficient profiles without affecting the data precision, as the system contains an ample number of solvent molecules. At the studied elution conditions, analyte molecules are rarely found in the bulk liquid region (ethylbenzene molecules to 0.1% and acetophenone molecules to 4.1% of the productive simulation time), so that stretching the pore entrance zone over the slit pore diameter did not result in a noticeable loss of analyte data. Analyte molecules not accounted for by the respective profiles are in contact with bonded-phase chains near the rim. To determine the average number of analyte molecules in the pore entrance zone, we compared the ensemble average determined without pore entrance zone to the time average obtained directly from the twenty simulation trajectories of the individual analyte molecules.[59] The comparison showed that, averaged over the productive simulation trajectory, about one analyte molecule of each species is located within the pore entrance zone.

1.2.4.2 Bonded-phase conformation

Contour plots describing the spatial distribution and conformation of the C_{18} chains of the bonded phase relied on the vector pointing from the grafting point (surface Si atom) of a chain to a specific alkyl group in the chain and the vector from the grafting point of a chain to the pore center (i.e., the surface normal). The length of the first vector gives the distance g of a group to the grafting point of the chain, the projection of this vector onto the surface normal quantifies the vertical displacement v of the group to the silica surface, and the distance between the end points of the first and second vectors quantifies the horizontal displacement h of the group from the chain grafting point (Figure 2.S2).

1.2.4.3 Density profiles

Bonded-phase, solvent, and analyte density profiles were calculated from the atom number densities of the CH_2 and CH_3 united-atom groups, the O atom of W, the central C atom of ACN, and the center-of-mass (cms) of analyte molecules. The distance *d* from the outer (planar) surface was measured relative to the position of the Si surface atoms. The distance *d* from the inner (curved) surface was measured relative to the pore axis, then the average pore radius of 4.50 nm was subtracted from the received values to obtain a surface-related density profile.
Bonded-phase density profiles were calculated from 40 ns trajectories using a bin size of 0.02 nm. Solvent density profiles were calculated from 40 ns trajectories, using a bin size of 0.02 nm for inside profiles and of 0.02 nm ($d \leq 1$ nm) and 0.1 nm ($d > 1$ nm) for outside density profiles. Analyte density profiles were calculated from the complete trajectories using a 0.05 nm bin size.

1.2.4.4 Surface-parallel diffusion coefficient profiles

The distance-dependent diffusion coefficient of bonded-phase groups, solvent and analyte molecules in parallel direction to the silica surface, $D_{\parallel}(d)$, was calculated as in our previous MD studies following an approach by Liu et al.[60] The mean squared displacement of bonded-phase groups, solvent and analyte molecules was repeatedly recorded as $\langle r^2(t)\rangle = \langle z^2(t)\rangle$ (inside) or $\langle r^2(t)\rangle = \langle x^2(t) + y^2(t)\rangle$ (outside) during 20 ps time intervals shifted consecutively in 0.5 ps time steps. For spatial resolution, only bonded-phase groups or molecules that remained within a ±0.3 nm interval around their initial *d*-position during the observation interval were counted. Profiles were determined from 40 ns trajectories for bonded-phase groups and solvent molecules and from the complete trajectories for analyte molecules using a bin size of 0.1 nm. Distance-dependent diffusion coefficients were calculated from the linear slope of the observation curve (t = 4–16 ps, Figure 2.S3) according to the Einstein equation

$$D_{\parallel}(d) = \frac{1}{2}\frac{\mathrm{d}\langle r^2(t)\rangle}{\mathrm{d}t} \text{ (inside) and } D_{\parallel}(d) = \frac{1}{4}\frac{\mathrm{d}\langle r^2(t)\rangle}{\mathrm{d}t} \text{ (outside)} \qquad (2.1)$$

$D_{\parallel}(d)$ is given as the average value with an error estimate calculated from the difference between the values obtained from the slope of the mean squared displacement curve over the two halves of the fit interval (i.e., t = 4–10 ps and t = 10–16 ps).

1.2.4.5 Analyte contacts

The number of contacts with bonded-phase groups or W molecules for analyte molecules at characteristic locations in the chromatographic interface was determined through the calculation of radial distribution functions (RDFs), as described previously.[21] The minimum following the first maximum in the RDF between the cms of an analyte molecule and united-atom groups of the bonded phase or the O atom of W was taken as the radius of the first coordination shell ($r_{\mathrm{cms–BP}}$ = 0.81 nm from the analyte–bonded-phase RDF, $r_{\mathrm{cms–O(W)}}$ = 0.55 nm from the acetophenone–W RDF). The number of bonded-phase united-atom groups or of O atoms of W within a radius of $r < r_{\mathrm{cms–BP}}$ or $r < r_{\mathrm{cms–O(W)}}$, respectively, around analyte molecules at positions of ±0.025 nm around the specified *d*-values (density peak maxima and shoulders) was counted and then divided by the

volume of a sphere with radius $r_{cms–BP}$ or $r_{cms–O(W)}$ to yield the average number of analyte contacts with bonded-phase groups or W molecules, C_{BP} or C_W, per nm^3. Contacts were determined from 10 ns trajectories using a bin size of 0.05 nm.

1.2.4.6 Analyte orientation

The orientation of analyte molecules at characteristic locations in the chromatographic interface was determined through calculating the probability distributions for the angle α between the surface normal and two orthogonal molecular vectors that indicate either the side chain direction or the orientation of the aromatic ring plane. Probability distributions were calculated from the complete trajectories for analyte molecules at positions of ±0.025 nm around the specified *d*-values (density peak maxima and shoulders) using a cosine bin size of 0.1 and a bin size of 0.05 nm for the spatial coordinate.

1.2.4.7 Acetophenone hydrogen bonding

The average number of acetophenone–W hydrogen bonds per acetophenone molecule, HB, at characteristic locations in the chromatographic interface was determined from the RDFs calculated between the O atom of acetophenone and the O and H atoms of W. A hydrogen bond was counted when the distance criteria for both atom pairs, derived from the first minima of the RDFs, was fulfilled ($r_{O–H(W)} < 0.26$ nm and $r_{O–O(W)} < 0.34$ nm). Hydrogen bonds were calculated from 10 ns trajectories for acetophenone molecules at positions of ±0.025 nm around the specified *d*-values (density peak maxima and shoulders) as well as for acetophenone molecules at $d = 3.525–4.225$ nm and $d = 3.025–5.025$ nm in the bulk liquid regions at the inner and outer surface, respectively, using a bin size of 0.05 nm.

2.3 Results and discussion

2.3.1 Properties of the chromatographic interface

In the results and discussion section, we first describe the conditions that analyte molecules meet at the inside and outside surface of a mesoporous particle located inside an equilibrated, endcapped C_{18} column, before we report how analyte molecules respond to these conditions. Please remember that the interstitial (void) space between the mesoporous particles in a chromatographic column, in our model represented by the outer slit pore, also constitutes a chromatographic pore.

The generic properties of the chromatographic interface in RPLC are briefly reiterated here. The terminology dates from seminal work of Siepmann and co-workers with slit pore models,[9,14] according to which three regions can be distinguished in a pore: bonded-phase, interfacial, and bulk liquid region. The notional limits of bonded-phase and interfacial region are drawn at 10% and 90%, respectively, of the total solvent density in the bulk liquid region. The bonded-phase region, which contains the majority of the bonded-phase groups in addition to the silica surface,[21] is characterized by the low diffusivity of solvent molecules and bonded-phase groups.[24] In contrast,

the interfacial region, which contains the flexible chain ends as well as the ACN ditch, is a region of high diffusivity.[5] The ACN ditch, which constitutes the transition between the terminal segment of the hydrophobic alkyl chains and the aqueous–organic bulk liquid, contains an excess of ACN molecules compared with the bulk liquid region of the pore.[13,24]

2.3.1.1 Conformation and spatial distribution of the bonded phase

The bonded phase is the natural starting point to investigate the properties of the chromatographic interface. The effect of cylindrical pore geometry on the bonded-phase conformation and spatial distribution is described through a combination of contour plots (Figure 2.2) and dihedral angle data (Table 2.2). Please note that the C_1 endcapping groups (whose conformation is fixed) were omitted from the analysis. The contour plots describe the spatial positions of particular alkyl groups in a chain by relating their vertical displacement *v* from the silica surface to their horizontal displacement *h* from the chain grafting point on the surface. Dihedral angle data connect different chain conformations to the average number of *gauche* defects per chain, N_{gauche}.

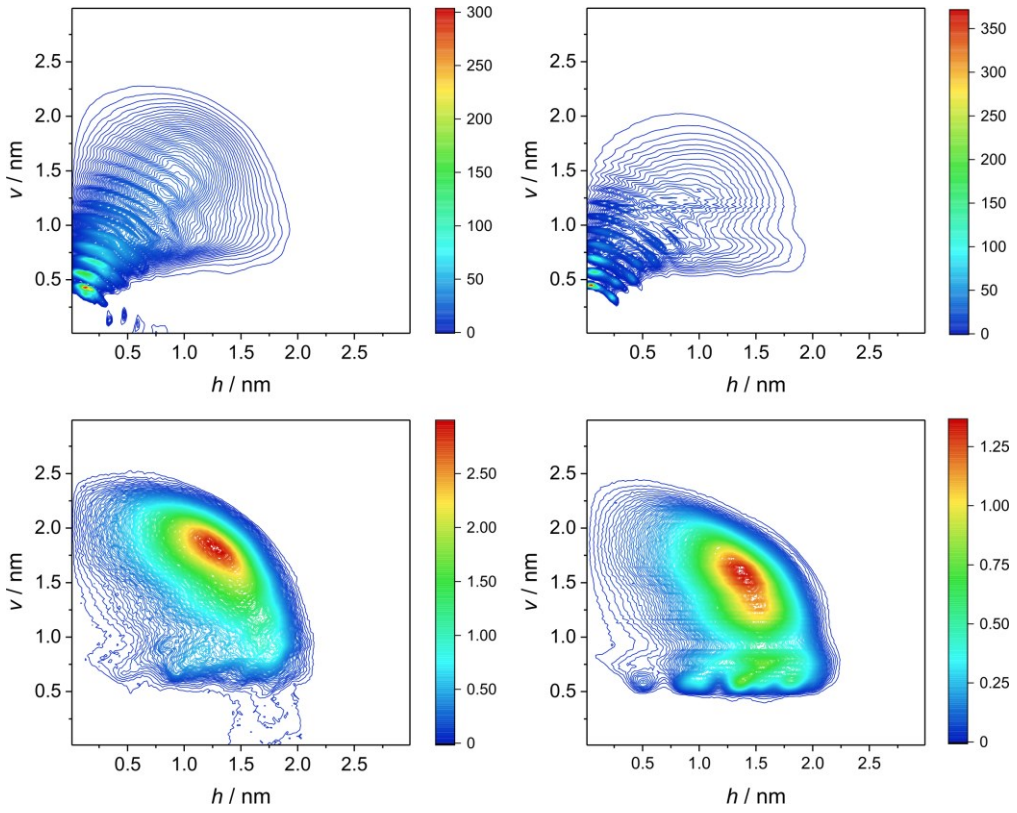

Figure 2.2. Spatial distribution of all alkyl groups in the C_{18} chains (top) and of the terminal methyl groups only (bottom) at the inner curved (left) and outer planar surfaces (right). Contour plots relate the vertical displacement *v* from the silica surface of a bonded-phase group to its horizontal displacement h from the chain grafting point on the silica surface (Figure 2.S2).

Table 2.2. Details of the bonded-phase conformation.

	Inner curved surface		Outer planar surface	
Chain conformation	Fraction	N_{gauche}	Fraction	N_{gauche}
Stretched[a]	5.4%	1.43	1.5%	1.34
Bent[b]	87.0%	3.70	77.2%	3.84
Backfolded[c]	7.6%	4.26	21.3%	4.19

[a] Distance of C_{18} from chain grafting point $g \geq 2.4$ nm.
[b] $g < 2.4$ nm and vertical displacement of C_{18} to silica surface $v \geq 0.94$ nm.
[c] $g < 2.4$ nm and $v < 0.94$ nm.

Figure 2.2 shows contour plots for all alkyl groups in the C_{18} chains and for the C18 groups only. The chain contour plots visualize that the bonded phase is more expansive and more evenly distributed over the pore radius at the inner curved surface than at the outer planar surface. While the first chain segment (up to C6) is generally focused, the mid and terminal chain segments (C6–C12 and C13–C18, respectively) are rather frayed at the outside surface. The chain contour plots also indicate that the chains are more extended inside than outside. This is also recognizable from the C18-only contour plots. The main C18 density is focused at v = 1.65–2.0 nm and h = 1.0–1.5 nm inside, compared with v = 1.35–1.75 nm and h = 1.2–1.6 nm outside, that is, inside chain ends are farther vertically displaced from the surface than outside and have a wider horizontal distribution relative to the chain grafting point.

From the distances of the C18 groups to the chain grafting points and the silica surface (g and h, respectively), we derived three types of chain conformations (Table 2.2): stretched ($g \geq 2.4$ nm), bent ($g < 2.4$ nm and $v \geq 0.94$ nm), and backfolded ($g < 2.4$ nm and $v < 0.94$ nm). Stretched chains represent a high degree of conformational order (N_{gauche} = 1.3–1.4), whereas the step from bent to backfolded chains represents a gradual decrease in conformational order (N_{gauche} = 3.7–3.8 and 4.2–4.3, respectively). Table 2.2, which lists the fraction of chains in each category, shows that stretched chains are rare and bent chains are the dominant conformation (>75% of chains). Inside and outside bonded-phase conformation differ mainly in the fraction of backfolded chains, which is substantially reduced at the inside surface (7.6% vs 21.3% outside). The bonded-phase conformation also contains more stretched chains inside than outside (5.4% vs 1.5%), but the decrease in backfolding occurs mainly in favor of bent chains (87.0% inside vs 77.2% outside).

Judging by the lower fraction of backfolded and higher fraction of stretched chains, the bonded-phase conformation can be regarded as more ordered inside than outside. Rafferty et al.[37] also asserted that the bonded phase in a 6 nm cylindrical pore (which bore the same C_{18} ligand density as the silica surface in our pore model) was more ordered than in a slit pore. The increase in conformational order caused by the cylindrical pore geometry differs, however, distinctly from the effects of shorter chain length or increased ligand density.[4,9,17] Exchanging C_{18} for C_8 chains decreases backfolding to a low level in favor of stretched chains; increasing the ligand density of

C_8 chains further raises the fraction of stretched chains at the cost of bent chains.[17] The former effect is related to the specific properties of C_{18} and C_8 chains, which do or do not tend to backfolding, respectively, and also differ in their degree of solvent penetration; the latter effect can be viewed as the result of ligand crowding.

2.3.1.2 Density distribution and diffusivity of bonded-phase groups

Before we look at the total bonded-phase density distribution, we compare the inside and outside bonded-phase density profiles group-by-group to analyze the influence of the pore geometry and the associated spatial restriction. The available space decreases towards the pore center in the cylindrical pore, but remains constant in the slit pore, as indicated in Figure 2.3.

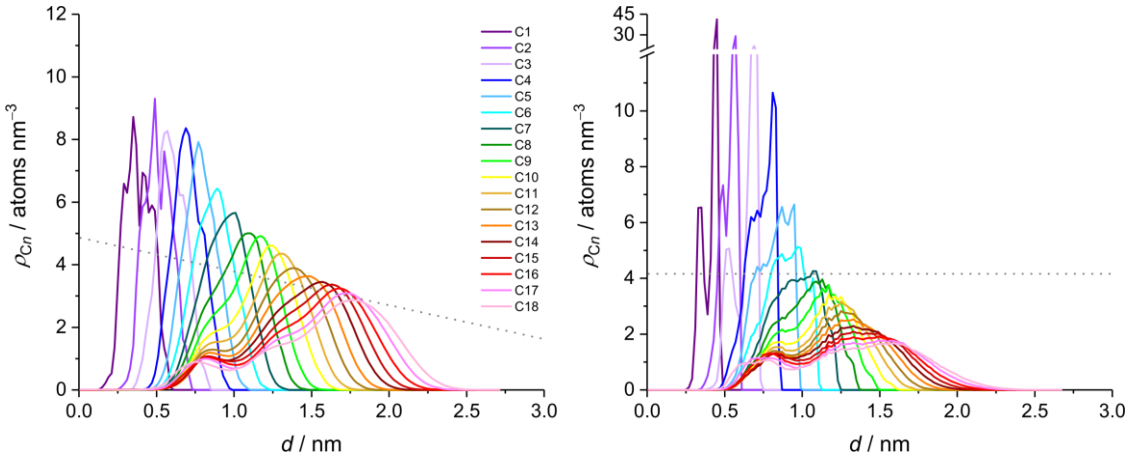

Figure 2.3. Density profiles of the alkyl groups Cn (n = 1−18) in the C18 chains at the inner curved (left) and outer planar surfaces (right). The dotted gray line indicates the volume (nm^3) of the 0.02 nm wide bins used for the bonded-phase density calculation at each surface.

Figure 2.3 shows that the outside distribution is dominated by the tall density peaks of the first three groups, C1–C3 ($\rho_{Cn,max}$ > 20 atoms nm^{-3}), which resemble the narrow density peaks of the uniformly located Si and O atoms at the outer planar surface (Figure 2.S4). The split in the density peaks reflects that chains can be upright (major fraction) or tilted compared with the surface normal, which was also visible in the contour plot for the C_{18} chains (Figure 2.2). The peaks of C4–C6 constitute the transition to the part of the density profile (≥C7), where the peaks are wide and low ($\rho_{Cn,max}$ < 5 atoms nm^{-3}). The bimodal density peaks of all groups ≥C8 indicate that the C_{18} chains can be backfolded or extended (bent or stretched).

The density peaks of the bonded-phase groups at the inner curved surface follow a more homogeneous, smoother distribution. The first two groups, C1 and C2, mirror the broader distribution of the Si and O atoms at the curved surface (Figure 2.S4). Judging by the maximum density and peak shape, the first five groups C1–C5 ($\rho_{Cn,max}$ = 8–9 atoms nm^{-3}) are similar, C6 and C7 form a transition, and from C8 on, backfolding is evident and the maximum peak density declines only gradually.

Figure 2.3 demonstrates that the bonded-phase density gradient is steep in the slit pore and shallow in the cylindrical pore. The ratio between the highest and lowest density peak maximum is ~25 at the outer planar surface compared with only ~3 at the inner curved surface. C5 has already higher maximum density inside than outside ($\rho_{Cn,max}$ = 8 and 7 atoms nm^{-3}, respectively). This also means that the cylindrical pore maintains a higher bonded-phase density towards the pore center than the slit pore. The outside bonded-phase density is concentrated near the silica surface, but loses definition beyond the first chain segment, because the slit pore does not exercise a spatial confinement on the flexible part of the C_{18} chains. The inner curved surface provides less density definition close to the chain grafting points, but the spatial restriction inside the cylindrical pore affects groups up to the chain ends.

Figure 2.3 reveals how the pore geometry shapes the relation between the solid silica surface and the soft hydrophobic surface formed by the alkyl chains grafted onto the silica surface. The roughness of the curved silica surface is smoothed out at the hydrophobic chain ends, whereas the perfection of the planar silica surface evolves into a rugged hydrophobic surface. The spatial confinement by the pore geometry is apparently of more relevance to the properties of the soft hydrophobic surface than the spatial distribution of chain grafting points.

After having shown that the cylindrical pore geometry has a major influence on the density distribution of the bonded-phase groups, we investigate how the cylindrical confinement affects the mobility of the bonded-phase groups along the chain length.

Figure 2.4 compares the surface-parallel diffusion coefficients of the alkyl groups in the C_{18} chains at the inner curved and outer planar surface. The comparison is made for the respective average and maximum values of the surface-parallel diffusion coefficient, $D_{\parallel,av}$ and $D_{\parallel,max}$, as both values are referred to later on. Exact numbers with errors are listed in Tables 2.S1 and 2.S2.

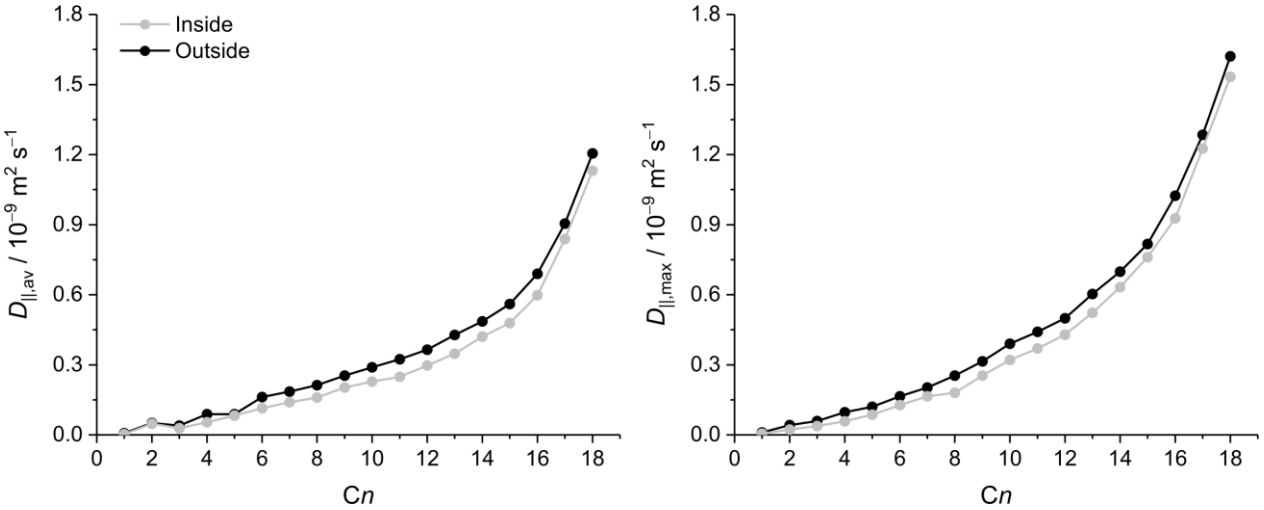

Figure 2.4. Comparison of the average (left) and maximum surface-parallel diffusion coefficients (right) of the alkyl groups C_n in the C_{18} chains at the inner curved and outer planar surface.

Generally, the curves in Figure 2.4 reflect that groups close to the silica surface (up to C5) have very low mobility ($D_{\parallel,av} < 0.1 \times 10^{-9}$ m^2 s^{-1}), intermediate groups (C6–C15) show a shallow

increase of mobility with group number, and the last three groups in the chain (C16–C18) show a steep mobility increase. Although the bonded-phase group diffusivity is consistently lower at the inner curved surface, the damping effect of the cylindrical confinement remains moderate. Averaged over the bonded-phase groups in extended C_{18} chains, the average surface-parallel diffusion coefficient is 15% lower inside than outside. But the mobility difference decreases towards the chain ends: the $D_{\parallel,av}$ values of C17 and C18 are only 6–7% lower inside than outside (Table 2.S1), an observation that we return to in the next section.

2.3.1.3 Density and diffusivity in the chromatographic interface

After the in-depth analysis of the bonded-phase properties, we provide an integral picture of the chromatographic interface that shows the interplay between bonded-phase and solvent properties. Figure 2.5 compares the inside and outside profiles for density and surface-parallel diffusivity of the total bonded phase (including the C_1 groups) and the solvent molecules. Subsets of Figure 2.5 that allow to compare the inside and outside density and diffusivity profiles for each component separately are additionally displayed in Figures 2.S5 and 2.S6.

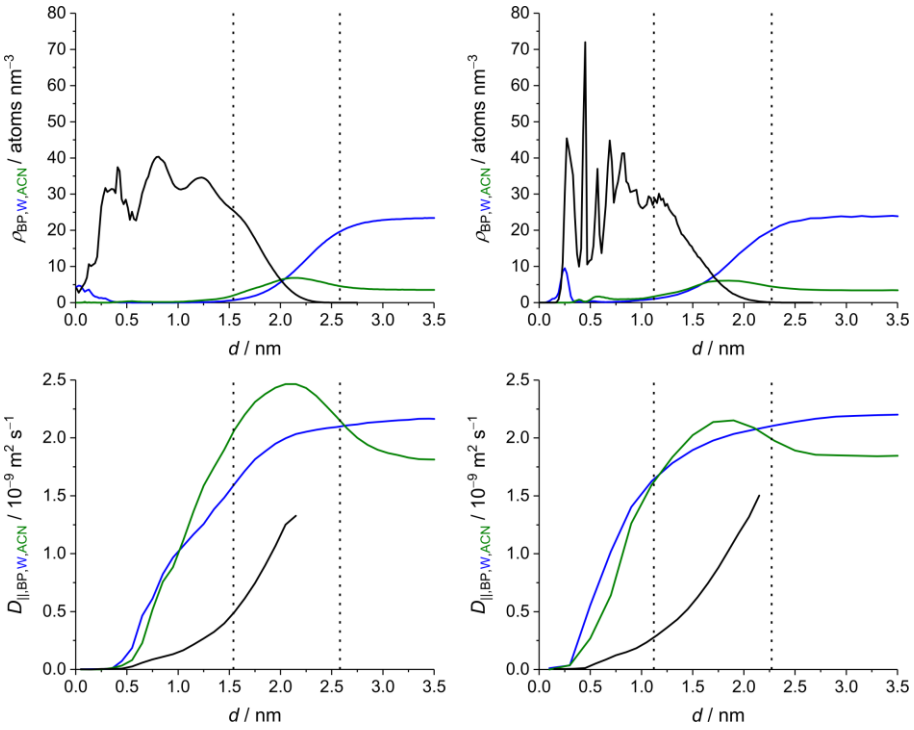

Figure 2.5. Density and surface-parallel diffusivity profiles for the bonded phase (BP, black), W (blue), and ACN (green) at the inner curved (left) and outer planar surface (right). Bonded-phase density profiles include the C1 endcapping groups. Vertical dashed lines indicate the limits of the bonded-phase and interfacial region at 10% and 90% of the total solvent density in the bulk-liquid region, respectively.

The outside total bonded-phase profile shows sharply defined density peaks up to d = 1.0 nm, which, as we know from the previous section, mostly represent the first chain segment (C1–C6) and the C_1 groups, followed by a drawn-out decline. The inside bonded-phase density profile is composed of broad peaks of similar maximum height. The first broad density peak (d < 0.6 nm) shows remnants of structure, the second broad peak (d = 0.6–1.0 nm) compares in height with the respective outside density segment, and at d > 1.0 nm, the inside profile maintains higher density than the outside profile, which means that a higher fraction of bonded-phase density is located away from the silica surface inside than outside (48.3% vs 39.6% at d > 1.0 nm). Overall, the bonded-phase density at the inner curved surface is more evenly distributed along the chain length as well as denser and more extended towards the pore center than the bonded-phase density at the outer planar surface. The same effect of concave pore curvature on the bonded-phase density distribution was observed for a 6 nm cylindrical pore by Rafferty et al.[37]

The differences in bonded-phase extension and density distribution between inner curved and outside planar surface affect the respective solvent density distributions. The solvent density distribution in an RPLC pore follows a general pattern.[4,24] The W density decreases over the interfacial region to very low values in the bonded-phase region, except for a local maximum at the silica surface. ACN also has small density peaks at the silica surface and low presence in the bonded-phase region, but goes through a density maximum in the interfacial region. Solvent density peaks at the silica surface are related to the coordination of residual OH groups. The solvent peaks at the planar outside surface are sharply defined and reflect a layer of surface-adsorbed solvent molecules, composed mostly of W molecules hydrogen-bonded to residual OH groups, and a second layer of ACN molecules that partially coordinate the first solvent layer.

The solvent density at the inner curved surface is smudged and closer to the surface Si atoms than at the outer planar surface, reflecting the silica-surface heterogeneity introduced by pore carving. Surface coordination by primarily W and secondarily ACN molecules is in principle as observed at the outer planar surface, except that there is less solvent presence overall (0.82 vs 1.01 O atoms nm^{-3} of W and 0.12 vs 0.40 C atoms nm^{-3} of ACN at the inner and outer surface, respectively) despite the higher residual surface hydroxylation (4.15 vs 3.50 μmol m^{-2}, Table 2.1). The inner pore generally contains less solvent density in the bonded-phase region than the outer pore (0.95 vs 1.26 atoms nm^{-3} of W and 0.63 vs 0.84 C atoms nm^{-3} of ACN), because the more compact bonded-phase density towards the cylindrical pore center makes solvent penetration into the bonded-phase region less likely. Additionally, formation of a denser solvent layer at the inner surface is hindered by the concave curvature that enhances the shielding effect of the endcapping C_1 groups (Figure 2.6). The comparison of the solvent layers associated with the inner curved and outer planar silica surface shows that the concave surface curvature outweighs the effect of higher residual hydroxylation.

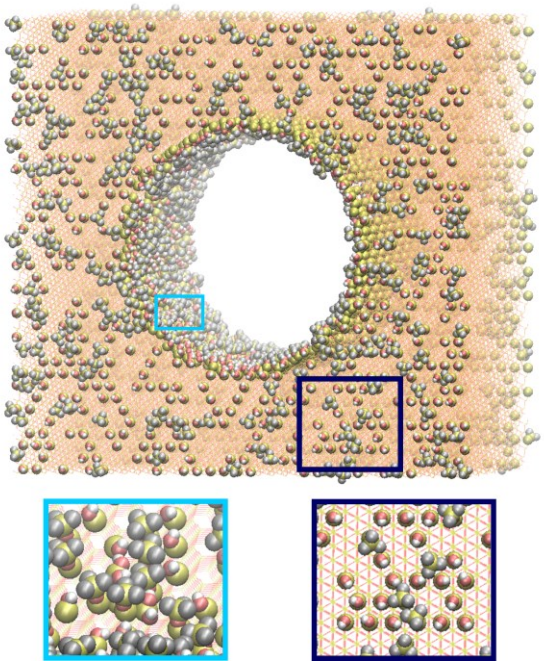

Figure 2.6. Accessibility of residual OH groups at the inner curved and outer planar silica surface. The tilted front view of the carved-out silica block shows only the residual OH groups and the C_1 endcapping groups on the surface. Close-ups visualize how well residual OH groups are shielded by the endcapping groups on the curved and planar surfaces. Si, O, and H atoms of the silica surface are represented by yellow, red, and white balls, respectively; CH_3 united-atom groups are represented by gray balls; Si and O atoms of the silica block are shown as thin, yellow, and red lines, respectively.

Compared to the outer planar surface, the interfacial region at the inner curved surface is narrower and shifted farther away from the silica surface, towards the cylindrical pore center, and is also richer in ACN due to the higher local bonded-phase density (Figure 2.5). Averaged over the interfacial region, the ACN excess compared with the bulk liquid region is 33 vol-% and 31 vol-% at the inner curved and outer planar surface, respectively. At the ACN density maximum in the interfacial region, the inside and outside local solvent compositions contain 39 vol-% and 32 vol-% more ACN than the bulk liquid region.

The increased ACN excess in the interfacial region at the inner curved surface translates into increased diffusivity for ACN molecules and is also behind the reduced bonded-phase mobility difference at the chain ends (Figure 2.4). The maximum mobility gain of ACN, calculated from $D_{\parallel,\max}$ and the average diffusion coefficient in the bulk region, $D_{\mathrm{m,bulk}}$, is 17% outside and 35% inside, that is, the cylindrical pore more than doubles the maximum mobility gain of ACN.

In summary, the analysis of the properties of the chromatographic interface has shown that the cylindrical pore contains a more homogeneous bonded-phase density distribution, less solvent presence in the bonded-phase region, and higher ACN excess and diffusivity in the interfacial region than the slit pore. What this means for the analyte density distribution remains to be seen, but we already know from slit pore simulations that higher ACN excess and diffusivity in the

interfacial region favor the local analyte diffusivity.[5,8,17,24] Therefore, we expect to see an enhancement of analyte surface diffusivity in the cylindrical pore.

2.3.2 Consequences of cylindrical pore geometry

2.3.2.1 Analyte diffusitivty

At 70/30 (v/v) W/ACN, ethylbenzene and acetophenone are strongly and moderately retained, respectively.[8] This means that analyte molecules are (very) rarely found in the bulk liquid region. Consequently, mass transport occurs nearly exclusively in the stationary phase, namely through surface diffusion in the interfacial region, as the analyte mobility in the bonded-phase region becomes progressively more hindered by the less flexible bonded-phase groups.[5] Figure 2.7, which shows the ethylbenzene and acetophenone diffusivity profiles, confirms that the analyte mobility in the interfacial region is distinctly increased at the inner curved compared with the outer planar surface. The maximum mobility gain from surface diffusion increases from 36% to 63% for ethylbenzene and from 11% to 37% for acetophenone between the slit pore and the cylindrical pore (Table 2.3). Interestingly, the moderately polar acetophenone profits as much from the cylindrical pore geometry as the apolar ethylbenzene. In the slit pore, analytes with polar groups are inferior to the solvents ACN and acetone regarding the maximum mobility gain from surface diffusion,[21] but in the cylindrical pore acetophenone compares to ACN in this respect.

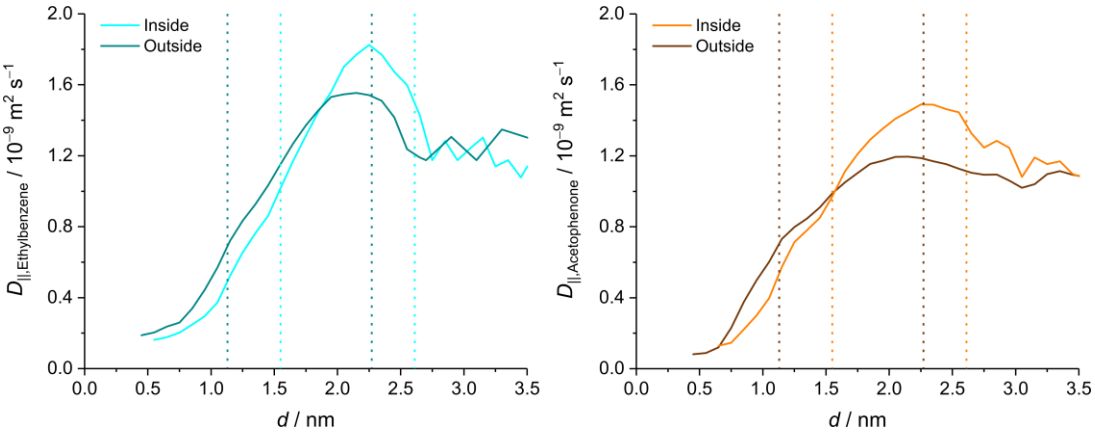

Figure 2.7. Surface-parallel diffusivity profiles for ethylbenzene (left) and acetophenone (right) at the inner curved and outer planar surface. Vertical dashed lines indicate the limits of the bonded-phase and the interfacial region at 10 and 90% of the total solvent density in the bulk-liquid region, respectively.

The favorable effect of the cylindrical pore geometry on the analyte surface diffusivity stems from three contributions: i) the ACN excess at the location of the analyte mobility maximum, $d(D_{\|,\text{max}})$, ii) the mobility of the bonded-phase groups present at $d(D_{\|,\text{max}})$, and iii) the bonded-phase density at $d(D_{\|,\text{max}})$. Generally, the analyte mobility maximum is located closer to the bulk liquid region

than the ACN density maximum ($d(\rho_{ACN,max})$), where contacts with the less mobile bonded-phase groups slow analyte molecules down.[5]

Table 2.3. Details of surface diffusion for ACN and the analytes.

Compound	Surface	$d(D_{\parallel,max})$ (nm)	$D_{\parallel,max}$ (10^{-9} m^2 s^{-1})	$D_{m,bulk}$ (10^{-9} m^2 s^{-1})	Maximum mobility gain
ACN	Inner curved	2.15	2.46±0.10	1.82±0.07	35%
	Outer planar	1.85	2.16±0.08	1.84±0.03	17%
Ethyl-benzene	Inner curved	2.25	1.83±0.11	1.12±0.13	63%
	Outer planar	2.15	1.55±0.12	1.14±0.15	36%
Aceto-phenone	Inner curved	2.25	1.49±0.10	1.09±0.11	37%
	Outer planar	2.15	1.19±0.07	1.07±0.09	11%

At the inner curved surface, the analyte mobility maximum is located closer to the ACN density and mobility maximum than at the outer planar surface ($\Delta d = d(D_{\parallel,max}) - d(\Delta_{ACN,max}) = 0.1$ nm and $\Delta d = 0.3$ nm, respectively) and thus profits from a larger local ACN excess (32 vol-% compared with only 15 vol-% outside). Second, the bonded-phase presence at $d(D_{\parallel,max})$, which is restricted to the terminal chain segment, consists inside to 75% of the most mobile alkyl groups C17 and C18 compared with 67% outside. Third, as we have shown in earlier MD simulation studies,[5,8,17] contact with the mobile ends of the C_{18} chains elevates the surface diffusivity of analyte molecules above the value expected from the local ACN excess. The higher bonded-phase density at $d(D_{\parallel,max})$ in the cylindrical pore raises the stationary-phase contribution to $D_{\parallel,max}$ from 18% to 25% for ethylbenzene and from 8% to 24% for acetophenone (Table 2.S3).

The strong maximum mobility gain of analytes in the cylindrical pore changes the relative mobility in the interfacial region (Tables 2.3 and 2.S2). Outside, ethylbenzene and acetophenone have lower maximum surface-parallel diffusivity ($D_{\parallel,max} = 1.55$ and 1.19×10^{-9} m^2 s^{-1}) than the alkyl groups C18 and C17 ($D_{\parallel,max} = 1.62$ and 1.28×10^{-9} m^2 s^{-1}), respectively, but this is reversed inside. The ethylbenzene diffusivity overtakes that of C18 ($D_{\parallel,max} = 1.83$ and 1.53×10^{-9} m^2 s^{-1}, respectively) and the acetophenone diffusivity overtakes the C17 diffusivity ($D_{\parallel,max} = 1.49$ and 1.23×10^{-9} m^2 s^{-1}) and approaches that of C18. This comparison shows that the analyte surface diffusivity benefits enormously from the cylindrical pore geometry, although the associated spatial confinement slightly attenuates the diffusivity of the bonded-phase groups with which the analyte molecules are in contact.

2.3.2.2 Density distribution and molecular orientation of ethylbenzene

From earlier slit pore simulations,[4,5] we know that small, stiff analyte molecules distinguish between the bonded-phase and the interfacial region of the chromatographic interface formed by

C_{18} stationary phases. Chromatographers interpret analyte presence in the bonded-phase region as the result of partitioning fully into the alkyl chains (reminiscent of liquid–liquid partitioning) and analyte presence in the interfacial region as the result of adsorption onto the soft hydrophobic surface formed by the alkyl chains.[18] The bonded-phase region affords analyte molecules immersion in a nearly completely hydrophobic environment (except for the solvent layer at the silica surface). The interfacial region provides a mixed environment consisting of bonded-phase groups as well as solvent molecules of the ACN ditch. Of the small solute molecules investigated in molecular simulation studies, those with polar groups decidedly prefer the interfacial over the bonded-phase region of a C_{18} stationary phase, whereas apolar molecules may show some preference for the interfacial region.[4–6,8,15,19–21]

Figure 2.8, which compares the analyte density profiles at the inner curved and outer planar surface, reflects the differences between the apolar ethylbenzene and the moderately polar acetophenone regarding the contribution from partitioning to the analyte density in the stationary phase accordingly. Partitioning accounts for 35% (ethylbenzene) and 22% (acetophenone) of the overall analyte density at the outer planar surface (Table 2.4). At the inner curved surface, the contribution from partitioning is reduced to 27% (ethylbenzene) and 8% (acetophenone) of the overall analyte density. These numbers indicate that the cylindrical pore geometry strengthens the preference of analytes for the interfacial region in general and of analytes with polar groups in particular.

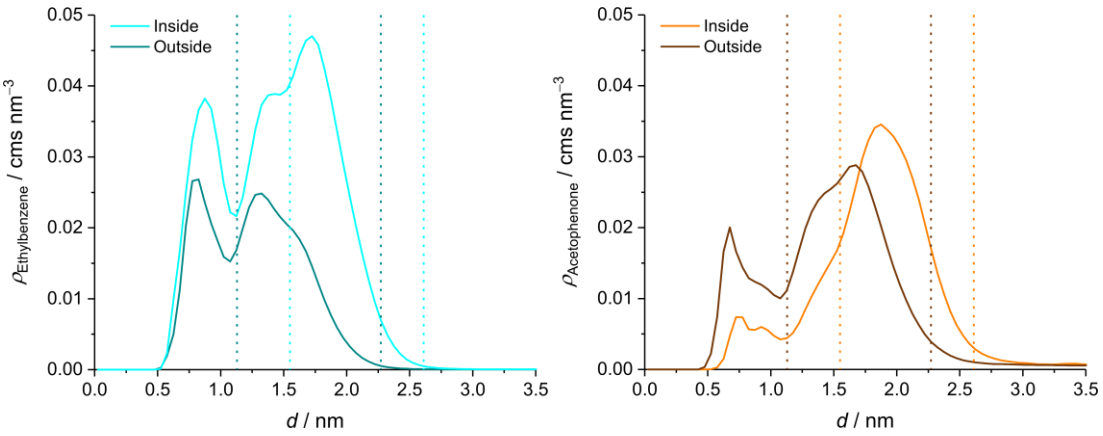

Figure 2.8. Density profiles for ethylbenzene (left) and acetophenone (right) at the inner curved and outer planar surface. Vertical dashed lines indicate the limits of the bonded-phase and interfacial region at 10 and 90% of the total solvent density in the bulk-liquid region, respectively. Density peaks are assigned to indicate analyte partitioning and adsorption, respectively, based on the limits of the bonded-phase and interfacial region in the slit pore.

All peaks in the ethylbenzene density profile are increased at the inner curved surface, which offers added bonded-phase contacts to ethylbenzene molecules at each location in the chromatographic interface (Table 2.5).

Table 2.4. Distribution of analyte density in the chromatographic interface.

Analyte	Interaction	Inner curved surface		Outer planar surface	
		d (nm)	Density	*d* (nm)	Density
Ethyl-benzene[a]	Partitioning	0.025–1.125	27%	0.025–1.075	35%
	Adsorption	1.125–1.475	22%	1.075–1.475	35%
	Adsorption	1.475–2.925	50%	1.475–2.675	30%
Aceto-phenone[b]	Partitioning	0.025–0.825	4%	0.025–0.825	13%
	Partitioning	0.825–1.075	4%	0.825–1.075	9%
	Adsorption	1.075–1.525	13%	1.075–1.525	28%
	Adsorption	1.525–2.875	75%	1.525–2.675	45%

[a] Total ethylbenzene density in partitioning and adsorption peaks at the inner curved and outer planar surface: $\rho_{\text{Ethylbenzene,inside}} = 1.79 \times 10^{-2}$ cms nm^{-3}, $\rho_{\text{Ethylbenzene,outside}} = 0.93 \times 10^{-2}$ cms nm^{-3}.
[b] Total acetophenone density in partitioning and adsorption peaks at the inner curved and outer planar surface: $\rho_{\text{Acetophenone,inside}} = 1.06 \times 10^{-2}$ cms nm^{-3}, $\rho_{\text{Acetophenone,outside}} = 1.12 \times 10^{-2}$ cms nm^{-3}.

The density enhancement is most pronounced in the bulk-liquid side of the adsorption peak, whose contribution to the overall ethylbenzene density increases from 30% outside to 50% inside. Overall, the density of ethylbenzene molecules in contact with bonded-phase groups (received through integration over the partitioning and adsorption peaks in the density profiles, Table 2.4) is $\rho_{\text{Ethylbenzene,inside}} = 1.79 \times 10^{-2}$ cms nm^{-3} and $\rho_{\text{Ethylbenzene,outside}} = 0.93 \times 10^{-2}$ cms nm^{-3}. The ethylbenzene density in the stationary phase is thus a factor of 1.9 higher at the inner curved surface compared with the outer planar surface.

Table 2.5. Bonded-phase contacts of ethylbenzene molecules at characteristic locations in the chromatographic interface.

Interaction	Inner curved surface		Outer planar surface	
	d (nm)	$C_{BP}^{a,b}$ (nm^{-3})	*d* (nm)	$C_{BP}^{a,b}$ (nm^{-3})
Partitioning	0.875	27.06	0.825	20.39
Adsorption	1.425	21.87	1.325	19.62
Adsorption	1.725	19.11	1.625	15.93

[a] Average number of contacts with bonded-phase groups. Distance criterion: $r_{\text{cms–BP}} < 0.81$ nm.
[b] Bonded-phase contacts consider C_{18} chains and C_1 groups.

Figure 2.9 shows the ethylbenzene orientation in the respective density peaks. For ease of perception, probability distributions visualize the direction of the ethylbenzene side chain as well as the orientation of the aromatic ring plane.

Generally, ethylbenzene molecules in the partitioning peak and the silica-surface side of the adsorption peak arrange the benzene ring parallel to the surface normal, whereas ethylbenzene molecules in the bulk-liquid side of the adsorption peak show a slight preference for a surface-parallel arrangement (outer planar surface) or no preference (inner curved surface). Ethylbenzene molecules in the partitioning peak point the side chain to or away from the silica surface, adapting the angle between molecular vector and surface normal to the surface curvature. Ethylbenzene molecules in the bulk-liquid side of the adsorption peak generally prefer to direct the side chain to the silica surface (i.e., to bury the side chain in the alkyl chains of the bonded phase). This side-chain direction is also preferred by ethylbenzene molecules in the silica-surface side of the adsorption peak at the outer planar surface, whereas at the inner curved surface the opposite orientation is also observed.

Overall, the cylindrical pore geometry induces only minor changes in the ethylbenzene orientation. This observation correlates with the enhancement of each ethylbenzene density peak at the inner curved surface. The combined density and orientation data for ethylbenzene show that a 9 nm cylindrical pore does not restrict the ethylbenzene density at any location in the chromatographic interface compared with the slit pore geometry, rendering larger changes in the molecular orientation unnecessary.

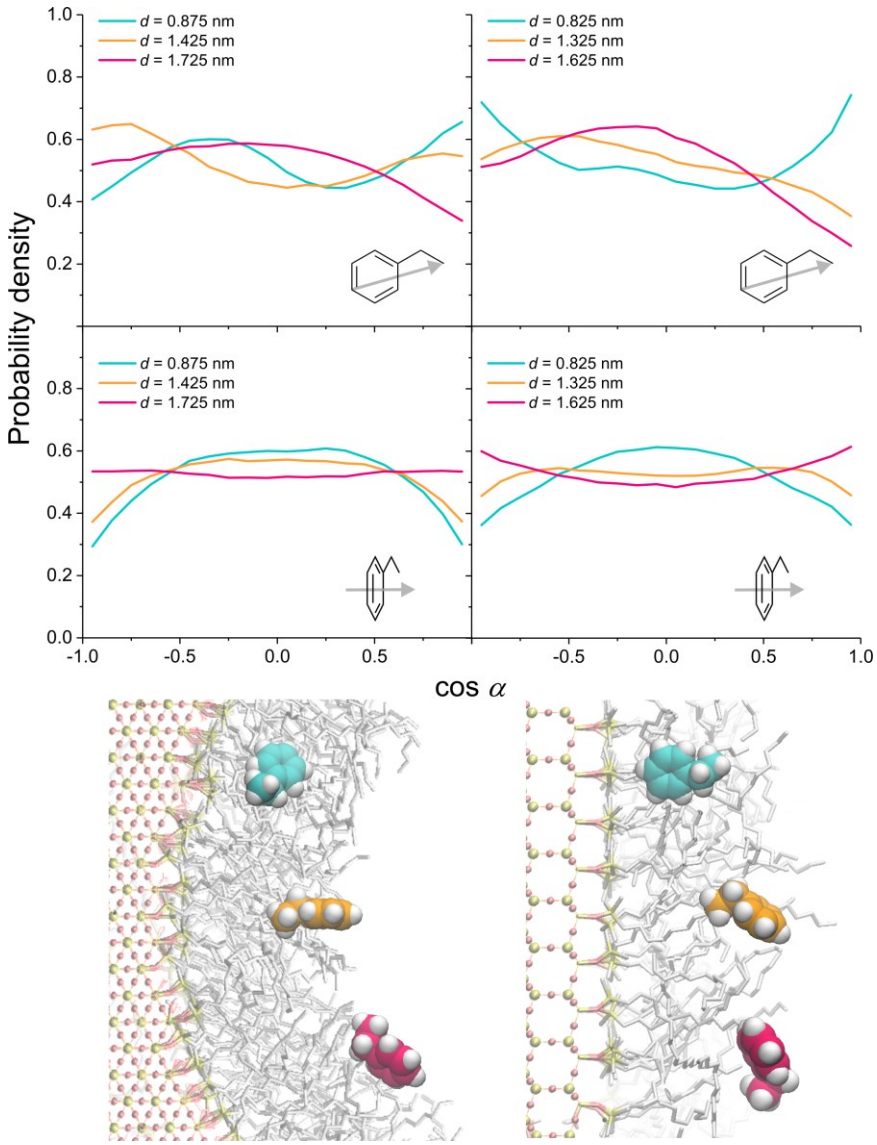

Figure 2.9. Orientation of ethylbenzene molecules at different locations in the chromatographic interface at the inner curved (left) and outer planar surface (right). Top: Probability distributions for the cosine of the angle α between the molecular vector and the surface normal indicate the sidechain direction. Bottom: Probability distributions for the cosine of the angle α between the vector perpendicular to the aromatic ring plane and the surface normal indicate the ring plane orientation. Snapshots visualize the typical ethylbenzene orientation at the indicated distances from the silica surface, which correspond to the peak maxima and shoulders in the ethylbenzene density distributions (cf. Figure 2.8).

2.3.2.3 Density distribution, hydrogen bonding, and molecular orientation of acetophenone

The comparison of the acetophenone density profiles at the inner curved and outer planar surface (Figure 2.8) shows that, contrary to ethylbenzene, the cylindrical pore geometry makes the

stationary phase not universally more attractive to acetophenone. This agrees with the molecular simulation results of Rafferty et al.,[37] who also found that the cylindrical pore geometry favored the density accumulation of an apolar solute in the stationary phase much more than that of a polar solute. The acetophenone partitioning peak loses density between outside and inside stationary phase, while the adsorption peak loses density at the silica-surface side and gains it at the bulk-liquid side. The contribution of the bulk-liquid side of the adsorption peak to the overall acetophenone density increases from 45% outside to 75% inside, and so nearly compensates for the loss of acetophenone density in the partitioning peak and the surface-side of the adsorption peak (Table 2.4). The density of acetophenone molecules in contact with bonded-phase groups is $\rho_{\text{Acetophenone,inside}} = 1.06 \times 10^{-2}$ cms nm^{-3} and $\rho_{\text{Acetophenone,outside}} = 1.12 \times 10^{-2}$ cms nm^{-3}, that is, the acetophenone density in the stationary phase is nearly equally distributed between inner curved and outer planar surface.

The commonality between the two analyte species regarding the effect of cylindrical pore geometry on the analyte density in the stationary phase is thus reduced to a density increase of the bulk-liquid side of the adsorption peak. This ties in with the respective change in the bonded-phase density profiles (Figure 2.5), that is, the cylindrical pore geometry shifts bonded-phase and analyte density away from the silica surface and towards the pore center.

Earlier slit pore simulations have shown that hydrogen-bonding opportunities to W molecules strongly influence the density distribution and molecular orientation of acetophenone in the chromatographic interface.[5,21] The partitioning peak of acetophenone contains two layers. Most acetophenone molecules in the silica-surface layer direct the O atom to the silica surface to form on average ~1 hydrogen bond per molecule with surface-adsorbed W molecules. Acetophenone molecules in the second layer prefer the opposite orientation. Figure 2.10 and Table 2.6 show that the orientational preference in the first and second layer of the acetophenone partitioning peak is less pronounced inside the cylindrical pore. The reduced density and orientational preference in the first partitioning-peak layer of acetophenone (d = 0.725 nm) is caused by the decreased density of surface-adsorbed W molecules at the inner curved surface, resulting in fewer W contacts (Table 2.7). The reduced availability of W molecules at the inner silica surface lowers the average number of acetophenone–W hydrogen bonds only slightly (Table 2.6), as acetophenone molecules adapt their orientation to maintain hydrogen bonding, for example, by changing their preferred orientation for the aromatic ring plane from parallel to the surface normal to parallel to the inner curved surface.

Acetophenone molecules in the second partitioning-peak layer (d = 0.925 nm) arrange the aromatic ring plane parallel to the surface normal at the inner curved and outer planar surface, but the incentive of hydrogen-bond formation is not strong (Table 2.6), as there is only limited access to W molecules at this location. At the outer planar surface, acetophenone molecules in this location have access to interfacial W, so that more molecules turn the O atom to the bulk liquid than to the silica surface, whose solvent layer is less accessible (but not completely out of reach). Acetophenone molecules in this location at the inner curved surface cannot access the interfacial W, as the W density profile is shifted to the bulk liquid region in the cylindrical pore (Figures 2.5 and 2.S3). Consequently, acetophenone molecules at d = 0.925 nm direct the O atom to or away

from the bulk liquid region with nearly equal probability (Table 2.6). As observed for the first layer of the partitioning peak, the loss of W contacts also translates to a density decrease in the second layer of the partitioning peak, albeit a less severe one.

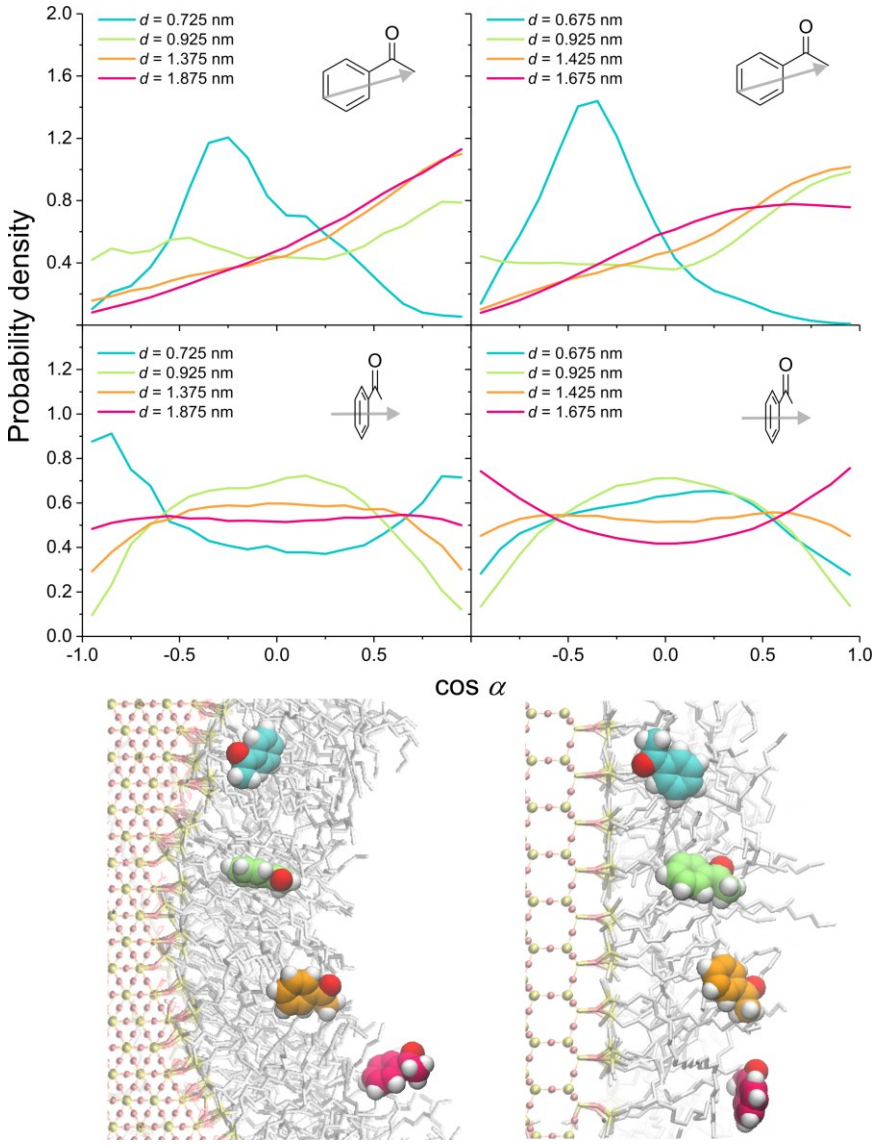

Figure 2.10. Orientation of acetophenone molecules at different locations in the chromatographic interface at the inner curved (left) and outer planar surface (right). Top: Probability distributions for the cosine of the angle α between the molecular vector and the surface normal indicate the side-chain direction. Bottom: Probability distributions for the cosine of the angle α between the vector perpendicular to the aromatic ring plane and the surface normal indicate the ring plane orientation. Snapshots visualize the typical acetophenone orientation at the indicated distances from the silica surface, which correspond to the peak maxima and shoulders in the acetophenone density distributions (cf. Figure 2.8).

Table 2.6. Orientation and hydrogen bonding of acetophenone molecules at characteristic locations in the chromatographic interface.

Interaction	Inner curved surface			Outer planar surface		
	d (nm)	O atom to bulk liquid	HB[a,b,c]	*d* (nm)	O atom to bulk liquid	HB[a,b,c]
Partitioning	0.725	30.5%	0.91 ± 0.06	0.675	12.3%	1.02 ± 0.15
Partitioning	0.925	51.7%	0.25 ± 0.30	0.925	60.8%	0.66 ± 0.19
Adsorption	1.375	69.4%	0.58 ± 0.17	1.425	69.8%	0.90 ± 0.05
Adsorption	1.875	72.7%	0.92 ± 0.05	1.675	66.4%	0.97 ± 0.02

[a] Average number of acetophenone–W hydrogen bonds per acetophenone molecule.
[b] Distance criteria: $r_{O–H(W)} < 0.26$ nm and $r_{O–O(W)} < 0.34$ nm.
[c] Acetophenone–W hydrogen bonds in the bulk liquid regions: $HB_{inside} = 1.49 \pm 0.20$ and $HB_{outside} = 1.46 \pm 0.23$.

Acetophenone molecules in the adsorption peak, whether on the silica-surface or the bulk-liquid side, preferentially direct the O atom towards the bulk liquid region for hydrogen-bond formation with W molecules there (Table 2.6). The shift of W density to the bulk liquid region in the cylindrical pore (Figures 2.5 and 2.S3) explains the decreased number of acetophenone–W hydrogen bonds as well as the decreased density in the silica surface-side of the adsorption peak. The bulk-liquid side of the acetophenone adsorption peak follows the shifted W density profile so that the average number of acetophenone–W hydrogen bonds at this location nearly recovers the corresponding value at the outer planar surface.

The compact bonded-phase density in the interfacial region of the cylindrical pore translates into increased bonded-phase contacts for acetophenone molecules at each location of the chromatographic interface compared with the outer planar surface (Table 2.7). The bulk-liquid side of the adsorption peak is the only location in the cylindrical pore where acetophenone density is increased compared with the slit pore. This indicates that acetophenone responds positively to a combination of adequate hydrogen-bonding opportunities and added bonded-phase contacts, though not to added bonded-phase contacts alone.

The cylindrical pore geometry changes the density distribution and molecular orientation of acetophenone more than that of ethylbenzene, because acetophenone molecules are forced to adapt their orientation and local density to the W density distribution. Acetophenone density decreases where the W density decreases and increases where W density is sufficient and the bonded-phase density raised. The increase in bonded-phase contacts afforded by the cylindrical pore does not compensate for a loss of W contacts. In the end, the cylindrical pore has no advantage over the slit pore for accumulating acetophenone density in the stationary phase.

Table 2.7. Bonded-phase and W contacts of acetophenone molecules at characteristic locations in the chromatographic interface.

Interaction	Inner curved surface			Outer planar surface		
	d (nm)	$C_{BP}^{a,b}$ (nm^{-3})	C_W^c (nm^{-3})	d (nm)	$C_{BP}^{a,b}$ (nm^{-3})	C_W^c (nm^{-3})
Partitioning	0.725	26.92	1.02	0.675	19.24	2.70
Partitioning	0.925	22.92	1.13	0.925	16.98	1.60
Adsorption	1.375	19.15	1.83	1.425	14.40	2.99
Adsorption	1.875	13.69	3.28	1.675	11.61	3.89

[a] Average number of contacts with bonded-phase groups. Distance criterion: $r_{cms–BP} < 0.81$ nm.
[b] Bonded-phase contacts consider C_{18} chains and C_1 groups.
[c] Average number of contacts with W molecules. Distance criterion: $r_{cms–O(W)} < 0.55$ nm.

2.4 Conclusions

In this study, we assessed how the cylindrical geometry of an average-sized mesopore in a column shapes the interfacial phenomena behind mass transport in RPLC. The cylindrical-inside-a-slit-pore model introduced for this purpose replicated the conditions inside an RPLC column, where the endcapped C_{18} stationary phase is present at the inner and outer surfaces of the mesoporous, μm-sized silica particles of the chromatographic bed. MD simulations performed for two analyte species in a weakly eluting W–ACN mobile phase monitored the competition between the stationary phase at the cylindrical inner and (at the mesopore scale) planar outer surface for a given number of analyte molecules in the system.

At 9 nm diameter, the cylindrical pore offers a decidedly more hydrophobic environment than the slit pore without placing spatial restrictions on the analyte density. At the molecular level, a more hydrophobic environment translates into more bonded-phase and fewer W contacts for analyte molecules. This favors the accumulation of an apolar analyte such as ethylbenzene in the stationary phase, but not necessarily that of a moderately polar analyte such as acetophenone, so that the cylindrical pore geometry effectively enhances the local (pore-scale) selectivity of the stationary phase.

The increased hydrophobicity of the cylindrical pore generally benefits the analyte mobility as both species experience a considerably increased surface diffusivity. At the same time, the cylindrical pore geometry shifts the analyte density towards the pore center. The combined effect of higher analyte density and mobility in the interfacial region achieved by the cylindrical pore geometry predicts a substantial increase of the pore diffusivity,[25] as surface diffusion is the primary mode of mass transport for retained analytes.[55]

Our results indicate that an average-sized cylindrical pore holds generous advantages for the local selectivity and the mass transport in an RPLC column. The cylindrical mesopore geometry of

chromatographic beds is neither a designed nor an intentionally employed feature (yet), but results from the sol–gel process preparation of the silica materials that also entails wide pore size distributions.[61,62] Because the surface curvature depends on the pore size, the extent to which the cylindrical mesopore geometry benefits RPLC processes is expected to vary over a mesoporous silica particle, a subject of further studies. Our results also reveal how different analyte species respond to the surface-curvature induced changes in the chromatographic interface. Molecular simulation studies, in which the properties of the chromatographic interface are varied through realistic parameters and probed with different analyte species, have the potential to contribute to a better understanding and prediction of analyte retention in RPLC.[63]

2.5 Supporting Information

Table 2.S1. Average surface-parallel diffusion coefficients of bonded-phase groups at the inner curved and outer planar surface.

	Inner curved surface	Outer planar surface
United-atom group number	$D_{\parallel,av}$ (10^{-9} m^2 s^{-1})	$D_{\parallel,av}$ (10^{-9} m^2 s^{-1})
1	0.003 ± 0.002	0.007 ± 0.003
2	0.048 ± 0.020	0.051 ± 0.019
3	0.028 ± 0.019	0.040 ± 0.016
4	0.054 ± 0.011	0.088 ± 0.011
5	0.082 ± 0.016	0.088 ± 0.013
6	0.114 ± 0.017	0.162 ± 0.019
7	0.139 ± 0.013	0.186 ± 0.020
8	0.160 ± 0.015	0.213 ± 0.021
9	0.203 ± 0.021	0.254 ± 0.026
10	0.228 ± 0.020	0.289 ± 0.021
11	0.249 ± 0.011	0.324 ± 0.034
12	0.298 ± 0.011	0.365 ± 0.033
13	0.347 ± 0.036	0.428 ± 0.051

14	0.420 ± 0.040	0.486 ± 0.049
15	0.479 ± 0.050	0.560 ± 0.052
16	0.598 ± 0.052	0.689 ± 0.056
17	0.838 ± 0.065	0.905 ± 0.069
18	1.131 ± 0.101	1.205 ± 0.095

Table 2.S2. Maximum surface-parallel diffusion coefficients of bonded-phase groups at the inner curved and outer planar surface.

	Inner curved surface	Outer planar surface
United-atom group number	$D_{\parallel,\max}$ (10^{-9} m^2 s^{-1})	$D_{\parallel,\max}$ (10^{-9} m^2 s^{-1})
1	0.005 ± 0.002	0.010 ± 0.005
2	0.022 ± 0.015	0.041 ± 0.006
3	0.038 ± 0.017	0.059 ± 0.026
4	0.058 ± 0.012	0.097 ± 0.012
5	0.087 ± 0.004	0.120 ± 0.073
6	0.128 ± 0.010	0.165 ± 0.022
7	0.165 ± 0.019	0.203 ± 0.025
8	0.180 ± 0.022	0.254 ± 0.030
9	0.253 ± 0.029	0.315 ± 0.037
10	0.321 ± 0.013	0.390 ± 0.016
11	0.370 ± 0.013	0.441 ± 0.041
12	0.429 ± 0.018	0.499 ± 0.055
13	0.523 ± 0.053	0.603 ± 0.073
14	0.632 ± 0.066	0.699 ± 0.080
15	0.761 ± 0.069	0.817 ± 0.082
16	0.927 ± 0.086	1.024 ± 0.075

17	1.225 ± 0.108	1.284 ± 0.115
18	1.533 ± 0.175	1.621 ± 0.142

Table 2.S3. Stationary-phase contribution to surface diffusion for ACN and the analytes.

Compound	Surface	$d(D_{\parallel,\max})$ (nm)	$D_{\parallel,\max}$ (10^{-9} m^2 s^{-1})	$D_{m,expected}$[a] (10^{-9} m^2 s^{-1})	Stationary-phase contribution
ACN	Inner curved	2.15	2.46±0.10	2.12±0.07	16%
	Outer planar	1.85	2.16±0.08	1.99±0.06	9%
Ethyl-benzene	Inner curved	2.25	1.83±0.11	1.46±0.10	25%
	Outer planar	2.15	1.55±0.12	1.31±0.07	18%
Aceto-phenone	Inner curved	2.25	1.49±0.10	1.20±0.06	24%
	Outer planar	2.15	1.19±0.07	1.10±0.04	8%

[a] Bulk molecular diffusion coefficient expected for the W/ACN ratio at $d(D_{\parallel,\max})$. Values were taken from Figure 7 in Rybka et al., *J. Phys. Chem. C* **2017**, *121*, 17907–17920.

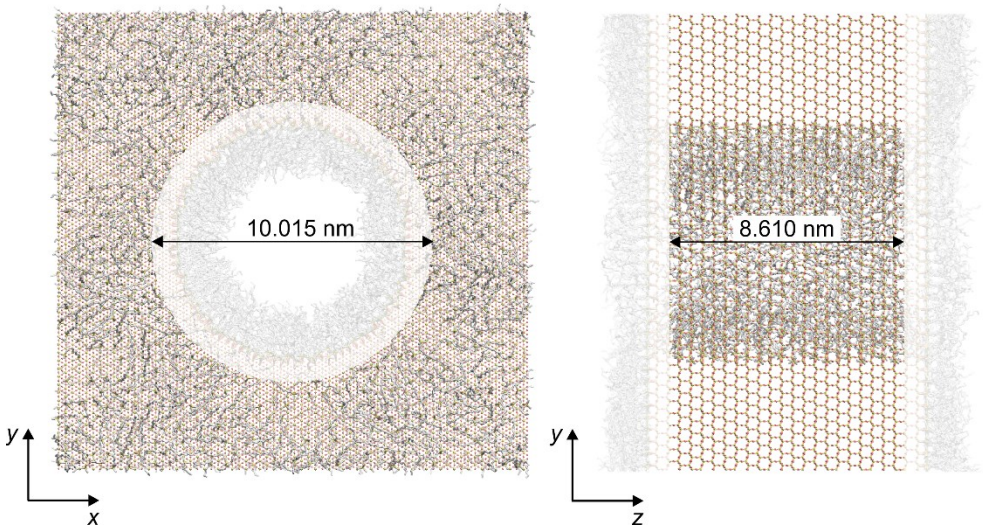

Figure 2.S1. Discrimination between inner curved and outer planar silica surface via exclusion of the pore entrance region. Front view (left) and side view (right) of the simulation box (shown without solvent molecules) indicate the dimensions of the volumes excluded for data calculation.

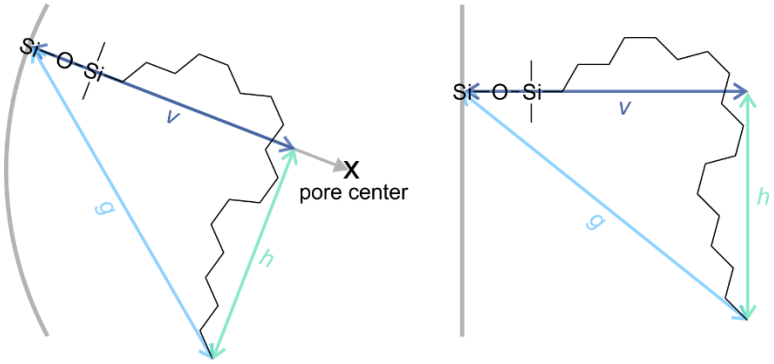

Figure 2.S2. Definition of parameters to describe the spatial distribution and conformation of the C_{18} chains of the bonded phase at the inner curved (left) and outer planar silica surface (right).

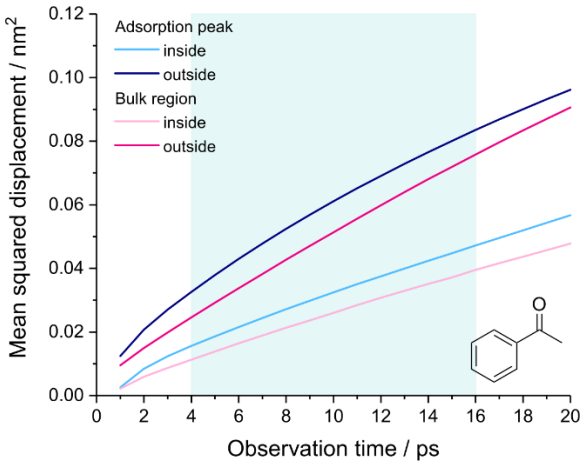

Figure 2.S3. Mean squared displacement of acetophenone molecules in the adsorption peak (density maximum) and in the bulk liquid region at the inner curved and outer planar surface. Surface-parallel diffusion coefficients were calculated from the data in the light blue box.

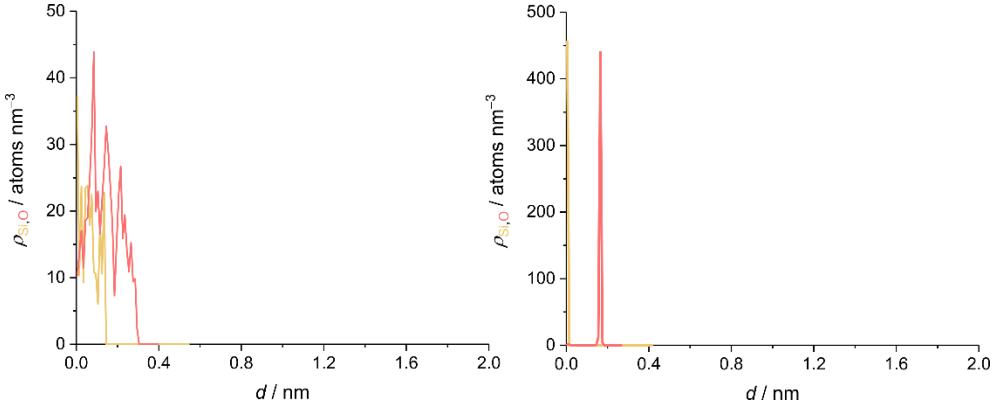

Figure 2.S4. Density profiles for the Si and O atoms (yellow and red, respectively) at the inner curved (left) and planar outside surface (right).

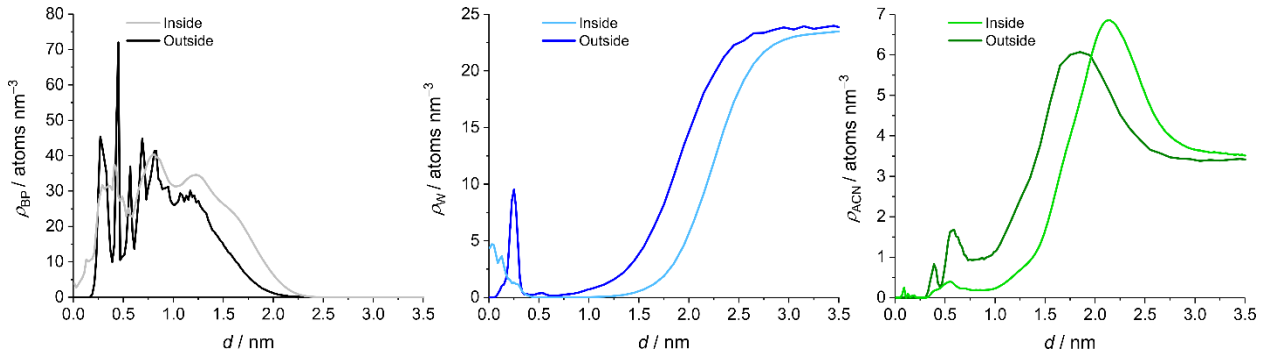

Figure 2.S5. Comparison of total bonded-phase (left), W (middle), and ACN density profiles (right) at the inner curved and outer planar surface.

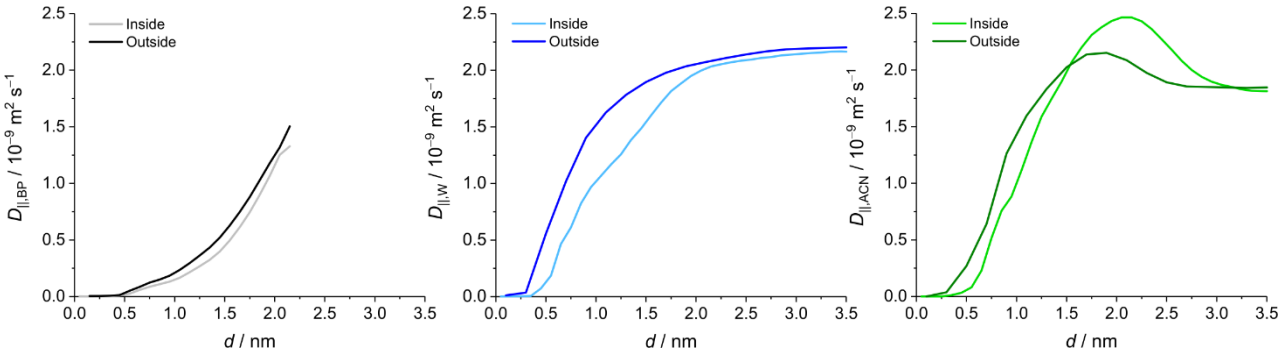

Figure 2.S6. Comparison of total bonded-phase (left), W (middle), and ACN surface-parallel diffusivity profiles (right) at the inner curved and outer planar surface.

Acknowledgments

This work was supported by the Deutsche Forschungsgemeinschaft DFG (Bonn, Germany) under grant TA 268/11-1. Simulations were performed on the supercomputer ForHLR II funded by the Ministry of Science, Research and the Arts Baden-Württemberg and by the Federal Ministry of Education and Research under the project acronym RPLCMD.

References

1 K. Broeckhoven, G. Desmet, *Anal. Chem.* **2021**, *93*, 257–272.
2 D. V. McCalley, *J. Chromatogr. A* **2017**, *1523*, 49–71.
3 P. Žuvela, M. Skoczylas, J. J. Liu, T. Bączek, R. Kaliszan, M. W. Wong, B. Buszewsk, K. Héberger, *Chem. Rev.* **2019**, *119*, 3674–3729.
4 R. K. Lindsey, J. L. Rafferty, B. L. Eggimann, J. I. Siepmann, M. R. Schure, *J. Chromatogr. A* **2013**, *1287*, 60–82.
5 J. Rybka, A. Höltzel, U. Tallarek, *J. Phys. Chem. C* **2017**, *121*, 17907–17920.

6 K. El Hage, P.K. Gupta, R.J. Bemish, M. Meuwly, *J. Phys. Chem. Lett.* **2017**, *8*, 4600–4607.

7 K. El Hage, R. J. Bemish, M. Meuwly, *Phys. Chem. Chem. Phys.* **2018**, *20*, 18610–18622.

8 J. Rybka, A. Höltzel, A. Steinhoff, U. Tallarek, *J. Phys. Chem. C* **2019**, *123*, 3672–3681.

9 L. Zhang, J. L. Rafferty, J. I. Siepmann, B. Chen, M. R. Schure, *J. Chromatogr. A* **2006**, *1126*, 219–231.

10 A. Fouqueau, M. Meuwly, R. J. Bemish, *J. Phys. Chem. B* **2007**, *111*, 10208–10216.

11 J. L. Rafferty, J. I. Siepmann, M. R. Schure, *Anal. Chem.* **2008**, *80*, 6214–6221.

12 J. L. Rafferty, J. I. Siepmann, M. R. Schure, *J. Chromatogr. A* **2008**, *1204*, 11–19.

13 J. Braun, A. Fouqueau, R. J. Bemish, M. Meuwly, *Phys. Chem. Chem. Phys.* **2008**, *10*, 4765–4777.

14 J. L. Rafferty, J. I. Siepmann, M. R. Schure, *J. Chromatogr. A* **2011**, *1218*, 2203–2213.

15 J. L. Rafferty, J. I. Siepmann, M. R. Schure, *J. Chromatogr. A* **2012**, *1223*, 24–34.

16 P. K. Gupta, M. Meuwly, *J. Phys. Chem. B* **2012**, *116*, 10951–10959.

17 J. Rybka, A. Höltzel, N. Trebel, U. Tallarek, *J. Phys. Chem. C* **2019**, *123*, 21617–21628.

18 J. L. Rafferty, L. Zhang, J. I. Siepmann, M. R. Schure, *Anal. Chem.* **2007**, *79*, 6551–6558.

19 J. L. Rafferty, J. I. Siepmann, M. R. Schure, *J. Chromatogr. A* **2008**, *1204*, 20–27.

20 J. L. Rafferty, J. I. Siepmann, M. R. Schure, *J. Chromatogr. A* **2011**, *1218*, 9183–9193.

21 N. Trebel, A. Höltzel, A. Steinhoff, U. Tallarek, *J. Chromatogr. A* **2021**, *1640*, 461958.

22 F. Gritti, G. Guiochon, *AIChE J.* **2011**, *57*, 333–345.

23 F. Gritti, G. Guiochon, *J. Chromatogr. A* **2013**, *1297*, 85–95.

24 J. Rybka, A. Höltzel, S. M. Melnikov, A. Seidel-Morgenstern, U. Tallarek, *Fluid Phase Equilib.* **2016**, *407*, 177–187.

25 U. Tallarek, D. Hlushkou, J. Rybka, A. Höltzel, *J. Phys. Chem. C* **2019**, *123*, 15099–15112.

26 T. S. Gulmen, W. H. Thompson, *Langmuir* **2009**, *25*, 1103–1111.

27 R. Busselez, R. Lefort, Q. Ji, F. Affouard, D. Morineau, *Phys. Chem. Chem. Phys.* **2009**, *11*, 11127–11133.

28 J. Rodrigues, M. D. Elola, D. Laria, *J. Phys. Chem. B* **2010**, *114*, 7900–7908.

29 M. D. Elola, J. Rodriguez, D. Laria, *J. Chem. Phys.* **2010**, *133*, 154707.

30 B. Coasne, J. T. Fourkas, *J. Phys. Chem. C* **2011**, *115*, 15471–15479.

31 S. M. Melnikov, A. Höltzel, A. Seidel-Morgenstern, U. Tallarek, *Anal. Chem.* **2011**, *83*, 2569–2575.

32 A. Ghoufi, I. Hureau, D. Morineau, R. Renou, A. Szymcyzk, *J. Phys. Chem. C* **2013**, *117*, 15203–15212.
33 C. D. Norton, W. H. Thompson, *J. Phys. Chem. C* **2013**, *117*, 19107–19114.
34 T. T. B. Le, A. Striolo, S. S. Gautam, D. R. Cole, *Langmuir* **2017**, *33*, 11310–11320.
35 W. H. Thompson, *J. Chem. Phys.* **2018**, *149*, 170901.
36 M. D. Elola, J. Rodriguez, *J. Phys. Chem. C* **2019**, *123*, 3622–3633.
37 J. L. Rafferty, J. I. Siepmann, M. R. Schure, *J. Chromatogr. A* **2009**, *1216*, 2320–2331.
38 S. M. Melnikov, A. Höltzel, A. Seidel-Morgenstern, U. Tallarek, *Angew. Chem. Int. Ed.* **2012**, *51*, 6251–6254.
39 S. M. Melnikov, A. Höltzel, A. Seidel-Morgenstern, U. Tallarek, *Anal. Chem.* **2013**, *85*, 8850–8856.
40 Q. P. Chen, M. R. Schure, J. I. Siepmann, *J. Chromatogr. A* **2018**, *1573*, 78–86.
41 R. S. Maier, M. R. Schure, *Chem. Eng. Sci.* **2018**, *185*, 243–255.
42 N. D. Zhuravlev, I. J. Siepmann, M. R. Schure, *Anal. Chem.* **2001**, *73*, 4006–4011.
43 Y. Han, I. I. Slowing, J. W. Evans, *J. Chem. Phys.* **2020**, *153*, 124708.
44 H. Kraus, J. Rybka, A. Höltzel, N. Trebel, U. Tallarek, N. Hansen, *Mol. Simul.* **2021**, *47*, 306–316.
45 F. Gritti, G. Guiochon, *J. Chromatogr. A* **2005**, *1099*, 1–42.
46 F. Gritti, G. Guiochon, *Anal. Chem.* **2006**, *78*, 5823-5834.
47 S. M. Melnikov, A. Höltzel, A. Seidel-Morgenstern, U. Tallarek, *J. Phys. Chem. C* **2013**, *117*, 6620–6631.
48 R. D. Mountain, *J. Phys. Chem. C* **2013**, *117*, 3923–3929.
49 B. Coasne, F. Di Renzo, A. Galarneau, R. J.-M. Pellenq, *Langmuir* **2008**, *24*, 7285–7293.
50 T. S. Gulmen, W. H. Thompson, *Langmuir* **2006**, *22*, 10919–10923.
51 M. G. Marin, J. I. Siepmann, *J. Phys. Chem. B* **1998**, *102*, 2569–2577.
52 C. D. Wick, J. M. Stubbs, N. Rai, J. I. Siepmann, *J. Phys. Chem. B* **2005**, *109*, 18974–18982.
53 H. J. C. Berendsen, J. R. Grigera, T. P. Straatsma, *J. Phys. Chem.* **1987**, *91*, 6269–6271.
54 K. Vanommeslaeghe, E. Hatcher, C. Acharya, S. Kundu, S. Zhong, J. Shim, E. Darian, O. Guvench, P. Lopes, I. Vorobyov, A.D. Mackerell Jr., *J. Comput. Chem.* **2010**, *31*, 671–690.
55 F. Gritti, G. Guiochon, *AIChE* **2011**, *57*, 346–358.
56 B. Hess, C. Kutzner, D. van der Spoel, E. Lindahl, *J. Chem. Theory Comput.* **2008**, *4*, 435–447.
57 M. J. Abraham, T. Murtola, R. Schulz, S. Páll, J. C. Smith, B. Hess, E. Lindahl, *SoftwareX* **2015**, *1–2*, 19–25.
58 U. Essmann, L. Perera, M. L. Berkowitz, T. Darden, H. Lee, L. G. Pedersen, *J. Chem. Phys.* **1995**, *103*, 8577–8593.

59 J. Rybka, J. Kärger, U. Tallarek, *ChemPhysChem* **2017**, *18*, 2094–2102.
60 P. Liu, E. Harder, B. J. Berne, *J. Phys. Chem. B* **2004**, *108*, 6595–6602.
61 I. Bacskay, A. Sepsey, A. Felinger, *J. Chromatogr. A* **2014**, *1339*, 110–117.
62 S.-J. Reich, A. Svidrytski, A. Höltzel, W. Wang, C. Kübel, D. Hlushkou, U. Tallarek, *Microporous Mesoporous Mater.* **2019**, *282*, 188–196.
63 F. Gritti, *Anal. Chem.* **2021**, *93*, 5653–5664.

Chapter 3

Confinement Effects on Distribution and Transport of Neutral Solutes in a Small Hydrophobic Nanopore

Authors

Nicole Trebel, Alexandra Höltzel, Ulrich Tallarek

State of publication

Published 23 September 2022 in *Journal of Physical Chemistry B*, Vol. 126, pp. 7781–7795.
DOI: 10.1021/acs.jpcb.2c04924

Table of content

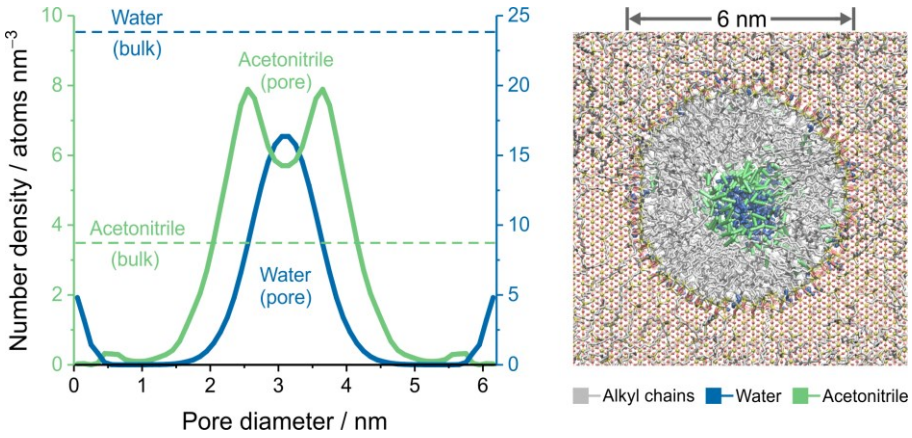

Abstract

Molecular dynamics simulations are used to study confinement effects in small cylindrical silica pores with extended hydrophobic surface functionalization as realized, for example, in reversed-phase liquid chromatography (RPLC) columns. In particular, we use a 6 nm cylindrical and a 10 nm slit pore bearing the same C_{18} stationary phase to compare the conditions inside the smaller-than-average pores within an RPLC column to column-averaged properties. Two small, neutral, apolar to moderately polar solutes are used to assess the consequences of spatial confinement for typical RPLC analytes with water (W)–acetonitrile (ACN) mobile phases at W/ACN ratios between 70/30 and 10/90 (v/v). The simulated data show that true bulk liquid behavior, as observed over an extended center region in the 10 nm slit pore, is not recovered within the 6 nm cylindrical pore. Instead, the ACN-enriched solvent layer around the C_{18} chain ends (the ACN ditch), a general

feature of hydrophobic interfaces equilibrated with aqueous–organic liquids, extends over the entire pore lumen of the small cylindrical pore. This renders the entire pore a highly hydrophobic environment, where, contrary to column-averaged behavior, neither the local nor the pore-averaged sorption and diffusion of analytes scales directly with the W/ACN ratio of the mobile phase. Additionally, the solute polarity-related discrimination between analytes is enhanced. The consequences of local ACN ditch overlap in RPLC columns are reminiscent of ion transport in porous media with charged surfaces, where electrical double layer overlap occurring locally in smaller pores leads to discrimination between co- and counterionic species.

3.1 Introduction

The selective sorption, diffusion, and resulting effective transport properties of liquids, simple ions, small solutes, macromolecules, and nanoparticles in nanometer-sized pores or channels (with characteristic diameters or conduit widths between ~1 and 100 nm) play a central role in many natural and technological processes related to sensing, energy conversion, catalysis, and separation science.[1–12] Effective transport properties are easily tailored through several critical principles available for the tuning of highly specific interactions between diffusant and the pore environment. This addresses especially electrostatic, steric, and (non)polar interactions, as well as host–guest (e.g., chiral) recognition.[13] These fundamentally different interaction motifs have evolved into mature and robust chemical separation techniques, namely, ion exchange and ion exclusion, size exclusion, normal-phase and reversed-phase as well as affinity liquid chromatography.[14]

In recent years, molecular simulations have become a highly attractive approach to analyze coupled transports in single nanopores and nanoporous materials with respect to their constituent contributions.[15–22] Because molecular simulations offer unprecedented insights into the interfacial dynamics resulting from the solute–solvent–surface interactions, they are key to unravel the fundamentals of separation and transport processes and to shape and refine the design principles for nanofiltration membranes,[23] supercapacitors,[24] catalysts,[25] and stationary phases for liquid chromatography.[26] The derived molecular-level picture can be subsequently embedded into multiscale simulation approaches that reproduce and even predict macroscopic behavior (e.g., the process performance).[27–32] If combined with physical reconstruction of the pore space morphology by tomographic methods, multiscale simulation approaches enable an unusually detailed and accurate unterstanding of the interplay between morphological properties, interfacial dynamics, and solute transport.[33]

The interfacial dynamics in a nanopore vary with the experimental conditions under which a process is performed. A particularly interesting situation arises when the physical scaling length of the liquid saturating the pore approaches its diameter. For electrostatic interactions, for example, the relevant scaling length is the extension of the electrical double layer.[34,35] When the double layer thickness approaches the pore diameter, the local electrical potential, which drops with increasing distance from the pore wall, does not recover the electrical potential of the bulk, electroneutral, electrolyte solution in the pore center, a situation referred to as double layer overlap. Because the electrical potential (of the same sign as the surface potential) extends over the complete pore cross-

section, the whole nanopore becomes ion-permselective: it enriches counterions and excludes co-ions. At electrochemical equilibrium, an electrical phase-boundary potential (Donnan potential) balances the tendency of ionic species to level out chemical potential gradients (i.e., the tendency of counterions to leave the pore and that of co-ions to enter it). The counterionic mobile space charge is then smeared over the complete pore cross-section by the thermal motion of the ions.

Ion-permselective transport often is a desirable property of porous media, such as in membrane science[36] or certain modes of liquid chromatography.[37] The transition from charge-nonselective to charge-selective behavior is realized simply by enforcing spatial confinement effects through reducing the pore size at constant ionic strength of the liquid. In a chromatographic column, for example, the double layer thickness is much smaller than the micrometer-sized pores between the particles in a chromatographic bed, but comparable to the nanometer-sized intraparticle pores.[38] In the micrometer-sized pores, the electrical double layer is confined to a thin region at the surface, so that most of the pore liquid is quasi-electroneutral. The micrometer-sized pores are not charge-selective and do not discriminate between counterionic and co-ionic species. Effects caused by the relatively strong interactions between charged species of the background electrolyte (e.g., buffer ions) and charged surfaces inside pores of varying size are at the heart of ion exchange chromatography[39] and critical to analyte transport in ion chromatography.[40]

Another important mode of liquid chromatography, where a phenomenon similar to double layer overlap occurs, is reversed-phase liquid chromatography (RPLC).[14,41] In RPLC, the hydrophobic bonded phase, typically octadecylsilane (C_{18}) chains, is tethered to the silica surface of the inter- and intraparticle pores in the chromatographic bed. Equilibration of the RPLC column with the aqueous–organic mobile phase, often water–acetonitrile (W–ACN) mixtures, results in formation of the chromatographic interface.[26] At the molecular level, column equilibration reconciliates the exisiting hydrophobicity differences in the system through adapting the solvent distribution to the local conditions. The residual hydroxylation of the silica surface is shielded from the hydrophobic bonded phase by an adsorbed solvent layer of first W and then ACN molecules, and the hydrogen-bond network of the W–ACN mobile phase is shielded from the hydrophobic bonded phase by an ACN-enriched solvent layer around the chain ends, referred to as the ACN ditch.[42] Although charges may be part of an RPLC system (in form of residual charges on the silica surface, protonated or deprotonated analytes, and buffer ions in the mobile phase), they are not prerequisite to formation of the ACN ditch.

Considering the wide pore size distributions of the amorphous silica materials used for chromatographic columns, ACN ditch overlap is bound to occur within the chromatographic bed. RPLC columns intended for small molecule separations typically have average pore sizes of 9–12 nm with relative standard deviations of 30–50%.[43] The column therefore contains a significant fraction of smaller-than-average intraparticle pores where ACN ditch overlap is probable. Because the ACN ditch is crucial to the favorable mass transport characteristics of RPLC by providing a low viscosity environment (compared with the bulk mobile phase) that favors the diffusivity of small, apolar to moderately polar molecules,[44–47] ACN ditch overlap can be expected to affect the local transport properties within the chromatographic bed. To our knowledge, however, the

consequences of ACN ditch overlap within an RPLC column for solute transport have not been considered so far.

In this molecular dynamics (MD) simulation study, we investigate the conditions inside a small cylindrical RPLC pore of 6 nm diameter (Figure 3.1) for mobile phases of 70/30 to 10/90 (v/v) W/ACN and their impact on the distribution, sorption, and diffusive mobility of an apolar and a moderately polar solute (ethylbenzene and acetophenone, respectively). The cross-sectional ACN density profiles (green lines in Figure 3.1) show that a bulk liquid region with the nominal solvent composition of the contacting mobile phase, here represented by the ACN density in the bulk liquid, $\rho_{ACN,bulk}$ (red line), is missing in the 6 nm cylindrical pore. Instead, the ACN ditch extends over the most of the pore lumen. This implies that the actual pore curvature exerts an influence on both position and intensity of the ditch, likely supported by a conformational change of the surface-tethered C_{18} chains (light gray in Figure 3.1) with respect to a planar silica surface.[48,49]

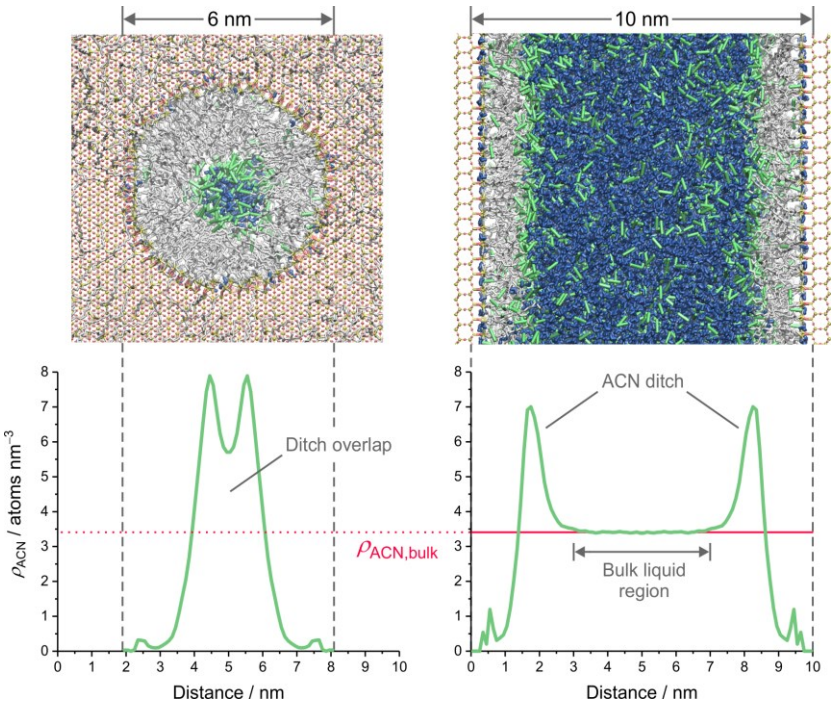

Figure 3.1. (Top) Snapshots of the RPLC pore models with cylindrical and slit geometry (left and right, respectively) when equilibrated with a mobile phase of 70/30 (v/v) W/ACN. The bare silica surface is functionalized with C_{18} chains and endcapping groups. (Bottom) ACN number density profiles for the two systems (ρ_{ACN}, green lines) are adjusted to the pore diameter (6 nm) and pore width (10 nm). Vertical dashed lines (gray) mark the innermost layer of surface Si atoms, and the red horizontal line (solid and dotted) indicates the ACN density in the bulk mobile phase ($\rho_{ACN,bulk}$), which is attained over a ~4 nm wide central region in the slit pore. Color code adapted in the snapshots: W and ACN molecules, dark blue and green sticks, respectively; united-atom groups of C_{18} chains and endcapping groups, gray sticks; Si, O, and H atoms of the silica surface, yellow, red, and white sticks, respectively; and Si and O atoms of the solid, impermeable silica block, yellow and red balls, respectively.

The interfacial dynamics inside the small cylindrical RPLC pore are assessed by comparison with a standard RPLC slit pore (Figure 3.1). The rationale for this is based on earlier work,[46] where we demonstrated for simple analytes, including ethylbenzene and acetophenone, that the standard RPLC slit-pore model reproduced experimental retention data acquired on an RPLC column over the complete range of W/ACN ratios encountered in RPLC practice. The column contains positive and negative surface curvature of different degrees, and the 10 nm slit pore is assumed to represent column-averaged data,[26,46] whereas the 6 nm cylindrical pore represents a tiny piece of a porous particle inside the column. We determine how the solvent and analyte distributions and mobilities in the narrow cylindrical pore, with its strong curvature and substantial ACN ditch overlap, differ from those in larger pores, where ACN ditch overlap does not occur and bulk liquid properties are attained in the pore center. Finally, we highlight the consequences of ACN ditch overlap for pore-averaged transport in dependence of the W/ACN ratio of the mobile phase and analyte properties.

3.2 Computational methods

3.2.1 Simulation systems

3.2.1.1 Cylindrical pore model

Generation of the cylindrical pore model was accomplished by a preliminary version of the object-oriented program PoreMS[50] and includes the following steps: (i) building a rectangular β-cristobalite SiO_2 structure with user-specified *xyz*-dimensions by repetitively extending the smallest possible grid unit of Si and O atoms; (ii) carving a cylindrical pore shape along a user-specified drill axis; (iii) full hydroxylation of the silica surface following the rules described by Coasne et al.[51] For this study, surface functionalization was carried out manually, but this feature is meanwhile supported by the current version of PoreMS.

For the cylindrical pore model in this work, we targeted a pore length and pore diameter of 10 and 6 nm, respectively. To ensure a realistic solvent equilibration process for such a narrow pore (expecting that a bulk liquid region will not be realized in the pore center, cf. Figure 3.1), we also specified 5 nm wide solvent reservoirs on both sides of the silica block. The drill axis for pore carving was aligned in *z*-direction to the simulation box center, yielding a cylindrical silica pore of 3.09 ± 0.15 nm radius inside a silica block of $14.17 \times 14.03 \times 9.61$ nm^3 (*xyz*) size between 5.53 nm wide adjoining solvent reservoirs. The carving process generates a certain surface roughness, which is visualized in Figure 3.2 that shows the Si and O atom density profiles at the inner cylindrical surface (left panel) and at the planar silica surface of the slit pore (right panel). To produce surface-related distance plots inside the cylinder, the *xy*-center of the simulation box was used as the pore axis. The distance *d* from the silica surface was then obtained by subtracting the average pore radius of 3.1 nm from the distance between the actual position and the pore axis. For the slit pore, *d* refers to the distance between the *z*-coordinate and the position of the innermost layer of Si atoms.

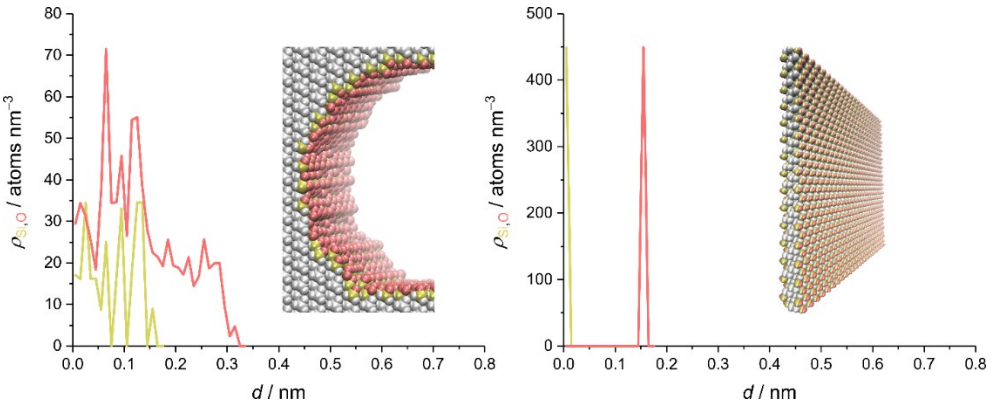

Figure 3.2. Density distribution of silica surface atoms inside the 6 nm cylindrical pore (left) and the slit pore (right) together with snapshots of the corresponding unfunctionalized silica surface. Si and O surface atoms are colored dark yellow and red, respectively; Si and O lattice atoms are shown in light gray. Surface atoms at the outer planar surface of the cylindrical pore model were omitted for clarity.

As pore carving generates a higher degree of surface hydroxylation than cutting parallel to a crystalline surface, the difference between inner and outer surface hydroxylation was first reduced by siloxane bridge formation at the inner curved surface (cf. Table 3.1). We then randomly grafted C_{18} chains as the main ligand and trimethyl silane (C_1) groups for endcapping onto the inner and outer silica surface at representative densities and bonded-phase coverages informed by RPLC columns for small molecule separations.[52] Functionalization of the outer surface is important to ensure RPLC conditions for solutes that travel from the outside reservoirs into the cylindrical pore.

Table 3.1. Silica surface functionalization in the 6 nm cylindrical and the slit pore model.

surface group	surface density (µmol m^{-2})		
	inner curved[a]	outer planar[a]	slit pore[a]
hydroxylation after pore carving	9.61	7.73	7.46
hydroxylation after siloxane bridge formation	8.74	7.73	7.46
C_{18} chains	2.87	2.95	3.11
endcapping groups	1.77	1.29	0.93
residual hydroxylation	4.10	3.49	3.42
bonded-phase coverage	53%	55%	54%

[a] Surface area: $A_{\text{inner,curved}} = 187$ nm^2, $A_{\text{outer,planar}} = 2 \times 169$ nm^2, and $A_{\text{slit pore}} = 2 \times 160$ nm^2.

3.2.1.2 Slit pore model

The slit pore model was generated as described earlier[42] by placing a three-layered silica slab (0.93 nm wide in *z*-direction) in the center of a quadrilateral simulation box with dimensions of 12.14 × 13.20 × 10.93 nm^3 (*xyz*). The empty volume at each side of the central slab is used as 5 nm wide solvent reservoirs. Applying periodic boundary conditions to the model generates the 10 nm wide slit pore seen in Figure 3.1. The slab was created from the (111) face of β-cristobalite SiO_2, which results in the narrow density distribution of surface Si and O atoms shown in Figure 3.2. The planar silica surface was randomly grafted with C_{18} chains and C_1 groups as stated in Table 3.1.
Please note that although the main ligand densities, endcapping densities, and residual surface hydroxylations of the three surfaces are not identical, they can be regarded as highly similar. In chromatographic practice, detectable differences in separation outcome between RPLC columns with these functionalizations would not be expected.

3.2.2 Force field parameters

Force field parameters from Gulmen and Thompson were taken for the silica surface atoms (Si, O, and H).[53] C_{18} chains and C_1 endcapping groups as well as ACN molecules were described by the transferable potentials for phase equilibria united-atom (TraPPE-UA) force field.[54,55] For W molecules, the simple point charge/extended (SPC/E) force field was used.[56] Ethylbenzene and acetophenone were described by the explicit CHARMM general force field (CGenFF).[57] Earlier validation of our force field combination[58] has shown it to be consistent with available experimental RPLC data. More specifically, we can reproduce the relationship between analyte retention and molecular properties as well as the dependence of analyte retention on the ACN volume fraction in the mobile phase.[46] Further, the surface diffusion of RPLC analytes simulated with this force field combination[45–47,49,58] was successfully explained and predicted according to available experimental data.[59,60]

3.2.3 Simulation details

MD simulations of the cylindrical pore systems were carried out using the GROMACS (Groningen Machine for Chemical Simulation) software version 2019.6[61,62] for a canonical *NVT* ensemble (constant number of molecules *N*, simulation box volume *V*, and temperature *T*) at a temperature of 300 K. To cover the behavior of an apolar and a moderately polar solute over the range from W-rich to ACN-rich mobile phases, the analytes ethylbenzene and acetophenone were each simulated at four W/ACN (v/v) ratios (70/30, 50/50, 30/70, and 10/90) of the mobile phase. Because the small cylindrical pore does not allow for a bulk liquid region (cf. Figure 3.1), system equilibration with the mobile phase was monitored in the bulk region of the adjacent solvent reservoirs. The solvent densities in the bulk region of the solvent reservoirs were monitored for 100 ns after reaching the targeted W/ACN to ensure complete equilibration of outer and inner pore space. The simulation box contained 15 analyte molecules; the exact number of solvent molecules in the simulation box

for each W/ACN ratio of the mobile phase is listed in Table 3.S1. Figure 3.3 shows a side view of the simulation box equilibrated with a mobile phase of 70/30 (v/v) W/ACN. Figure 3.S1 in the Supporting Information contains complementary snapshots of both pore geometries, including relevant dimensions and coordinate axes.

Besides illustrating the simulation box dimensions in *z*-direction, this snapshot captures the formation of the ACN ditch in the adjoining outer reservoirs and, more importantly, highlights the direct and constant interaction between outer planar and inner curved surface, which was already described for an average-sized cylindrical RPLC pore (9 nm diameter) in a previous study.[49]

Slit pore data were extracted from trajectories previously simulated at 300 K for the two analytes at the W/ACN ratios mentioned above.[46]

Energy minimization was conducted with the steepest descent method and initial velocities were randomly assigned and obtained from a Maxwell–Boltzmann distribution. Long-range electrostatic interactions were provided by the particle-mesh Ewald algorithm,[63] and nonbonded interactions were modeled with a 12–6 Lennard-Jones potential. Lennard-Jones parameters for unlike interactions were treated with the Lorentz–Berthelot combination rules. A cutoff radius of 1.4 nm, validated earlier,[42] was used for all interactions. Simulations were run on the high-performance computer HoreKa of the Steinbuch Center for Computing at the Karlsruhe Institute of Technology (Karlsruhe, Germany). After an equilibration period of 100 ns, productive simulations were performed for up to 1 µs with a 1 fs time step for integrating the equations of motion, setting the output frequency to 0.5 ps.

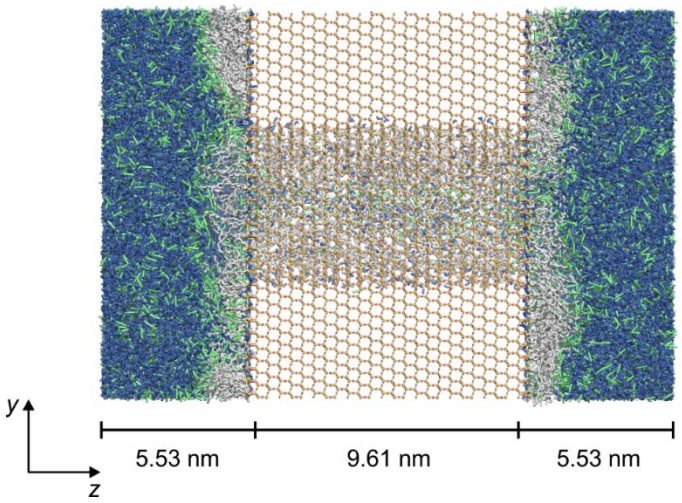

Figure 3.3. Side view of the simulation box with *z*-dimensions of the 6 nm cylindrical pore and the solvent reservoirs after equilibration with a mobile phase of 70/30 (v/v) W/ACN, realized in the bulk region of the solvent reservoirs. Si and O atoms of the silica block are represented by yellow and red balls, respectively, and Si, O, and H atoms of the silica surface as yellow, red, and white sticks, respectively; united-atom groups of the bonded phase (C_{18} chains and C_1 endcapping groups) are shown as gray sticks; W and ACN molecules are shown as dark blue and green sticks, respectively.

3.2.4 Data analysis

For analysis of data from the cylindrical pore, two 0.5 nm wide cylindrical segments (in *z*-direction) at each entrance were discarded from the calculations to eliminate edge effects at the pore entrance zone.

3.2.4.1 Density profiles

For the calculation of density profiles, we first specified a bin width and counted the number of atoms, atom groups, or molecules in each bin over the chosen time span. This count was then normalized to the respective bin volume and observation time. Bonded-phase and solvent density profiles (based on the atom number densities of the CH_2 and CH_3 united-atom groups of the bonded phase, the O atom of W, and the central C atom of ACN) were calculated from 40 ns trajectories with a bin size of 0.02 and 0.1 nm, respectively. Analyte density profiles based on the center-of-mass (cms) of the analyte molecules were calculated from the complete trajectories using a 0.05 nm bin size.

3.2.4.2 Surface-parallel-and-pore-averaged diffusion coefficients

Distance-dependent diffusion coefficients $D_{\parallel}(d)$ were calculated as in our previous MD studies following an approach by Liu et al.[64] Mean squared displacements of bonded-phase groups, solvent, and analyte molecules were repeatedly recorded as $\langle r^2(t)\rangle = \langle z^2(t)\rangle$ inside the cylindrical pore and as $\langle r^2(t)\rangle = \langle x^2(t) + y^2(t)\rangle$ in the slit pore during 20 ps time intervals shifted consecutively in 0.5 ps time steps. For spatial resolution, a maximum shift of ±0.3 nm around the initial *d*-position during the observation interval was allowed or the displacement discarded otherwise. $D_{\parallel}(d)$ of the bonded-phase groups, solvent, and analyte molecules were calculated from the linear slope of the observation curve (t = 4–16 ps) according to the Einstein equation:

$$D_{\parallel}(d) = \frac{1}{2}\frac{\mathrm{d}\langle r^2(t)\rangle}{\mathrm{d}t} \quad \text{(cylindrical pore) and} \tag{3.1}$$

$$D_{\parallel}(d) = \frac{1}{4}\frac{\mathrm{d}\langle r^2(t)\rangle}{\mathrm{d}t} \quad \text{(slit pore),} \tag{3.2}$$

using bin sizes of 0.01 nm inside the cylindrical pore and of 0.02 nm in the slit pore. Figure 3.4 shows log–log plots of the mean squared displacements of ethylbenzene and acetophenone molecules for 70/30 and 30/70 (v/v) W/ACN, proving that a 20 ps observation time is sufficient to establish diffusive motion. Following GROMACS procedure,[65] an error estimate of $D_{\parallel}(d)$ was calculated as the difference of the diffusion coefficients obtained from the mean-squared displacement curve over the two halves of the fit interval (i.e., 4–10 and 10–16 ps). While Figure 3.4 exemplarily shows the mean squared displacements of analyte molecules at their mobility maximum in the cylindrical pore, the slope of these displacement curves generally varies with the distance from the surface in both pore geometries, reflecting spatially-dependent mobility. Mobility profiles of individual alkyl groups in the C_{18} chains, ACN molecules, and analyte molecules are

discussed in detail below (Figures 3.7, 3.8, and 3.12, respectively). Uncertainty estimates for the calculated $D_{\|}(d)$-values are in the range of ±0.01–0.22 (C_{18}), ±0.01–0.16 (ACN), and ±0.02–0.20 (analytes).

The pore-averaged mobility was calculated using the following equations:

$$\langle D_{\|} \rangle = \frac{\int \rho(r) D_{\|}(r) r \, \mathrm{d}r}{\int \rho(r) \, r \mathrm{d}r} \quad \text{(cylindrical pore) and} \tag{3.3}$$

$$\langle D_{\|} \rangle = \frac{\int \rho(d) D_{\|}(d) \mathrm{d}d}{\int \rho(d) \, \mathrm{d}d} \quad \text{(slit pore),} \tag{3.4}$$

where r and d denote, respectively, the radial position from the center of the cylindrical pore and the distance from the silica surface in the slit pore. Uncertainty estimates for the calculated $\langle D_{\|} \rangle$-values are in the range of ±0.09–0.11 (ACN, Figure 3.9) and ±0.07–0.18 (analytes, Figure 3.13).

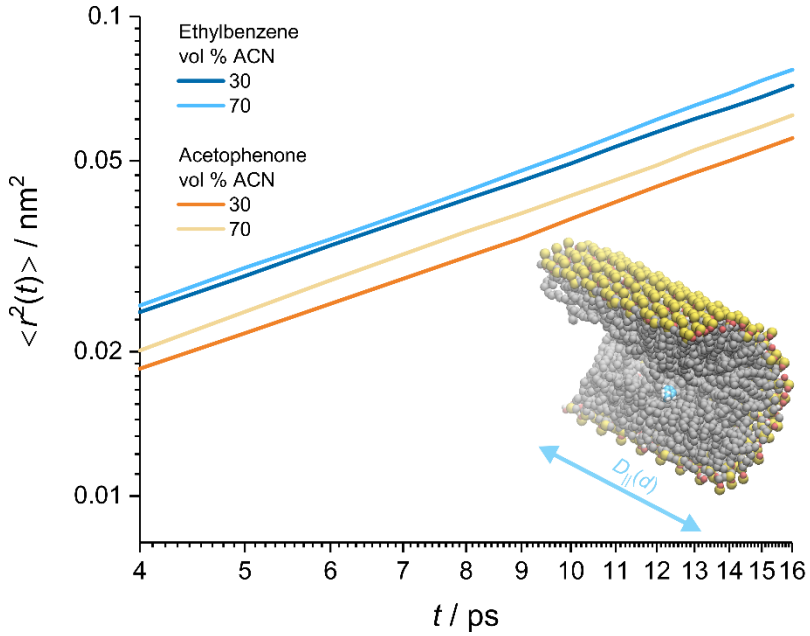

Figure 3.4. Log–log plots of the mean squared displacements of ethylbenzene and acetophenone molecules at their mobility maximum inside the cylindrical pore for two W/ACN ratios of the mobile phase. The snapshot visualizes the surface diffusion of an ethylbenzene molecule parallel to the curved surface (i.e., along the pore axis). Solvent molecules were omitted for better visibility. Color code adapted in the snapshot: Si and O surface atoms, yellow and red, respectively; united-atom groups of the bonded phase, gray; C and H atoms of ethylbenzene, light blue and white, respectively.

3.3 Results and discussion

3.3.1 Solvent and bonded-phase distribution and mobility

Returning to the central picture of pore-level ACN ditch overlap introduced in Figure 3.1, we begin Section 3.3 with the evolution of the solvent density distribution depending on the W/ACN ratio

of the mobile phase (Figure 3.5, bottom to top profiles for ACN and top to bottom profiles for W). Solvent distributions are shown from the silica surface up to the pore center of the cylindrical pore (at d = 3.09 nm), but are terminated after d = 3.5 nm for the slit pore, because this distance is sufficient to reveal the constant solvent density values representing the bulk mobile phase.
Figure 3.5 indicates several important points related to the presence or absence of a bulk liquid region in the pore, the solvent density near the silica surface, the solvent penetration of the C_{18} chains, and the properties of the ACN ditch.

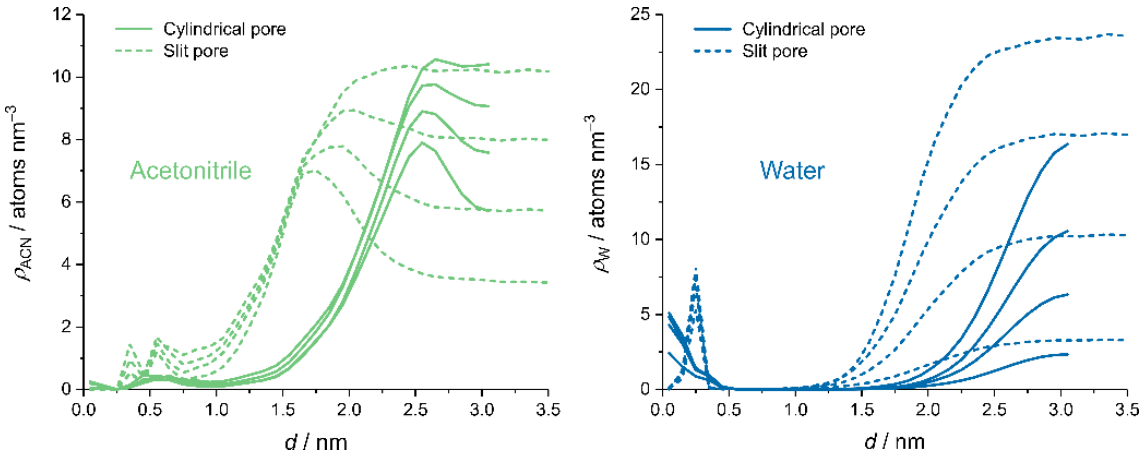

Figure 3.5. Solvent density distributions in the 6 nm cylindrical pore and the slit pore at a mobile phase of 70/30, 50/50, 30/70, and 10/90 (v/v) W/ACN (bottom to top profiles for ACN and, correspondingly, top to bottom profiles for W).

First, the solvent density values of the bulk mobile phase are not recovered in the 6 nm cylindrical pore. In fact, neither the ACN nor the W density even reach constant values in the cylindrical pore, reflecting ACN ditch overlap (aka W depletion) in the small pore. As expected from the evolution of the ACN ditch with the ACN content of the mobile phase,[46] the ditch overlap is most pronounced at 70/30 (v/v) W/ACN and has nearly faded at 10/90 (v/v) W/ACN.
The overall ACN enrichment (or W depletion) in a pore can be quantified by the pore-averaged ACN excess (compared with the ACN content of the mobile phase, Table 3.2), which can be positive or negative. With a mobile phase of 70/30 (v/v) W/ACN, the 6 nm cylindrical pore generates a remarkable +45 vol % ACN excess, more than twice the ACN excess in the slit pore. At 10/90 (v/v) W/ACN, both pores exhibit a small negative ACN excess, demonstrating the vanishing impact of pore size and shape on ACN enrichment at high ACN content of the mobile phase.
Negative ACN excess originates at the silica surface. The first solvent density peaks in the profiles are directly associated with the coordination of residual surface OH groups through silica–solvent hydrogen bonds.[26,45–47] Because silica surface coordination is predominantly carried out by W molecules, even at high ACN volume fraction in the mobile phase,[66] negative ACN excess is then observed.

Table 3.2. Pore-averaged ACN excess.

mobile phase	6 nm cylindrical pore[a]	slit pore[a]
W/ACN (v/v)	ACN excess (vol %)	
70/30	+45	+19
50/50	+30	+12
30/70	+13	+5
10/90	–2	–2

[a] Ratio calculated from the number of solvent molecules in the entire pore volume.

Whereas the solvent peaks at the planar surface of the slit pore are sharply defined and represent a layer of surface-adsorbed solvent (mostly W) molecules and a second layer of ACN molecules that partially coordinate the surface-adsorbed W molecules, the solvent density distribution at the curved surface of the small cylindrical pore is diffuse, reflecting the actual surface roughness (cf. Figure 3.2). In contrast, the higher residual hydroxylation of the cylindrical pore (4.10 vs 3.42 µmol m^{-2} in the slit pore, Table 3.1) has little impact on the solvent density at the surface, because endcapping groups placed on a concave surface are more effective shielders of neighboring OH groups.[49]

A further important observation in Figure 3.5 relates to shape and location of the ACN ditch. Compared with the slit pore, the ditch in the cylindrical pore is sharper, more intense, and shifted much farther away from the surface. At 70/30 (v/v) W/ACN, for example, the ditch maximum of $\rho_{ACN,max}$ = 7.9 atoms nm^{-3} is observed at d = 2.55 nm (lowest solid green line in Figure 3.5), compared with $\rho_{ACN,max}$ = 7.0 atoms nm^{-3} at d = 1.75 nm in the slit pore (lowest dashed green line). The difference in ditch intensity observed between the two pores decreases with increasing ACN content of the bulk mobile phase and has almost disappeared at 10/90 (v/v) W/ACN, with $\rho_{ACN,max}$ =10.6 and 10.4 atoms nm^{-3} in the cylindrical and slit pore, respectively. At the same time, the position of the ACN ditch maximum moves further toward the center of the slit pore (from d = 1.75 nm to 2.45 nm), but shifts comparatively little in the small cylindrical pore (from d = 2.55 nm to 2.65 nm).

To understand the differences in width, height, and location of the ACN ditch between the two pores, we take a closer look at the bonded phase. Figure 3.6 compares the bonded-phase density profiles for the cylindrical (top panel) and the slit pore (bottom panel). An observation immediately relevant to the ditch position is that the C_{18} chains are more extended in the cylindrical pore. Furthermore, as the insets in Figure 3.6 show in more detail, the extension of the C_{18} chains in the cylindrical pore is rather insensitive to the W/ACN ratio of mobile phase.

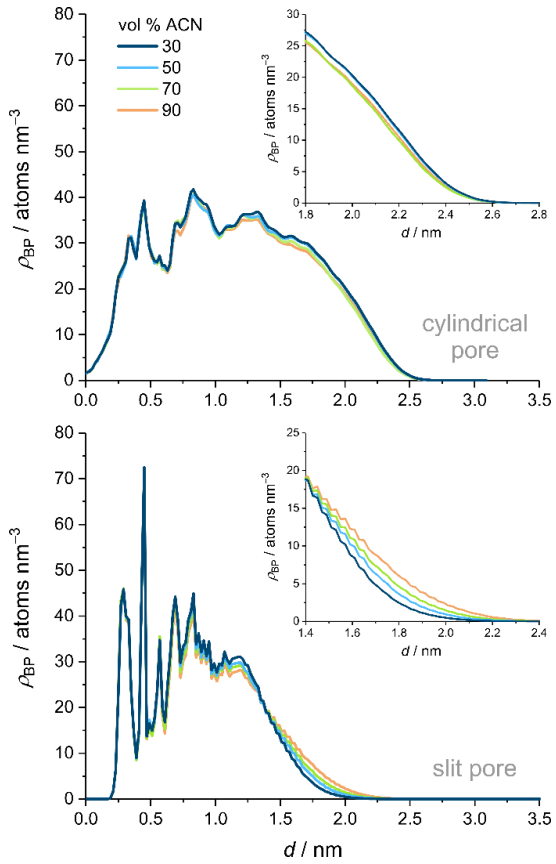

Figure 3.6. Bonded-phase density profiles (C_{18} chains and C_1 endcapping groups) in the 6 nm cylindrical pore (top panel) and the slit pore (bottom panel) at different W/ACN ratios of the mobile phase. Insets highlight the extension of the C_{18} chains toward the pore center (cf. Table 3.3).

The maximum C_{18} chain extension is d_{max} = 2.77 ± 0.02 nm in the small cylindrical pore, but increases systematically in the slit pore with increasing ACN content of the mobile phase, from d_{max} = 2.47 nm at 30/70 (v/v) W/ACN to d_{max} = 2.61 nm with 10/90 (v/v) W/ACN (Table 3.3).

Table 3.3. Maximum extension of C_{18} chains.

mobile phase	6 nm cylindrical pore	slit pore
W/ACN (v/v)	d_{max} (nm)[a]	
70/30	2.79	2.47
50/50	2.75	2.53
30/70	2.77	2.57
10/90	2.77	2.61

[a] Distance d from the surface after which $\rho_{BP}(d) < 10^{-3}$ atoms nm^{-3} in Figure 3.6.

The constrictive forces brought about by pore geometry and size determine the chain extension (via the chain conformation) and thus the bonded-phase density distribution over a distinctive distance. In the slit pore (bottom panel in Figure 3.6), the influence of the pore geometry on the bonded-phase density distribution, recognizable by sharply defined peaks that mirror the planar surface geometry, extends up to $d \approx 1.0$ nm. The sharply defined peaks represent mostly the first chain segment (C1–C6) and the endcapping groups. Most of the C_{18} chain length is not restricted at all in the slit pore, which leads to a slowly decaying bonded-phase density distribution at $d > 1.0$ nm. In the 6 nm cylindrical pore (top panel in Figure 3.6), the bonded-phase density is rather equally distributed over most of the pore diameter, with little to no structure recognizable in the wide peaks. At $d > 1.0$ nm, the cylindrical pore has more bonded-phase density than the slit pore, that is, the cylindrical pore carries a much a larger fraction of its bonded-phase density farther away from the surface and closer to the pore center. The insets in Figure 3.6, which visualize the final and most important part of the bonded-phase density distribution for the ditch, show the sharp contrast between the compact bonded-phase density in the cylindrical pore and the faded-out bonded-density in the slit pore. The compact bonded-phase density in the cylindrical pore makes solvent penetration deeper into the chains less likely and explains why the ACN ditch is located further away from the silica surface than in the slit pore: in the cylindrical pore the ACN ditch is placed in front of dense chain ends, in the slit pore the ACN ditch is placed between frayed chain ends.

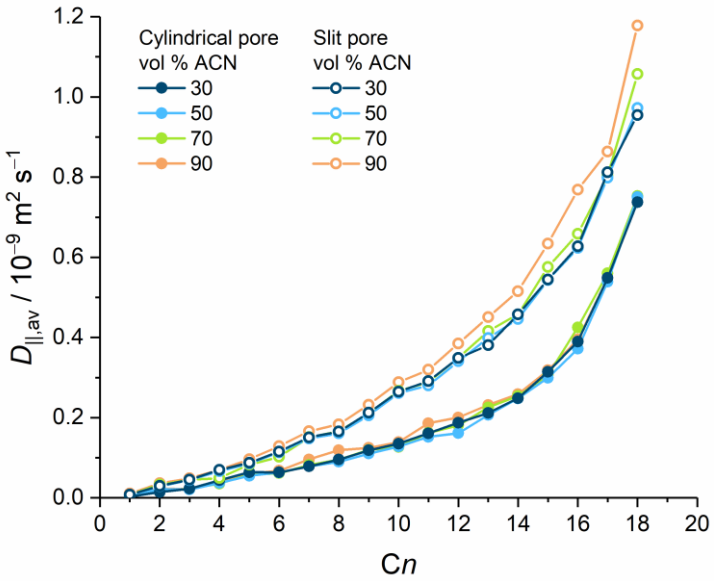

Figure 3.7. Average surface-parallel diffusion coefficients of the individual alkyl groups C*n* in the C_{18} chains in the 6 nm cylindrical pore and the slit pore.

The constrictions of pore geometry and size necessarily apply to the bonded-phase mobility. Figure 3.7 shows the average surface-parallel diffusion coefficients of the individual alkyl groups in the C_{18} chains between the two pores. Generally, the curves reflect that the bonded-phase diffusivity near the silica surface is very restricted ($D_{\parallel,av} < 0.1 \times 10^{-9}$ m^2 s^{-1}) and increases most

steeply between the final three groups (C16–C18) in the chain, which also constitute the main bonded-phase presence in the ditch. Figure 3.7 shows that, as expected, the bonded-phase group diffusivity is consistently lower in the cylindrical pore. The confinement effect is significant: the diffusivity of the C15 group in the cylindrical pore compares to that of the C11 group in the slit pore and is ~50% lower than the C15 group diffusivity in the slit pore. On the other hand, the bonded-phase diffusivity difference between cylindrical and slit pore decreases towards the chain ends, notably for the C17 and C18 groups, because of the higher local ACN excess around these groups in the cylindrical pore, as inspection of Figures 3.5 and 3.6 proves.

Overall, the properties of the ACN ditch in the cylindrical pore can be consistently explained by the higher density (Figure 3.6) and lower mobility (Figure 3.7) of the bonded phase, which (i) acts as a denser physical barrier to solvent molecules, (ii) is more extended and less sensitive to the W/ACN ratio of the mobile phase, and (iii) presents a more hydrophobic interface to solvent molecules, favoring the accumulation of ACN excess.

The increased ACN excess in the cylindrical pore is expected to translate into higher local ACN mobility in the ditch, as confirmed by Figure 3.8, which shows spatially-resolved mobility data for ACN through the surface-parallel diffusion coefficient profiles. Generally, $D_{\parallel,ACN}(d)$-profiles go through a maximum in the ACN ditch, before decreasing steadily over the bonded-phase region to zero at the silica surface.[65] In correspondence with the ACN density profiles from Figure 3.5, the $D_{\parallel,ACN}(d)$-profiles in the small cylindrical pore do not recover bulk behavior toward the pore center, in contrast to the extended horizontal parts of the $D_{\parallel}(d)$-profiles for the slit pore, which reflect the ~4 nm wide bulk liquid region in the pore lumen (cf. Figure 3.1).

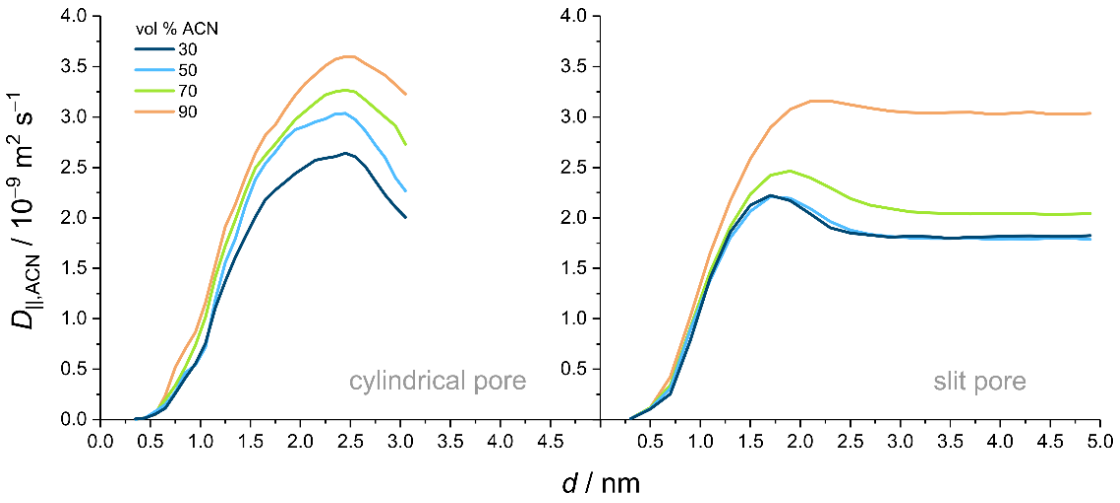

Figure 3.8. Surface-parallel diffusion coefficient profiles for ACN in the 6 nm cylindrical pore (left panel) and the slit pore (right panel) at different W/ACN ratios of the mobile phase. $D_{\parallel,ACN}(d)$-values were calculated with Eqs 3.1 and 3.2.

Surface-parallel diffusion coefficients extracted from Figure 3.8 at the ACN mobility maximum in the ditch are listed in Table 3.4. The comparison shows that $D_{\parallel,ACN,max}$ in the small cylindrical pore exceeds $D_{\parallel,ACN,max}$ in the slit pore over the full range of W/ACN ratios by up to ~38%. The maximum difference in $D_{\parallel,ACN,max}$ is observed with a mobile phase of 50/50 instead of 70/30 (v/v) W/ACN, where the two pores have the largest difference in maximum and pore-averaged ACN excess (Figure 3.5 and Table 3.2). The value of $D_{\parallel,ACN,max}$ does not only depend on the local solvent composition (i.e., the local ACN excess), but also on the sensitivity of the ACN diffusivity to the local solvent composition.[45] The ACN diffusivity varies comparatively little up to 40/60 (v/v) W/ACN and increases strongly from 30/70 (v/v) W/ACN in the mobile phase (Figure 3.S2).

Table 3.4. Maximum surface-parallel ACN diffusivity.

mobile phase	6 nm cylindrical pore	slit pore
W/ACN (v/v)	$D_{\parallel,ACN,max}$ (10^{-9} m^{-2} s^{-1})	
70/30	2.64 ± 0.13	2.21 ± 0.14
50/50	3.04 ± 0.11	2.21 ± 0.11
30/70	3.27 ± 0.13	2.46 ± 0.11
10/90	3.58 ± 0.15	3.16 ± 0.17

Another point emerging from Figure 3.8 concerns the sensitivity of the $D_{\parallel}(d)$-profiles to the W/ACN ratio of the mobile phase. For the slit pore, the $D_{\parallel,ACN}(d)$-profiles are practically collapsed with 70/30 and 50/50 (v/v) W/ACN (dark blue and cyan) and show a nonlinear upward shift with 30/70 and 10/90 (v/v) W/ACN, whereas $D_{\parallel,ACN}(d)$-profiles for the small cylindrical pore are almost equally distanced between the different W/ACN ratios. This again reflects the sensitivity of the ACN diffusivity to the local solvent composition (Figure 3.S2). Due to the increased ACN excess in the small cylindrical pore (cf. Figure 3.5), the diffusivity difference between bulk and ditch region (i.e., before the bonded phase enforces a general mobility descent) corresponds to the regime of high ACN volume fractions in Figure 3.S2, characterized by a strong, nearly linear diffusivity increase. The $D_{\parallel,ACN}(d)$-profiles for the slit pore, on the other hand, involve transitions from the plateau region (associated with <60 vol % ACN) into the linear region in Figure 3.S2, which leads to the nonlinear spacing of the $D_{\parallel,ACN}(d)$-profiles seen in Figure 3.8.

This relationship (Figure 3.S2) also explains the dependence of pore-averaged ACN diffusivities $\langle D_{\parallel,ACN} \rangle$ in both pores, recorded using Eqs 3.3 and 3.4, on the ACN volume fraction in the bulk mobile phase, as shown in Figure 3.9. $\langle D_{\parallel,ACN} \rangle$-values for the cylindrical pore demonstrate a nearly linear increase with the ACN volume fraction in the mobile phase, from $\langle D_{\parallel,ACN} \rangle = 2.28 \times 10^{-9}$ m^2

s^{-1} to $\langle D_{\parallel,ACN} \rangle = 3.01 \times 10^{-9}$ m^2 s^{-1}. The pore-averaged ACN diffusivity in the slit pore remains relatively low at low to medium ACN volume fraction in the mobile phase (at $\langle D_{\parallel,ACN} \rangle = 1.88$ and 1.86×10^{-9} m^2 s^{-1}) and ends with a steep increase up to $\langle D_{\parallel,ACN} \rangle = 3.02 \times 10^{-9}$ m^2 s^{-1} for 10/90 (v/v) W/ACN, reflecting the nonlinear spacing of the corresponding $D_{\parallel}(d)$-profiles in Figure 3.8. The pore-averaged ACN diffusivity data in Figure 3.9 are consistent with the pore-averaged ACN excess in Table 3.2, that is, the pore-averaged ACN excess can fully rationalize the considerable, linear increase of $\langle D_{\parallel,ACN} \rangle$ with the ACN volume fraction in the small cylindrical pore compared with the highly nonlinear increase of $\langle D_{\parallel,ACN} \rangle$ in the slit pore. With a mobile phase of 50/50 (v/v) W/ACN, the pore-averaged ACN mobility in the cylindrical pore exceeds that in the slit pore by ~39%, but the advantage of a small, confined pore space vanishes with a mobile phase of 10/90 (v/v) W/ACN, when the ACN excess and the associated mobility gain taper off substantially.

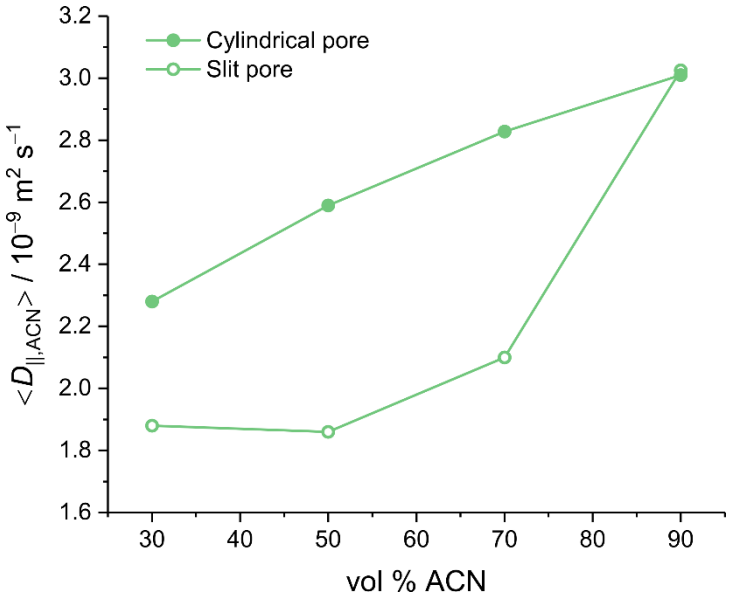

Figure 3.9. Pore-averaged, surface-parallel diffusion coefficients of ACN in the 6 nm cylindrical pore and the slit pore at different W/ACN ratios of the mobile phase. $\langle D_{\parallel,ACN} \rangle$-values were calculated with Eqs 3.3 and 3.4.

This relationship (Figure 3.S2) also explains the dependence of pore-averaged ACN diffusivities $\langle D_{\parallel,ACN} \rangle$ in both pores, recorded using Eqs 3.3 and 3.4, on the ACN volume fraction in the bulk mobile phase, as shown in Figure 3.9. $\langle D_{\parallel,ACN} \rangle$-values for the cylindrical pore demonstrate a nearly linear increase with the ACN volume fraction in the mobile phase, from $\langle D_{\parallel,ACN} \rangle = 2.28 \times 10^{-9}$ m^2 s^{-1} to $\langle D_{\parallel,ACN} \rangle = 3.01 \times 10^{-9}$ m^2 s^{-1}. The pore-averaged ACN diffusivity in the slit pore remains relatively low at low to medium ACN volume fraction in the mobile phase (at $\langle D_{\parallel,ACN} \rangle = 1.88$ and 1.86×10^{-9} m^2 s^{-1}) and ends with a steep increase up to $\langle D_{\parallel,ACN} \rangle = 3.02 \times 10^{-9}$ m^2 s^{-1} for 10/90 (v/v) W/ACN, reflecting the nonlinear spacing of the corresponding $D_{\parallel}(d)$-profiles in Figure 3.8.

The pore-averaged ACN diffusivity data in Figure 3.9 are consistent with the pore-averaged ACN excess in Table 3.2, that is, the pore-averaged ACN excess can fully rationalize the considerable, linear increase of $\langle D_{\parallel,\mathrm{ACN}} \rangle$ with the ACN volume fraction in the small cylindrical pore compared with the highly nonlinear increase of $\langle D_{\parallel,\mathrm{ACN}} \rangle$ in the slit pore. With a mobile phase of 50/50 (v/v) W/ACN, the pore-averaged ACN mobility in the cylindrical pore exceeds that in the slit pore by ~39%, but the advantage of a small, confined pore space vanishes with a mobile phase of 10/90 (v/v) W/ACN, when the ACN excess and the associated mobility gain taper off substantially.

To summarize this section, our analysis of the bonded-phase and solvent properties has shown that compared with the slit pore, the small cylindrical pore contains a more homogeneous bonded-phase density distribution, which leads to higher ACN excess and higher ACN diffusivity in the ditch as well as averaged over the pore. The small diameter of the cylindrical pore engenders a severe spatial confinement, creating the unique situation of ACN ditch overlap over the entire pore diameter, that is, properties of the bulk liquid phase as supplied by the mobile phase are not attained within the confines of the pore. This amplifies the local and pore-averaged effects of ACN excess and ACN diffusivity compared with the slit pore and creates a pore environment, where solute distribution and transport can be expected to deviate dramatically from that in a slit pore with an extended bulk liquid region.

3.3.2 Analyte dynamics

In this section, we study the consequences of a missing bulk liquid region resulting from ACN ditch overlap in the small cylindrical pore for the distribution and mobility of typical RPLC analytes, which are small, neutral, apolar to moderately polar molecules.

We begin with the analyte density distributions, which require consideration of the possibilities for analyte presence offered by each pore model. Analyte molecules in the slit pore model are distributed between the chromatographic interface at the planar surface and the bulk liquid region, whereas analyte molecules in the cylindrical pore model are distributed between the chromatographic interfaces at the inner curved and outer planar surface and the bulk liquid region in the solvent reservoirs (cf. Figures 3.1 and 3.3).[49] To remove the bias associated with the internal competition between inner and outer chromatographic interface for analyte presence inherent to the cylindrical pore model and thus enable the direct comparison between the small cylindrical pore and the slit pore, the analyte density profiles received from the inside of the cylindrical pore were normalized to the respective slit pore profiles. Using the slit pore as reference shows how a given number of analyte molecules is distributed in the slit pore and the 6 nm cylindrical pore under the actual conditions of spatial confinement and the locally established solvent composition.

In discussing the ethylbenzene density profiles (Figure 3.10), we mention several characteristics of RPLC separations. The ethylbenzene density profiles for the slit pore contain a peak in the bonded-phase region, around d = 0.83 nm, and a second, broader peak (with shoulder) in the interfacial region. Analyte density in the bonded-phase region is typically viewed to result from complete partitioning of the analyte molecule into the C_{18} chains (reminiscent of liquid–liquid partitioning), whereas analyte density in the interfacial region is considered to result from adsorption of the

analyte molecule to the soft, hydrophobic surface formed by the C_{18} chains.[67] The bonded-phase region allows analyte molecules to enter a highly hydrophobic environment, tempered only by the solvent layer at the silica surface (cf. Figure 3.5). The interfacial region allows analyte molecules contact with bonded-phase groups as well as with solvent molecules of the ACN ditch and the bulk liquid region, if present. From the profiles in Figure 3.10 we also recognize that ethylbenzene density in the bulk region of the slit pore ($d > 3$ nm) increases with the ACN content of the mobile phase, indicating higher elution strength of the running mobile phase to elute analytes from the RPLC column.[46]

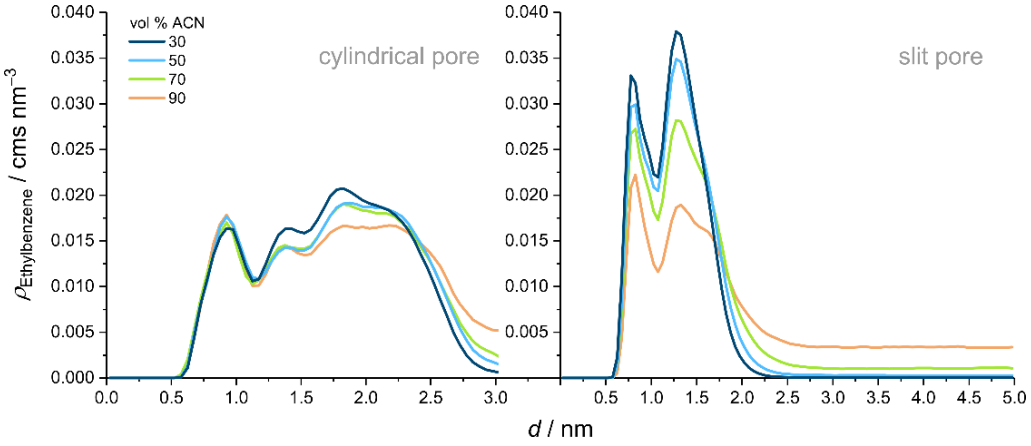

Figure 3.10. Ethylbenzene density distribution in the 6 nm cylindrical pore (left panel) and the slit pore (right panel) at different W/ACN ratios of the mobile phase.

For ethylbenzene density profiles in the cylindrical pore (left panel in Figure 3.10), we note the following features through comparison with the respective slit pore profiles. First, the intensity differences between the ethylbenzene density profiles for the different W/ACN ratios are much smaller than in the slit pore, that is, the analyte density profiles are less sensitive to the W/ACN ratio of the mobile phase. Second, the profiles in the cylindrical pore contain an additional ethylbenzene density peak at around $d = 1.4$ nm next to the partitioning peak at $d = 0.93$ nm.

The first feature is related to the spatial confinement effect engendered by the small cylindrical pore. The strong surface curvature causes the bonded phase to stretch over most of the pore cross-section. The C_{18} chain extension in the cylindrical pore leaves an inner solvent-filled lumen of only ~0.66 nm diameter — barely sufficient to accomodate even small solute molecules such as ethylbenzene (~0.75 nm).[45] Therefore, the ethylbenzene density in the cylindrical pore responds only weakly to changes in the W/ACN ratio of the mobile phase, as opposed to the ethylbenzene density in the slit pore, which contains an extended bulk liquid region. The local ethylbenzene density close to the center of the cylindrical pore, however, reflects a similar sensitivity to the elution strength of the running mobile phase as the ethylbenzene density in the bulk liquid region of the slit pore.

The second feature is a direct response of ethylbenzene molecules to the different bonded-phase conformations met in the two pores. The bonded phase in the small cylindrical pore is more evenly distributed along the C_{18} chain length as well as denser and more extended toward the pore center

than in the slit pore. This together enables population of the bonded-phase region between the partitioning peak close to the surface (at d = 0.93 nm) and the broad adsorption peak (at $d \approx$ 1.83 nm with a shoulder around d = 2.2 nm). Ethylbenzene molecules belonging to this additional peak at d = 1.4 nm have little contact with the few solvent molecules there (cf. Figure 3.5) and are immersed into the hydrophobic environment provided by the C_{18} chains.

Whereas the ethylbenzene density profiles generally show a sizable partitioning contribution, the acetophenone density profiles (Figure 3.11) are dominated by adsorption. Only a small fraction of acetophenone molecules occupies the bonded-phase region, because hydrogen-bonding opportunities to W molecules there are practically limited to the surface-adsorbed W layer.[58] The accessibility of surface-adsorbed W molecules for acetophenone molecules is hindered, even more so in the small cylindrical pore.[49] The additional acetophenone molecules that need to be accomodated due to the missing bulk liquid region (compared with the slit pore in the right panel of Figure 3.11) are adsorbed into the broad density peak centered at around d = 2.4 nm (left panel). As opposed to the additional partitioning peak observed in the ethylbenzene density profiles, the acetophenone density profiles feature a broader, asymmetric adsorption peak weighted toward the interfacial region.

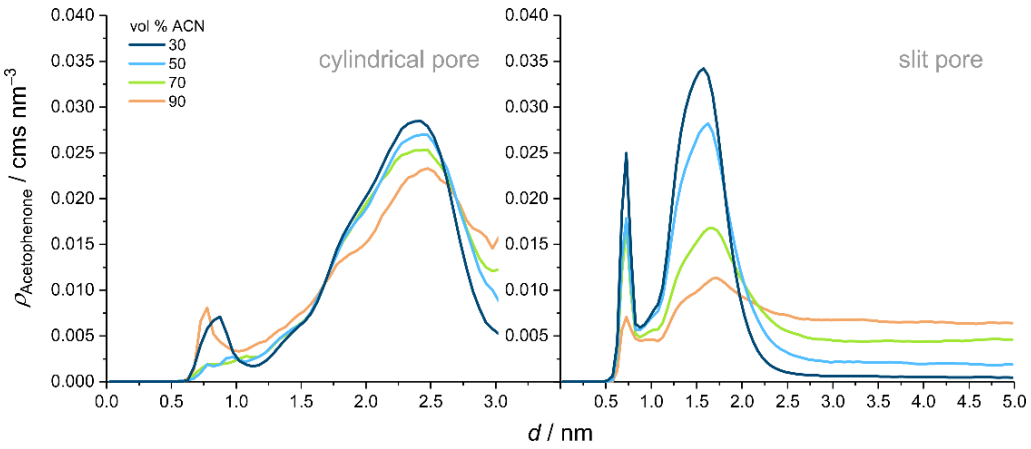

Figure 3.11. Acetophenone density distribution in the 6 nm cylindrical pore (left panel) and the slit pore (right panel) at different W/ACN ratios of the mobile phase.

As noticed for the ethylbenzene density profiles, the acetophenone density in the pore center reflects the expected retention behavior, that is, the analyte density there increases with decreasing retention (at increasing ACN content of the mobile phase). The acetophenone density in the pore center is higher than the corresponding ethylbenzene density, in agreement with the lower retention of acetophenone in RPLC.[46]

The comparison of Figures 3.10 and 3.11 suggests at first that the two analytes respond differently to the actual conditions in the small cylindrical pore; the apolar ethylbenzene by distributing its density more uniformly along the bonded-phase chains (and thus mimicking the response of the bonded-phase density distribution itself), and the moderately polar acetophenone by increasing its density in the interfacial region. But if peak width is taken into account, the acetophenone reponse

does not really differ from the ethylbenzene response. In both cases, analyte density in the favorite location is increased, either by a distinct second density peak or by widening an existing one.
Overall, Figures 3.10 and 3.11 demonstrate that the narrow cylindrical confinement and the resulting ACN ditch overlap enforce the preferences of different analyte types for a particular retention mechanism, namely the preference of the apolar ethylbenzene for partitioning and the preference of the moderately polar acetophenone for adsorption.

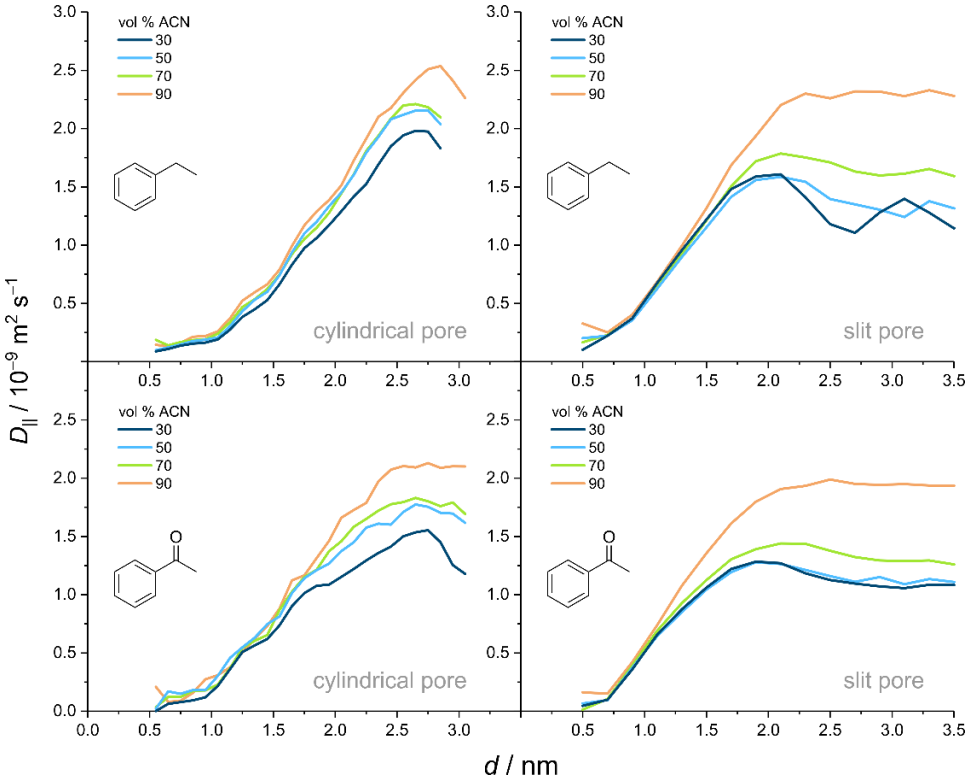

Figure 3.12. Surface-parallel diffusion coefficient profiles for ethylbenzene (top panels) and acetophenone (bottom panels) in the 6 nm cylindrical pore (left panels) and the slit pore (right panels) at different W/ACN ratios of the mobile phase. $D_{||}(d)$-values were calculated with Eqs 3.1 and 3.2. Analyte mobilities in the bulk region of the slit pore (d > 3 nm) recover diffusion coefficients simulated in the corresponding bulk, unconfined W–ACN mixtures (cf. Figure 3.S2).

As observed for the ACN diffusivity (Figure 3.8), the analyte diffusivity profiles go through a maximum in the ACN ditch, before decreasing steadily over the bonded-phase region to zero at the silica surface (Figure 3.12). Compared to the slit pore, the analyte diffusvity in the interfacial region of the small cylindrical pore is increased. This meets our expectations, as we know from previous work that higher ACN excess and higher ACN diffusivity in the interfacial region favor local analyte diffusivity there.[45–47,49,58] The question is by how much the narrow cylindrical confinement and the unique conditions of ACN overlap increase the local analyte diffusivity in the interfacial region and how much this local diffusivity increase contributes to the pore-averaged analyte diffusivity.

Table 3.5. Maximum surface-parallel analyte diffusivity.

	6 nm cylindrical pore		slit pore	
mobile phase	ethylbenzene	acetophenone	ethylbenzene	acetophenone
W/ACN (v/v)	$D_{\parallel,\max}$ (10^{-9} m^{-2} s^{-1})			
70/30	1.98 ± 0.20	1.55 ± 0.12	1.60 ± 0.09	1.26 ± 0.13
50/50	2.16 ± 0.18	1.78 ± 0.13	1.58 ± 0.13	1.27 ± 0.09
30/70	2.21 ± 0.08	1.83 ± 0.11	1.78 ± 0.16	1.44 ± 0.08
10/90	2.54 ± 0.16	2.13 ± 0.09	2.29 ± 0.05	1.98 ± 0.04

Diffusion coefficients extracted at the mobility maxima of the analytes ($D_{\parallel,\max}$) are summarized in Table 3.5. The maximum analyte diffusivity profits generously from the narrow cylindrical confinement: $D_{\parallel,\max}$ of ethylbenzene by 36.7% and $D_{\parallel,\max}$ of acetophenone by 40.2% compared to the slit pore. Because the analyte diffusivity relies mostly on the solvent ratio in the local analyte environment and the analyte-specific sensitivity to this local solvent ratio, the observed diffusivity increase of the analytes can be rationalized by the local ACN excess, which is listed for the analyte mobility maximum in Table 3.S2, and the bulk molecular diffusivity curves of the two analytes in W–ACN mixtures (Figure 3.S2).

As for analysis of the ACN dynamics in Figure 3.9, we now take a look at the pore-averaged analyte diffusivities $\langle D_{\parallel} \rangle$ in the two pores (Figure 3.13). The pore-averaged analyte mobility in the slit pore shows the same dependence on the ACN volume fraction in the running mobile phase for ethylbenzene and acetophenone, because the pore-averaged mobility in the slit pore is dominated by the contribution from the bulk liquid region. Consequently, the $\langle D_{\parallel} \rangle$-curves of the analytes in the slit pore reflect the sensitivity of the analyte mobility to the ACN volume fraction in the mobile phase (cf. Figure 3.S2).

As for analysis of the ACN dynamics in Figure 3.9, we now take a look at the pore-averaged analyte diffusivities $\langle D_{\parallel} \rangle$ in the two pores (Figure 3.13). The pore-averaged analyte mobility in the slit pore shows the same dependence on the ACN volume fraction in the running mobile phase for ethylbenzene and acetophenone, because the pore-averaged mobility in the slit pore is dominated by the contribution from the bulk liquid region. Consequently, the $\langle D_{\parallel} \rangle$-curves of the analytes in the slit pore reflect the sensitivity of the analyte mobility to the ACN volume fraction in the mobile phase (cf. Figure 3.S2).

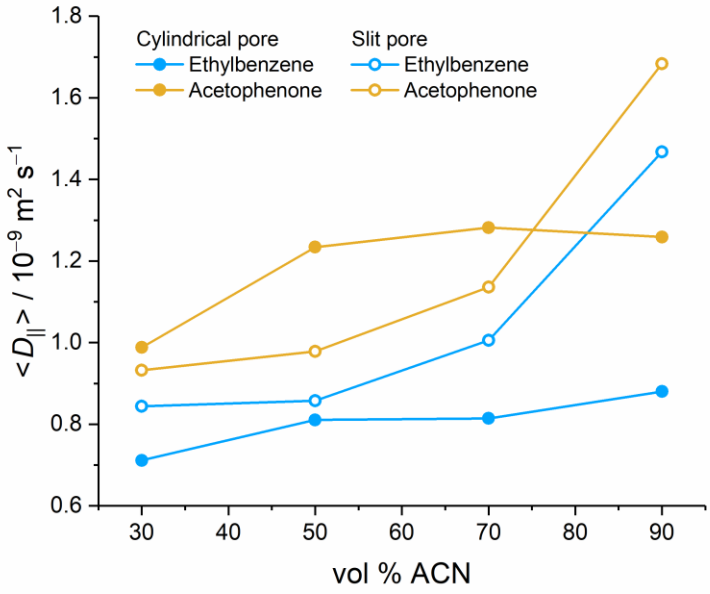

Figure 3.13. Pore-averaged, surface-parallel diffusion coefficients of ethylbenzene and acetophenone in the 6 nm cylindrical pore and the slit pore at different W/ACN ratios of the mobile phase. $\langle D_{\parallel} \rangle$-values were calculated with Eqs 3.3 and 3.4.

Figure 3.13 shows that the missing bulk liquid region in the small cylindrical pore attenuates the sensitivity of the pore-averaged analyte diffusivities to the W/ACN ratio of the mobile phase. The pore-averaged analyte diffusivities in the slit pore are lower than those in the cylindrical pore, except at 10/90 (v/v) W/ACN. High ACN content (aka high elution strength of the mobile phase) means that a comparatively high fraction of the analyte density is located in the bulk liquid region of the slit pore (cf. right panel in Figure 3.10 and 3.11) and that the analytes have a comparatively high mobility there (right panels in Figure 3.12). The favorable conditions in the bulk region of the slit pore promote the pore-averaged analyte diffusivity to a high value (Figure 3.13). This, however, does not translate into a practical advantage, as with a mobile phase of 10/90 (v/v) W/ACN, neither ethylbenzene nor acetophenone are sufficiently retained on a C_{18} column.[46]

The data collected in Figure 3.13 for the small cylindrical pore reflect the different consequences of the spatial confinement on the density distribution of ethylbenzene (Figure 3.10) and acetophenone (Figure 3.11). Compared to the slit pore, more ethylbenzene molecules populate the bonded-phase region (additional peak at d = 1.4 nm, left panel in Figure 3.10), where analyte molecules cannot profit from the ACN excess in the ditch. Additionally, the bonded-phase mobility in this region is low. The location of the additional bonded-phase peak in the ethylbenzene density profiles corresponds to the C10 and C11 groups of the C_{18} chains, which have low mobility ($D_{\parallel,av}$ = 0.1–0.2 × 10^{-9} m^2 s^{-1}) according to Figure 3.7. Consequently, the pore-averaged mobility of ethylbenzene in the small cylindrical pore becomes lower than in the slit pore, despite the generous mobility increase provided to the ethylbenzene molecules in the interfacial region. Because the ethylbenzene density distribution in the small cylindrical pore is rather insensitive to the W/ACN

ratio of the mobile phase (Figure 3.10), the pore-averaged ethylbenzene mobility remains low ($\langle D_{\parallel} \rangle < 0.9 \times 10^{-9}$ m^2 s^{-1}), even at 90 vol % ACN in the mobile phase.

Contrary to ethylbenzene, acetophenone responds to the confinement exercised by the small cylindrical pore by placing more molecules in the interfacial region (Figure 3.11), where analyte molecules can profit from the high ACN excess in the ditch. Additionally, the density increase is co-localized with the third segment of the C_{18} chains, whose bonded-phase groups (≥C13 groups) have higher mobility (Figure 3.7). Increasing the analyte density in the interfacial region raises the pore-averaged diffusivity of acetophenone in the small cylindrical pore compared to the slit pore for most W/ACN ratios in the mobile phase (Figure 3.13), up to $\langle D_{\parallel} \rangle \approx 1.3 \times 10^{-9}$ m^2 s^{-1} at 30/70 (v/v) W/ACN. Because the observed pore-averaged diffusivity increase of acetophenone occurs at W/ACN ratios that provide sufficient retention on a C_{18} column,[46] the narrow cylindrical confinement translates into a practical advantage, albeit only locally on the column.

To summarize the results of this section, the absence of a bulk liquid region in the small cylindrical pore due to ACN ditch overlap results in (i) analyte density distributions that are rather insensitive to the ACN content of the mobile phase and (ii) pore-averaged analyte diffusivities that do not reflect the dependence of the bulk molecular diffusivities of the analytes on the ACN content of the mobile phase. The 6 nm cylindrical pore contains a more hydrophobic bonded-phase region than the slit pore, which enforces the differentiation between analytes according to their polarity. The apolar ethylbenzene increases its density in the bonded-phase region, where analyte molecules do not profit from the high ACN excess in the ditch and are slowed-down by contact with the lower-numbered bonded-phase groups, resulting in a decreased pore-averaged diffusivity compared to the slit pore. The moderately polar acetophenone increases its density in the interfacial region, where the high ACN excess favors the local acetophenone diffusivity so much that the pore-averaged diffusivity of acetophenone is raised compared to the slit pore.

3.4 Conclusions

In this MD simulations study we investigated the spatial confinement effects associated with the combination of concave surface curvature and small pore size for the RPLC interface formed by equilibration of a silica-based, endcapped, C_{18} stationary phase with a W–ACN mobile phase as well as the response of small, neutral solutes as typical RPLC analytes. The confinement effects in a 6 nm cylindrical pore were quantified by comparison with a 10 nm slit pore representing column-averaged properties.

The narrow cylindrical confinement governs the density and diffusivity distributions of bonded-phase groups and solvent molecules. The strong concave surface curvature forces the C_{18} chains into a more ordered, and thus more extended, conformation. This pushes bonded-phase density towards the pore center, resulting in a rather even bonded-phase density distribution along most of the pore radius. The compact bonded-phase density that solvent molecules meet in the interfacial region of the small cylindrical pore does not require chain solvation by ACN molecules. Instead, ACN molecules accumulate close to the chain ends to form a ditch with high ACN excess. The

absence of spatial confinement in the slit pore yields an interfacial region with a thinned-out bonded-phase density, inviting chain solvation by ACN and limiting the ACN excess in the ditch. Together, the bonded-phase extension and the high ACN excess in the ditch of the small cylindrical pore result in ACN ditch overlap in the pore center at the cost of an eliminated bulk liquid region. The 6 nm cylindrical pore is in its entirety a highly hydrophobic environment, where neither local nor pore-averaged sorption and diffusion scale directly with the W/ACN ratio of the bulk mobile phase, in contrast to the slit pore, which is dominated by its bulk liquid region that matches the running mobile phase.

The high hydrophobicity of the small cylindrical pore enhances the solute polarity-related differences between the analytes, namely the preference of apolar analytes for partitioning into the low-mobility bonded-phase region and the preference of moderately polar analytes for adsorption in the high-mobility interfacial region. The changes effected by the narrow cylindrical confinement decrease the pore-averaged mobility of apolar analytes and increase that of moderately polar ones. Thus, the spatial confinement effects engendered by the narrow cylindrical pore induce a transport selectivity according to details of the retention mechanism. The confinement effects therefore alter the general structure–retention–transport relationship on the local pore scale within the interconnected pore network of the mesoporous support particles used in RPLC.

At last, we consider the implications of our results for RPLC practice. RPLC columns contain a sizable fraction of smaller-than-average pores prone to ACN ditch overlap. The solvent and analyte distributions and mobilities in these pores do not only differ from those in the larger pores, but also respond only weakly to changes in the W/ACN ratio of the mobile phase, which is the main mode of manipulation during an RPLC separation. Under gradient elution conditions (moving continuously from a W-rich to an ACN-rich mobile phase), the actual solvent composition in pores with ditch overlap is very different from that of the externally applied one. At the beginning of a gradient, these pores contain already much more ACN, equivalent to higher elution strength, than the W-rich mobile phase. Consequently, the local gradient window narrows substantially inside these pores, which makes it difficult to predict their contribution to analyte retention from a general point-of-view. The situation is further complicated by the wide, continuous pore size distributions of chromatographic beds, predicting a smooth transition from small pores with complete ditch overlap via intermediate-sized pores with restricted bulk liquid regions to pores that accomodate an extended bulk liquid region.

This situation is reminiscent of ion transport in porous media with charged surfaces, for example, ion-exchange membranes, where electrical double layer overlap and thus discrimination between co- and counterionic species occurs locally in smaller pores.[68] A further complicated situation arises in mixed-mode RPLC separations, where the mostly hydrophobic stationary phase contains charges to widen the analyte spectrum.[69] Mixed-mode RPLC separations may entail local ACN ditch as well as electrical double layer overlap inside the particles, which makes the prediction of the separation outcome a highly complex task.

3.5 Supporting Information

Table 3.S1. Number of W and ACN molecules in the simulation box during productive simulations with the 6 nm cylindrical pore model.

W/ACN (v/v)	N_W	N_{ACN}
70/30	37749	7834
50/50	26500	11450
30/70	16000	15000
10/90	5500	18150

Table 3.S2. Local ACN excess at the analyte mobility maxima in cylindrical and slit pore (cf. Figure 3.12 in the main text).

	6 nm cylindrical pore		slit pore	
mobile phase	ethylbenzene	acetophenone	ethylbenzene	acetophenone
W/ACN (v/v)	ACN excess (vol %)			
70/30	+38	+31	+20	+27
50/50	+25	+29	+17	+22
30/70	+17	+19	+9	+9
10/90	+4	+5	+2	+1

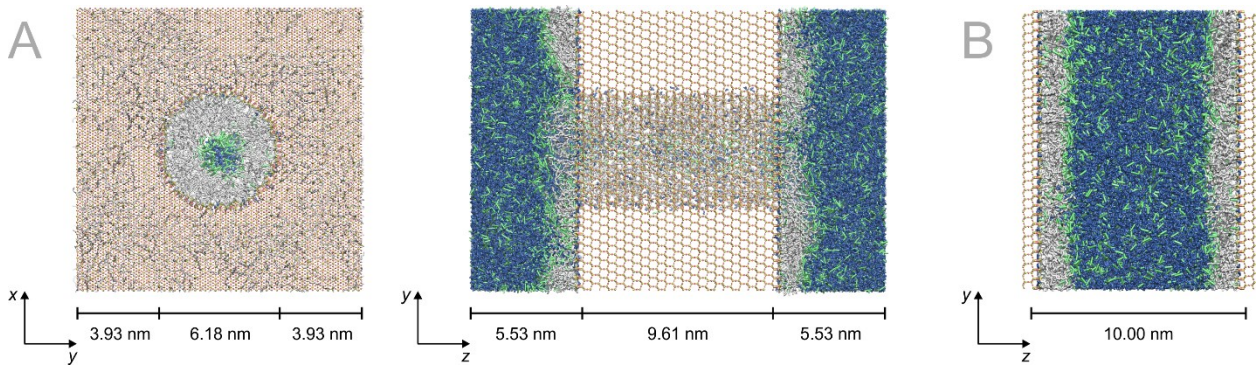

Figure 3.S1. (A) Cylindrical pore model. Front (left) and side views (right) of the simulation box. Dimensions of the silica block and the cylindrical pore in *xy*-direction (front view, pore diameter) and in *yz*-direction (side view, pore length) are indicated. In the front view, only solvent molecules

inside the cylindrical pore are shown to visualize the modification of inner curved and outer planar silica surface with the bonded phase. (B) Slit-pore model. Both pore models are equilibrated with a mobile phase of 70/30 (v/v) W/ACN. Si and O atoms of the silica block are represented by yellow and red balls, respectively, and Si, O, and H atoms of the silica surface as yellow, red, and white sticks, respectively; united-atoms groups of the bonded phase are shown as grey sticks; W and ACN molecules are shown as dark blue and green sticks, respectively.

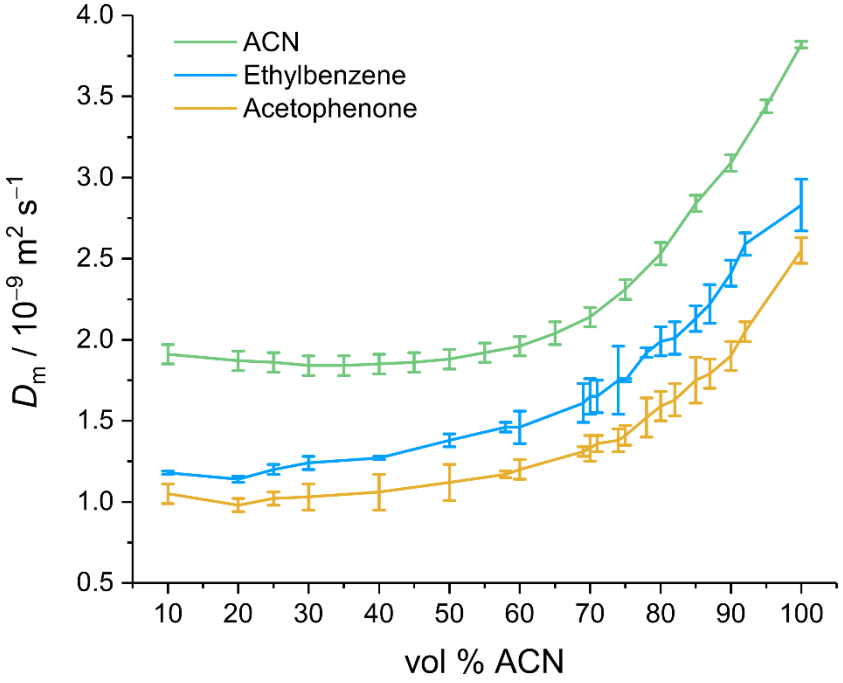

Figure 3.S2. Bulk molecular diffusion coefficients of ACN (central C atom, green) and the analytes (center of mass; blue and yellow for ethylbenzene and acetophenone, respectively) simulated for solvent ratios between 90/10 and 0/100 (v/v) W/ACN. Reproduced with permission from J. Rybka, A. Höltzel, and U. Tallarek, *J. Phys. Chem. C* **2017**, *121*, 17907–17920. Copyright 2017 American Chemical Society.

Acknowledgments

This work was supported by the Deutsche Forschungsgemeinschaft DFG (Bonn, Germany) under grant TA 268/11-1. MD simulations were performed on the supercomputer HoreKa funded by the Ministry of Science, Research and the Arts Baden-Württemberg and by the Federal Ministry of Education and Research under the project acronym RPLCMD. We thank Andreas Steinhoff and Dr. Dzmitry Hlushkou for fruitful discussions.

References

1 Y. Kurachi, A. North, *J. Physiol.* **2004**, *554*, 245–247.

2 S. Howorka, Z. Siwy, *Chem. Soc. Rev.* **2009**, *38*, 2360–2384.
3 J. Kärger, D. M. Ruthven, D. N. Theodorou, *Diffusion in Nanoporous Materials*; Wiley–VCH: Weinheim, **2012**.
4 M. Tagliazucchi, I. Szleifer, *Mater. Today* **2015**, *18*, 131–142.
5 T. Ma, M. Bechelany, J.-M. Janot, S. Balme, *Adv. Colloid Interface Sci.* **2017**, *250*, 195–213.
6 F. Zhang, Y. Sun, D. Tian, H. Li, *Angew. Chem. Int. Ed.* **2017**, *56*, 7186–7190.
7 W. H. Thompson, *J. Chem. Phys.* **2018**, *149*, 170901.
8 S. Faucher, N. Aluru, M. Z. Bazant, D. Blankschtein, A. H. Brozena, J. Cumings, J. P. de Souza, M. Elimelech, R. Epsztein, J. T. Fourkas, *J. Phys. Chem. C* **2019**, *123*, 21309–21326.
9 J. Kärger, D. M. Ruthven, R. Valiullin, *Adsorption* **2021**, *27*, 267–281.
10 H. Wang, M. Wang, X. Liang, J. Yuan, H. Yang, S. Wang, Y. Ren, H. Wu, F. Pan, Z. Jiang, *Chem. Soc. Rev.* **2021**, *50*, 5468–5516.
11 K.-D. Kreuer, A. Münchinger, *Annu. Rev. Mater. Res.* **2021**, *51*, 21–46.
12 S. Agrawal, M. Elmehlawy, M. P. Hoepfner, *J. Phys. Chem. C* **2021**, *125*, 11097–11106.
13 Z. Zhu, D. Wang, Y. Tian, L. Jiang, *J. Am. Chem. Soc.* **2019**, *141*, 8658–8669.
14 L. R. Snyder, J. J. Kirkland, J. W. Dolan, *Introduction to Modern Liquid Chromatography*, 3rd ed.; John Wiley & Sons: Hoboken, NJ, 2010.
15 T. A. Pham, S. M. G. Mortuza, B. C. Wood, E. Y. Lau, T. Ogitsu, S. F. Buchsbaum, Z. S. Siwy, F. Fornasiero, E. Schwegler, *J. Phys. Chem. C* **2016**, *120*, 7332–7338.
16 Z. Tian, S. Dai, D. Jiang, *Comput. Mol. Sci.* **2016**, *6*, 173–197.
17 A. Striolo, A. Phan, M. R. Walsh, *Curr. Opin. Chem. Eng.* **2019**, *25*, 57–66.
18 C. I. Lynch, S. Rao, M. S. P. Sansom, *Chem. Rev.* **2020**, *120*, 10298–10335.
19 J. W. Polster, E. T. Acar, F. Aydin, C. Zhan, T. A. Pham, Z. S. Siwy, *ACS Nano* **2020**, *14*, 4306–4315.
20 M. Heiranian, Y. Noh, N. R. Aluru, *J. Chem. Phys.* **2021**, *154*, 134703.
21 B. C. Bukowski, F. J. Keil, R. I. Ravikovitch, G. Sastre, R. Q. Snurr, M.-O. Coppens, *Adsorption* **2021**, *27*, 683–760.
22 R. T. Cygan, J. A. Greathouse, A. G. Kalinichev, *J. Phys. Chem. C* **2021**, *125*, 17573–17589.
23 P. A. Cazade, J. Dweik, B. Coasne, F. Henn, J. Palmeri, *J. Phys. Chem. C* **2010**, *114*, 12245–12257.
24 C. Zhan, C. Lian, Y. Zhang, M. W. Thompson, Y. Xie, J. Wu, P. R. C. Kent, P. T. Cummings, D. Jiang, D. J. Wesolowski, *Adv. Sci.* **2017**, *4*, 1700059.
25 D. Dubbeldam, K. S. Walton, T. J. H. Vlugt, S. Calero, *Adv. Theory Simul.* **2019**, *2*, 1900135.
26 R. K. Lindsey, J. L. Rafferty, B. L. Eggimann, J. I. Siepmann, M. R. Schure, *J. Chromatogr. A* **2013**, *1287*, 60–82.
27 B. Coasne, *New J. Chem.* **2016**, *40*, 4078–4094.

28 B. E. Basconi, G. Carta, M. R. Shirts, *AIChE J.* **2017**, *63*, 4564–4575.
29 U. Tallarek, D. Hlushkou, J. Rybka, A. Höltzel, *J. Phys. Chem. C* **2019**, *123*, 15099–15112.
30 A. Phan, D. Fan, A. Striolo, *Phys. Fluids* **2020**, *32*, 101301.
31 H. You, H. Xu, J. Fan, Y.-B. Zhu, F. Wang, H. Wu, *Energy Fuels* **2021** *35*, 911–943.
32 C. Bousige, P. Levitz, B. Coasne, *Nat. Commun.* **2021**, *12*, 1043.
33 U. Tallarek, D. Hlushkou, A. Höltzel, *J. Phys. Chem. C* **2022**, *126*, 2336–2348.
34 R. B. Schoch, J. Han, P. Renaud, *Rev. Mod. Phys.* **2008**, *80*, 839–883.
35 L. Bocquet, E. Charlaix, *Chem. Soc. Rev.* **2010**, *39*, 1073–1095.
36 T. S. (Ed.) Sørensen, *Surface Chemistry and Electrochemistry of Membranes*; Marcel Dekker: New York, NY, **1999**.
37 F. C. Leinweber, M. Pfafferodt, A. Seidel-Morgenstern, U. Tallarek, *Anal. Chem.* **2005,** 77, 5839–5850.
38 I. Nischang, G. Chen, U. Tallarek, *J. Chromatogr. A* **2006**, *1109*, 32–50.
39 F. Helfferich, *Ion Exchange*; Dover Publications: New York, NY, **1995**.
40 J. S. Fritz, D. T. Gjerde, *Ion Chromatography*, 3rd ed.; Wiley–VCH: Weinheim, **2000**.
41 U. D. Neue, *HPLC Columns: Theory, Technology, and Practice*; Wiley–VCH: New York, NY, **1997**.
42 J. Rybka, A. Höltzel, S. M. Melnikov, A. Seidel-Morgenstern, U. Tallarek, *Fluid Phase Equilib.* **2016**, *407*, 177–187.
43 I. Bacskay, A. Sepsey, A. Felinger, *J. Chromatogr. A* **2014**, *1339*, 110–117.
44 F. Gritti, G. Guiochon, *J. Chromatogr. A* **2013**, *1297*, 85–95.
45 J. Rybka, A. Höltzel, U. Tallarek, *J. Phys. Chem. C* **2017**, *121*, 17907–17920.
46 J. Rybka, A. Höltzel, A. Steinhoff, U. Tallarek, *J. Phys. Chem. C* **2019**, *123*, 3672–3681.
47 J. Rybka, A. Höltzel, N. Trebel, U. Tallarek, *J. Phys. Chem. C* **2019**, *123*, 21617–21628.
48 J. L. Rafferty, J. I. Siepmann, M. R. Schure, *J. Chromatogr. A* **2009**, *1216*, 2320–2331.
49 N. Trebel, A. Höltzel, J. K. Lutz, U. Tallarek, *J. Phys. Chem. B* **2021**, *125,* 11320–11336.
50 H. Kraus, J. Rybka, N. Trebel, A. Höltzel, U. Tallarek, *Mol. Simul.* **2021**, *47*, 306–316.
51 B. Coasne, F. Di Renzo, A. Galarneau, R. J.-M. Pellenq, *Langmuir* **2008**, *24*, 7285–7293.
52 F. Gritti, G. Guiochon, *J. Chromatogr. A* **2005**, *1099*, 1–42.
53 T. S. Gulmen, W. H. Thompson, *Langmuir* **2006**, *22*, 10919–10923.
54 M. G. Marin, J. I. Siepmann, *J. Phys. Chem. B* **1998**, *102*, 2569–2577.
55 C. D. Wick, J. M. Stubbs, N. Rai, J. I. Siepmann, *J. Phys. Chem. B* **2005**, *109*, 18974–18982.

56 H. J. C. Berendsen, J. R. Grigera, T. P. Straatsma, *J. Phys. Chem.* **1987**, *91*, 6269–6271.

57 K. Vanommeslaeghe, E. Hatcher, C. Acharya, S. Kundu, S. Zhong, J. Shim, E. Darian, O. Guvench, P. Lopes, I. Vorobyov, A.D. Mackerell Jr., *J. Comput. Chem.* **2010**, *31*, 671–690.

58 N. Trebel, A. Höltzel, A. Steinhoff, U. Tallarek, *J. Chromatogr. A* **2021**, *1640*, 461958.

59 F. Gritti, G. Guiochon, *AIChE* **2011**, *57*, 333–345.

60 F. Gritti, G. Guiochon, *AIChE* **2011**, *57*, 346–358.

61 B. Hess, C. Kutzner, D. van der Spoel, E. Lindahl, *J. Chem. Theory Comput.* **2008**, *4*, 435–447.

62 M. J. Abraham, T. Murtola, R. Schulz, S. Páll, J. C. Smith, B. Hess, E. Lindahl, *SoftwareX* **2015**, *1–2*, 19–25.

63 U. Essmann, L. Perera, M. L. Berkowitz, T. Darden, H. Lee, L. G. Pedersen, *J. Chem. Phys.* **1995**, *103*, 8577–8593.

64 P. Liu, E. Harder, B.J. Berne, *J. Phys. Chem. B* **2004**, *108*, 6595–6602.

65 M. J. Abraham, D. van der Spoel, E. Lindahl, B. Hess, the GROMACS Development Team. *GROMACS User Manual*, version 2019; GROMACS Development Team, **2022** (accessed Sept 09, 2022).

66 S. M. Melnikov, A. Höltzel, A. Seidel-Morgenstern, U. Tallarek, *J. Phys. Chem. C* **2013**, *117*, 6620–6631.

67 J. L. Rafferty, L. Zhang, J. I. Siepmann, M. R. Schure, *Anal. Chem.* **2007**, *79*, 6551–6558.

68 V. Nikonenko, A. Nebavsky, S. Mareev, A. Kovalenko, M. Urtenov, G. Pourcelly, *Appl. Sci.* **2019**, *9*, 25.

69 F. Gritti, *Anal. Chem.* **2021**, *93*, 5653–5664.

Chapter 4

Prediction of surface excess adsorption and retention factors in reversed-phase liquid chromatography from molecular dynamics simulations

Authors

Fabrice Gritti, Nicole Trebel, Alexandra Höltzel, Ulrich Tallarek

State of publication

Published 6 December 2022 in *Journal of Chromatography A*, Vol. 1685, 463627.
DOI: 10.1016/j.chroma.2022.463627

Abstract

An alternative method to the classical fit of semi-empirical, statistical, or artificial intelligence-based models to retention data is proposed to predict surface excess adsorption and retention factors in liquid chromatography. The approach is based on a fundamental, microscopic description of the liquid-to-solid adsorption of analytes taking place at the interface between a bulk liquid phase and a solid surface. Molecular dynamics (MD) simulations are performed at $T = 300$ K in a 100 Å wide slit-pore model (β-cristobalite-C_{18} surface in contact with an acetonitrile/water mobile phase) to quantify a priori the retention factors of small molecules expected in reversed phase liquid chromatography (RPLC). Uracil is chosen as the reference "non-retained" marker, whereas benzyl alcohol, acetophenone, benzene, and ethylbenzene are four selected retained, neutral compounds. The MD simulations allow to determine the pore-level density profiles of these five compounds, i.e., the variation of the analyte concentration as a function of distance from the silica surface. The retention factors of the retained analytes are expressed using their respective calculated surface excess adsorption relative to uracil. By definition, the retention factors are proportional to the surface excess adsorbed and the proportionality constant is directly scaled to the retention time of the "non-retained" marker. Experimentally, a 4.6 mm ×150 mm RPLC-C_{18} column packed with 5 μm 100 ˚A High Strength Silica (HSS)-C_{18} particles is used and the retention times of these five compounds are measured. The volume fraction of acetonitrile in water increases from 20 to 90% generating a wide range of retention factors from 0.15 to 183 at $T = 300$ K. The results demonstrate very good agreement between the MD-predicted surface excess adsorption data and measured retention factors ($R^2 > 0.985$). A systematic error is observed as the proportionality constant is not exactly scaled to the retention time of uracil. This is most likely caused by the differences between the chemical and morphological features of the slit-pore model adopted in the MD simulations and

those of the actual HSS-C_{18} particles: the average surface coverage with C_{18} chains, the geometry of the mesopores, and the pore size distribution. Specifically, the impact on RPLC retention of slight, local variations in surface chemistry (e.g., functional group density and uniformity) and how this aspect is affected by the pore space morphology (e.g., pore curvature and size) is worth investigating by future MD simulations.

4.1 Introduction

The development of isocratic and gradient separation methods in liquid chromatography is critical to the pharmaceutical, biological, and food industries,[1–3] which have to comply with current regulations in order to successfully bring new chemicals on the market.[4] In particular, RPLC methods have always represented about 70% of all the methods developed,[5] while the plethora of column manufacturers are proposing a large variety of RPLC columns (silica- or silica/inorganic based particles, C_4, C_8, C_{18} hydrophobic surface bonding, different surface coverages, etc.). This makes the selection of the most suitable column and the optimization of the operating conditions for common LC users a quite daunting task. They cannot afford spending extensive lab time needed to acquire all the chromatographic data necessary to select the best column and separation parameters. In practice and under economic constraints, this whole optimization process has to be accelerated. For these reasons, the retention mechanism in RPLC has become a major topic of research over the past years with the promise to deliver physically sound and robust retention models and speed up method development.[5–9]

Retention prediction has been playing a key role for the last four decades to solve this practical problem. To date, method development is essentially supported by computerized retention prediction: it requires 1) a minimum set of retention data covering a wide enough range of experimental parameters (temperature, gradient time, pH, etc.), 2) the best fit of arbitrarily chosen empirical, statistical, or artificial intelligence-based retention models to these data, and 3) a classical optimization software to find the optimum separation conditions.[1,4,10–18] These software-based approaches are categorized as inverse methods,[19–21] because their output relies on preliminary retention time data necessary for the calibration of the retention models. In contrast, direct methods can also be applied to predict the retention of analytes from independent measurements of column properties (hold-up volume, temperature, pressure), LC system features (gradient dwell volume and dispersion), strong solvent interaction with the stationary phase (excess adsorption isotherm), and the analyte distribution between liquid and solid phase (adsorption isotherm or Henry's constant).[21–34] The advantage of these direct methods is that they are not biased by the arbitrary selection of the retention model and its calibration.

Another practical problem relates to the identification of unknown compounds by LC/MS analyses, which is also supported by computerized retention prediction.[35] The sole measurement of the analyte mass is often insufficient to unambiguously determine the complete chemical structure of the detected compound. A second dimension can then be added such as the measurement of the retention time of the unknown analyte. Assuming an exhaustive list of molecular structures generating the same molecular weight and predicting accurately their retention times enables the

analyst to discard a large number of possibilities and reveal the true structure of the unknown compound. To date, the most common approaches to predict retention times from the molecular structure of the analytes are the linear solvent strength relationships[36–40] (LSER) and the quantitative structure-retention relationships[41–52] (QSRR). Many review articles have been devoted to the prediction of analyte retention times in liquid chromatography over the last three decades based on QSSR/artificial intelligence (AI).[41,45,46,49,52–68] All these approaches require a long list of molecular descriptors for each analyte investigated[36,37,39] Additionally, their suitability to predict accurately the retention time is often subject to large relative errors because the underlying assumptions of both LSER and QSSR are infringing the fundamentals of liquid-solid adsorption thermodynamics in liquid chromatography.[6,27]

Alternatively, as is the case when the observations result from a mechanism too complex to be captured and interpreted from a mere empirical model, Monte-Carlo (MC) and molecular dynamics (MD) simulations are usually the last resort. Both MC or MD simulations have been used in the past to tackle the retention mechanism in RPLC.[8,9,70–81] The advantage of these simulation methods of molecular motion at the interface between a solid surface and a liquid phase is that they do not rely on experimental data once the force fields in the dynamic system have been validated.[82–84] They can then be considered as a priori approach for the prediction of retention times when the molecular structure of the analyte, surface modification, and mobile phase are known. The pore-level density distribution of a retained analyte can be calculated from MC and MD simulations[8,85] in order to reach that goal. To the best of our knowledge, no such attempt has been meticulously carried out to 1) investigate the relationship between MD simulation data and LC retention factors from the most fundamental relationship between the capacity factors in LC and the surface excess adsorption of the analyte present in the mesopore volume which can be calculated directly from the MD simulations-based density profiles and 2) assess the relevance of MD simulations to predict retention in RPLC. In the first part of this work, MD simulations are used to calculate the density profiles of a "non-retained" marker (uracil) and four small and neutral, retained RPLC analytes (benzyl alcohol, acetophenone, benzene, and ethylbenzene). A planar slit pore model (β-cristobalite-C_{18}, 100 Å pore width) in equilibrium with eight different bulk mobile phases (acetonitrile/water, from 20 to 90% volume fraction acetonitrile) has been built to mimic the adsorption behavior of these five compounds at T = 300 K. Their density profiles are computed and the fundamental relationship between these profiles and the retention factors is derived from the definition of the capacity factor in liquid chromatography. In the second part, the calculated surface excess adsorption of the analyte molecules are directly compared to the experimental retention factors (uracil as t_0 marker) using a 4.6 mm × 150 mm column packed with mesoporous C_{18} -silica particles. The quality of the expected relationship between the calculated surface excess adsorption of the analyte molecules and the observed retention factors is reported and discussed.

4.2 Theory

4.2.1 Dynamic experimental retention factor

Irrespective of the physical state of the mobile and stationary phases, the retention (or capacity) factor, *k*, is an equilibrium property of the separation system.[86] The true and absolute retention factor always refers to a so-called "inert" compound: this implies that the mass density of the inert compound over the entire volume accessible by the mobile phase is rigorously uniform and equal to its bulk density. Ideally, an inert tracer is any compound molecule used as the pure one-component mobile phase.[24] However, the selective detection of the injected molecules becomes impossible. So, in liquid chromatography (liquid-solid adsorption), the best practice so far consists of injecting a labelled solvent molecule (usually a deuterated solvent molecule detected by mass spectrometry) using the non-labelled solvent as the mobile phase,[23,24,87,88] assuming that the isotopic effect is negligible from an adsorption viewpoint. In most practical cases, an arbitrary and UV-active "non-retained" marker is usually chosen even though its retention may severely depend on the selected experimental conditions. Therefore, the chromatographers always measure arbitrary retention factors which relate to both a particular "non-retained" marker and specific elution conditions. The experimental retention factor of an analyte *i*, $k_{exp,i}$, is then measured from

$$k_{exp,i} = \frac{t_i - t_0}{t_0} \tag{4.1}$$

where t_i and t_0 are the retention times of the analyte and "non- retained" marker, respectively.

4.2.2 Molecular dynamics-predicted retention factor

The total number $n_{t,i}$ of any molecule *i* present in the chromatographic column is the sum of the number of molecules present in the mesopore volume ($n_{p,i}$) and that present in the interparticle volume ($n_{e,i}$):

$$n_{t,i} = n_{p,i} + n_{e,i} \tag{4.2}$$

By definition, the retention factor is a static property of the LC system at thermodynamic equilibrium. It is equal to the ratio of the total amount of the retained analyte molecule *i* ($n_{t,i}$) minus the total amount of any arbitrary "non-retained" marker molecules ($n_{t,0}$) to the total amount of the same "non-retained" marker molecules present in the column for the same concentration of both compounds in the bulk volume. Therefore, $n_{e,i} = n_{e,0}$ and the general expression of the retention factor is written

$$k = \frac{n_{t,i} - n_{t,0}}{n_{t,0}} = \frac{n_{p,i} - n_{p,0}}{n_{t,0}} \tag{4.3}$$

From MD simulations and considering a slit pore model, the density profiles (number of molecules per unit mesopore volume), $\rho_i(z)$ and $\rho_0(z)$, of the analyte *i* and "non-retained" t_0-marker, respectively, can be calculated as a function of the distance *z* from the silica surface. Therefore, the number of molecules *i* present in the mesopore volume is written as

$$n_{p,i} = 2 \int_0^{z_p} \rho(z) S \mathrm{d}z \tag{4.4}$$

where z_p and *S* are half the width and surface area, respectively, of the slit pore in the simulation model. Both z_p (monosized pore) and *S* (flat silica walls) are assumed constant. The factor 2

accounts for the presence of two surfaces in the slit pore model. After normalization of the density profiles $\rho_i(z)$ to their respective bulk density in the interparticle volume, $\rho_{i,bulk}$, the expression of the retention factor calculated from MD simulations is directly given from Eq. 4.3:

$$k_{\mathrm{MD}} = \frac{\int_0^{zp}\left(\frac{\rho_i(z)}{\rho_{i,bulk}} - \frac{\rho_0(z)}{\rho_{0,bulk}}\right)\mathrm{d}z}{\int_0^{zp}\rho_{0,bulk}\mathrm{d}z + \frac{n_{e,0}}{2S}} \qquad (4.5)$$

The denominator in Eq. 4.5 is independent of the nature of the analyte but cannot be determined by MD, because the simulations do not describe molecular motions in the interparticle volume of the column ($n_{e,0}$ is unknown). In contrast, the numerator is fully determined with the MD results as it only depends on the density profiles of the analyte and the arbitrary "non-retained" marker. As shown by the example in Figure 4.1, this integral corresponds to the area below the normalized density profile of the analyte and above that of the "non-retained" marker. The hatched area in Figure 4.1 represents the surface excess of adsorbed analyte molecules (here benzene, solid red curve) present in an RPLC column (100 Å C_{18}-silica slit-pore model, acetonitrile/water, 70/30, v/v, T = 300 K) with respect to the arbitrary "non-retained" marker molecules (here uracil, solid black curve) selected in the experiments. The calculated surface excess adsorption data is expected to be directly proportional to the experimental retention factor, while the proportionality constant (the denominator in Eq. 4.5) is directly scaled to the retention time of the "non-retrained" marker. It is the main purpose of this work to verify whether or not this linear relationship between k_{exp} and the MD-calculated surface excess adsorption holds in practice.

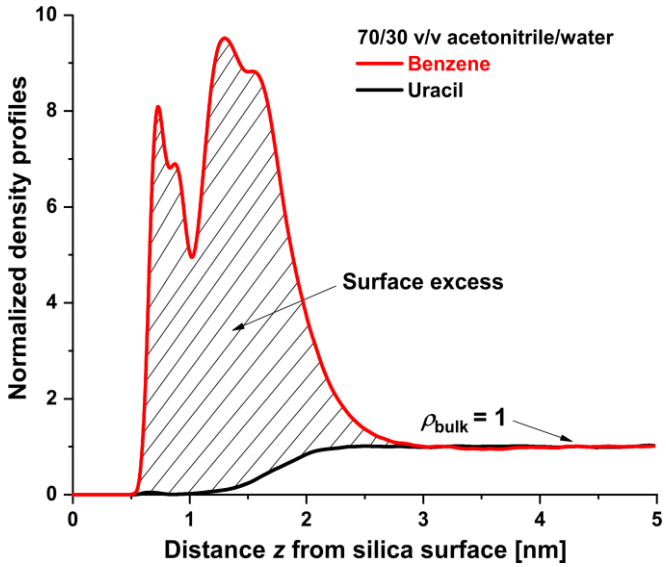

Figure 4.1. Representation of the surface excess adsorption (hatched area) of a retained analyte (benzene, solid red curve) relative to an arbitrary "non-retained" marker (uracil, solid black curve) at equilibrium at the interface between a C_{18}-silica stationary phase and an acetonitrile/water (70/30, v/v) bulk mobile phase. This area is located below the normalized (to the respective bulk density) profile of benzene and above that of uracil. For a distance z > 3 nm from the silica surface (z = 0), i.e., in the bulk region of the pore, the density profiles of all species are unity.

4.3 Experiments and methods

4.3.1 Chemicals

The solvents used in this work were water and acetonitrile and were Optima grade from Fisher Scientific (Fair Lawn, NJ, USA). Uracil, benzyl alcohol, acetophenone, benzene, and ethylbenzene were purchased from Millipore Sigma (St. Louis, Groton, CT, USA) with a minimum purity of 99%.

4.3.2 Liquid chromatography

Eight mobile phase mixtures were directly prepared from the binary solvent pump of the HPLC instrument. The programmed volume fraction of acetonitrile in water is then increased from 20% to 30%, 40%, 50%, 60%, 70%, 80% and to 90%. The chromatographic column used is a 4.6 mm ×150 mm column packed with 5 µm C_{18}-bonded High Strength Silica^{TM} (HSS) provided by Waters (Milford, MA, USA). The average mesopore size of these particles is 105 Å with a relative standard deviation (RSD) of about 15%. The surface coverage with C_{18}-chains as measured by elemental analysis is 2.7 µmol/m^2. The derivatized silica particles were endcapped with trimethylchlorosilane leading to an overall carbon content of 13.9% (elemental analysis). The HPLC system used in this work is a 1220 Infinity HPLC system (Agilent Technologies, Waldbronn, Germany). This instrument is equipped with a binary solvent pump, an autosampler (needle seat capillary, 20 µL flow through needle loop), a column oven (6 µL inlet tube volume), and a photodiode array detector (14 µL optical cell volume). The total extra-column volume is smaller than 25 µL. For the sake of comparison, the hold-up volume of the HSS-C_{18} column is around 1500 µL. Therefore, all measured retention factors were uncorrected for the contribution of the extra-column volume.
Each analyte was injected separately from the others and dissolved in a 50/50 v/v mixture of acetonitrile in water. The diluent-to-eluent mismatch has no impact on the observed retention because the injected sample volume is only 5 µL (< 0.5% of the hold-up volume). The oven temperature was set to T = 300 K. Retention factors of benzyl alcohol, acetophenone, benzene, and ethylbenzene were measured by selecting uracil as "non-retained" dead time marker. In fact, it is well-known that uracil is not an ideal marker in RPLC because its retention time depends on the content of acetonitrile in water.[23] The experimental retention factors of the analytes were then related to uracil by

$$k_{exp} = \frac{t_{r,i} - t_{r,uracil}}{t_{r,uracil}} \tag{4.6}$$

where $t_{r,i}$ is the observed retention time of the retained analyte i and $t_{\mathrm{r,uracil}}$ is the retention time of uracil.

4.3.3 Molecular dynamics simulations

The MD simulation results that form the basis in the current study for the construction of a framework enabling the prediction of RPLC retention factors (analyte density profiles in an RPLC

slit-pore model) have been published before.[9,89] These simulations have been performed with an established RPLC slit-pore model, acetonitrile/water mobile phases, and a chosen set of analytes.[9,72,73,75,89] Four aromatic hydrocarbons were selected that are typical analytes in RPLC.[73] Benzene and ethylbenzene are apolar molecules that differ in size; acetophenone and benzyl alcohol are weakly to moderately polar molecules that differ in their hydrogen bonding capabilities, i.e., acetophenone is a hydrogen bond acceptor, benzyl alcohol can act as hydrogen bond donor and acceptor. Each analyte species was introduced separately to our RPLC slit-pore model, which consists of a three-layer silica slab of 0.93 nm width (z-direction) placed between 5 nm wide solvent reservoirs in a ($x \times y \times z$) = 12.14 ×13.20 ×10.93 nm^3 simulation box. With periodic boundary conditions, the system equals a 10 nm wide slit pore. The slab was cut from β-cristobalite SiO_2 parallel to the (111) face, resulting in a surface with 4.5 silanol groups nm^{-2}. The surface was randomly grafted with C_{18} chains and trimethylsilyl groups at densities of 1.87 chains $nm^{-2}$and 0.56 groups nm^{-2}, respectively. This left 2.06 residual OH groups nm^{-2}on the surface. For the silica surface atoms (Si, O, and H), the force-field parameters from Gulmen and Thompson[90] were taken. C_{18} chains, trimethylsilyl groups, and acetonitrile molecules were described by the transferable potentials for phase equilibria united-atom (TraPPE-UA) force field.[91.92]. For acetonitrile/water, the simple point charge/extended (SPC/E) force field was used for water molecules.[93]. All analytes were treated with the explicit CHARMM general force field (CGenFF).[94] Force fields used for MD simulations of RPLC systems have to account for the following interactions: solvent–solvent, solvent–silica surface, solvent–bonded phase, solvent–analyte, analyte–silica surface, and analyte–bonded phase. Thus, the force field chosen for a specific component may differ from the appropriate force-field choice for the same component in a different setting, e.g., when predicting the fluid phase equilibria of water–alkane mixtures.[95] Our force-field selection focused on finding the right combination to closely approximate experimental conditions in RPLC. For the acetonitrile/water system, we arrived at the described combination in several stages. First, the force fields for acetonitrile (TraPPE- UA) and water (SPC/E) molecules of the mobile phase were chosen following Mountain,[82] who showed that the combination of SPC/E and TraPPE-UA reproduces hydrogen bonding in and liquid density of acetonitrile/water mixtures well. This is a major requisite for recovering the experimental diffusion coefficients of solvent and analyte molecules in the bulk liquid. It was next established that the chosen force fields for mobile-phase solvents and silica surface account for the interaction of acetonitrile/water mixtures with bare-silica surfaces and reproduce the experimentally observed dependence of the retention factor on the acetonitrile fraction in the mobile phase in hydrophilic interaction liquid chromatography (HILIC).[83,96] Introduction of the force field for the bonded phase yielded solvent and solute density profiles[9,73] that were consistent with those simulated earlier for RPLC systems by the Siepmann group[97,98] and the Meuwly group,[76,99] who had used different force fields for the mobile-phase solvents. The CHARMM force field for the solutes was chosen, because it provided parameters for every analyte species we intended to study. Comparison of distribution coefficients calculated from the simulated density profiles of RPLC analytes with their experimental retention factors proved that our mesopore model and particular force-field combination are able to reproduce the retentive properties of an RPLC column.[9] MD simulations using the described force-field

combination[72,73,75,96,100] have successfully explained and predicted the experimentally observed retention and surface diffusion behavior of analytes in RPLC and HILIC systems.[79,101,102] The MD simulations were run with GROMACS[103,104] at 300 K for a canonical *NVT* ensemble (constant number of molecules *N*, simulation box volume *V*, and temperature *T*). Analyte species were each simulated ($N_{analyte}$ = 10 corresponding to *c* analyte ≈ 10 mmol L^{-1}) for eight acetonitrile/water ratios between 20/80 and 90/10 v/v, yielding a total of 5 × 8 = 40 simulation systems. The necessary number of acetonitrile and water molecules in the simulation box, $N_{acetonitrile}$ and N_{water}, respectively, to recover mobile phase of targeted acetonitrile/water ratio were determined in preliminary simulations for an *NPT* ensemble (constant number of molecules, pressure *P*, and temperature). Values for $N_{acetonitrile}$ and N_{water} were manually adjusted between simulation runs until acetonitrile and water densities in the center of the slit pore approached the respective solvent densities of the targeted acetonitrile/water mixture to an accuracy of 1%. This procedure ensured that equilibrated systems reproduce the result of column equilibration in chromatographic practice, that is, the acetonitrile and water number densities in the bulk region of the pore recovered the targeted acetonitrile/water ratio of the mobile phase after acetonitrile ditch formation was complete. The acetonitrile ditch is an acetonitrile-rich border region between the ends of the bonded- phase chains and the bulk region of the pore.[73] Ditch formation is driven by the hydrophobic effect.[105] Our MD simulations have proven that the local solvent ratio in the acetonitrile ditch favors the diffusivity of acetonitrile and small organic analytes compared to the water-rich mobile phase in the bulk region and have shown how surface diffusion and retention in RPLC are connected to this enrichment of acetonitrile molecules around the ends of the C_{18} chains. For the calculation of analyte density profiles as a function of *z*, the distance normal to the slit-pore surface, we first specified a bin width and counted the number of molecules in each bin over the chosen time span. This count was then normalized to the respective bin volume and observation time. Analyte density profiles $\rho(z)$ based on the center-of-mass of the analyte molecules were calculated from the complete trajectories (500–1000 ns) using a 0.05 nm bin size. These profiles were subsequently normalized to the constant analyte density ρ_{bulk} observed in the bulk region of the pore for z > 3 nm, where all properties of the bulk, unconfined solvent mixtures like the acetonitrile/water ratio and the diffusive mobility of solvent and analyte molecules are recovered.

4.4 Results and discussion

In the first part of the results and discussion section, the MD-based density profiles of the five small, neutral compounds (uracil, benzyl alcohol, acetophenone, benzene, and ethylbenzene) are reported for the 100 Å RPLC slit pore model and eight mobile phase compositions (acetonitrile/water mixtures with 20 to 90% acetonitrile by volume). This model mimics the analyte distribution across the actual mesopores (average mesopore size 105 Å, RSD 15%) of the 5 µm HSS-C_{18} fully porous particles. Insight into their retention mechanism in RPLC is revealed and the challenge for the chromatographers to find accurate retention models in RPLC is stressed. In the second part, the predicted retention factors are compared with the experimental ones. Eventual discrepancies are discussed and possible interpretations are proposed to be tested in the future.

4.4.1 Molecular dynamics simulations

MD simulations-based density profiles of uracil, benzyl alcohol, acetophenone, benzene, and ethylbenzene are shown in Figure 4.2, spanning from the silica surface ($z = 0$) to the center of the pore ($z = 5$ nm). For $z > 3$ nm a bulk region is realized, in which the concentrations of all species (water, acetonitrile, and analytes) are uniform.

It is important to note that density profiles were normalized to unity in the bulk region in order to visualize directly the excess adsorbed amount of the four retained analytes (benzyl alcohol, acetophenone, benzene, and ethylbenzene) relative to the reference "hold-up" marker (uracil). It is also important to mention that uracil is not an ideal column hold-up marker[23,89] but will be the one used in the experiments.

As expected, the smaller the volume fraction of acetonitrile in the bulk region (i.e., the higher the retention), the larger the intensity of the normalized densities and the least visible the bulk density of unity for distances of $d > 3$ nm from the surface.

Remarkably, irrespective of the mobile phase composition and the polarity of the retained analyte, the MD simulations reveal unambiguously that the underlying retention mechanism of these small, neutral compounds is qualitatively the same: the analytes tend to preferentially accumulate either at the very interface between the end of the C_{18} chains and the bulk eluent (a so-called "adsorption site" located at an average distance of about 1.5 nm from the surface) or deeper within the C_{18} chains (a so-called "partitioning site" at about 0.8 nm from the surface).[9,74,75,78,89,106] These MD simulations applied to small, neutral analytes with a single aromatic ring confirm predictions from previous MD simulations considering benzene derivative analytes[78] and MC simulations related to the density profiles of smaller alkane (n-butane) and alcohol (1-propanol) analytes in RPLC.[8,107]

The present simulation results also agree with experimental data regarding the heterogeneity of adsorption of similar sized analytes in RPLC: for instance, the adsorption isotherms of the small molecules phenol and caffeine on various endcapped C_{18}-silica stationary phases were unambiguously described by a bi-Langmuir adsorption isotherm.[108–110]

It was hypothesized that at least two distinct sites had to be involved in the retention of these two compounds: one at the very interface between the C_{18} chains and the bulk eluent ("low-energy site") and the second within the C_{18} chains ("high-energy site") which surround the analyte.[7,110,111]

The area under the two main peaks of the density profiles shown in Figure 4.2 provide then a direct estimate of the relative importance of the adsorption- and partitioning-like sites for the retention of the analytes. Interestingly, the larger the hydrophobic character of the small, neutral compound, the larger the contribution of the partitioning-like relative to the adsorption-like mechanism: although very similar in molecular size and weight, it is largest for ethylbenzene and smallest for benzyl alcohol because of the unfavorable interaction between the polar hydroxyl group of benzyl alcohol and the apolar methylene groups of the C_{18} chains.

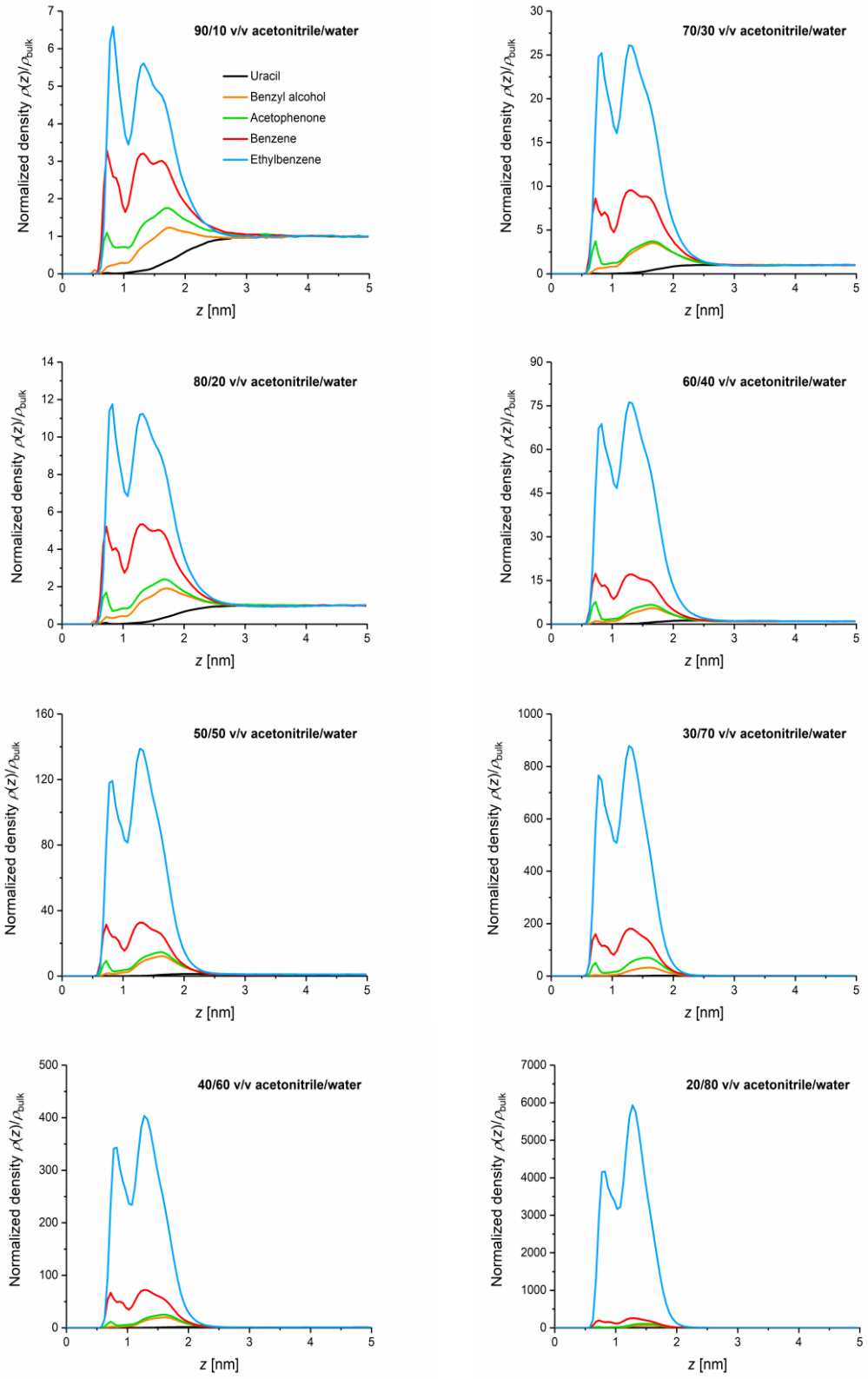

Figure 4.2. MD simulation-based density profiles (normalized to the bulk density) of uracil (solid black curve), benzyl alcohol (solid orange curve), acetophenone (solid green curve), benzene (solid red curve), and ethylbenzene (solid blue curve) at equilibrium between the C_{18}-silica surface and

eight different bulk aqueous mixtures containing 20%, 30%, 40%, 50%, 60%, 70%, 80%, and 90% acetonitrile by volume. The temperature in the MD simulation was set to 300 K.

This effect is mainly enthalpic. From an experimental viewpoint, it was shown that steric hindrance can also play a decisive role regarding the importance of the partitioning-like sites on retention in RPLC: for instance, despite the same polarity of the hydroxyl group, the partitioning-like sites account for nearly 40% of the retention of phenol (six carbon atoms),[110] roughly 10% of the retention of benzyl alcohol (one more carbon atom, this work), and they are virtually absent for the retention of 4-t*ert*-butylphenol (4 more carbon atoms, Langmuir isotherm).[112] This is explained by the increasing size of the side group attached to the phenyl ring, hence, the decreasing access of the analyte in between the C_{18} chains. This effect is essentially entropic. In particular, El Hage et al.[78] have used a combination of accurate force fields and free-energy simulations that allow to interpret experiments at a quantitative level, and their computed free-energy curves provide valuable insight into the retention mechanism. These curves support a RPLC retention model in which the analytes explore either an equilibrium between partitioned and desorbed state or coupled equilibria (adsorbed ↔ partitioned) ↔ desorbed. In conclusion, the present MD simulations fully support the importance of both enthalpic and entropic effects on the retention mechanism in RPLC with the invaluable addition of visualizing and providing a clear microscopic interpretation for the variation of the macroscopic retention factors of a large variety of analytes measured by the chromatographer. Most importantly, these simulation studies emphasize the current challenge to provide physically sound and simple a priori retention models capable of predicting accurately the retention factors in RPLC. This point is underlined by the complexity of the reported analyte density profiles. In the next section, we investigate the alternative possibility of predicting the retention of small, neutral compounds from MD simulations using a single slit-pore model to represent the morphology and dynamics in a manufactured C_{18}-silica particle.

4.4.2 Prediction of retention factors by molecular dynamics simulations

In this section, the results obtained by the MD simulations (density profiles $\rho(z)$ as a function of distance z from the silica surface) and the corresponding calculation of the expected surface excess adsorption of the four analytes with respect to that of uracil (see numerator in Eq. 4.5 and corresponding hatched area in Figure 4.1) are reported and directly compared to the experimental retention factors measured under the same conditions of temperature (T = 300 K) and mobile phase composition (eight acetonitrile/water mixtures from 20/80 to 90/10 v/v). In addition to the necessary physicochemical prerequisites in this work (MD simulation box and force fields, Section 4.3.3), it is important to recall here the main points (inherently) made in the MD simulations when used to predict the retention factors of small, neutral compounds on the HSS-C_{18} RPLC column.

- The morphology of the actual mesopore network of the particles is represented by a slit pore geometry with parallel, flat surfaces (see the two top graphs in Figure 4.3).

- The actual pore size distribution of the mesoporous particles (average pore size 105 Å, standard deviation 15 Å) is reduced to a constant pore width of 100 Å in the slit pore model (see the two bottom graphs in Figure 4.3).

- The surface coverage with C_{18} chains is 3.11 µmol m^{-2} for the slit pore model but only 2.70 µmol m^{-2} for the HSS-C_{18} particles.

With a properly set up simulation system and validated force field combinations (Section 4.3.3), the MD simulations can become a truly a priori approach for the prediction of retention in liquid chromatography. The remaining question is to know whether or not these predictions are accurate when compared to experiments. In theory and by the definition of the capacity factor in chromatography, the plots of the surface excess of adsorption of the analytes against the retention factors are expected to be linear (see numerator in Eq. 4.5) and the slopes of these plots should be directly proportional to the retention times of the column "hold-up" marker (denominator in Eq. 4.5).

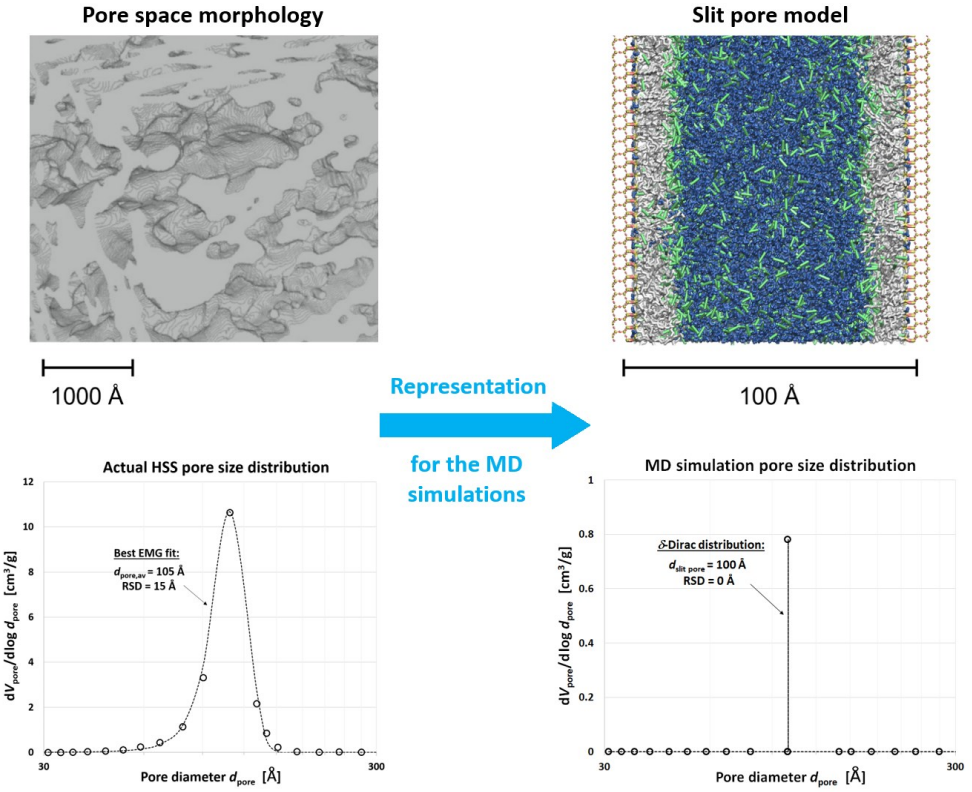

Figure 4.3. Comparison between the actual silica mesopore space morphology (top left tomographic reconstruction) and the slit mesopore model used in the MD simulations (top right snapshot) and between the actual mesopore size distribution of the 5 µm HSS particles (bottom left graph) and that in the simulations (bottom right graph).

Plots of the MD-based surface excess of adsorption versus the experimental retention factors are shown in Figure 4.4 for the eight mobile phase compositions investigated. First, it is important to

note that the elution order of the four analytes selected in this work is correctly predicted by the MD simulations: this is the most essential requirement for the MD simulations because the variations in polarity and hydrophobicity between analytes are noticeable: the polarity clearly increases from ethylbenzene to acetophenone and to benzyl alcohol, while the hydrophobicity increases from benzene to ethylbenzene.

Secondly, the calculated surface excess of adsorption should be directly proportional to the experimental retention factors. The eight plots shown in Figure 4.4 reveal that the best linear fits (*y*-intercept fixed at 0) to the data are always good with $R^2 > 0.985$. The most remarkable achievement is that the linear range covers about three orders of magnitude for the retention factor, i.e., from $k_{exp,min} = 0.15$ (benzyl alcohol, 90% acetonitrile) to $k_{exp,max} = 183$ (ethylbenzene, 20% acetonitrile). The second requirement, agreement over a wide range of retention factors, is then also satisfied by the MD simulations.

Finally, the last requirement is that the slopes of the linear fits should in theory be scalable to the amount of uracil molecules present in the entire column, that is, to the retention time of uracil. The slopes of the linear fits represented by the black dotted lines in Figure 4.4 vary from 9.1 to 8.7, 8.9, 8.3, 8.8, 10.5, 11.3, and to 10.8 nm when decreasing the volume fraction of acetonitrile from 90% to 80%, 70%, 60%, 50%, 40%, 30%, and to 20%, respectively.

Even though these slopes are quite consistent around 10 nm, it is important to mention that they do not correlate perfectly with the observed variation of the retention times of uracil. Indeed, the measured retention times, t_0, of uracil vary from 1.50 to 1.44, 1.40, 1.38, 1.39, 1.42, 1.48, and 1.57 min, respectively. This is illustrated in Figure 4.5 where the plot of these slopes versus the retention times of uracil is shown. R^2 is only 0.29, but still, the overall trend makes sense: the retention times of uracil are first reduced when decreasing the volume fraction of acetonitrile from 90 to 60% (slight uracil exclusion from the formed acetonitrile ditch,[23,89] the slope is smallest at 8.3 nm for 60% acetonitrile) and then increase when decreasing further the volume fraction of acetonitrile from 60 to 20% (slight uracil retention,[23] the slopes are highest for 30 and 20% acetonitrile). To summarize, the slopes of the plots shown in Figure 4.4 are expected to be proportional to the amount of the selected non-retained marker uracil in the column, that is, to its retention time (see Eq. 4.5). It has been observed that the retention time of uracil is minimum for volume fractions of acetonitrile in the range from 60 to 90% acetonitrile in water. This is due to the thick acetonitrile ditch present on top of the C_{18} -bonded layer and to the near zero solubility of uracil in acetonitrile-rich eluents.[23,73] Eventually, the plot in Figure 4.5 confirms these observations even though the correlation between the slopes and the retention times of uracil is not perfect.

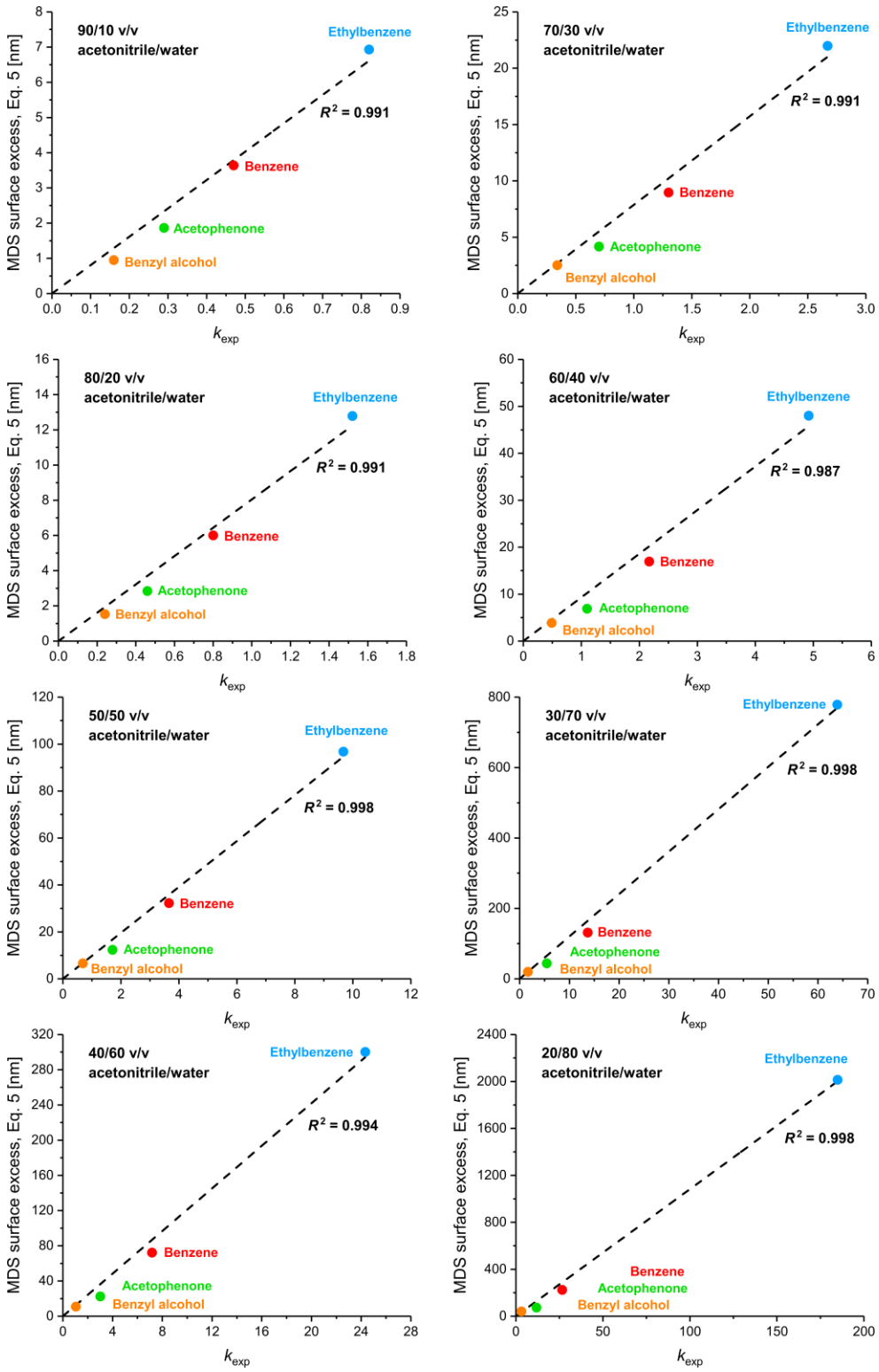

Figure 4.4. Plots of the MD simulation-based surface excess adsorption (relative to uracil) of the retained analytes benzyl alcohol (solid orange circle), acetophenone (solid green circle), benzene (solid red circle), and ethylbenzene (solid blue circle) as a function of the experimental retention factor, k_{exp}, of the four compounds measured on the 4.6 mm ×150 mm column packed with 5 µm

HSS-C_{18} particles (x-axis). The MD surface excess adsorption data (y-axis) correspond to equilibrium between the C_{18}-silica surface, the analytes, and the bulk acetonitrile/water mobile phases (eight different mixtures containing 20%, 30%, 40%, 50%, 60%, 70%, 80%, and 90% acetonitrile by volume) at $T = 300$ K. Note the good linear correlation between MD surface excess adsorption and k_{exp} ($R^2 > 0.98$).

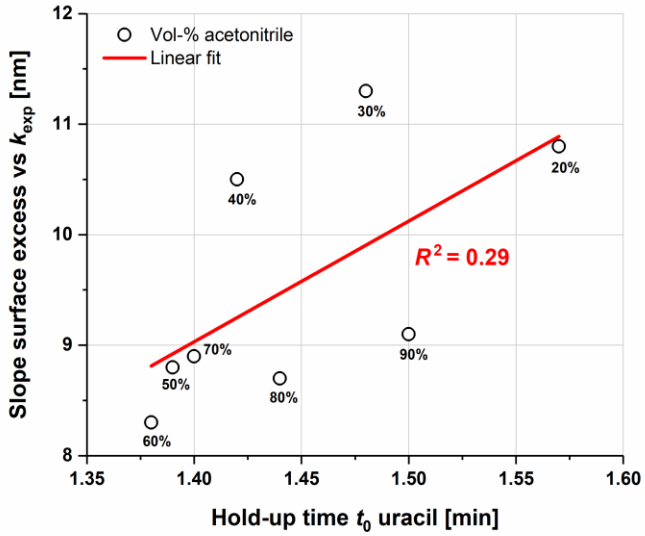

Figure 4.5. Plot of the best slopes for the surface excess adsorption of the four analytes versus their experimental retention factors (see Figure 4.4) as a function of the experimental retention time of the selected column "hold-up" marker, uracil.

In conclusion, the present MD simulations are well suited to predict the retention factors of small, neutral analytes in RPLC. Still, they are somewhat limited for predicting very accurately (< 1% relative error) the observed retention factors of such analytes in RPLC. Remarkably, the discrepancies observed in Figure 4.4 between the calculated surface excess of adsorption and k_{exp} appear to be systematic: for instance, the excess adsorbed amount of acetophenone and ethylbenzene are apparently slightly under- and overestimated, respectively, with respect to their experimental retention factors. This remains true for all the mobile phase compositions. It is still speculative at this point to provide a clear and convincing explanation for such a minor disagreement. First and foremost, the MD simulation box does not exactly recover the actual microstructure and, thus, the retentive properties of the bonded phase due to the difference in C_{18} surface coverages (3.11 µmol m^{-2} in the simulations versus 2.70 µmol m^{-2} in the experiments). That is, the reduction of the surface coverage from 3.11 to 2.70 µmol m^{-2} in the simulations would immediately decrease the surface excess of adsorption of ethylbenzene and improve the agreement with experiments. In addition, the local surface curvature and pore size distribution of the particles may become experimentally relevant in RPLC. In this respect, a recent MD simulation study has demonstrated the impact of pore shape (planar versus cylindrical) on the pore-level density

distribution of the C_{18} chains and, thus, on the retentive properties of the bonded phase in RPLC.[106] The impact of pore curvature is enhanced with decreasing pore size and, ultimately, for sufficiently small pores (about 6-nm diameter and smaller), a bulk mobile phase will not be realized any longer in the center of the pore due to acetonitrile ditch overlap.[113] This leads to different surface excess of adsorption in comparison to those of the analyte in larger mesopores. These hypotheses deserve attention and careful evaluation in future MD simulation studies.

4.5 Conclusions

In this work, MD simulations have been used to calculate the surface excess of adsorption of small, neutral RPLC analytes (benzyl alcohol, acetophenone, benzene, and ethylbenzene) in an RPLC slit pore model (100 Å slit width) in equilibrium with various acetonitrile/water mobile phases. The surface excesses referred to uracil, a classical column hold-up marker in RPLC. The goal was to predict a priori the retention factors measured with a commercially available C_{18}-silica stationary phase (HSS-C_{18} column, 105 Å average pore size, 15 Å standard deviation) using the same mobile phase compositions, analytes, and temperature as in the MD simulations. The results have demonstrated that the expected linear correlation between the surface excess of adsorption of an analyte based on the MD simulations with the RPLC slit-pore model and the experimental retention factor is good ($R^2 > 0.985$). Retention factors varied from 0.15 to 183, that is, they covered three orders of magnitude of retention. The MD simulations account very well for the methylene selectivity and for the change in analyte polarity from an alcohol to a ketone and to an alkyl group. Still, the reported agreement is not quantitative and some subtle differences between the MD-calculated results and the experimental retention factors remain. In this respect, the retentive properties of the bonded phase would have to be perfectly matched. This first and foremost addresses the density of the C_{18} chains and endcapping groups on the silica surface. It is important to recall that the direct comparison between the experimental retention factor and the MD-calculated retention factor is possible when either 1) preliminary calibration data is carried out for a single retained analyte from which the unique column phase ratio is extracted or 2) the ratio of the external pore volume to the internal pore volume of the column is known and the density profile of an ideally inert compound (e.g., deuterated acetonitrile in an acetonitrile mobile phase) is calculated by MD. In this latter case, no preliminary calibration data are needed to predict retention factors in LC. In perspective, the next challenging application of the MD simulations for column selection, characterization, and retention prediction in RPLC will be an extension to charged analytes often encountered in the pharmaceutical industry. This task is currently under investigation and will shed light on the still debated retention mechanism of ionizable compounds in RPLC.

References

1 L.R. Snyder, J.J. Kirkland, J.L. Glajch, *Practical HPLC Method Development*, 2nd Ed, John Wiley and Sons, New York, **1997**.

2 S. Ahuja, H. Rasmussen, HPLC Method Development for Pharmaceuticals, Vol 8, Academic Press, New York, **2007**.

3 Y. Kazakevich, R. Lobrutto, HPLC for Pharmaceutical Scientists, Wiley, Hoboken, **2007**.

4 F.T. Mattrey, A. A. Makarov, E. L. Regalado, F. Bernardoni, M. Figus, M. B. Hicks, J. Zheng, L. Wang, W. Schafer, V. Antonucci, S. E. Hamilton, K. Zawatzky, C.J. Welch, *TrAC* **2017**, *95*, 36–46.

5 C. Horvath, W. Melander, I. Molnár, *J. Chromatogr. A* **1976**, *125*, 129–156.

6 P.W. Carr, L.C. Choo, J.H. Park, *J. Chromatogr. A* **1996**, *724*, 1–12.

7 F. Gritti, G. Guiochon, *J. Chromatogr. A* **2005**, *1099*, 1–42.

8 R. K. Lindsey, J. L. Rafferty, B. L. Eggimann, J. I. Siepmann, M. R. Schure, *J. Chromatogr. A* **2013**, *1287*, 60–82.

9 J. Rybka, A. Höltzel, A. Steinhoff, U. Tallarek, *J. Phys. Chem. C* **2019**, *123*, 3672–3681.

10 I. Molnar, *J. Chromatogr. A* **2002**, *965*, 175–194.

11 A. Schmidt, I. Molnar, *J. Chromatogr. A* **2002**, *948*, 51–63.

12 M. R. Euerby, F. Scannapieco, H.-J. Rieger, I. Molnar, *J. Chromatogr. A* **2006**, *1121*, 219–227.

13 S. Fekete, J. Fekete, I. Molnar, K. Ganzler, *J. Chromatogr. A* **2009**, *1216*, 7816–7823.

14 M. Swartz, P. H. Lukulay, I. Krull, J. Turpin, R. Verseput, *LC-GC North America* **2008**, *26*, 1190–1197.

15 S. C. Porter, R. P. Verseput, C. R. Cunningham, *Pharm. Technol.* **1997**, *21*, 1–7.

16 P. K. Sahua, N. R. Ramisetti, T. Cecchi, S. Swain, C. S. Patro, J. Panda, *J. Pharm. Biomed. Anal.* **2018**, *147*, 590–611.

17 T. Bolanca, S. Cerjan-Stefanovica, M. Regelja, H. Regelja, S. Loncaric, *J. Chromatogr. A* **2005**, *1085*, 74–85.

18 K. Heberger, *J. Chromatogr. A* **2007**, *1158*, 273–305.

19 A. Felinger, A. Cavazzini, G. Guiochon, *J. Chromatogr. A* **2003**, *986*, 207–225.

20 A. Cavazzini, A. Felinger, G. Guiochon, *J. Chromatogr. A* **2003**, *1012*, 139–149.

21 G. Guiochon, A. Felinger, A. Katti, D. Shirazi, Fundamentals of Preparative and Nonlinear 492 Chromatography, 2nd ed, Academic Press, Boston, MA, 2006.

22 F. Gritti, *Anal. Chem.* **2021**, *93(14)*, 5653–5664.

23 F. Gritti, K. Smith, *LC-GC North America* **2022**, *40(11)*, 2–4.

24 J. Knox, R. Kaliszan, *J. Chromatogr. A* **1985**, *349*, 211–234.

25 Y. V. Kazakhevich, H. M. McNair, *J. Chromatogr. Sci.* **1993**, *31*, 317–322.

26 Y. V. Kazakhevich, H. M. McNair, *J. Chromatogr. Sci.* **1995**, *33*, 321–327.

27 F. Gritti, G. Guiochon, *J. Chromatogr. A* **2007**, *1155*, 85–99.

28 F. Gritti, J. Sehajpal, J. Fairchild, *J. Chromatogr. A* **2017**, *1489*, 95–106.
29 F. Gritti, G. Guiochon, *J. Chromatogr. A* **2014**, *1340*, 50–58.
30 F. Gritti, G. Guiochon, *J. Chromatogr. A* **2014**, *1344*, 66–75.
31 F. Gritti, G. Guiochon, *J. Chromatogr. A* **2014**, *1356*, 96–104.
32 D. Asberg, J. Samuelsson, M. Lesko, A. Cavazzini, K. Kaczmarski, T. Fornstedt, *J. Chromatogr. A* **2015**, *1401*, 52–59.
33 D. Asberg, J. Samuelsson, T. Fornstedt, *J. Chromatogr. A* **2016**, *1457*, 97–106.
34 J. Kostka, F. Gritti, K. Kaczmarski, G. Guiochon, *J. Chromatogr. A* **2010**, *1217*, 4704–4712.
35 P. G. Boswell, J. R. Schellenberg, P. W. Carr, J. D. Cohen, A. D. Hegeman, *J. Chromatogr. A* **2011**, *1218*, 6732–6741.
36 R. W. Taft, J.-L. M. Abboud, M. J. Kamlet, M. A. Abraham, *J. Solution Chem.* **1985**, *14*, 153–186.
37 P.C. Sadek, P.W. Carr, R.M. Doherty, M.J. Kamlet, R.W. Taft, M.A. Abraham, *Anal. Chem.* **1985**, *57*, 2971–2978.
38 A. Wang, P.W. Carr, *J. Chromatogr. A* **2002**, *965*, 3–23.
39 A. Wang, L.C. Tan, P.W. Carr, *J. Chromatogr. A* **1999**, *848*, 21–37.
40 M. Vitha, P.W. Carr, *J. Chromatogr. A* **2006**, *1126*, 143–194.
41 T. Hanai, *J. Chromatogr. A* **1991**, *550*, 313–324.
42 R. Kaliszan, *Chem. Rev.* **2007**, 3212–3246.
43 R. Kaliszan, *J. Chromatogr. A* **1993**, *656*, 417–435.
44 R. Kaliszan, *Anal. Chim. Acta* **2013**, *797*, 13–19.
45 Y. Wen, R. I. J. Amos, M. Talebi, R. Szücs, J. W. Dolan, C. A. Pohl, P. R. Haddad, *Anal. Chem.*, **2018**, *1000*, 20–40.
46 R. I. J. Amos, P. R. Haddad, R. Szücs, J. W. Dolan, C. A. Pohl, *TrAC* **2018**, *105*, 352–359.
47 P. Žuvela, J. Jay Liu, K. Marcur, T. Baczek, *Chem. Rev.* **2015**, *87*, 9876–9883.
48 P. Žuvela, K. Marcur, J. Jay Liu, T. Baczek, *J. Pharm. Biomed. Anal.* **2016**, *127*, 94–100.
49 P. Žuvela, M. Skoczylas, J. Jay Liu, T. Baczek, R. Kaliszan, M. Wong, B. Buszewski, *Chem. Rev.* **2019**, *119*, 3674–3729.
50 B. K. Ng, T. T. Y. Tan, R. A. Shellie, G. W. Dicinoski, P. R. Haddad, *TrAC*, **2016**, *80*, 625–635.
51 M. Taraji, P. R. Haddad, R. I. J. Amos, M. Talebi, R. Szücs, J. W. Dolan, C. A. Pohl, *J. Chromatogr. A* **2017**, *1507*, 53–62.
52 M. Taraji, P. R. Haddad, R. I. J. Amos, M. Talebi, R. Szücs, J. W. Dolan, C. A. Pohl, *Anal. Chim. Acta* **2018**, *1000*, 20–40.
53 P.R. Haddad, M. Taraji, R. Szücs, *Anal. Chem.* **2021**, *93*, 228–256.
54 M. Witting, S. Böcker, *J. Sep. Sci.* **2020**, *43*, 1746–1754.
55 L. Moruz, L. Käll, *Mass Spectrom. Rev.* **2017**, *36*, 615–623.
56 M. H. Abraham, W. E. Acree, *J. Chromatogr. A* **2016**, *1430*, 2–14.

57 E. Tyteca, J.-L. Veuthey, G. Desmet, D. Guillarme, S. Fekete, *Analyst* **2016**, *141*, 5488–5501.

58 I. A. Tarasova, C. D. Masselon, A. V. Gorshkov, M. V. Gorshkov, *Analyst* **2016**, *141*, 4816–4832.

59 D. Sykora, J. Vozka, E. Tesarova, *J. Sep. Sci.* **2016**, *39*, 115–131.

60 O. Krokhin, V. Spicer, *Curr. Protoc. Bioinform.* **2010**, *31*, 13.14.1–13.14.15.

61 C. Liu, H. Wang, Y. Fu, Z. Yuan, H. Chi, L. Wang, R. Sun, S. He, *J. Chromatogr. A* **2010**, *28*, 529–534.

62 R. Kaliszan, T. Baczek, *Proteomics* **2009**, *9*, 835–847.

63 T. Baczek, *Curr. Pharm. Anal.* **2008**, *4*, 151–161.

64 K. Shinoda, M. Sugimoto, M. Tomita, Y. Ishihama, *Proteomics* **2008**, *8*, 787–798.

65 R. Put, Y. Vander Heyden, *Anal. Chim. Acta* **2007**, *602*, 164–172.

66 M. Garca-lvarez Coque, J. R. Torres-Lapasi, J. J. Baeza-Baeza, *Anal. Chim. Acta* **2006**, *579*, 125–145.

67 C. H. Lochmüller, C. Reese, A. J. Aschman, S. J. Breiner, *Anal. Chim. Acta* **1993**, *656*, 3–18.

68 Y. Baba, *J. Chromatogr. A* **1989**, *485*, 143–168.

69 J. Walczak-Skierska, M. Szultka-Mlynska, K. Pauter, B. Buszewski, *J. Pharm. Biomed. Anal.* **2020**, *184*, 113187.

70 L. Zhang, J. L. Rafferty, J. I. Siepmann, B. Chen, M. R. Schure, *J. Chromatogr. A* **2006**, *1126*, 219–231.

71 J. L. Rafferty, L. Zhang, J. I. Siepmann, M. R. Schure, *Anal. Chem.* **2007**, *79*, 6551–6558.

72 J. Rybka, A. Höltzel, S. M. Melnikov, A. Seidel-Morgenstern, U. Tallarek, *Fluid Phase Equilib.* **2016**, *407*, 177–187.

73 J. Rybka, A. Höltzel, U. Tallarek, *J. Phys. Chem. C* **2017**, *121*, 17907–17920.

74 J. Rybka, J. Kärger, U. Tallarek, *ChemPhysChem* **2017**, *18*, 2094–2102.

75 J. Rybka, A. Höltzel, N. Trebel, U. Tallarek, *J. Phys. Chem. C* **2019**, *123*, 21617–21628.

76 J. Braun, A. Fouqueau, R. J. Bemish, M. Meuwly, *Phys. Chem. Chem. Phys.* **2008**, *10*, 4765–4777.

77 K. El Hage, R. J. Bemish, M. Meuwly, *Phys. Chem. Chem. Phys.* **2018**, *20*, 18610–18622.

78 K. El Hage, P.K. Gupta, R.J. Bemish, M. Meuwly, *J. Phys. Chem. Lett.* **2017**, *8*, 4600–4607.

79 F. Gritti, A. Höltzel, U. Tallarek, G. Guiochon, *J. Chromatogr. A* **2015**, *1376*, 112–125.

80 F. Gritti, *J. Chromatogr. Sep. Tech.* **2015**, *6*, 1000309.

81 F. Gritti, J. Hochstrasser, A. Svidrytski, D. Hlushkou, U. Tallarek, *J. Chromatogr. A* **2020**, *1620*, 460991.

82 R. D. Mountain, *J. Phys. Chem. B* **2010**, *114*, 16460–16464.

83 R. D. Mountain, *J. Phys. Chem. C* **2013**, *117*, 3923–3929.

84 M. A. Gonzalez, *Collection SFN* **2011**, *12*, 169–200.
85 U. Tallarek, D. Hlushkou, A. Höltzel, *J. Phys. Chem. C* **2022**, *126*, 2336–2348.
86 F. Riedo, E. Kováts, *J. Chromatogr. A* **1982**, *239*, 1–28.
87 R. M. McCormick, B. L. Karger, *J. Chromatogr. A* **1980**, *199*, 259–273.
88 R. M. McCormick, B. L. Karger, *Anal. Chem.* **1980**, *52*, 2249–2257.
89 N. Trebel, A. Höltzel, A. Steinhoff, U. Tallarek, *J. Chromatogr. A* **2021**, *1640*, 461958.
90 T. S. Gulmen, W. H. Thompson, *Langmuir* **2006**, *22*, 10919–10923.
91 M. G. Marin, J. I. Siepmann, *J. Phys. Chem. B* **1998**, *102*, 2569–2577.
92 C. D. Wick, J. M. Stubbs, N. Rai, J. I. Siepmann, *J. Phys. Chem. B* **2005**, *109*, 18974–18982.
93 H. J. C. Berendsen, J. R. Grigera, T. P. Straatsma, *J. Phys. Chem.* **1987**, *91*, 6269–6271.
94 K. Vanommeslaeghe, E. Hatcher, C. Acharya, S. Kundu, S. Zhong, J. Shim, E. Darian, O. Guvench, P. Lopes, I. Vorobyov, A.D. Mackerell Jr., *J. Comput. Chem.* **2010**, *31*, 671–690.
95 B. Xue, D.B. Harwood, J.L. Chen, J.I. Siepmann, *J. Chem. Eng. Data* **2018**, *63*, 4256–4268.
96 S. M. Melnikov, A. Höltzel, A. Seidel-Morgenstern, U. Tallarek, *Angew. Chem. Int. Ed.* **2012**, *51*, 6251–6254.
97 J. L. Rafferty, J. I. Siepmann, M. R. Schure, *J. Chromatogr. A* **2011**, *1218*, 2203–2213.
98 J. L. Rafferty, J. I. Siepmann, M. R. Schure, *J. Chromatogr. A* **2011**, *1218*, 9183–9193.
99 A. Fouqueau, M. Meuwly, R. J. Bemish, *J. Phys. Chem. B* **2007**, *111*, 10208–10216.
100 S. M. Melnikov, A. Höltzel, A. Seidel-Morgenstern, U. Tallarek, *Anal. Chem.* **2013**, *85*, 8850–8856.
101 F. Gritti, G. Guiochon, *J. Chromatogr. A* **2013**, *1297*, 85–95.
102 F. Gritti, *J. Chromatogr. A* **2015**, *1140*, 90–98.
103 B. Hess, C. Kutzner, D. van der Spoel, E. Lindahl, *J. Chem. Theory Comput.* **2008**, *4*, 435–447.
104 M. J. Abraham, T. Murtola, R. Schulz, S. Páll, J. C. Smith, B. Hess, E. Lindahl, *SoftwareX* **2015**, *1–2*, 19–25.
105 D. Chandler, *Nature* **2005**, *437*, 640–647.
106 N. Trebel, A. Höltzel, J. K. Lutz, U. Tallarek, *J. Phys. Chem. B* **2021**, *125*, 11320–11336.
107 J. L. Rafferty, J. I. Siepmann, M. R. Schure, *J. Chromatogr. A* **2008**, *1204*, 20–27.
108 F. Gritti, G. Gotmar, B. J. Stanley, G. Guiochon, *J. Chromatogr. A* **2003**, *988*, 185–203.
109 F. Gritti, G. Guiochon, *J. Chromatogr. A* **2006**, *995*, 37–54.
110 F. Gritti, G. Guiochon, *Anal. Chem.* **2003**, *75*, 5726–5738.
111 F. Gritti, G. Guiochon, *Anal. Chem.* **2005**, *77*, 4257–4272.
112 F. Gritti, G. Guiochon, *J. Chromatogr. A* **2003**, *1008*, 23–41.

113 N. Trebel, A. Höltzel, U. Tallarek, *J. Phys. Chem. B* **2022**, *126*, 7781–7795.

Chapter 5

Probing Surface Chemistry Effects on Effective Diffusion Coefficients in Hierarchically Porous Media Through Multiscale Simulations

Authors

Ulrich Tallarek, Dzmitry Hlushkou, Nicole Trebel, Alexandra Höltzel

State of publication

Published 06 June 2023 in *Chemie Ingenieur Technik*, Vol. 95, in press.
DOI: 10.1002/cite.202300027

Abstract

Multiscale diffusion simulations in a realistic macro–mesoporosity model of a silica-based chromatographic bed are performed to study the effect of relevant surface chemistry parameters, namely length and ligand density of surface-tethered alkyl chains, on effective mesopore and bed diffusion coefficients. Efficient linker schemes enable integration of interfacial dynamics information obtained from molecular dynamics simulations at the single-mesopore level into the hierarchical porosity and multiscale transport model.

5.1 Introduction

Transport in surface-functionalized porous media involves time and length scales ranging from solute–surface interactions to restricted, tortuous diffusion through hierarchical pore spaces.[1–5] Realistic multiscale simulations therefore combine molecular-level information of the interfacial dynamics[6–8] with porosity models from tomographic reconstructions[9–11] to investigate the relationships between surface functionality, pore space morphology, and effective transport.[12] Although multiscale simulations of transport in porous media have advanced in recent years,[13–33] connecting the different modeling scales is still challenging and requires suitable linker schemes.[16,18]

Reversed-phase liquid chromatography (RPLC),[34,35] the most important chemical separation and purification technique today, is a multiscale process taking place inside a macro–mesoporous, often silica-based adsorbent, the chromatographic bed.[36] An aqueous–organic liquid (the mobile phase) is pumped through the chromatographic bed to separate compounds (analytes) based on their differential retention by the hydrophobically-modified silica surface (the stationary phase). The hydrophobic modification typically consists of long alkyl chains (the bonded phase). Mass transport through the chromatographic bed combines advective flow in the macropore space with pore liquid diffusion in the mesopore space and surface diffusion along the soft surface of the bonded phase.[37–39]

Knowledge about the interfacial dynamics in RPLC comes essentially from molecular simulations conducted in a computer-generated mesopore of simple geometry,[40–47] and realistic porosity of chromatographic beds are accessible through different tomographic methods.[9–11,48,49] Tomographic reconstructions of the mesopore space of ordered and random mesoporous silicas, for example, have been used in Brownian dynamics (BD) diffusion simulations of finite-size tracers to derive hindrance factor expressions.[50,51] Earlier, we presented a bottom-up approach that considers the analyte distribution and mobility at the functionalized solid–liquid interface, as received from molecular dynamics (MD) simulations in an RPLC mesopore model, in BD diffusion simulations implemented in a macro–mesoporosity model of the chromatographic bed.[15] This simulation approach traces the impact of changes in the interfacial dynamics, originating from the experimental conditions, on the effective diffusion coefficient in the interconnected mesopore space (D_{meso}) and finally the effective diffusion coefficient in the chromatographic bed (D_{bed}). The approach was later extended by the lattice-Boltzmann method to include fluid flow in the macropore space of the chromatographic bed,[18] allowing us to study the influence of mass transfer resistance in the stagnant mobile phase (inside the mesopores) on longitudinal and transverse dispersion coefficients as a function of the average flow velocity.[52]

Through our multiscale simulation approach we have already demonstrated that the key interfacial phenomena of RPLC, namely analyte partitioning into and adsorption onto the bonded-phase chains as well as surface diffusion along the bonded-phase chains, significantly influence the effective diffusion and dispersion coefficients in the chromatographic bed.[15,18] In this work, we investigate the effect of relevant surface chemistry parameters in stationary-phase design on

effective diffusion coefficients, namely length and ligand density of the surface-tethered alkyl chains.

5.2 Methods and models

5.2.1 RPLC mesopore model

The RPLC mesopore model consisted of a solid silica slab of 0.93 nm width (*z*-direction) placed between 5 nm wide solvent reservoirs in a 12.14 × 13.2 × 10.93 nm^3 ($x \times y \times z$) simulation box. With periodic boundary conditions, this system equals a 10 nm wide slit pore. The surfaces of the silica slab carried the respective modification for a given stationary-phase chemistry. Dimethyl-*n*-octadecylsilyl (C_{18}) chains, followed by dimethyl-*n*-octylsilyl (C_8) chains, are the most popular bonded phases in RPLC pratice. C_8 phases can be prepared with higher ligand density than C_{18} phases,[53] for example, to achieve increased shape selectivity for the separation of isomeric/isobaric compounds.[54] RPLC stationary phases with moderate ligand density typically carry trimethylsilyl (C_1) groups to reduce the density of residual OH groups at the silica surface. The surface chemistries probed in this work are based on hydroxylated silica with the following functionalizations:[46] (i) C_{18} chains, moderate density (3.11 µmol m^{-2}) plus C_1 groups (0.93 µmol m^{-2}); (ii) C_8 chains, moderate density, plus C_1 groups; and (iii) C_8 chains, high density (hd, 4.04 µmol m^{-2}), no C_1 groups. The C_8 phase was created from the C_{18} phase by shortening C_{18} to C_8 chains. The hd-C_8 phase was generated from the C_8 phase by replacing all C_1 groups with C_8 chains. Each phase carried the same residual surface hydroxylation (3.42 µmol m^{-2}).

MD simulations in the RPLC mesopore model were conducted for a 70/30 (v/v) water/acetonitrile mobile phase to realize conditions conducive to fast surface diffusion,[45] and an established solute ensemble (ethylbenzene, benzene, acetophenone, and benzyl alcohol) representing typical RPLC analytes of different polarity.[42] Each analyte species was modeled separately. MD simulations were run with GROMACS 2016.5[55,56] for a canonical *NVT* ensemble (constant number of molecules *N*, simulation box volume *V*, and temperature *T*) at $T = 300$ K. The simulation box contained $N_{analyte} = 10$ (corresponding to $c_{analyte} \approx 10^{-2}$ mol L^{-1}), $N_{water} = 23970$, and $N_{acetonitrile} = 4902$. The system was equilibrated for 60 ns prior to productive runs of up to 1.0 µs. Sections 5.S1.1 and 5.S1.2 in the Supporting Information provide more information about the force-field parameters and the simulation protocol.

5.2.2 Hierarchical porosity model

Morphological data refer to a commercial, narrow-bore analytical RPLC column (2.1 mm inner diameter × 50 mm length) for ultrahigh performance liquid chromatography.[57] The column was packed with 1.7 µm (nominal mean particle size) bridged-ethyl hybrid C_{18} silica particles (mean mesopore size 14.6 nm).[58] For reconstruction of a representative region from the bulk packing, the bed was filled with divinylbenzene, which was then polymerized to allow extrusion of the stabilized bed from the steel casing. The extruded bed was prepared for focused ion-beam scanning

electron microscopy to enable three-dimensional imaging of the packing microstructure.[57] The macropore space reconstruction had dimensions of 21.6 × 21.2 × 21.6 μm^3 with 41.5 × 41.5 × 150 nm^3 voxels (Figure 5.1A), and yielded a mean particle diameter of 1.97 μm and an external bed porosity of 0.39. The mesopore space inside the C_{18}-silica particles was reconstructed using scanning transmission electron microscopy.[58] The mesopore space reconstruction had dimensions of 220 × 202 × 275 nm^3 (with 0.64^3 nm^3 voxels) and yielded a mesoporosity of 0.49 (Figure 5.1B).

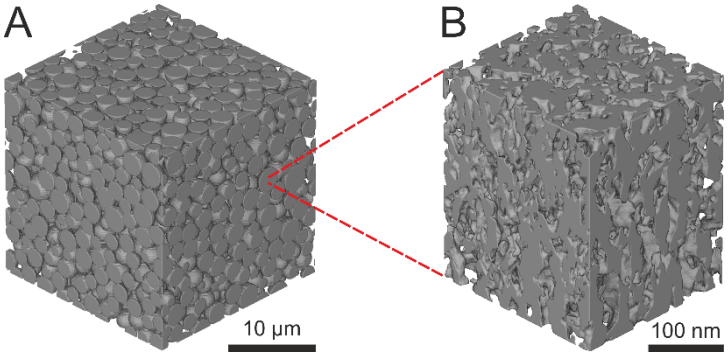

Figure 5.1. Geometrical models derived from physical reconstructions for the interparticle macropore space (A) and the intraparticle mesopore space (B) of a particle-packed RPLC column.[57,58]

5.2.3 Multiscale simulation model

Figure 5.2 gives an overview of the multiscale simulation approach. MD simulations (Figure 5.2A) characterize the interfacial dynamics at the single-mesopore level through analyte density $\rho(z)$ and surface-parallel diffusivity profiles $D_{\parallel}(z)$. (Section 5.S1.3 in the Supporting Information describes the calculation of $\rho(z)$ and $D_{\parallel}(z)$ for bonded-phase groups, solvent molecules, and analyte molecules; the distance z from the surface is measured from the position of the surface Si atoms.) Analyte-specific interaction with the functionalized silica surface contributes significantly to the value of D_{meso}.[15] Information contained in $\rho(z)$ and $D_{\parallel}(z)$ is translated into a distance map assigning analyte density and diffusion coefficient values according to the distance from the solid silica surface.[15,18] Analyte transport in the mesopore space is simulated by BD simulations, specifically with a random-walk particle-tracking (RWPT) method. Probabilistic-reflection and time-splitting schemes are applied to capture analyte travel over different distances from the surface. These linker schemes (see Section 5.S2 in the Supporting Information for details) ensure that random walkers in the RWPT simulation, sampling the mesopore space to indicate D_{meso}, retain the information about $\rho(z)$ and $D_{\parallel}(z)$. At the top level (Figure 5.2C), we simulate exchange (mass transfer) of analyte molecules between mesopore space and macropore space of the adsorbent. To progress from D_{meso} to D_{bed}, we use an effective homogeneous medium representation of the mesopore space in the explicit macropore space morphology (Figure 5.S1, Supporting Information), with probabilistic-reflection and time-splitting (linker) schemes applied to the interface between these two spatial domains.

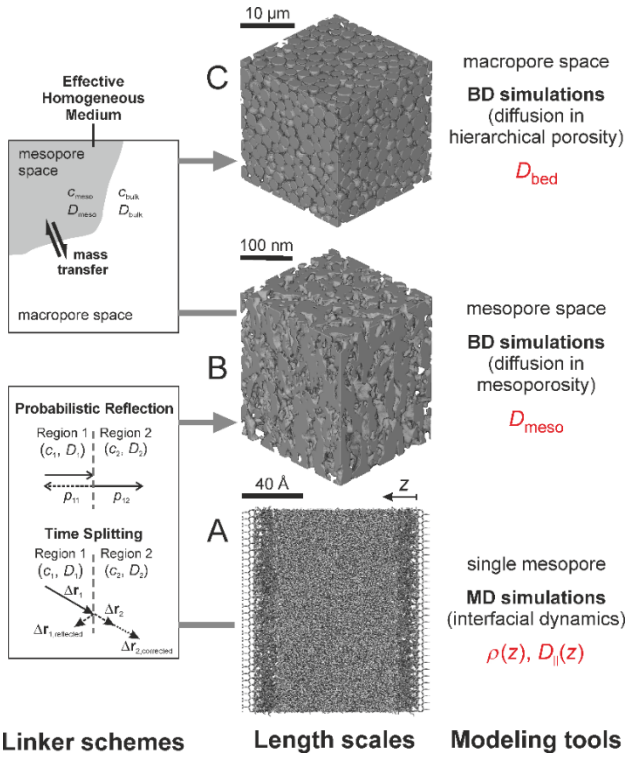

Figure 5.2. Multiscale approach to the simulation of effective mesopore and bed diffusion coefficients (D_{meso} and D_{bed}) in a hierarchically porous silica adsorbent with a functionalized surface. Details about the embedding of analyte density $\rho(z)$ and diffusivity $D_{||}(z)$ profiles into the BD diffusion simulations in the hierarchical porosity model can be found in Section 5.S2 of the Supporting Information. Adapted with permission from Tallarek et al.[18] Copyright 2022 American Chemical Society.

5.3 Results and discussion

The first simulation level incorporates the relevant chemical information underlying analyte retention by an RPLC column for a defined combination of stationary-phase chemistry, mobile-phase composition, and analyte compound. Importantly, the RPLC mesopore model represents the column-averaged analyte presence and diffusivity at the functionalized solid–liquid interface, as validated by comparison with experimental data.[45] The spatially-resolved information contains a wealth of detail that illuminates different aspects of RPLC retention.[40–47] For brevity, only the salient features of the bonded-phase and solvent density profiles (Figure 5.3) are summarized and the essential differences between the three surface chemistries pointed out. The bonded-phase density profiles reflect increasing flexibility along the chain length through sharply defined peaks closer to the solid silica surface followed by a smooth decline toward the bulk liquid region. The flexible bonded-phase region is naturally wider in the C_{18} phase than in the C_8 phases. The alkyl chains of the hd-C_8 phase are slightly more extended and a bit stiffer compared with the C_8 phase, as high ligand density increases the conformational order.[46]

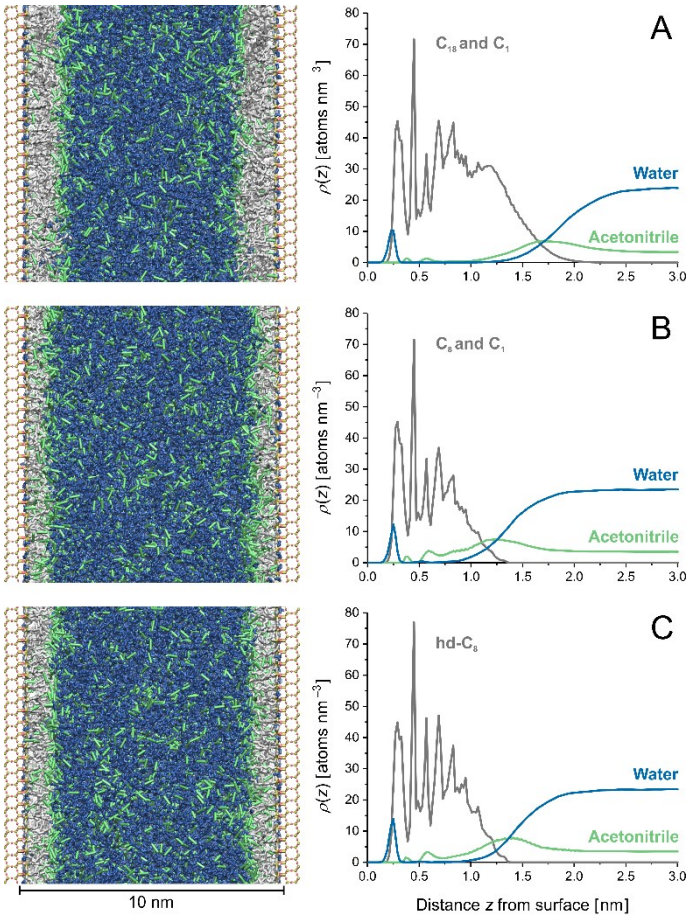

Figure 5.3. Snapshots of the RPLC mesopore model equilibrated with a 70/30 (v/v) water/acetonitrile mobile phase and associated bonded-phase and solvent density distributions for three surface chemistries. Adapted with permission from Rybka et al.[46] Copyright 2019 American Chemical Society.

The solvent density profiles show that water (apart from the immediate vicinity of the silica surface) is mostly confined to the bulk liquid region, whereas acetonitrile penetrates deeper into the bonded phase. The acetonitrile density profiles exhibit a density maximum in the interfacial region around the flexible part of the alkyl chains. This acetonitrile "ditch", a consequence of the hydrophobic effect,[59] is the most important characteristic of the RPLC solid–liquid interface regarding surface diffusion.[41] The viscosity decrease accompanying the acetonitrile enhancement promotes fast surface diffusion by favoring the local diffusive mobility of bonded-phase groups and analyte molecules.[41,42,46,60] The extent to which the local organic-solvent density is enhanced over its value in the bulk liquid region depends on the organic solvent in and the water/organic solvent ratio of the mobile phase,[45,60] as well as on the surface chemistry of the stationary phase.[46] A shorter chain length (C_8 vs C_{18}) allows for complete organic-solvent penetration of the bonded phase, which, in turn, engenders a higher maximum acetonitrile excess in the ditch. Higher ligand density (C_8 vs hd-C_8) reinforces these effects through increased bonded-phase density and conformational order in the interfacial region.[46]

The surface-parallel diffusivity profile of an analyte compound depends on its density distribution at the functionalized solid–liquid interface, which, in turn, depends on length and ligand density of the alkyl chains as well as on analyte properties. Figure 5.4 reveals these relations by showing the density profiles for the four analyte compounds as well as their surface-parallel diffusivity profiles, both relative to the respective bonded-phase density profile for each surface chemistry.

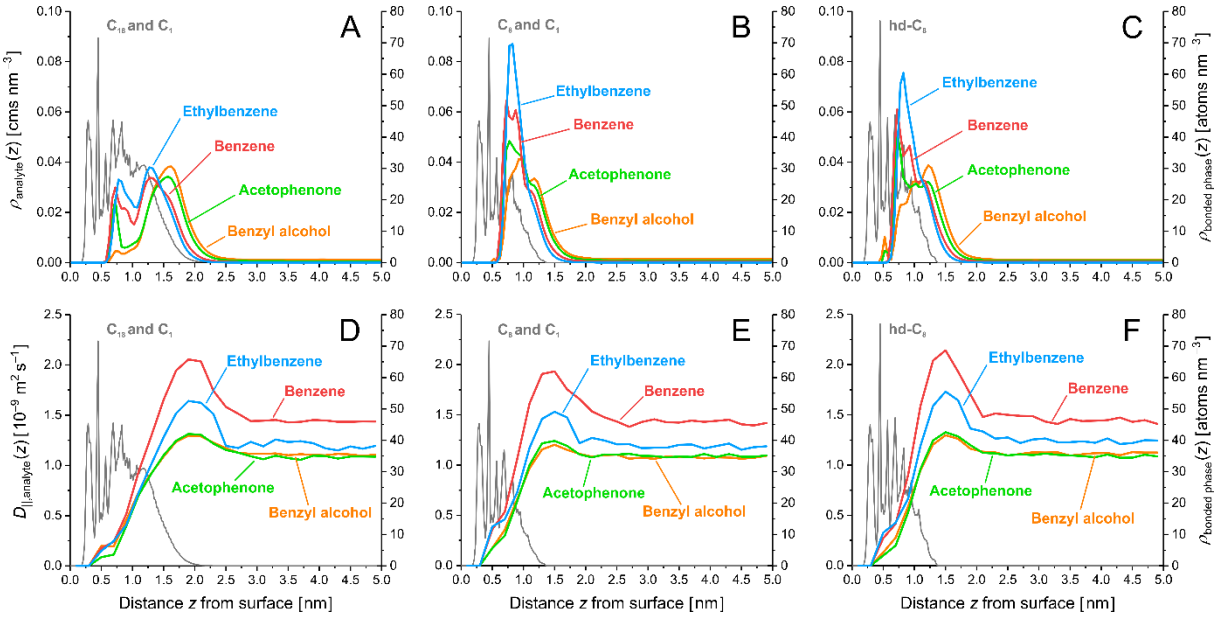

Figure 5.4. Distribution of analyte density (A–C) and surface-parallel diffusivity (D–F) in the RPLC mesopore model equilibrated with a 70/30 (v/v) water/acetonitrile mobile phase for three surface chemistries. Bonded-phase density profiles are shown as reference. $D_{\parallel}(z)$-profiles were calculated using Eq. 5.S1 (Supporting Information). Adapted with permission from Rybka et al.[46] Copyright 2019 American Chemical Society.

Analyte molecules have low mobility when they are located deeper in the bonded phase associated with the less flexible part of the alkyl chains, and enhanced mobility when they are placed in the interfacial region containing the flexible part of the alkyl chains surrounded by the acetonitrile ditch. Analyte density in the former and latter location is associated with the partitioning and adsorption mechanism of retention, respectively.[40] Partitioning refers to full immersion, adsorption to partial immersion of an analyte molecule in the bonded-phase chains. Consequently, partitioned analyte molecules have predominantly contacts with bonded-phase groups, whereas adsorbed analyte molecules also sustain numerous contacts with solvent molecules.[42] Figures 5.4A–5.4C show a clear distinction between partitioning and adsorption peak on the C_{18} phase compared with a much narrower analyte density distribution on the C_8 phases. Higher ligand density has a comparatively small effect, in that some analyte density is shifted toward the bulk liquid region. The analyte density distribution is essentially governed by analyte properties. The apolar analytes (ethylbenzene and benzene), which are more retained on an RPLC column, have more density closer to the silica surface than the less retained, polar analytes (acetophenone and benzyl alcohol),

which strongly favor adsorption over partitioning. Polar analytes thus have a density distribution advantage over apolar analytes. On the other hand, the comparison of the analyte $D_{\|}$-profiles (Figure 5.4D–5.4F) shows a less pronounced mobility maximum in the acetonitrile ditch for polar analytes.

The consequences of the analyte-specific density and diffusivity profiles for the effective transport properties in the RPLC mesopore model are revealed in Figure 5.5 through pore-averaged diffusivities $<D_{\|}>$ calculated with Eq. 5.S2. $<D_{\|}>$ values are normalized by D_{bulk}, the analyte diffusion coefficient in the bulk mobile phase. (In the RPLC mesopore model, D_{bulk} is recovered in the bulk liquid region, which is characterized by constant solvent and analyte density and diffusivity values, cf. Figures 5.3 and 5.4.) For the C_{18} phase, a monotonic increase in $< D_{\|}>/D_{bulk}$ is observed from ethylbenzene to benzyl alcohol in Figure 5.5. This observation can be explained by a lower partitioning contribution to retention at increasing analyte polarity.[42] Because partitioned analyte molecules have low diffusive mobility (Figure 5.4D), a lower partitioning peak density raises the pore-averaged diffusive mobility of an analyte.

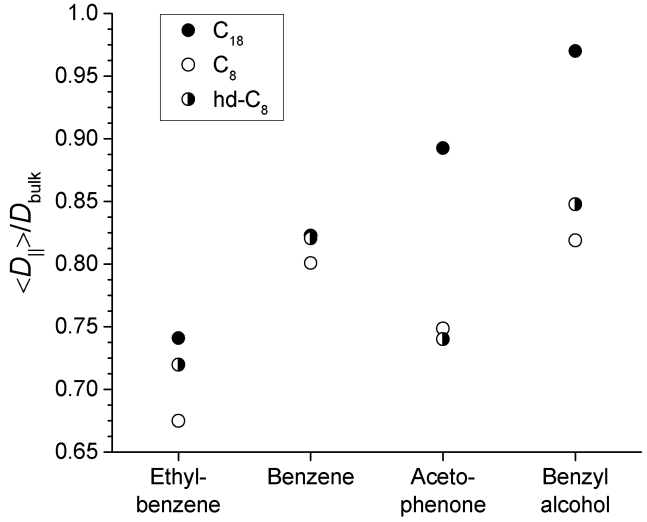

Figure 5.5. Pore-averaged, surface-parallel diffusivity $<D_{\|}>$ of the analytes in the RPLC mesopore model for three surface chemistries. $<D_{\|}>$ was calculated with Eq. 5.S2 (Supporting Information) and normalized by D_{bulk}, the analyte diffusivity in the bulk mobile phase.

On the shorter C_8 phases, a distinct partitioning peak cannot develop (Figure 5.4B and 5.4C). This should bring the $<D_{\|}>/D_{bulk}$-values of the apolar analytes closer to that of the polar analytes, which is indeed observed in Figure 5.5. The pore-averaged analyte diffusivities on the C_8 phases remain, however, below the corresponding $<D_{\|}>/D_{bulk}$-values on the C_{18} phase. The C_{18} phase has a wider interfacial region than the C_8 phases, so that more analyte density can be placed within the flexible part of the bonded phase (Figure 5.4D–F). Additionally, bonded-phase groups in the interfacial region of the C_{18} phase have higher mobility than the corresponding groups in the interfacial region of a C_8 phase.[46] The influence of higher ligand density is smaller than that of longer chain length, as expected from the analyte density and surface-parallel diffusivity profiles (Figure 5.4). The hd-

C_8 phase offers higher acetonitrile excess in the ditch than the C_8 phase, but the extent to which the pore-averaged diffusivity of an analyte can profit from this depends primarily on how much of the analyte density is located in the interfacial region.

The next simulation level introduces the mesopore space morphology. The D_{meso}-values obtained for the three surface chemistries are shown in Figure 5.6. For direct comparison with Figure 5.5, the D_{meso}-values are also normalized by D_{bulk}. Two observations are important. First, all D_{meso}-values are strongly reduced compared with $<D_{\|}>$ due to the tortuosity of the diffusion paths in random mesoporous silica (Figure 5.2B). For the C_{18} phase, for example, the average ratio between the analyte D_{meso}- and $<D_{\|}>$-values is 0.29. Second, analyte D_{meso}-values for the C_8 phases have increased relative to those for the C_{18} phase. The D_{meso}-values of the two apolar compounds are above the corresponding values for the C_{18} phase, the D_{meso}-values of the polar analytes are closer to those for the C_{18} phase compared to the pore-averaged diffusivities (Figure 5.5). This means that the impact of the surface chemistry on the analyte diffusivity is attenuated at the mesopore space level compared to the single-mesopore level.

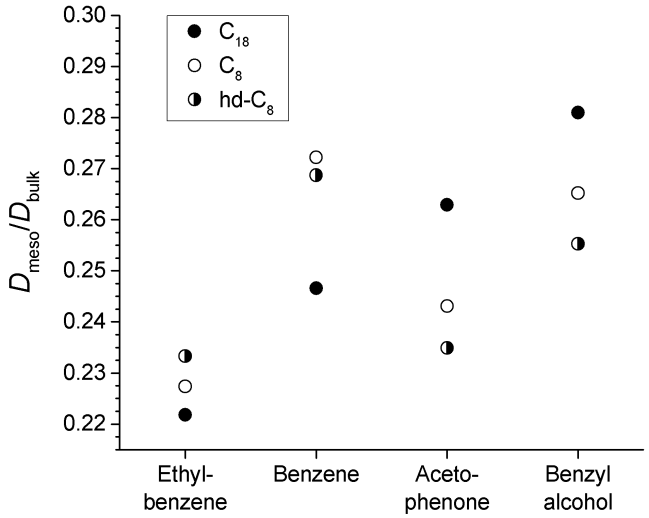

Figure 5.6. Effective diffusion coefficient D_{meso} in the reconstructed mesopore space of the adsorbent (cf. Figure 5.1B), normalized by D_{bulk}, the analyte diffusivity in the bulk mobile phase. D_{meso} is simulated with the approach described in Section 5.S2 of the Supporting Information.

To understand the evolution of the analyte diffusivity from Figure 5.5 to Figure 5.6, one has to remember that surface diffusion in the interfacial region is the primary mode of analyte transport, as the analyte mobility decreases strongly towards the silica surface and the analyte density in the bulk liquid region is very low (Figure 5.4). The two-dimensional visualization of the distance map (Figure 5.7) implemented in the mesopore space reconstruction shows that opposite pore walls can approach each other so closely (e.g., at pore necks) that interfacial analyte density and mobility regions start to overlap significantly[61] and the high-mobility interfacial regions for fast surface diffusion ultimately cannot fully develop. Because analyte mobility maxima are located at a larger distance from the silica surface on the C_{18} phase (at $z \approx 2$ nm, Figure 5.4D) than on the C_8 phases (at $z \approx 1.5$ nm, Figure 5.4E and 5.4F), the analyte diffusivity decreases more strongly for the C_{18}

phase than the C_8 phases upon moving from the RPLC slit-pore model (Figure 5.2A) to the irregularly shaped mesopore space (Figure 5.2B).

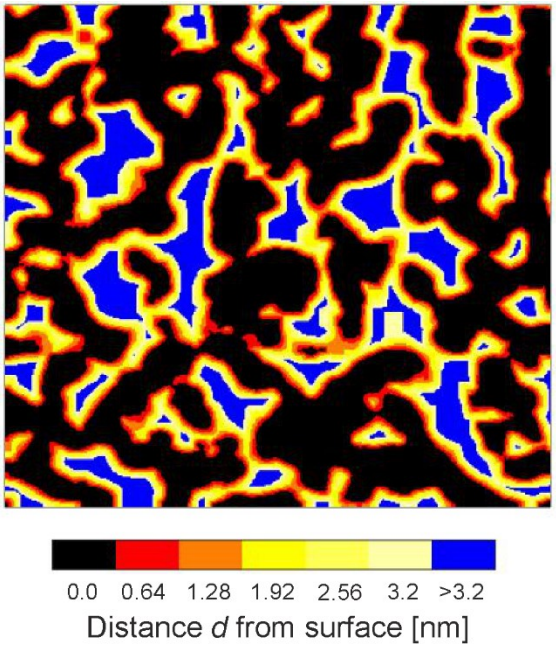

Figure 5.7. Distance map for voxels in the mesopore space indicating their shortest distance from the silica surface (two-dimensional representation for a layer from the reconstruction in Figure 5.1B). Black is solid silica, colors denote void space in the reconstruction.

Also because surface diffusion is the main transport mode, the general reduction of the D_{meso}-values with respect to the $<D_{||}>$-values should primarily reflect changes in surface tortuosity. To prove this hypothesis, we adapted the RWPT method to simulate the distance-dependent diffusion coefficient $D(d)$ of passive, pointlike tracers parallel to the curved silica surface of the mesopore space (see Section 5.S2 of the Supporting Informations for details). Unlike analytes that interact with the bonded phase, tracers sample the surface curvature at different distances from the solid silica surface as if the bonded phase were not present, neither for physical nor for chemical interaction. The void space of the mesopore reconstruction was divided into surface-parallel layers (Figure 5.7), and tracers were confined to their initially assigned layer during the simulation by applying a specular reflection scheme. Figure 5.8 shows the simulated $D(d)$-values normalized by the tracer diffusivity in bulk void space. The values of $D(d)/D_{bulk} = 0.26–0.31$ for $d \leq 1.92$ nm excellently agree with the analyte-averaged ratio between D_{meso} and $<D_{||}>$ for the C_{18} phase, confirming that analyte transport in the mesopore space reflects the respective surface tortuosity.

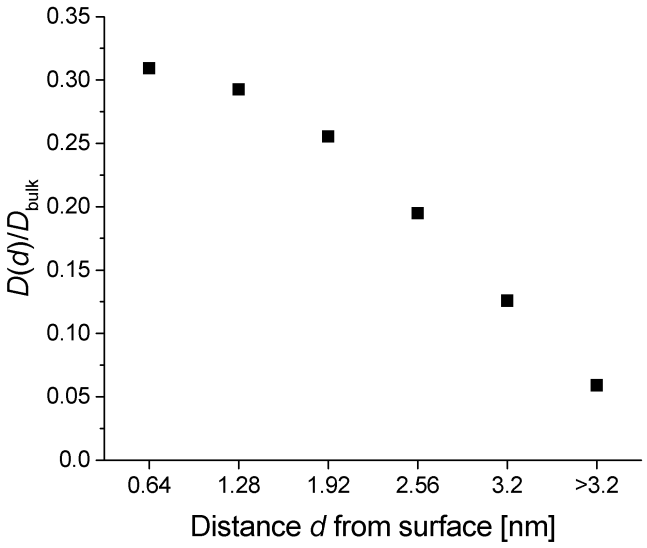

Figure 5.8. Distance-dependent diffusion coefficient of passive, pointlike tracers parallel to the curved silica surface of the mesopore space, normalized by D_{bulk}, the tracer diffusivity in bulk void space.

The final simulation level introduces the macropore space morphology or packing structure. Figure 5.9, which contains the simulated effective bed diffusion coefficients, reveals that the surface chemistry has a much smaller effect on the bed diffusivity than analyte properties. The D_{bed}/D_{bulk}-values increase significantly from the most retained analyte compound (D_{bed}/D_{bulk} = 0.076–0.091 for ethylbenzene) to the least retained one (D_{bed}/D_{bulk} = 0.337–0.377 for benzyl alcohol). The D_{bed}/D_{bulk}-values result from the dynamic interplay between the D_{meso}-values of the analytes and the analyte density distribution between mesopore space and macropore space of the bed (cf. Figure 5.S2 in the Supporting Information), reflecting the actual analyte retention by the mesopores. Thus, we observe $D_{bed} < D_{meso}$ for the more strongly retained compounds ethylbenzene and benzene and $D_{bed} > D_{meso}$ for the less retained compounds acetophenone and benzyl alcohol. Overall, Figure 5.9 shows that the bed diffusivity is limited by the analyte-specific retention rather than by length and ligand density of the alkyl chains on the adsorbent silica surface.

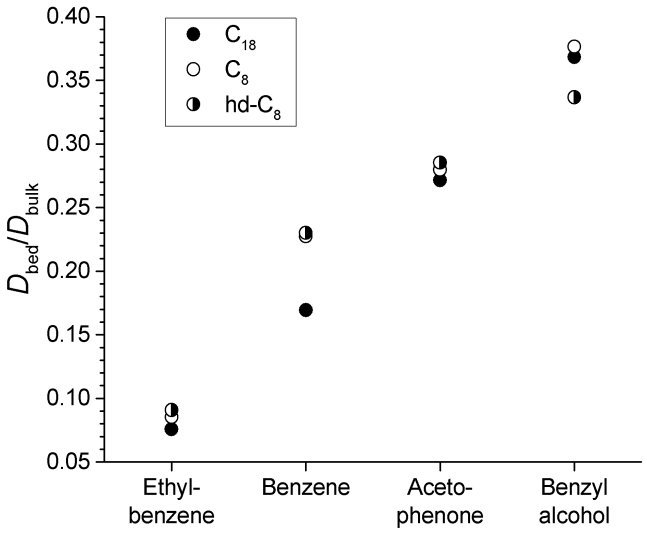

Figure 5.9. Effective bed diffusion coefficient D_{bed} in the reconstructed macro–mesoporous adsorbent (cf. Figure 5.1), normalized by D_{bulk}, the analyte diffusivity in the bulk mobile phase. D_{bed} is simulated with the approach described in Section 5.S2 of the Supporting Information.

5.4 Conclusions

Multiscale diffusion simulations combining interfacial dynamics information from MD simulations with BD diffusion simulations in a reconstruction-based hierarchical porosity model have shown how the analyte-specific interaction with a particular surface chemistry influences the diffusivity at various length scales up to the effective bed diffusion coefficient. The reproduced experimental conditions comprised four analyte compounds on a particle-packed RPLC column containing a silica-based C_{18}, C_8, or hd-C_8 stationary phase equilibrated with a 70/30 (v/v) water–acetonitrile mobile phase.

At the single-mesopore level, pore-averaged analyte diffusivities reflect analyte-specific retention properties as well as the surface chemistry. Longer chains and, to a much lesser degree, higher ligand density favor fast surface diffusion and thus the main mode of analyte transport. At the mesopore space level, analyte diffusivities become significantly reduced from the surface tortuousity inside the random mesoporous silica particles. Additionally, a mobility-reducing overlap between interfacial regions from opposite pore walls develops locally at pore necks and other constrictions in the irregularly shaped mesopore space. The overlap occurs despite a comparatively wide mean mesopore size of 14.6 nm and is naturally more pronounced for the C_{18} phase, which loses some of its advantage over the C_8 phases. At the bed level, surface chemistry effects are hardly detectable any more. The stronger an analyte is retained by the RPLC solid–liquid interface inside the mesopores, the slower becomes the mass transfer between the pore space hierarchies and the lower is the bed diffusivity. Diffusive mass transport through the column is limited by the analyte properties that govern RPLC retention rather than by the surface chemistry of the stationary phase.

5.5 Supporting Information

5.S1 Molecular dynamics (MD) simulations at the single-mesopore level

5.S1.1 Force-field parameters and their validation

The force-field parameters used for the simulation of reversed-phase liquid chromatography (RPLC) systems have to account appropriately for the interactions between all components of a RPLC mesopore, namely solvent–solvent, solvent–silica surface, solvent–bonded phase, solvent–analyte, analyte–silica surface, and analyte–bonded phase interactions. The force field chosen for a specific component, for example, water molecules, may therefore differ from the appropriate force-field choice for the same component in a different system, for example, the hydration of macromolecules. The MD simulations deliver density and diffusivity data, which have to be validated independently. The density data predict analyte retention. For investigating the retention mechanisms in RPLC, simulated retention data should be validated against experimental values for a wide range of retention factors.[62] From our own experience as well as the results of other groups we know that solvent and analyte density profiles (and therefore retention data) are much less sensitive to the force-field parameters than diffusion coefficients.

The Si, O, and H atoms of the silica surface were represented by the force-field parameters from Gulmen and Thompson.[63] C_1 groups, C_8 chains, and C_{18} chains of the bonded phase as well as acetonitrile molecules of the mobile phase were described by the transferable potentials for phase equilibria united-atom (TraPPE-UA) force field.[64,65] The simple point charge/extended (SPC/E) force field was used for water molecules.[66] All analytes were treated with the explicit CHARMM general force field (CGenFF).[67,68]

We arrived at the described combination in several stages. First, the force fields for the solvent molecules of the mobile phase were chosen following a recommendation of Mountain,[69] who showed that the combination of SPC/E (for water) and TraPPE-UA (for acetonitrile) reproduces the hydrogen bonding and liquid density of water–acetonitrile mixtures very well. This is the major requisite for recovering the experimental diffusion coefficients of solvent and analyte molecules in the bulk liquid region of the pore. In developing our simulation approach, we tried and excluded, for example, the TIP3P model for water. This model does not appropriately represent the microstructure of water, so that the experimental self-diffusion coefficient of water is severely overestimated:[70] The newer TIP4P/2005 force field recovers the water self-diffusion coefficient in neat water as well as in water–methanol mixtures,[71] but not in water–acetonitrile mixtures.[72]

Next we established that the chosen force fields for the mobile-phase solvents and the silica surface account for the interaction of water–acetonitrile mixtures with bare-silica surfaces and reproduce the experimentally observed dependence of the retention factor from the acetonitrile fraction of the mobile phase in hydrophilic interaction liquid chromatography (HILIC).[73,74] Importantly, the introduction of the force field for the bonded phase yielded solvent and analyte density profiles that were consistent with those simulated earlier for RPLC systems by the Siepmann group[75,54] and the Meuwly group[76,77] who had used different force fields for the mobile-phase solvents. The CHARMM force field was chosen because it provides parameters for every analyte compound

studied. Comparison of analyte distribution coefficients calculated from the simulated analyte density profiles with the respective experimental retention factors proved that our RPLC mesopore model and force-field combination reproduce the retentive properties of an RPLC column.[45] MD simulations performed with the described force-field combination[62,73,45,47,78] have successfully explained and predicted the experimentally observed analyte retention and surface diffusion behavior in RPLC and HILIC systems.[37,79,80]

5.S1.2 Additional Simulation Details

The silica slab of the RPLC mesopore model was cut from β-cristobalite SiO_2 parallel to the (111) face. The number of solvent molecules in the simulation box was determined in preliminary *NPT* ensemble (constant number of molecules *N*, pressure *P*, and temperature *T*) simulations. The number of water and acetonitrile molecules in the simulation box was manually adjusted between *NPT* simulation runs until the water and acetonitrile densities in the bulk liquid region of the mesopore approached the respective densities for a mobile phase of 70/30 (v/v) water/acetonitrile to ±1%. The procedure recreated the column equilibration process of RPLC practice, where the mobile phase is pumped through the column containing the stationary phase, until a steady state is reached and the column is ready for sample injection.

A Nosé–Hoover thermostat (with a coupling constant of 0.25 ps) was used to keep the temperature at T = 300 K. Equations of motion were integrated with a 1 fs time step. The steepest descent method was used for energy minimization. Initial velocities were randomly assigned through a Maxwell–Boltzmann distribution. After a 60 ns equilibration period, productive simulations were run for up to 1 µs. The output frequency for the trajectory was set to 0.5 ps. Long-range electrostatic interactions were treated with the particle-mesh Ewald algorithm,[81] and non-bonded interactions were modeled with a 12–6 Lennard-Jones potential. Lennard-Jones parameters for unlike interactions were calculated using Lorentz–Berthelot combination rules. A cutoff radius of 1.4 nm, validated earlier,[41] was used for all interactions. MD simulations were run on the ForHLR1 cluster at the Steinbuch Center for Computing (of the Karlsruhe Institute of Technology) under the project acronym RPLCMD.[46]

5.S1.3 Analysis of Density and Surface-Parallel Diffusivity Profiles

For the calculation of density profiles as a function of the distance z from the surface, $\rho(z)$, we first specified a bin width and counted the number of atoms, atom groups, or molecules in each bin over the chosen time span. This count was normalized to the respective bin volume and observation time. Bonded-phase and solvent density profiles (based on the atom number densities of the CH_2 and CH_3 united-atom groups of the bonded phase, the O atom of water, and the central C atom of acetonitrile) were calculated from 40 ns trajectories with a bin size of 0.02 and 0.1 nm, respectively. Analyte density profiles (based on the center-of-mass of the analyte molecules) were calculated from the complete trajectories using a 0.05 nm bin size.

Distance (z-)dependent diffusion coefficients in direction parallel to the surface, $D_{\parallel}(z)$, were calculated as in our previous MD simulation studies following the approach of Liu et al.[82] The mean squared displacements of bonded-phase groups, solvent molecules, and analyte molecules were repeatedly recorded as $\langle r^2(t)\rangle = \langle x^2(t) + y^2(t)\rangle$ during 20 ps observation-time intervals, shifted consecutively in 0.5 ps time steps throughout the whole trajectory. For spatial resolution, a maximum shift of ±0.3 nm around the initial z-position during the observation interval was allowed. Because GROMACS computes mean squared displacements from a set of initial molecular positions, this provides an easy way to compute diffusion coefficients using the Einstein relation. Therefore, $D_{\parallel}(z)$ of the bonded-phase groups, solvent molecules, and analyte molecules were calculated from the linear slope of the observation curve (t = 4–16 ps) according to

$$D_{\parallel}(z) = \frac{1}{4}\frac{\mathrm{d}\langle r^2(t)\rangle}{\mathrm{d}t} \tag{5.S1}$$

using a bin size of 0.02 nm. According to GROMACS procedure,[83] an error estimate of $D_{\parallel}(z)$ was calculated as the difference of the diffusion coefficients obtained from the mean squared displacement curve over the two halves of the fit interval (i.e., 4–10 and 10–16 ps).
A slit-pore-averaged mobility is then calculated using the following equation:

$$\langle D_{\parallel}\rangle = \frac{\int \rho(z) D_{||}(z)\mathrm{d}z}{\int \rho(z)\mathrm{d}z} \tag{5.S2}$$

5.S2 Brownian Dynamics (BD) Simulations in the Hierarchical Porosity Model

Diffusion in the reconstructed macropore space and mesopore space of the chromatographic bed (cf. Figure 5.1 of the main text) was modeled with a random-walk particle-tracking (RWPT) approach.[84] It is based on the equivalence of the diffusion equation

$$\frac{\partial c(\mathbf{r},t)}{\partial t} = D\nabla^2 c(\mathbf{r},t) \tag{5.S3}$$

(where D denotes the diffusion coefficient and c concentration) and the stochastic differential equation describing the random walk of a tracer, presented in discrete form as

$$\mathbf{r}(t+\delta t) = \mathbf{r}(t) + \Delta\mathbf{r} = \mathbf{r}(t) + \boldsymbol{\alpha}\sqrt{6D\delta t} \tag{5.S4}$$

$\mathbf{r}(t)$ is the tracer position at time t, δt is the elementary time step of the random walk, and $\boldsymbol{\alpha}$ is a vector with random orientation and a length defined by a Gaussian distribution with zero mean and unity variance. A large number N of passive (i.e., non-adsorbing and non-reacting) tracers is initially distributed in the system. In the present work, we used $N = 10^7$ for all RWPT simulations. During each time step δt, the displacement of every tracer due to random diffusive motion was determined according to Eq. 5.S4. A time-dependent diffusion coefficient $D(t)$ was calculated from

$$D(t) = \frac{1}{6N}\frac{\mathrm{d}}{\mathrm{d}t}\sum_{n=1}^{N}[\Delta r_n(t)]^2 \tag{5.S5}$$

where $\Delta r_n(t)$ is the displacement of the nth tracer after time t.

Eqs. 5.S3–5.S5 assume that the diffusion coefficient is spatially independent. In a chromatographic bed, however, the analyte diffusion coefficients depend on the analyte position in the system. Analyte diffusion coefficients within the functionalized solid–liquid interface, for example, depend on whether analyte molecules are placed closer to the silica surface or the bulk liquid region (reflecting analyte partitioning or adsorption, respectively). Analyte diffusion coefficients within the chromatographic bed depend on whether the analyte molecules are located within or between the mesoporous particles. To account for this, we implemented a reflection-barrier method,[15] in which asymmetric reflectivity is introduced at the interface between two regions with different diffusion coefficients. Accordingly, when a tracer reaches the interface between region *i* and region *j*, the probability p_{ij} that the tracer enters region *j* from region *i* is

$$p_{ij} = 1 - \frac{c_i\sqrt{D_i}}{c_i\sqrt{D_i} + c_j\sqrt{D_j}} \tag{5.S6}$$

where c_i and c_j denote the tracer concentrations in regions *i* and *j*, respectively, and D_i and D_j are the associated diffusion coefficients. Correspondingly, $p_{ii} = 1 - p_{ij}$ can be interpreted as the probability that a tracer reaching the interface during its move in region *i* is specularly reflected. Similarly, the probability p_{ji} that a tracer reaching the interface from region *j* will enter region *i* is

$$p_{ji} = 1 - \frac{c_j\sqrt{D_j}}{c_i\sqrt{D_i} + c_j\sqrt{D_j}} \tag{5.S7}$$

and the tracer is specularly reflected into region *j* with probability $p_{jj} = 1 - p_{ji}$.
This "probabilistic reflection" scheme is complemented by a "time splitting" scheme. That is, if a tracer crosses the interface from region *i*, its move in region *j* must be recalculated, because it was computed with D_i instead of D_j. For this purpose, we adapted the following approach:[85] The initial move $\Delta\mathbf{r}$ of the tracer (Eq. 5.S4) is divided into $\Delta\mathbf{r}_i$ and $\Delta\mathbf{r}_j$ and the associated time step of the random walk is split according to a nonlinear time-splitting scheme

$$\sqrt{\delta t} = \sqrt{\delta t_i} + \sqrt{\delta t_j} \tag{5.S8}$$

where δt_i and δt_j are times spent in regions *i* and *j*, respectively. The corrected tracer displacement in region *j* is then calculated as[15]

$$\left|\Delta\mathbf{r}_{j,\mathrm{corrected}}\right| = \sqrt{6D_j\delta t}\left(1 - \frac{|\Delta\mathbf{r}_i|}{|\Delta\mathbf{r}|}\right) \tag{5.S9}$$

For diffusion simulations in the physically reconstructed mesopore space (cf. Figure 5.1B and 5.2B in the main text) this approach was implemented as follows: Each analyte density $\rho(z)$ and diffusivity $D_{\|}(z)$ profile from the MD simulations was split into the bulk liquid region ($z > 3.2$ nm), where analyte density and diffusivity are constant, and five 0.64 nm wide regions between pore wall and bulk liquid region ($0 < z_1 \leq 0.64$ nm, 0.64 nm $< z_2 \leq 1.28$ nm, ..., 2.56 nm $< z_5 \leq 3.2$ nm). The width of the five regions covering the functionalized solid–liquid interface was adjusted to the spatial resolution of the reconstruction (0.64 nm) shown in Figure 5.1B.

Average values of analyte density and diffusivity were calculated for and assigned to the bulk liquid region and each interfacial sub-region, so that the simulated analyte density $\rho(z)$ and diffusivity $D_{\|}(z)$ profiles were approximated by piecewise-constant functions. Afterwards, we determined the shortest distance from the solid surface for each voxel in the void space of the reconstruction. Corresponding density and diffusivity values obtained by the piecewise-constant approximation of the analyte density and diffusivity profiles were then assigned to every voxel of the void space depending on its distance from the solid surface.[15]

In the next step, the RWPT method for discontinuous media described above was adapted to simulate diffusion in the reconstructed mesopore space. At each iteration, Eq. 5.S4 was used to determine the next position of a tracer. If it resulted in crossing the border between voxels with different distance labels, probabilistic-reflection and time-splitting schemes (Eqs. 5.S6–5.S9) were applied to correct the tracer displacements. The long-time asymptotic values D_{meso} were extracted for each system from the corresponding $D(t)$-curves.[15]

The calculated D_{meso}-values were then used to simulate analyte diffusion in the hierarchical porosity model by considering the analyte density exchange between mesopore space and macropore space of the chromatographic bed (see Figure 5.2B → 5.2C in the main text). For this purpose, the macropore space reconstruction (Figure 5.1A, main text) was used as explicit geometrical model, while diffusion in the mesopore space was accounted for by adapting an effective homogeneous medium (EHM) approach.[86] The basic idea of this approach is to replace a heterogeneous material by a (hypothetical) homogeneous one that recovers all essential properties of the original material. With this approach, the spatially dependent concentrations and diffusivities of the analyte molecules in the mesopore space were replaced by constant, that is, effective values. The described simulation approach (Eqs. 5.S4–5.S9) was applied again, but in a different setting, assuming now the presence of only two regions, the interparticle macropore space as physically reconstructed using focused ion-beam scanning electron microscopy and the intraparticle mesopore space, represented as EHM (Figure 5.S1).[15]

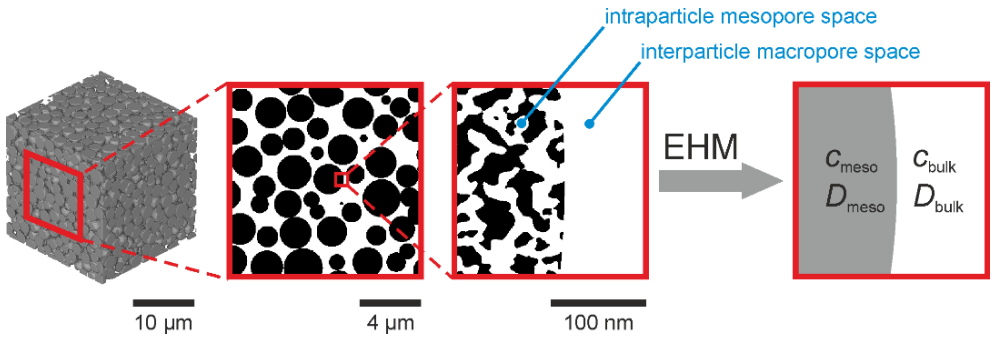

Figure 5.S1. EHM representation of the mesopore space inside the spherical silica particles of the packed bed. The microscopically disordered mesopore space of the reconstruction in Figure 5.1B (main text), with spatially dependent analyte concentration and diffusivity, is replaced by a homogeneous medium with constant (effective) concentration c_{meso} and diffusivity D_{meso} simulated at the mesopore level (Figure 5.2B, main text).

Similar to D_{meso}, the effective macroscopic (bed) diffusion coefficients D_{bed} in this hierarchical porosity model were determined from the long-time asymptotes of the simulated transient diffusion curves. The simulated D_{bed}-values account for the mesopore space phenomenology (i.e., functionalized solid–liquid interface plus morphology) and the macropore space morphology (packing microstructure).

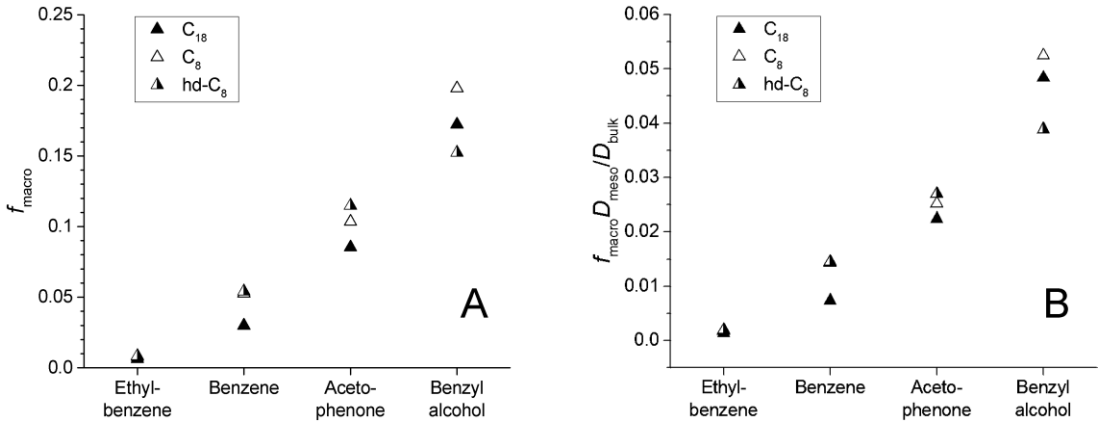

Figure 5.S2. (A) Fraction f_{macro} of tracers in the macropore space (Eq. 5.S10) for each analyte compound and surface chemistry. (B) Product of f_{macro} and effective diffusion coefficient D_{meso} in the mesopore space of the adsorbent normalized by D_{bulk}, the analyte diffusivity in the bulk mobile phase.

The EHM approach adapted for the diffusion simulations in the hierarchical macro–mesoporosity model requires to determine the tracer fractions in the macropore space (f_{macro}) and the mesopore space ($f_{meso} = 1 - f_{macro}$). The value of f_{macro} was defined as

$$f_{\mathrm{macro}} = \frac{N_{\mathrm{macro}}}{N_{\mathrm{macro}} + N_{\mathrm{meso}}} \tag{5.S10}$$

where N_{meso} and N_{macro} denote the number of tracers in the mesopore space and the macropore space, respectively. N_{meso} and N_{macro} were calculated from the corresponding total volumes of and analyte concentrations in the voxels of the mesopore space ($v_{meso,i}$ and $c_{meso,i}$ with distance labels i = "1", "2", "3", "4", "5", and "bulk") and the macropore space (v_{macro} and c_{bulk}).[15]

Resulting f_{macro}-values are displayed in Figure 5.S2A. The D_{bed}-value for each analyte compound and surface chemistry is proportional to f_{macro} and D_{meso}. Figure 5.S2B shows the product of f_{macro} and D_{meso}/D_{bulk}. The behavior for f_{macro} D_{meso}/D_{bulk} reflects the simulated D_{bed}/D_{bulk}-values presented in Figure 5.9 of the main text.

Acknowledgment

Open access funding enabled and organized by Projekt DEAL.

References

1 I. Bocquet, E. Charlaix, *Chem. Soc. Rev.* **2010**, *39*, 1073–1095.
2 J. Kärger, D. M. Ruthven, D. N. Theodorou, *Diffusion in Nanoporous Materials*, Wiley–VCH, Weinheim **2012**.
3 J.-D. Grunwaldt, J. B. Wagner, R. E. Dunin-Borkowski, *ChemCatChem* **2013**, *5*, 62–80.
4 P. Trogadas, V. Ramani, P. Strasser, T. F. Fuller, M.-O. Coppens, *Angew. Chem. Int. Ed.* **2016**, *55*, 122–148.
5 M.-H. Sun, S.-Z. Huang, L.-H. Chen, Y. Li, X.-Y. Yang, Z.-Y. Yuan, B.-L. Su, *Chem. Soc. Rev.* **2016**, *45*, 3479–3563.
6 C. Bousige, C. M. Ghimbeu, C. Vix-Guterl, A. E. Pomerantz, A. Suleimenova, G. Vaughan, G. Garbarino, M. Feygenson, C. Wildgruber, F.-J. Ulm, R. J.-M. Pellenq, B. Coasne, *Nat. Mater.* **2016**, *15*, 576–582.
7 G. Tabacchi*, ChemPhysChem* **2018***, 19, 1249–1297.*
8 *W. H. Thompson*, *J. Chem. Phys.* **2018**, *149*, 170901.
9 A. P. Cocco, G. J. Nelson, W. M. Harris, A. Nakajo, T. D. Myles, A. M. Kiss, J. J. Lombardo, W. K. S. Chiu, *Phys. Chem. Chem. Phys.* **2013**, *15*, 16377–16407.
10 D. Stoeckel, C. Kübel, K. Hormann, A. Höltzel, B. M. Smarsly, U. Tallarek, *Langmuir* **2014**, *30*, 9022–9027.
11 S. Mitchell, A. B. Pinar, J. Kenvin, P. Crivelli, J. Kärger, J. Pérez-Ramírez, *Nat. Commun.* **2015**, *6*, 8633.
12 T. Müllner, K. K. Unger, U. Tallarek, New J. Chem. 2016, 40, 3993–4015.
13 B. Coasne, *New J. Chem.* **2016**, *40*, 4078–4094.
14 F. J. Keil, *Annu. Rev. Chem. Biomol. Eng.* **2018**, *9*, 201–227.
15 U. Tallarek, D. Hlushkou, J. Rybka, A. Höltzel, *J. Phys. Chem. C* **2019**, *123*, 15099–15112.
16 A. Phan, D. Fan, A. Striolo, *Phys. Fluids* **2020**, *32*, 101301.
17 C. Bousige, P. Levitz, B. Coasne, *Nat. Commun.* **2021**, *12*, 1043.
18 U. Tallarek, D. Hlushkou, A. Höltzel, *J. Phys. Chem. C* **2022**, *126*, 2336–2348.
19 N. Hansen, R. Krishna, J. M. van Baten, A. T. Bell, F. J. Keil, *J. Phys. Chem. C* **2009**, *113*, 235–246.
20 N. Hansen, R. Krishna, J. M. van Baten, A. T. Bell, F. J. Keil, *Chem. Eng. Sci.* **2010**, *65*, 2472–2480.
21 P. Koči, V. Novák, F. Štepánek, M. Marek, M. Kubícek, *Chem. Eng. Sci.* **2010**, *65*, 412–419.
22 V. Novák, P. Koči, F. Štepánek, M. Marek, *Ind. Eng. Chem. Res.* **2011**, *50*, 12904–12914.
23 N. Hansen, F. J. Keil, *Soft Mater.* **2012**, *10*, 179–201.
24 *Modeling of Heterogeneous Catalytic Reactions: From the Molecular Process to the Technical System* (Ed: O. Deutschmann), Wiley–VCH, Weinheim **2012**.

25 C. Schaefer, A. P. J. Jansen, *J. Chem. Phys.* **2013**, *138*, 054102.
26 S. Matera, M. Maestri, A. Cuoci, K. Reuter, *ACS Catal.* **2014**, *4*, 4081–4092.
27 G. D. Wehinger, F. Klippel, M. Kraume, *Comput. Chem. Eng.* **2017**, *101*, 11–22.
28 M. Hettel, M. Wörner, O. Deutschmann, in *Handbook of Materials Modeling* (Eds: W. Andreoni, S. Yip), Springer Nature **2018**, Ch. 6-1.
29 H. Rusinque, G. Brenner, *Microporous Mesoporous Mater.* **2019**, *280*, 157–165.
30 S. Molins, P. Knabner, Rev. Mineral. *Geochem.* **2019**, 85, 27–48.
31 N. Jurtz, M. Kraume, G. D. Wehinger, *Rev. Chem. Eng.* **2019**, *35*, 139–190.
32 A. Bruix, J. T. Margraf, M. Andersen, K. Reuter, *Nat. Catal.* **2019**, *2*, 659–670.
33 N. Kulyk, D. Berger, A.-S. Smith, J. Harting, *Comp. Phys. Commun.* **2020**, *256*, 107443.
34 U. D. Neue, *HPLC Columns: Theory, Technology, and Practice*, Wiley–VCH, NewYork **1997**.
35 P. Žuvela, M. Skoczylas, J. J. Liu, T. Bączek, R. Kaliszan, M. W. Wong, B. Buszewski, K. Héberger, *Chem. Rev.* **2019**, *119*, 3674–3729.
36 D. Enke, R. Gläser, U. Tallarek, *Chem. Ing. Tech.* **2016**, *88*, 1561–1585.
37 F. Gritti, G. Guiochon, *J. Chromatogr. A* **2013**, *1297*, 85–95.
38 F. Gritti, G. Guiochon, *AIChE J.* **2011**, *57*, 333–345.
39 F. Gritti, G. Guiochon, *AIChE J.* **2011**, *57*, 346–358.
40 R. K. Lindsey, J. L. Rafferty, B. L. Eggiman, J. I. Siepmann, M. R. Schure, *J. Chromatogr. A* **2013**, *1287*, 60–82.
41 J. Rybka, A. Höltzel, S. M. Melnikov, A. Seidel-Morgenstern, U. Tallarek, *Fluid Phase Equilib.* **2016**, *407*, 177–187.
42 J. Rybka, A. Höltzel, U. Tallarek, *J. Phys. Chem. C* **2017**, *121*, 17907–17920.
43 K. El Hage, P. K. Gupta, R. J. Bemish, M. Meuwly, *J. Phys. Chem. Lett.* **2017**, *8*, 4600–4607.
44 K. El Hage, R. J. Bemish, M. Meuwly, *Phys. Chem. Chem. Phys.* **2018**, *20*, 18610–18622.
45 J. Rybka, A. Höltzel, A. Steinhoff, U. Tallarek, *J. Phys. Chem. C* **2019**, *123*, 3672–3681.
46 J. Rybka, A. Höltzel, N. Trebel, U. Tallarek, *J. Phys. Chem. C* **2019**, *123*, 21617–21628.
47 N. Trebel, A. Höltzel, A. Steinhoff, U. Tallarek, *J. Chromatogr. A* **2021**, *1640*, 461958.
48 R. Leary, P. A. Midgley, J. M. Thomas, *Acc. Chem. Res.* **2012**, *45*, 1782–1791.
49 J. Zečević, K. P. de Jong, P. E. de Jongh, *Curr. Opin. Solid State Mater. Sci.* **2013**, *17*, 115–125.
50 J. Hochstrasser, A. Svidrytski, A. Höltzel, T. Priamushko, F. Kleitz, W. Wang, C. Kübel, U. Tallarek, *Phys. Chem. Chem. Phys.* **2020**, *22*, 11314–11326.
51 U. Tallarek, J. Hochstrasser, J. Ziegler, X. Huang, C. Kübel, M. R. Buchmeiser, *ChemCatChem* **2021**, *13*, 281–292.

52 A. Daneyko, D. Hlushkou, V. Baranau, S. Khirevich, A. Seidel-Morgenstern, U. Tallarek, *J. Chromatogr. A* **2015**, *1407*, 139–156.

53 C. Stella, S. Rudaz, J.-L. Veuthey, A. Tchapla, *Chromatographia* **2001**, *53*, S113–S131.

54 J. L. Rafferty, J.-I. Siepmann, M. R. Schure, *J. Chromatogr. A* **2011**, *1218*, 9183–9193.

55 B. Hess, C. Kutzner, D. van der Spoel, E. Lindahl, *J. Chem. Theory Comput.* **2008**, *4*, 435–447.

56 M. J. Abraham, T. Murtola, R. Schulz, S. Páll, J. C. Smith, B. Hess, E. Lindahl, *SoftwareX* **2015**, *1–2*, 19–25.

57 A. E. Reising, S. Schlabach, V. Baranau, D. Stoeckel, U. Tallarek, *J. Chromatogr. A* **2017**, *1513*, 172–182.

58 F. Gritti, J. Hochstrasser, A. Svidrytski, D. Hlushkou, U. Tallarek, *J. Chromatogr. A* **2020**, *1620*, 460991.

59 D. Chandler, *Nature* **2005**, *437*, 640–647.

60 A. Steinhoff, A. Höltzel, N. Trebel, U. Tallarek, *J. Phys. Chem. B* **2022**, *126*, 10554–10568.

61 N. Trebel, A. Höltzel, U. Tallarek, *J. Phys. Chem. B* **2022**, *126*, 7781–7795.

62 F. Gritti, N. Trebel, A. Höltzel, U. Tallarek, *J. Chromatogr. A* **2022**, *1685*, 463627.

63 T. S. Gulmen, W. H. Thompson, *Langmuir* **2006**, *22*, 10919–10923.

64 M. G. Martin, J. I. Siepmann, *J. Phys. Chem. B* **1998**, *102*, 2569–2577.

65 C. D. Wick, J. M. Stubbs, N. Rai, J. I. Siepmann, *J. Phys. Chem. B* **2005**, *109*, 18974–18982.

66 H. J. C. Berendsen, J. R. Grigera, T. P. Straatsma, *J. Phys. Chem.* **1987**, *91*, 6269–6271.

67 K. Vanommeslaeghe, E. Hatcher, C. Acharya, S. Kundu, S. Zhong, J. Shim, E. Darian, O. Guvench, P. Lopes, I. Vorobyov, A. D. Mackerell Jr., *J. Comput. Chem.* **2010**, *31*, 671–690.

68 N. M. Fischer, P. J. van Maaren, J. C. Ditz, A. Yildirim, D. van der Spoel, *J. Chem. Theory Comput.* **2015**, *11*, 2938–2944.

69 R. D. Mountain, *J. Phys. Chem. B* **2010**, *114*, 16460–16464.

70 I. N. Tsimpanogiannis, O. A. Moultos, L. F. M. Franco, M. B. de M. Spera, M. Erdös, I. G. Economou, *Mol. Simul.* **2019**, *45*, 425–453.

71 G. Guevara-Carrion, J. Vrabec, H. Hasse, *J. Chem. Phys.* **2011**, *134*, 074508.

72 Z. S. Vokáčová, E. Pluhařová, *J. Mol. Liquids* **2019**, *288*, 110778.

73 S. M. Melnikov, A. Höltzel, A. Seidel-Morgenstern, U. Tallarek, *Angew. Chem. Int. Ed.* **2012**, *51*, 6251–6254.

74 R. D. Mountain, *J. Phys. Chem. C* **2013**, *117*, 3923–3929.

75 J. L. Rafferty, J. I. Siepmann, M. R. Schure, *J. Chromatogr. A* **2011**, *1218*, 2203–2213.

76 A. Fouqueau, M. Meuwly, R. Bemish, *J. Phys. Chem. B* **2007**, *111*, 10208–10216.

77 J. Braun, A. Fouqueau, R. J. Bemish, M. Meuwly, *Phys. Chem. Chem. Phys.* **2008**, *10*, 4765–4777.
78 S. M. Melnikov, A. Höltzel, A. Seidel-Morgenstern, U. Tallarek, *Anal. Chem.* **2013**, *85*, 8850–8856.
79 F. Gritti, A. Höltzel, U. Tallarek, G. Guiochon, *J. Chromatogr. A* **2015**, *1376*, 112–125.
80 F. Gritti, *J. Chromatogr. A* **2015**, *1410*, 90–98.
81 U. Essmann, L. Perera, M. L. Berkowitz, T. Darden, H. Lee, L. G. Pedersen, *J. Chem. Phys.* **1995**, *103*, 8577–8593.
82 P. Liu, E. Harder, B. J. Berne, *J. Phys. Chem. B* **2004**, *108*, 6595–6602.
83 M. J. Abraham, D. van der Spoel, E. Lindahl, B. Hess, and the GROMACS development team, *GROMACS User Manual version 2019*. https://manual.gromacs.org/documentation/2019/ onlinehelp/gmx-msd.html
84 P. Salamon, D. Fernàndez-Garcia, J. J. Gómez-Hernández, *J. Contamin. Hydrol.* **2006**, *87*, 277–305.
85 M. Bechtold, J. Vanderborght, O. Ippisch, H. Vereecken, *Water Resour. Res.* **2011**, *47*, W10526.
86 Y. Guéguen, M. Le Ravalec, L. Ricard, *Pure Appl. Geophys.* **2006**, *163*, 1175–1192.

IV. Conclusions and perspective

This thesis comprises MD simulation studies of RPLC mesopore models with differenty geometry and surface modification to elucidate the molecular interactions at the chromatographic interface directly on the molecular level. The simulations mimic RPLC conditions in a single mesopore of the mesoporous network of silica particles inside a chromatographic column. All molecular simulations were carried out with the open-source software GROMACS. The starting point was the well-established RPLC slit pore with a surface coverage of 3.11 µmol m^{-2} C_{18} chains and 0.93 µmol m^{-2} C_1 endcapping groups, simulated with different W/ACN mixtures and four analyte molecules (benzene, ethylbenzene, acetophenone, benzyl alcohol) prior to this work. The characteristics of the chromatographic interface in this column-average mesopore model was then extended by MD simulations of acetone and uracil (Chapter 1), two commonly used dead time markers in RPLC practice. With the obtained density distribution data, it was possible to develop a theoretical approach for the calculation of analyte surface excess and connect the results to experimentally measured retention factors (Chapter 4). In Chapter 5, the MD slit pore data (of the analyte molecules) were implemented in a hierarchical multiscale simulation approach to investigate the effects of surface chemistry on analyte mobility. The second part of this work deals with MD simulations using cylindrical RPLC mesopores, which are far more complex to generate and require more computing resources (due to larger box sizes). For this work, two cylindrical RPLC pores of different diameter were generated with the object-oriented program PoreMS; both with adjoining solvent reservoirs and identical surface coverage (C_{18} and C_1 endcapping) at the inner curved and outer planar surface. Data analysis was carried out with self-written MATLAB scripts to calculate specific characteristics such as distribution and mobility of bonded-phase, solvent, and analyte molecules. As described in Chapter 2, the larger cylindrical pore has a diameter of 9 nm and was simulated with a W-rich mobile phase (70/30 (v/v) W/ACN) for two analyte molecules differing in polarity (ethylbenzene and acetophenone). For the smaller cylindrical pore (6 nm in diameter), the same analyte molecules were chosen and simulated for four different mobile phase compositions (Chapter 3). With these simulation systems, the influence of pore curvature on bonded-phase structure and the distribution and mobility of solvent and analyte molecules in the chromatographic interface were analyzed and compared to the molecular level-picture at planar surfaces.

The investigation of the dead time markers shed light on the elution time behavior observed for acetone and uracil in RPLC practice. Acetone shows a decline with increasing amount of organic solvent in the mobile phase mixture and uracil has a U-shaped elution time curve for W-ACN mobile phases. With the simulated data in the slit pore, it was shown that both solutes accumulate in the bonded-phase region of the pore, from which acetone exhibits density peaks of higher intensity, and, thus, is less suitable for RPLC separations than uracil. Uracil, on the other hand, has a very weak interaction with the bonded-phase, but tries to maximize its hydrogen bonds due to its hydrophilic character and is susceptible for HILIC retention.

This study can easily be extended with another mobile phase, such as W/MeOH, which is also widely applied in chromatographic practice. Steinhoff et al.[1] investigated the organic-solvent excess adsorption and surface diffusion for a wide range of W/MeOH mobile phases simulated with in the 10-nm slit pore and compared their results to W/ACN phases, showing how the hydrogen-bonding capabilities of the organic solvent influences its accumulation in the interfacial region and, thus, affecting surface diffusion of both solvent and analyte molecules. An MD simulation study comprising acetone and uracil for W/MeOH mixtures or further mobile phases can complement the data of dead time marker behavior in chromatographic systems and help chromatographers to chose the most suitable solute for their separations.

As shown in Chapter 4, the simulated interactions of analytes and dead time markers in a single mesopore account for analyte retention measured in an experimental chromatographic (RPLC) setup. Density profiles of the analytes ethylbenzene, benzene, acetophenone and benzyl alcohol and the dead time marker uracil were normalized to their bulk value and used to calculate the surface excess adsorption of each analyte species. A linear correlation between these values and measured retention factors of the same analyte set was found, which is the first step towards retention factor prediction, proving that the MD simulations account for methylene selectivity and the retentive behavior based on analyte polarity. In general, this study had some limitations based on the assumptions that were made. Using a slit pore model with a defined width neglects the morphology of the actual mesopore network. Additionally, the surface coverage and the average pore size of the measured RPLC column and the slit pore model were not exactly identical, which leads to deviations between calculated and measured values. The approach of predicting retention factors can be improved by a model adjusted more precisely to the experiment, which should then be testet for different surface chemistries and also for a variety of mobile phases and solute molecules. An interesting field of research would be the study of charged analytes and/or charged surfaces, as encountered, for example, in mixed-mode HPLC, with MD simulations.

Analysis of pore curvature in RPLC mesopores gave new insights into bonded-phase selectivity and pore-level transport. The cylindrical mesopore models were built with solvent reservoirs, to i) guarantee an equilibrated bulk liquid mixture, which is in contact with the inner pore, and ii) provide external, planar surfaces with C_{18} and C_1 coverage to avoid HILIC retention at the pore entrances. In Chapter 2, the exchange between inner and outer surface was analyzed, which is why the investigated pore structure was described as cylindrical-inside-a-slit-pore model. It was shown in detail how the surface curvature influences the bonded-phase conformation, which in turn affects ACN-enrichment and surface diffusion of solvent and analyte molecules. Due to the curved pore space, C_{18} chains are more extended, enhancing the local bonded-phase density. Consequently, the interfacial region at the inner surface accumulates more ACN, resulting in a region of higher mobility compared to the outer planar surface. Regarding the distribution of the analyte molecules ethylbenzene and acetophenone, it was shown how the higher local bonded-phase density at the

inner surface leads to a different distribution between inner and outer surface area: the apolar ethylbenzene favors the curved surface due to its higher local hydrophobicity, whereas acetophenone exhibits a nearly equal distribution. Further, it was shown that both analyte species have an increased surface diffusivity along the interfacial region of the curved surface. These observations were also found for the smaller 6-nm cylindrical pore, which showed the interesting phenomenon of organic-solvent ditch overlap as a consequence of spatial confinement. With a C_{18} chain extension of about 2.8 nm from the surface, ACN molecules inside the pore cannot reach their bulk density, yielding a highly hydrophobic environment. The local increase in ACN and the local analyte mobility in the ditch region is noticeably higher than observed with the larger cylindrical pore diameter. The pore-averaged mobility, however, is only increased for acetophenone, whereas ethylbenzene shows an even lower mobility compared to the slit pore. This is explained by the different analyte distribution inside the 6-nm pore, depending on analyte polarity: ethylbenzene mostly distributes over the low-mobility bonded-phase region, whereas acetophenone density is dominated by adsorption and accumulates in the interfacial region. The narrow cylindrical confinement therefore enhances transport selectivity of analytes.

Silica particles used in RPLC practice feature wide pore size distributions, which is why further simulation studies with varying pore size extends the knowledge of pore-level transport of analyte molecules. In a current MD study,[2] two additional cylindrical mesopores (7 and 12 nm diameter) are simulated with a W/ACN and W/MeOH mobile phase of equal elution strength to investigate the influence of the degree of curvature on solvent structure and mobility gradually. The surface of all pore systems is covered with ~2.9 µmol m^{-2} C_{18} chains, which allows a direct comparison of the analyzed solvent characteristics. In Figure IV, the equilibrated, cross-sectional density profiles of each solvent species is shown for the four mesopore sizes, combined with a respective snapshot in *xy*-plane of the simulation system. Figures IV.A–IV.D illustrate a 70/30 (v/v) W/ACN mobile phase and Figures IV.E–IV.H a 60/40 (v/v) W/MeOH mobile phase, both representing a highly retentive RPLC conditions. For the 12-nm diameter pore, a bulk liquid region of ~6 nm can be identified, which narrows with decreasing pore diameter, until the interfacial area of organic-solvent enrichment overlaps in the pore center, referred to as ditch overlap. Regarding the W/ACN mobile phase, the beginning of ditch overlap is already noticeable in the 7-nm pore (Figure IV.C) and fully pronounced in the 6-nm pore (Figure IV.D). For MeOH, however, ditch overlap in the 6-nm pore is only indicated (Figure IV.H) and, thus, expected for pore diameters < 6nm, which is explained by intrinsic differences in ditch formation and morphology with both organic solvent species and a higher number density of MeOH in the bulk liquid mixture. A decreasing pore diameter is inherently accompanied by an extension of bonded-phase chains due to less available pore space. As a consequence, the bonded-phase region becomes more compact (local bonded-phase density increases), reducing solvent penetration into the bonded-phase chains and, therefore, shifting the ditch region closer to the pore center, increasing the overall organic-solvent excess. The pore-averaged organic solvent excess (relative to the ACN content of the bulk liquid phase) is more pronounced for the ACN systems, ranging from 45 vol % in the 6-nm pore to 18 vol % in the

12-nm pore. Mobility data of the solvent species further show an increase of surface diffusion with decreasing pore diameter (as a consequence of the increasing organic-solvent excess).

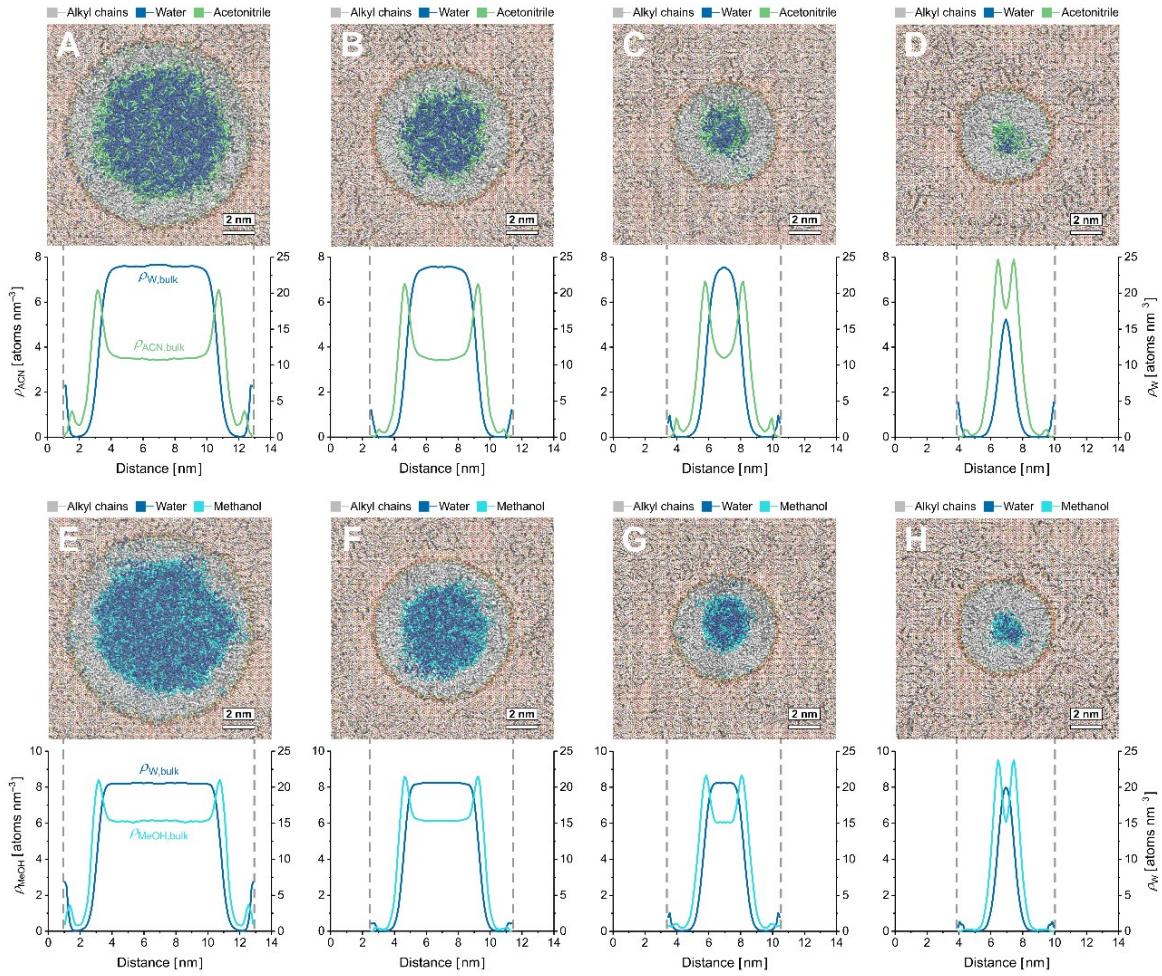

Figure IV. Cross-sectional density profiles of solvent molecules with aligned snapshots of the front view onto cylindrical mesopores with varying pore diameter (from left to right: 12, 9, 7, and 6 nm diameter). (A–D) Pore systems equilibrated with a 70/30 (v/v) W/ACN mobile phase, (E–H) pore systems equilibrated with a 60/40 (v/v) W/MeOH mobile phase. Color code: W, dark blue; ACN, green; MeOH, aqua; C_{18} and C_1 groups, silver; Si, yellow; O, red; H, white.[2]

This project could further be extended by the simulation of different analyte species, not only in analytical concentrations, but also with a set up mimicking column overloading to investigate nonlinear adsorption on the molecular scale. The calculation of adsorption isotherms requires a wide range of analyte concentrations and, therefore, a large number of independent simulation systems. At this point, the technical procedure of simulating and especially finalizing multiple RPLC pore models (as used in this thesis) on a reasonable time schedule should be optimized in the future. In particular, the step from setting up a simulation system to running an equilibrated *NVT* simulation could be accelerated. Prior to productive *NVT* simulation runs of the pore models, a tedious equilibration process is necessary to obtain the correct mobile phase composition in the

solvent reservoirs. The final number of solvent molecules in the system is unknown, which is why this procedure is carried out manually in three steps: i) guessing the number of solvent molecules, ii) running short *NVT* runs (50–100 ns), and iii) comparing the number density of the solvent species to their respective bulk value obtained from *NPT* box simulations. If the calculated solvent number densities in the reservoirs deviate by >1% from the targeted bulk values, the number of solvent molecules is adjusted and the process repeated. In the case of large simulation boxes as for the 12 nm pore, required computational resources accumulate significantly. For future projects, optimizing this process would save massive amounts of core time and ideally prevent a large number of trial runs (with incorrectly assumed ratios of solvent molecules). A promising approach in this regard is the grand canonical Monte Carlo (GCMC) method. The GCMC method is widely used for gas adsorption in equilibrium with a constant temperature T, constant volume V, and constant chemical potential μ.[3,4] Instead of *NVT* runs of the RPLC pore models with guessed particle numbers, the simulation system can exchange particles with a solvent reservoir in equilibrium, bearing the same temperature and chemical potential until the targeted solvent density is reached. After the GCMC equilibration process, the simulation system can then be used for productive *NVT* MD-simulation runs.

As shown in Chapter 5, MD-generated density and diffusion profiles of analyte molecules can be implemented as input parameters for a multiscale simulation approach to obtain effective bed diffusion coefficients (D_{bed}) in hierarchically structured macro-/mesoporous materials used for chromatographic separation or heterogeneous catalysis. MD slit pore data with three different surface modifications (C_{18}, C_8, and hd-C_8 coverage) were combined with Brownian dynamics diffusion simulations in a reconstruction-based hierarchical porosity model to investigate the influence of surface chemistry on the diffusivity of analyte molecules at different length scales. It was shown that the analyte diffusivities at the single-mesopore level reflect their retention properties, but also the effect of chain length and density on surface diffusion. Analyte diffusivity at the mesopore level is influenced by the surface tortuosity and pore shapes of the mesoporous silica particle and at the bed level, it is mostly limited by the analyte-specific retention.

In general, mass transport in hierarchically, porous materials is a combination of advective flow in the macropore space with pore liquid diffusion in the mesopore space. The lattice-Boltzmann method, representing an alternative to the conventional computational fluid dynamics approaches, allows the modeling of fluid flow in complex morphologies and was already implemented to modeling advection in the interparticle macropore space in combination with the multiscale approach to calculate effective mesopore diffusion coefficients.[5] From the simulation of advective-diffusive transport in physically reconstructed macropore space of the chromatographic bed, longitudinal and transverse dispersion coefficients can be obtained, from which chromatographic plate heights can be derived that include the entire mass transfer characteristics of the mesopore space. Consequently, this approach provides access to the description of separation efficiency in

RPLC as a function of retention and surface diffusion and could therefore be a promising tool for column design regarding improved selecitivty and performance of various adsorbent morphologies.

References

1 A. Steinhoff, A. Höltzel, N. Trebel, U. Tallarek, *J. Phys. Chem. B* **2022**, *126*, 10554–10568.

2 N. Trebel, A. Höltzel, D. Frerichs, U. Tallarek, *J. Chromatogr. A* **2023**, in preparation.

3 M. D. Macedonia, E. J. Maginn, *Fluid Phase Equilib.* **1999**, *158–160*, 19–27.

4 R. S. Pillai, S. A. Peter, R. V. Jasra, *Microporous Mesoporous Mater.* **2012**, *162*, 143–151.

5 U. Tallarek, D. Hlushkou, A. Höltzel, *J. Phys. Chem. C* **2022**, *126*, 2336–2348.

V. Appendix

V.1 Curriculum Vitae

removed for data protection reasons

V.2 Publikationsverzeichnis

1 C. K. Krug, Q. Fan, F. Fillsack, J. Glowatzki, N. Trebel, L. J. Heuplick, T. Koehler, J. M. Gottfried
„Organometallic ring vs. chain formation beyond kinetic control: Steering their equilibrium in two-dimensional confinement"
Chem. Commun. **2018**, *54*, 9741–9744. DOI: 10.1039/C8CC05357J.

2 J. Rybka, A. Höltzel, N. Trebel, U. Tallarek
„Stationary-phase contributions to surface diffusion in reversed-phase liquid chromatography: Chain length versus ligand density"
J. Phys. Chem. C **2019**, *123*, 21617–21628.

3 H. Kraus, J. Rybka, N. Trebel, A. Höltzel, U. Tallarek, N. Hansen
„PoreMS: a software tool for generating silica pore models with user-defined surface functionalisation and pore dimensions"
Mol. Simul. **2021**, *47*, 306–316.

4 J. Rybka, A. Höltzel, N. Trebel, U. Tallarek,
„Characteristics of Surface Diffusion and Effective Pore Diffusion in Reversed-Phase Liquid Chromatography from Molecular Dynamics Simulations"
in: W. E. Nagel, D. H. Kröner, M. M. Resch (eds) *High Performance Computing in Science and Engineering '19*, Springer, Cham, **2021**. DOI: 10.1007/978-3-030-66792-4_7.

5 N. Trebel, A. Höltzel, A. Steinhoff, U. Tallarek
„Insights from molecular simulations about dead time markers in reversed-phase liquid chromatography"
J. Chromatogr. A **2021**, *1640*, 461958. DOI: 10.1016/j.chroma.2021.461958.

6 N. Trebel, A. Höltzel, J. K. Lutz, U. Tallarek
„Consequences of Cylindrical Pore Geometry for Interfacial Phenomena in Reversed-Phase Liquid Chromatography"
J. Phys. Chem. B **2021**, *125*, 11320−11336. DOI: 10.1021/acs.jpcb.1c06732.

7 N. Trebel, A. Höltzel, U. Tallarek
„Confinement Effects on Distribution and Transport of Neutral Solutes in a Small Hydrophobic Nanopore"
J. Phys. Chem. B **2022**, *126*, 7781–7795. DOI: 10.1021/acs.jpcb.2c04924.

8 F. Gritti, N. Trebel, A. Höltzel, U. Tallarek
„Prediction of surface excess adsorption and retention factors in reversed-phase liquid chromatography from molecular dynamics simulations"
J. Chromatogr. A **2022**, *1685*, 463627. DOI: 10.1016/j.chroma.2022.463627.

9 A. Steinhoff, A. Höltzel, N. Trebel, U. Tallarek
"Mobile-phase contributions to organic-solvent excess adsorption and surface diffusion in reversed-phase liquid chromatography"
J. Phys. Chem. B **2022**, *126*, 10554–10568. DOI: 10.1021/acs.jpcb.2c06871.

10 U. Tallarek, D. Hlushkou, N. Trebel, A. Höltzel
„Probing Surface Chemistry Effects on Effective Diffusion Coefficients in Hierarchically Porous Media Through Multiscale Simulations"
Chem. Ing. Tech. **2023**, *95*, in press. DOI: 10.1002/cite.202300027.

V.3 Erklärungen

Erklärung zum Eigenanteil

Die vorliegende Dissertation mit dem Titel „Structure and mobility of solvents and solutes at solid-liquid interfaces in mesopore models with different pore geometries obtained from molecular dynamics simulations" habe ich selbstständig verfasst. Der kumulative Teil dieser Arbeit (Chapter 1–5) beinhaltet veröffentlichte Fachartikel, die in Kooperation mit Koautoren verfasst wurden. Die Beiträge der einzelnen Koautoren werden im Folgenden in Anlehnung an die Contributor Roles Taxonomy (CRediT) dargestellt.

Kapitel 1: Insights from molecular simulations about dead time markers in reversed-phase liuqid chromatography

N. Trebel, A. Höltzel, A. Steinhoff, U. Tallarek
J. Chromatogr. A **2021**, *1640*, 461958. DOI: 10.1016/j.chroma.2021.461958.

N. Trebel führte die Simulationen durch und wirkte an den Auswertungen und Visualisierung der Daten sowie am Schreiben des Entwurfs mit. A. Höltzel arbeitete das Manuskript aus und wirkte bei der Konzeptualisierung mit. A. Steinhoff wirkte an der Datenauswertung mit. U. Tallarek wirkte bei der Konzeptualisierung und der Editierung des Textes mit.

Kapitel 2: Consequences of Cylindrical Pore Geometry for Interfacial Phenomena in Reversed-Phase Liquid Chromatography

N. Trebel, A. Höltzel, J. K. Lutz, U. Tallarek
J. Phys. Chem. B **2021**, *125*, 11320−11336. DOI: 10.1021/acs.jpcb.1c06732.

N. Trebel erstelle das Porenmodell, führte die Simulationen durch und wirkte an den Auswertungen und Visualisierung der Daten sowie am Schreiben des Entwurfs mit. A. Höltzel arbeitete das Manuskript aus und wirkte bei der Konzeptualisierung mit. J. K. Lutz wirkte bei der Datenauswertung mit. U. Tallarek wirkte bei der Konzeptualisierung und der Editierung des Textes mit.

Kapitel 3: Confinement Effects on Distribution and Transport of Neutral Solutes in a Small Hydrophobic Nanopore

N. Trebel, A. Höltzel, U. Tallarek
J. Phys. Chem. B **2022**, *126*, 7781–7795. DOI: 10.1021/acs.jpcb.2c04924.

N. Trebel erstelle das Porenmodell, führte die Simulationen und Datenauswertung durch. Außerdem übernahm N. Trebel die Visualisierung der Daten und wirkte bei der Konzeptualisierung

mit. A. Höltzel wirkte bei der Überarbeitung des Textes mit. U. Tallarek wirkte bei der Konzeptualisierung mit und arbeitete das Manuskript aus.

Kapitel 4:

F. Gritti, N. Trebel, A. Höltzel, U. Tallarek
J. Chromatogr. A **2022**, *1685*, 463627. DOI: 10.1016/j.chroma.2022.463627.

F. Gritti führte die experimentellen Messungen durch, wirkte bei der Konzeptualisierung und Datenauswertung mit und verfasste den ersten Entwurf. N. Trebel wirkte bei der Datenauswertung und –visualisierung sowie der Überarbeitung des Textes mit. A. Höltzel wirkte bei der Konzeptualisierung des Simulationsteils mit. U. Tallarek überarbeitete den Text und wirkte bei der Konzeptualisierung mit.

Kapitel 5:

U. Tallarek, D. Hlushkou, N. Trebel, A. Höltzel
Chem. Ing. Tech. **2023**, *95(11)*, 1–10. DOI: 10.1002/cite.202300027.

U. Tallarek übernahm die Konzeptualisierung und arbeitete das Manuskript aus. D. Hlushkou führte die Diffusionssimulationen und deren Auswertung durch. N. Trebel wirkte an den Molekulardynamiksimulationen und an der Datenvisualisierung mit. A. Höltzel wirkte an der Editierung des Manuskriptes mit.

(Ort, Datum, Unterschrift des Promovierenden)

(Ort, Datum, Unterschrift des Betreuers)

Erklärung zum selbstständigen Verfassen

Ich erkläre, dass eine Promotion noch an keiner anderen Hochschule als der Philipps-Universität Marburg, Fachbereich Chemie, versucht wurde.

Hiermit versichere ich, dass ich die vorliegende Dissertation mit dem Titel

„Structure and mobility of solvents and solutes at solid-liquid interfaces in mesopore models with different pore geometries obtained from molecular dynamics simulations"

selbstständig, ohne unerlaubte Hilfe Dritter angefertigt und andere als die in der Dissertation angegebenen Hilfsmittel nicht benutzt habe. Alle Stellen, die wörtlich oder sinngemäß aus veröffentlichten oder unveröffentlichten Schriften entnommen sind, habe ich als solche kenntlich gemacht. Dritte waren an der inhaltlich-materiellen Erstellung der Dissertation nicht beteiligt; insbesondere habe ich hierfür nicht die Hilfe eines Promotionsberaters in Anspruch genommen. Kein Teil dieser Arbeit ist in einem anderen Promotions- oder Habilitationsverfahren verwendet worden. Mit dem Einsatz von Software zur Erkennung von Plagiaten bin ich einverstanden.

Ort/Datum	Unterschrift
	(Vor- und Nachname)